CHARACTERIZATION OF MATERIALS BY USING IN-SITU AND PRECESSION ELECTRON DIFFRACTION TECHNIQUES IN TEM

PhD Thesis

Umut SAVACI

Eskişehir 2018

CHARACTERIZATION OF MATERIALS BY USING IN-SITU AND PRECESSION ELECTRON DIFFRACTION TECHNIQUES IN TEM

Umut SAVACI

PhD THESIS

Programme in Materials Science and Engineering
Supervisor: Prof. Dr. Servet TURAN

Eskişehir
Anadolu University
Graduate School of Sciences
August 2018

This thesis work is supported by the Scientific Research Project Commission of Anadolu University (Project number 1504F168) and The Scientific and Technological Research Council of Turkey (TUBITAK), Directorate of Science Fellowships and Grant Programmes (BİDEB) 2211 National Ph.D scholarship.

FINAL APPROVAL FOR THESIS

This thesis titled “Characterization of Materials by Using In-situ and Precession Electron Diffraction Techniques in TEM” has been prepared and submitted by Umut SAVACI in partial fulfillment of the requirements in “Anadolu University Directive on Graduate Education and Examination” for the Degree of Doctor of Philosophy (PhD) in Materials Science and Engineering Department has been examined and approved on 09/08/2018.

Committee Members	**Title Name Surname**	**Signature**
Member (Supervisor)	: Prof. Dr. Servet TURAN	.....
Member	: Prof. Dr. Ferhat KARA	.....
Member	: Prof. Dr. Mehmet Ali GÜLGÜN	.....
Member	: Assoc. Prof. Dr. Hilmi YURDAKUL	.....
Member	: Assist. Prof. Dr. Aziz GENÇ	.....

Prof.Dr. Ersin YÜCEL
Director of Graduate School of Sciences

ABSTRACT

CHARACTERIZATION OF MATERIALS BY USING IN-SITU AND PRECESSION ELECTRON DIFFRACTION TECHNIQUES IN TEM

Umut SAVACI

Department of Materials Science and Engineering
Anadolu University, Graduate School of Sciences, August 2018

Supervisor: Prof. Dr. Servet TURAN

The goal of this thesis is the characterization of different type of materials by using in-situ heating for the investigation of sintering behavior and by using precession electron diffraction (PED) method for the determination orientation relations between present phases and phase analysis. In SiC-hBN ceramic composite, orientation relations of in-situ formed hBN with SiC phases, twist boundary character within hBN particles were characterized with PED method. B_4C-TiB_2 composites produced with different methods were investigated. In R-SPS'ed sample, orientation relation between in-situ formed graphite and TiB_2 phases was studied and reactions occur during R'SPS are discussed. In hot pressed samples, addition of WC and different mixing methods resulted in formation of different core-rim type structures were carried out. SEM and XRD results of hot pressed sample showed the variation of microstructure and mechanical properties were measured depending on the pressing direction. In β-SiAlON-cBN ceramic composites orientation relation between in-situ formed hBN transformation layer and cBN particles were investigated to understand its formation mechanism. In X70 petroleum steel, phase analysis of the precipitate particles were studied. In addition to these studies, characterization of Ar implantation into hBN depending on the orientation of particles were carried out. Lastly, in-situ sintering of ZnO nano particles in TEM was studied.

Keywords: Transmission electron Microscope (TEM), Precession electron diffraction (PED), In-situ heating, Orientation relation

ÖZET

GEÇİRİMLİ ELEKTRON MİKROSKOBU İLE İN-SİTU VE DEVİNİMLİ ELEKTRON DİFRAKSİYONU TEKNİKLERİ KULLANILARAK MALZEME KARAKTERİZASYONU

Umut SAVACI

Malzeme Bilimi ve Mühendisliği Anabilim Dalı
Anadolu Üniversitesi, Fen Bilimleri Enstitüsü, Ağustos 2018

Danışman: Prof. Dr. Servet TURAN

Tez çalışmasının amacı farklı türdeki malzemelerin geçirimli elektron mikroskobunda in-situ ısıtma ile sinterleme davranışlarının incelenmesi ve devinimli elektron difraksiyonu (DED) metotları ile karakterizasyonudur. DED yöntemi, yapıda bulunan fazların içindeki ve arasındaki yönlenme ilişkilerinin incelenmesi ve faz analizidir. SiC-hBN seramik kompozit içerisinde in-situ oluşan hBN ve SiC partiküllerinin arasındaki yönlenme ilişkisi ve hBN taneleri içerisinde bulunan burulma sınırı karakteri, farklı yöntemler ile üretilmiş B_4C-TiB_2 kompozitlerde bulunan in-situ oluşmuş grafit ile TiB_2 tanelerinin arasındaki yönlenme, HP ile üretilen örnekte WC ilavesine bağlı olarak oluşan çekirdek-çerçeve tipi yapıların karakterizasyonu ile SEM ve XRD tekniklerine göre mikroyapıdaki yönlenmeye bağlı olarak mekanik özelliklerdeki değişim, β-SiAlON-cBN kompozitinde meydana gelen hBN dönüşüm tabakası ile cBN arasındaki yönlenme ilişkileri incelenmiştir. X70 çeliğinde ise DED yöntemi çökelti taneciklerinin faz doğrulamasında kullanılmıştır. Ayrıca, hBN tanelerinde yönlenmeye bağlı Ar implantasyonu incelenmiştir. Son olarak, ZnO nanotaneciklerinin TEM içerisinde in-situ sinterlenme çalışması yapılmıştır.

Anahtar Sözcükler: Geçirimli elektron mikroskobu (TEM), Devinimli elektron difraksiyonu (DED), İn-situ ısıtma, Yönlenme ilişkisi

Dedicated to My Family

ACKNOWLEDGEMENTS

I would first like to acknowledge and thank my advisor Prof. Dr. Servet TURAN, who encouraged me to solve my problems, for his support and guidance throughout my Ph.D. thesis work in Department of Materials Science and Engineering in Anadolu University. I would also like to thank my thesis committee members, Prof. Dr. Ferhat KARA and Prof. Dr. Mehmet Ali GÜLGÜN for their helps and valuable suggestions.

I would like to thank Rafal BARTOSIEWICS from JEOL, Peter STIEGLER from GATAN, Thanos GALANIS and Spiros PANARETOS from NanoMEGAS for their helps and efforts to train me besides fixing the problems of our microscope.

I would like to acknowledge Dr. Zuhal YILMAZ, Ufuk AKKAŞOĞLU, Simone FAILLA, Oktay ELHOCA (Ereğli Iron and Steel Company), Prof. Dr. Ender SUVACI for providing samples and Dr. Meltem SEZEN, who prepared samples with FIB, Semih ENGÜN and Ahmet Hamdi YAMAK for their help on sample preparation. Moreover I would like to thank Sinem BAŞKUT for keeping the electron microscope laboratory in good condition.

I would also like to acknowledge the financial support from the Scientific Research Project Commission of Anadolu University (grant no:1504F168) and The Scientific and Technological Research Council of Turkey (TUBITAK) Directorate of Science Fellowships and Grant Programmes (BİDEB) 2211 National Ph.D scholarship programme.

Special thanks to my wife Yonca SAVACI, I would not be able to finish this journey without her support and encouragement. Last but not least I want to thank my parents, without their support I would not be here today.

Umut SAVACI

09/08/2018

STATEMENT OF COMPLIANCE WITH ETHICAL PRINCIPLES AND RULES

I hereby truthfully declare that this thesis is an original work prepared by me; that I have behaved in accordance with the scientific ethical principles and rules throughout the stages of preparation, data collection, analysis and presentation of my work; that I have cited the sources of all the data and information that could be obtained within the scope of this study, and included these sources in the references section; and that this study has been scanned for plagiarism with "scientific plagiarism detection program" used by Anadolu University, and that "it does not have any plagiarism" whatsoever. I also declare that, if a case contrary to my declaration is detected in my work at any time, I hereby express my consent to all the ethical and legal consequences that are involved.

Umut SAVACI

TABLE OF CONTENTS

Page

LIST OF FIGURES

Page

LIST OF TABLES

INDEX OF ABBREVIATIONS AND SYMBOLS

// : Parallel

⊥ : Perpendicular

° : Degrees

µ : Microns

AlN : Aluminum nitride

Ar+ : Argon ion

B_4C : Boron carbide

BF : Bright field

BSE : Backscattered Electron

cBN : Cubic Boron Nitride

EDX : Energy dispersive spectroscopy

EELS : Electron energy loss spectroscopy

eV : Electron volt

HAADF: High angle annular dark field

hBN : Hexagonal Boron Nitride

HP : Hot Press

K : Kelvin

keV : Kilo electron volt

NBD : Nano beam diffraction

Pa : Pascal

PED : Precession electron diffraction

ROI : Region of interest

R-SPS : Reaction Spark Plasma Sinter

SEM : Scanning electron microscope

SiC : Silicon carbide

STEM : Scanning Transmission Electron Microscope

TEM : Transmission electron microscope

TiB_2 : Titanium diboride

TiC : Titanium carbide

VBF : Virtual bright field

W : Tungsten

WC : Tungsten carbide

XRD : X-ray diffraction

ZnO : Zinc oxide

ΔG : Change in Gibbs free energy

1. INTRODUCTION

Structure and property relation is possibly the most important relation in materials tetrahedron since this relation directly affects the performance of the material and this relation cannot be understood without microstructural characterization.

Properties of the materials can be modified with changing variables in structure of the material and production processes. For example; depending on the boundary angle between grains mechanical properties of the bulk material can be changed and low angle grain boundaries resulted in higher mechanical properties compared to the same structure having high angle grain boundaries. Electrical properties of the materials also are affected from the change in grain boundary energies that is, special boundaries having low boundary energy even if they have high misorientation angles, resulted in better electrical properties of bulk material [1]. In composite materials bonding characteristic is important due to the increased mechanical properties with better bonding between reinforcement and matrix materials [1-3]. These examples show the direct effect of structural changes on the properties of materials and production processes that can change the structure during manufacturing also affect the final properties. For example, pressure-less and pressure assisted sintering methods resulted in different microstructures. Pressure assisted methods like hot pressing and spark plasma sintering, resulted in grains which are elongated in one direction and having preferred orientation. Many of the material properties such as Young's modulus, toughness, electrical conductivity and thermal expansion vary depending on the preferred orientation of the microstructure. Because of the significant effects of microstructural features on the bulk properties as stated above, characterization of this type of features has become very important to reveal relation between structure and property, and such knowledge led to the development of the new materials. In literature, such properties were characterized locally with orientation imaging methods with mainly using scanning electron microscopes.

1.1. In-Situ Electron Microscopy

In addition to the microstructural relations between grains stated above, properties of each grain such as its' size and morphology, have significant effect on the bulk properties like mechanical properties therefore they should be tailored depending on the required bulk properties. Grain size of the bulk material can be changed during sintering

of loose ceramic powders with process parameters such as sintering time and temperature. It is possible to predict optimum process parameters for required properties by using kinetic models, however these models become fail when nano scale particles are used. In order to obtain optimum process parameters for nanoscale powders, a lot of experiments should be done, at the expense of labor and time losses. In order to understand the kinetic behavior during sintering, in-situ experiments should be done that is sintering is carried out while observing the microstructural changes in electron microscopes.

From the beginning of the invention of first electron microscope all structural characterizations were done at static conditions inside microscope and the structural changes during dynamical processes are investigated by the comparison of the structure before and after dynamical effect. Same is also true for the production processes and working conditions, during production or working conditions of a certain material, effect of various parameters are investigated after each change. With this type of *"ex-situ"* characterizations in electron microscopy, structure-property relations are made with information obtained before and after dynamical effect without knowing what exactly happens during intermediate stage. In order to find out what exactly happens in the microstructure, *"in-situ"* characterization of the sample during certain dynamical effect needs to be done. In the last decade with the developing technology, in-situ experiments within TEM become possible with various sample holders. Currently, there are several different types of sample holders to conduct heating, cooling, biasing, mechanical deformation as well as provide gaseous and liquid atmospheres inside electron microscopes during imaging and spectroscopic characterizations.

The aim of this study is *"phase identification, characterization of orientation relations and grain boundary characteristics between phases present in various materials with orientation imaging method by using newly developed precession electron diffraction method and characterization of sintering behavior of ZnO nanoparticles produced with MicNo® method with in-situ heating attachment in TEM".*

1.2. Structure of the Thesis

This thesis contains eight chapters followed by a references section. In each chapter, different materials systems were studied therefore, each chapter has its own introduction and conclusions sections. This general introduction chapter is followed by Chapter 2 that provides definition of texture with its characterization and representation methods as well

as definition of in-situ TEM experiments and summary of literature about in-situ heating experiments in TEM.

In Chapter 3 details about characterization and sample preparation methods used in this thesis are given. Experimental details about Precession electron diffraction method and description of results given by ASTAR^{TM} are discussed.

In chapter 4, detailed conventional TEM/STEM and precession electron diffraction characterizations of SiC-hBN ceramic composites are given. Orientation relationship between present phases as well as defects within hBN particles were characterized with TEM-PED method including related grain boundary characteristics are given. Additionally, delamination defects of hBN formed during production of composites and orientation dependent Ar implantation into hBN during sample preparation were discussed.

In chapter 5, Detailed characterizations of B_4C-TiB_2 composites prepared with both reaction spark plasma sintering (R-SPS) and hot pressing are given. R-SPS'ed samples contains additional phases within the system due to the reactions occurring during sintering and their formation mechanism and additionally orientation relation between graphite and TiB2 phases are discussed. Microstructural characterizations and effects of pressing on directional properties of hot pressed composited were done by conventional SEM, TEM, XRD as well as advanced TEM-PED method and these results are given and discussed.

In chapter 6 characterizations of hBN transformation layer around cBN particles added to the SiAlON composite done by SEM, TEM and Raman spectroscopy are presented and orientation relationship between hBN and cBN phases obtained by using TEM-PED method are discussed in order to understand the transformation mechanism. During these analyses orientation mapping of SiAlON particles were carried out for the first time in the literature.

In the following chapter phase analysis results of precipitate particle found in the petroleum steel by TEM-PED method in order to confirm which phase is formed during production are given.

In the 8th Chapter, Ar ion implantation into the hBN particles which found in the samples studied in this thesis

Finally in the 9th Chapter, in-situ sintering results of nano sized ZnO particle produced with MicNo® methodology are given and discussed.

2. BACKGROUND

2.1. Texture

Great majority of the materials in nature are crystalline in solid state and they composed of small crystalline building blocks called as “grain”. Most of the materials are formed with combination of many individual crystalline grains and called as “polycrystalline”. “Orientation” of the grains is defined with the relative positions of each grain with respect to each other. In polycrystalline materials, these building blocks can be oriented either “randomly” or with a “special relation” with respect to each other. As a result of the thermomechanical production processes, grains have tendency to have “preferred orientation” and this phenomenon results in the presence of “texture” in the microstructure of material. Figure 2.1 shows the microstructure of a steel with randomly oriented grains and textured microstructure having grains in a preferred orientation along rolling direction after rolling process.

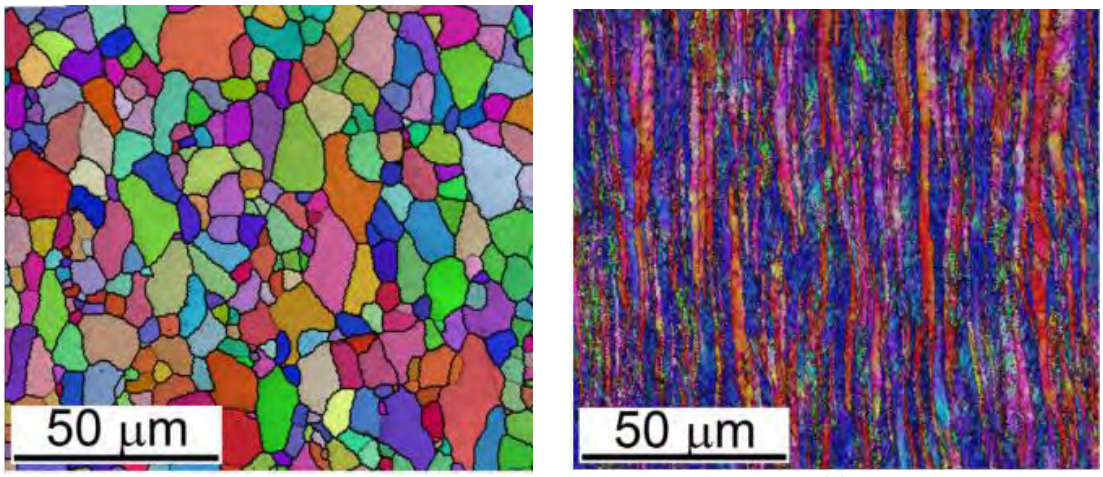

(a) **(b)**

Figure 2.1. *Orientation imaging results of (a) randomly oriented and (b) textured iron [4]*

2.1.1. Representation of texture

Crystallographic texture representation is done for the characterization of preferential orientations without taking into consideration of their morphology, size etc. Texture characterization methods, which will be covered in Section 2.2, mostly give an overall and relative information, like orientation maps, about texture at first sight, however with the representation of texture of grains/crystals with different methods additional and valuable information can be extracted from the orientation maps. For

example, characterization of orientation relation between specific grains can be valuable more than the overall texture of the material. For this purpose, texture can be represented in numerous ways like Miller notation, pole figure, inverse pole figure, Euler angles etc.

Before going into details about how texture is represented, it is worth to define the Cartesian coordinate systems used for representation. Sample coordinate system consist of three axes called as rolling direction (RD), transverse direction (TD) and normal direction (ND) [5]. Second coordinate system is called as crystal coordinate system and its axes are defined as [100], [010], [001] for orthogonal symmetry and $[10\bar{1}0]$, $[\bar{1}2\bar{1}0]$, [0001] for hexagonal and trigonal symmetry [5]. The representation of orientation is defined as *"the position of the crystal of the coordinate system with respect to the specimen coordinate system"* and this process is done with proper rotation of the reference coordinate systems called as rotation matrix [5].

One of the most practical representation of texture is done by the Miller (or Miller-Bravais or Ideal Orientation) notation as {hkl}<uvw> or (hkl)[uvw]. In this notation (hkl) plane normal is parallel to normal direction, in other words (hkl) planes are parallel to rolling direction and [uvw] direction is parallel to rolling direction [6]. Representation of Miller notation is given in Figure 2.2.

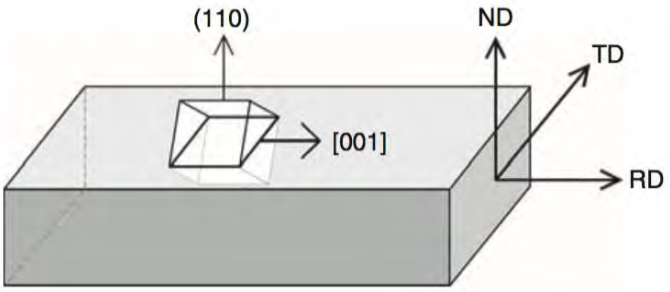

Figure 2.2. *Representation of (110)[001] oriented crystal in specimen coordinate system [5]*

Orientation of every single grain/crystal within the polycrystalline material can be described with this notation; in addition, it is possible to represent overall texture of the material with the expression given below, where w_i is weighting factor [6].

$$\text{Overall Texture} = \sum w_i \cdot \{hkl\}_i \cdot \langle uvw \rangle_i \qquad (2.1)$$

Pole figure representation is another most commonly used method for the texture representation especially in EBSD analysis. Pole figure is a stereographic representation of specific orientation of crystal and to interpret the pole figure, first stereographic projection needs to be understood. Stereographic projection is used for the representation of three-dimensional orientation information in two-dimensional plane e.g. paper and resulted figure is called as stereogram. For example, an orientation of a plane is represented in a three-dimensional reference sphere and normal of this plane intersect with surface of reference sphere, that point in the reference sphere is projected into a two-dimensional plane, which is placed in equatorial plane of reference sphere, with stereographic projection as drawing a line from the point in the sphere to the opposite pole point of sphere (e.g. if normal of an arbitrary plane cross at the north hemisphere surface, other end of the line have to intersect with south hemisphere pole point) and intersection of line with the equatorial plane is the stereographic projection representation of this plane. Three-dimensional unit cell can also be represented with stereogram. In that case poles of the reference sphere are the faces of the unit cell i.e. (001), (010), (001) for cubic system as shown in Figure 2.3.

Pole figure is used for the representation of crystal coordinate system in specimen coordinate system and it is basically nothing but the stereogram with specific poles which are same with the sample reference system called RD, TD, ND (as shown in Figure 2.4) and their positions are same with (100), (010), (001), respectively. In pole figure, every single direction/plane normal is shown as a point and cubic unit cell is represented with 3 points for a single orientation.

Inverse pole figure is another way to represent a crystal orientation and it shows the distribution of directions in the sample and help to visualize different types of textures. In contrast to the pole figure, inverse pole figure represents the coordinate system in specimen coordinate system. Example of an inverse pole figure is given in Figure 2.5 (a). According to the symmetry of crystal inverse pole figure divided into smaller triangles with equivalent orientation information called as standard triangle and it is worth to note that crystal symmetry defines the poles of standard triangle [5, 7].

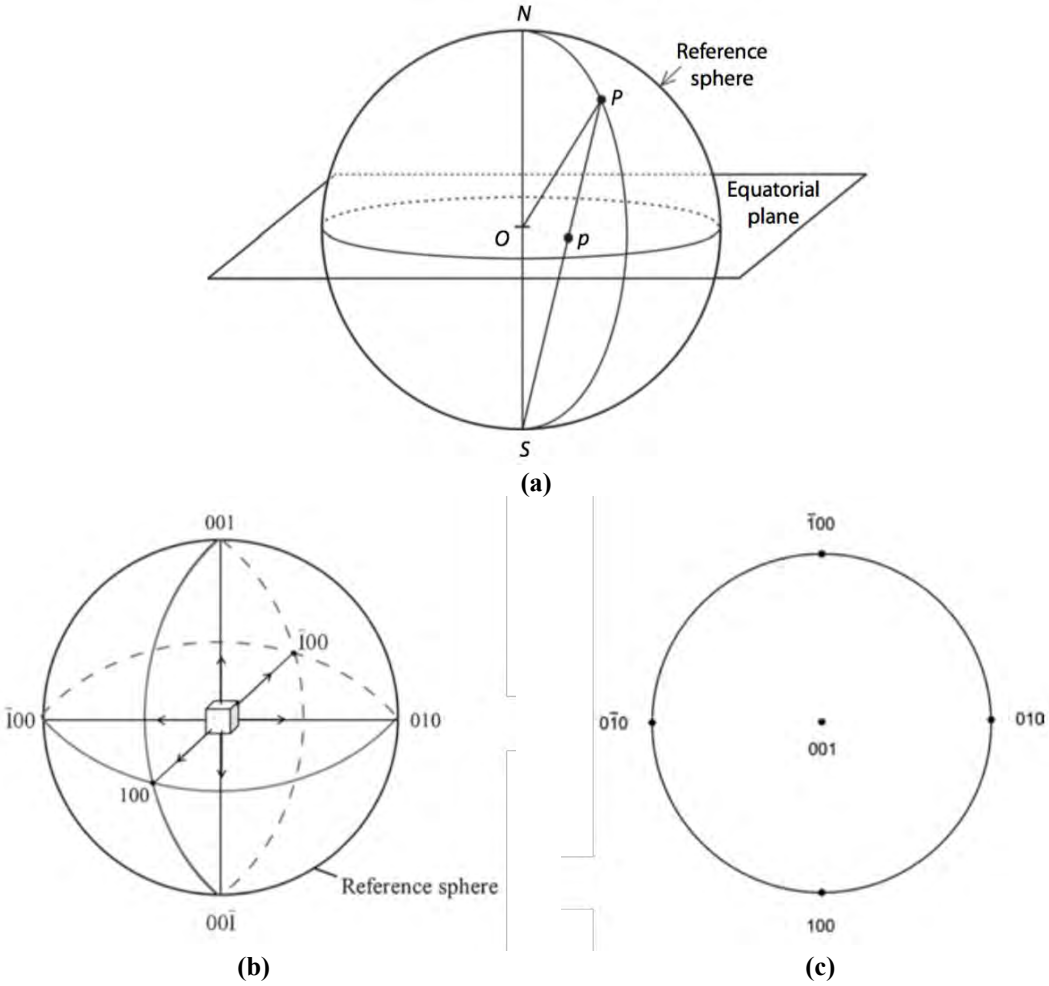

Figure 2.3. *(a) Stereographic projection of a plane [5], (b) Cubic unit cell within reference sphere and (c) equatorial plane of (b) [6]*

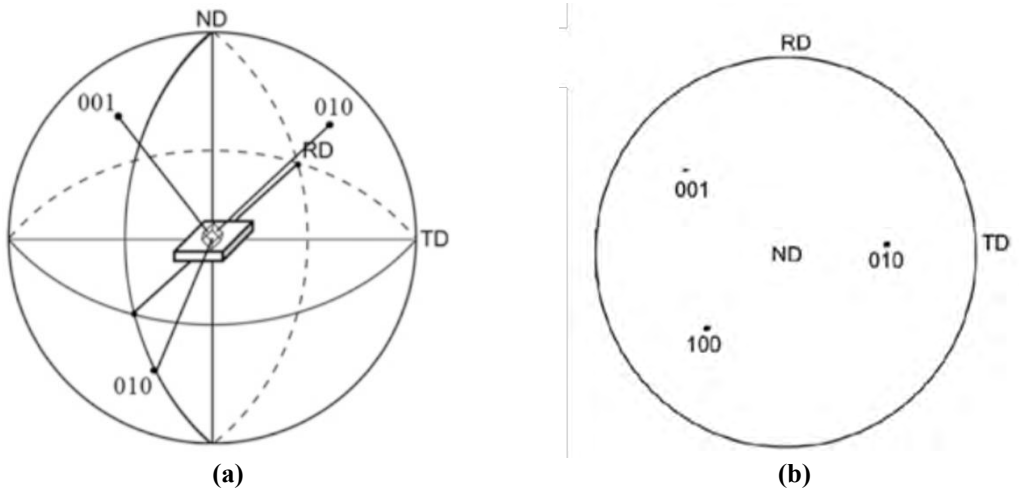

Figure 2.4. *(a) Pole figure with specimen coordinate system with a grain having an arbitrary orientation and (b) projection plane of the pole figure, three dots describe the orientation of the grain in two-dimensional space [6]*

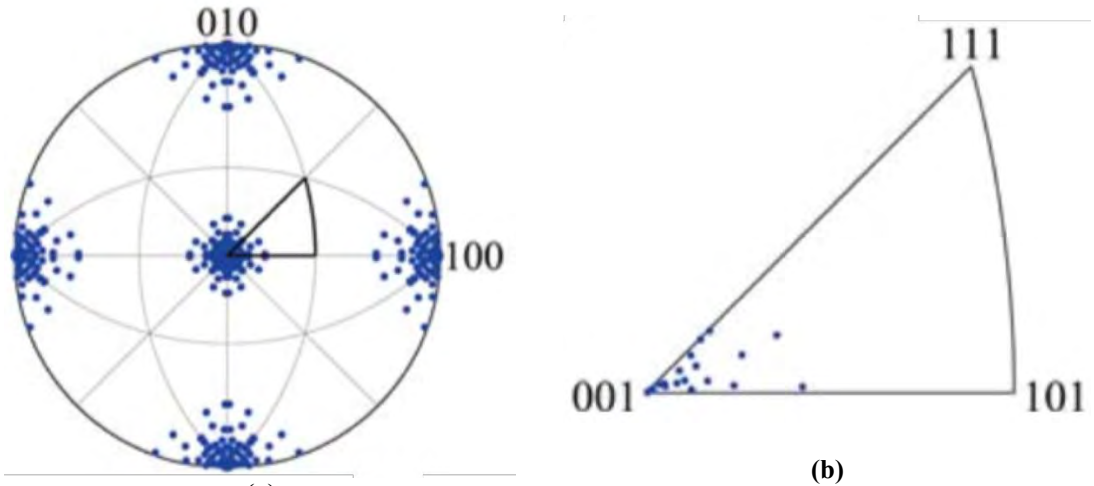

Figure 2.5. *(a) Inverse pole figure of a material with (001) orientation and (b) standard triangle of inverse pole figure that shows the (001) orientation of different grains with dots [7]*

Euler representation is an alternative way to represent an orientation. In this representation sample coordinate system is transformed to specimen crystal system with series of rotations around specified axes with specified angles (φ_1, Φ, φ_2) called as Euler angles, defined by Bunge [5]. In this notation, every orientation is represented with different Euler angles, thus grains in the orientation maps with different colors have different Euler angles and orientations, vice versa grains with same Euler angle represented with same color. Summary of the rotation operations and its sequence can be seen in Figure 2.6 and details about the rotation operations can be found elsewhere [5-7].

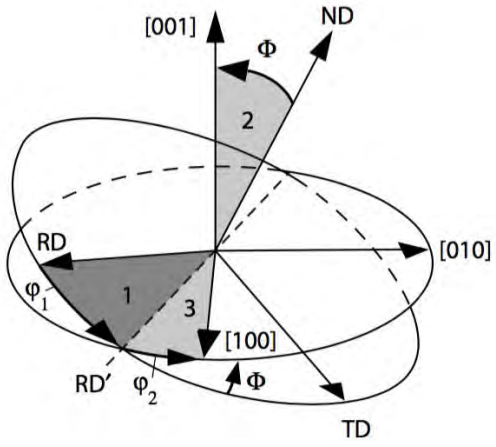

Figure 2.6. *Sequence of rotation operations for sample coordinate system that describes the Euler angles [5]*

2.1.1.1. Texture analysis in hexagonal materials

Hexagonal crystal system is defined with an axial relation of a=b≠c and α=β=90°, γ=120° interaxial angles as shown in Figure 2.7. In hexagonal crystal system three axes (a_1,a_2, a_3) exist within the same plane, called as basal plane, with an angle of 120° each other and z axis is perpendicular to basal plane, because of this reason conventional three index notation [u'v'w'] cannot be used and it needs to be converted into new Miller-Bravais four index notation [uvtw] where t = -(u+v).

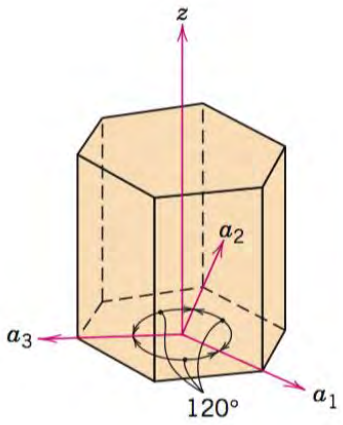

Figure 2.7. *Hexagonal crystal system [8]*

Due to the Miller-Bravais four index system in hexagonal system, texture in hexagonal materials is represented as {hkil}<uvtw> or (hkil)[uvtw], and in that notation {hkil} planes are parallel to sheet plane and <uvtw> direction is parallel to rolling direction [6]. Due to the change of notations in hexagonal systems, overall texture notation is also modified and given in (2.2.

$$\text{Overall Texture} = \sum w_i \cdot \{hkil\}_i \cdot \langle uvtw \rangle_i \qquad (2.2)$$

The relation between the Euler angles of Bunge system (ϕ_1, ϕ, ϕ_2) and {hkil}<uvtw> is given in (2.3 and (2.4 according to [9]. In hexagonal crystal systems, pole figure representation has some limitations. These limitations arisen due to the change in miller indices of crystallographic plane and its normal direction for many planes and indexing texture components become difficult. To solve that problem double stereogram, that is constructed with plane normal and direction projections, needs to be used [6].

$$\begin{bmatrix} h \\ k \\ i \\ l \end{bmatrix} = \begin{bmatrix} \frac{\sqrt{3}}{2} & -\frac{1}{2} & 0 \\ 0 & 1 & 0 \\ -\frac{\sqrt{3}}{2} & -\frac{1}{2} & 0 \\ 0 & 0 & c/a \end{bmatrix} x \begin{bmatrix} \sin\phi_2 \sin\phi \\ \cos\phi_2 \sin\phi \\ \cos\phi \end{bmatrix} \quad (2.3)$$

$$\begin{bmatrix} u \\ v \\ t \\ w \end{bmatrix} = \begin{bmatrix} \frac{2}{3} & -\frac{1}{3} & 0 \\ 0 & \frac{2}{3} & 0 \\ -\frac{2}{3} & -\frac{1}{3} & 0 \\ 0 & 0 & c/a \end{bmatrix} x \begin{bmatrix} \cos\phi_1 \cos\phi_2 - \sin\phi_1 \sin\phi_2 \cos\phi \\ -\cos\phi_1 \sin\phi_2 - \sin\phi_1 \cos\phi_2 \cos\phi \\ \sin\phi_1 \sin\phi \end{bmatrix} \quad (2.4)$$

2.2. How to Characterize Texture?

Texture characterization methods can be divided into two categories according to the reconstruction of the microstructure; microscopic and non-microscopic methods. Non-microscopic methods are basically a technique that does not require any type of microscopy to do analyses though there is no reconstruction of microstructure that gives visual representation of textured microstructure, distribution etc.

2.2.1. Non-microscopic orientation determination methods

X-ray diffraction is the most widely used non-microscopic orientation determination method and this method is utilized by the use of x-ray diffraction with a known wavelength, mostly Cu or Mo-alpha radiation, and special texture goniometer. In this method, sample is irradiated with X-rays and reflected X-rays, according to the Bragg's law, collected at the goniometer and pole figures are formed by systematic rotation of sample. Formed pole figures are the average of all crystals within the X-ray's penetration depth, which is about 100 μm, it is not possible to determine a site specific orientation and it's distribution. Additionally because of the high penetration depth this method is mainly referred as macrotexture determination method [5]. Even though this method can be applied to the crystals of micrometer range, however due to the broadening and peak shift diffraction patterns become less characteristic and application of this method become complicated [10].

2.2.2. Microscopic orientation determination methods

Microscopic orientation determination methods can be mainly divided into two categories depending on which equipment is used, these are SEM and TEM based methods.

2.2.2.1. SEM based methods

In SEM electron backscatter diffraction (EBSD) technique electrons in primary beam (mostly from a field emission source) is scattered from lattices inside of crystal structure and creates Kikuchi cones with a specific distances and intensity variations between Kikuchi lines/bands. In this method, electron beam is scanned across the region of interest (ROI) in a flat, polished surface and back scattered Kikuchi bands are collected from the phosphorus screen and then Kikuchi pattern at each pixel is indexed through software packages. The interaction volume of the primary beam basically determines the spatial resolution of this technique. The resolution can be 50 to 200 nm depending on the density and atomic number of the inspected material and accelerating voltage of SEM. Additionally this method provides 0.5° to 1° of angular resolution. Even though this method is widely used the resolution of this method is not suitable for nano scale features in the structure.

The spatial resolution limitation of EBSD method can be improved by the use of transmitted Kikuchi diffraction (TKD) method by using an electron transparent sample. In this method forward scattered Kikuchi patterns are collected below the sample instead of EBSD that use back scattered Kikuchi patterns. Since electron transparent samples are used in this method, smaller diffraction volume is the key parameter to improve lateral resolution to 2 nm depending to atomic number and density of the investigated sample [11, 12].

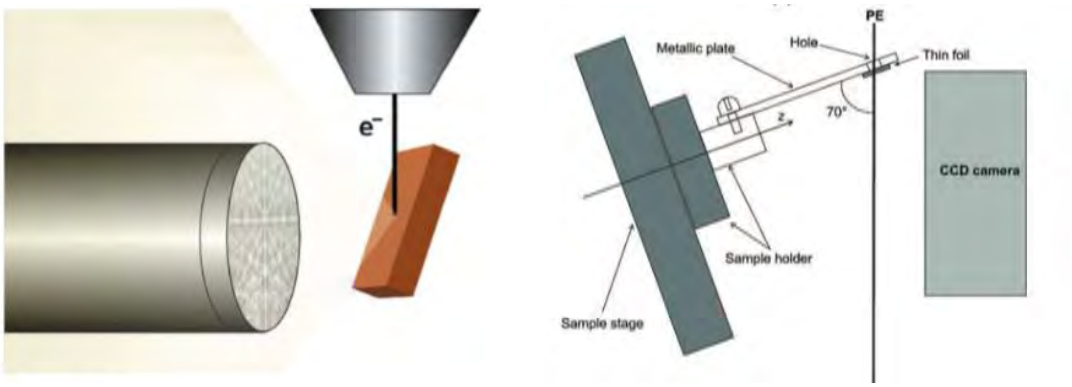

(a) **(b)**

Figure 2.8. *Schematic view of (a) EBSD [7] and (b) TKD [12] sample-camera configurations*

2.2.2.2. TEM based methods

Transmission electron microscope based orientation determination techniques can be divided into two distinct categories according to the application; automated or non-automated methods. Non-automated orientation determination methods include acquisition of Kikuchi diffraction patterns, selected area electron diffraction (SAED) patterns and small angle convergent beam electron diffraction (SCBED or micro/nano beam) patterns. Automated methods are the acquisition of spot patterns with electron beam precession (PED) and conical dark field scanning (CDFS).

(i) Non-automated orientation determination methods

Non-automated orientation determination methods include acquisition of Kikuchi diffraction patterns (KDP), selected area electron diffraction (SAED) patterns and small angle convergent beam electron diffraction (SCBED or micro/nano beam) patterns.

Transmitted Kikuchi diffraction pattern (KDP) method is similar to the EBSD method in that physical principles in formation; coherent scattering of primary beam at the lattice. However, Kikuchi patterns have a few advantages over other TEM based methods. One advantage is the very high angular resolution. In this method orientation is calculated from the Kikuchi diffraction patterns and sharpness of the Kikuchi lines determines the angular resolution and with an application of appropriate line recognition algorithm angular resolution can reach up to 0.01°. Another advantage is the absence of the 180° ambiguities (will be explained in Section 3.5.1) in the Kikuchi patterns. Besides its advantages there are several disadvantages. Very high angular resolution of this method turns into the biggest disadvantage that is the sensitivity to defect density that

cause the detoriation of Kikuchi pattern quality. Another problem is the requirement of extreme thinness to obtain high lateral resolution. Last but not least, small solid angle of the patterns limits the orientation determination. Because of these disadvantages this method has been made redundant [13].

Another orientation determination method in TEM is the use of selected area electron diffraction (SAED) patterns which is obtained by the illumination of thin specimen with a parallel electron beam. If there is a texture present in the sample diffraction pattern become arched as incomplete Debye Scherrer rings due to the specific orientation of the grains cause specific lattice planes to satisfy Bragg's condition as shown in Figure 2.9. However, the texture of the investigated sample cannot be interpreted completely from the single diffractogramme thus series of diffractogrammes needs to be acquired by tilting. The intensity distribution of the rings represents to pole density distribution however dynamical diffraction within sample become hard to interpret intensity distribution [14].

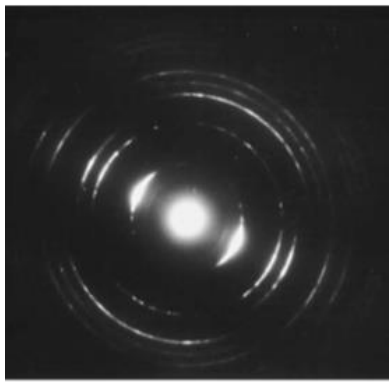

Figure 2.9. *Polycrystalline diffraction pattern of textured material [15]*

Additionally, misorientation angle between more than one grains can be interpreted from the SAED patterns after tilting to the special common zone axis of the grains however if misorientation between hundreds of grains needs to be characterized this method become a time consuming process [16]. SAED method is actually used for orientation determination rather than orientation microscopy because of its' disadvantages. This method has very low lateral (Spatial?) resolution of 0.5µm due to the aberrations present in the objective lens and additionally angular resolution is limited to 3°, which limits to precise determination of orientations. Lastly, necessity of selected area

aperture movement to scan a ROI over the sample become this technique rather difficult [13].

The lateral resolution can be increased by the use of micro/nano beam or small angle convergent beam to obtain diffraction patterns (SCBED). In this method, instead of using a convergent beam with a large convergence angle obtained with large condenser aperture that gives diffraction (CBED) disks instead of spots, electron beam is focused onto the sample with a small convergence angle by using small condenser aperture to shrink CBED disks into a sharp diffraction spots as in SAED method. This method make orientation determination of small grains (minimum 10 nm) become possible and also insensitive to the defect density compared with the KDP method however diffraction patterns suffers from the 180° ambiguity problem [13].

(ii) Automated orientation determination methods

Aforementioned TEM orientation determination methods are non-automated methods and they are difficult to apply to a large ROI with high lateral resolution. Besides the SCBED method it is also possible to obtain indirect convergent beam with a focused primary beam called as precession electron diffraction method due to the precession movement of electron beam and it gives focused diffraction spots as in SAED. Basically, there are two main advantages of this method is to obtain higher order Laue zones to become visible and the dynamical diffraction effects are minimized thus diffraction spot intensity distribution can be treated as quasi-kinematical or kinematical diffraction patterns to interpret orientations with a very high lateral resolution of few nanometers. This method also allows users to scan a custom defined ROI over the sample. Details of the precession electron diffraction will be given in the following section.

The last method is the conical dark field scanning method which utilized in STEM by using a conical beam scanned across the ROI and while this dark field images are acquired and then diffraction patterns are reconstructed at the basis of dark field images. Even though this method has a lateral resolution above 1 nm, sample drift and microscope misalignment during very long (~2 hours) acquisition times and unavoidable dynamical diffraction effects on the diffraction patterns made this method become unpractical for orientation determination [13].

2.3. Precession Electron Diffraction

Electron diffraction is widely used for structure determination, solving and refinement using diffracted spot intensities. The main principle for doing that is the correlation between kinematic diffraction intensities and materials structure factors. However, in TEM it is hard to obtain kinematic electron diffraction patterns, due to the sample thickness and strong interaction between electrons and atoms resulted in the dynamical (multiple) scattering within the sample. As a result of the dynamical diffraction, diffracted intensities cannot be used to interpret crystal structure [17].

Electron beam precession (or precession electron diffraction) method was invented by P. Midgley to minimize the dynamical character and increase the kinematical character of the electron diffraction in TEM. For doing this, electron beam is tilted at fixed angle (few angles depending to TEM) with optical axis and precessed to form a hollow cone above the sample and below the sample electron beam is de-scanned to form a stationary diffraction pattern image. Ray diagram of PED is given in Figure 2.10. The resulted image is considered as kinematical and effects of dynamical diffraction like forbidden reflections are eliminated.

The combination of PED, scanning a nanoprobe over the sample while using TEM scanning coils leads to make PED assisted automated crystal orientation mapping (ACOM) method in TEM. The data cube is formed by collecting kinematical diffraction patterns at every pixel with a defined step size across the sample surface. This method is commercialized as ASTAR by NanoMEGAS company (Brussels, Belgium). ASTAR system composed of scan generator (called as DigiSTAR), high speed CCD camera and a computer for scan control and data collection. Even though this method is usually called as ASTAR due to its commercialized name from NanoMEGAS, it can also be called with different names like ACOM, PACOM, IFPOM, D-STEM and SPED in the literature [18].

The data cube obtained from a scan contains diffraction pattern for each pixel and it needs to be decoded by template matching strategy. The diffraction pattern is solved by template matching. During template matching, pre-formed kinematical diffraction pattern templates for a given structure are compared with the experimental diffraction patterns via comparison of spot positions and their intensities [18]. Details about the template matching will be given in Section 3.

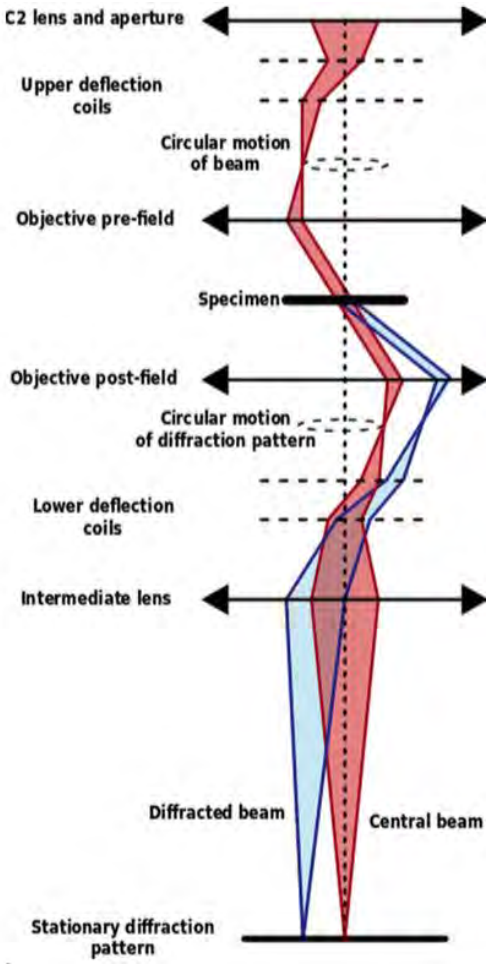

Figure 2.10. *Ray diagram for precession electron diffraction [17]*

The spatial resolution of this method is limited by the minimum probe size that can be formed in TEM. It is possible to obtain 0.5 nm parallel probe size recent FEG-TEMs however it increases for LaB_6 or W sources. The angular resolution however is not limited by TEM, it is limited with angular step size during template formation, which is 1° [18].

Even though this method has significant importance due to its high resolution, the main challenge is the overlapped grains or crystals that cause two or more different diffraction spots are overlapped within a single image and in such case template matching become inaccurate [19].

Application areas of this method is not only limited with phase and orientation mapping in TEM, but it can also be used for structure refinement via diffraction tomography (ADT-3D) [20], determination of space and point group symmetries [21],

EELS [22] and EDS [23] signal enhancement, chemical bonding determination [24] and strain mapping [25] with appropriate attachments.

2.4. In-Situ Heating in TEM

Almost all materials production processes and working conditions include heating of materials from room temperatures to above thousand degrees. For example, microstructures of metallic and glass materials can be modified up to a thousand degrees in order to modify properties of the product and in order to find out the optimum process conditions quite a lot of experiments needs to be conducted depending on the application and material. In-situ characterization of materials during the heating process can reduce the required experiments thus save labor and cost while providing valuable information about structural changes. Because of these reasons stated above, in-situ heating sample holders are possibly the most widely used in the literature and probably they are the first type of in-situ sample holders used in TEM. First commercial in-situ heating holders used in TEM was furnace based holders, it can be thought as miniature furnace placed in the sample holder and samples placed with special grid. These holders can reach up to 1200°C however, their temperature accuracy were low and requires time for temperature and drift stabilization, which makes them not appropriate for relatively fast changes [26, 27]. With technology, furnace based heating holders replaced with holders that use micro electro mechanical systems (MEMS) chips for heating the sample up to 1500°C which opens wide range of new experiments due to very high heating and cooling rates (about 1000°C/s) as well as high temperature accuracy (<0.1°C) [28]. With this type of in-situ heating holders, characterizations during experiments like phase transformations, solid reactions, nanoparticle or bulk material sintering and grain growth behavior, heat treatment and crystallization become possible at high resolution with imaging and spectroscopic techniques.

In the literature there are several in-situ heating experiments and increasing exponentially due to significance of information gather. Thermal stability of various materials such as perovskite solar cells [29], during working conditions can be simulated and mechanism behind thermal degradation can be understood, which can be crucial to improve properties and life of materials. In the literature thermal stability of perovskite solar cells at operation temperatures were investigated and mechanism behind the

photovoltaic performance degradation was understood [29]. Similar methodology was applied in order to investigate;

(i) Shape stability of PtNi nano catalysts used for oxygen reduction that affect the catalyst performance [30],

(ii) Morphological stability of CdSe/CdS octapods at elevated temperatures that can change the electronic properties in photovoltaic applications [31],

(iii) Stability variations Au nano particles having different aspect ratios [32],

(iv) Precipitate formation and its dissolution in AA2024 Al alloy during heat treatment [33],

(v) Phase transformation mechanisms between orthogonal, tetragonal and cubic structure were studied during heating of $SrRuO_3$ [34].

Investigations of solid-solid interactions at elevated temperatures can be also studies and in the literature;

(i) Reaction between Si and graphite was done to understand SiC formation mechanism [35],

(ii) Epitaxial growth at the interface between CdSe and Au [36],

(iii) Formation of CdSe-CdS-ZnS core multishell formation with Zn diffusion [37],

(iv) Epitaxial growth of PbSe nanocrystals over CdSe with solid-solid-vapor growth mechanism [38] were monitored.

Last but not least, in-situ sintering of nanoparticles such as MgO [39], ZrO_2 [40], Ag [41], Ni [42] and Pt [43] were studied in order to understand the sintering mechanisms and kinetics, which is quite important since theoretical sintering models may fail at nanoscale. It is worth to noting that these studies are just a small fraction of the literature to give information about the capabilities and importance of in-situ heating experiments.

3. EXPERIMENTAL DETAILS

In this section details of the characterization methods used in this thesis is given.

3.1. Scanning Electron Microscopy (SEM)

In this thesis, SEM was used to understand the general features present in the samples that will be analyzed in TEM. For this purpose, Zeiss Supra 50-VP SEM, attached with secondary electron (SE), back-scattered electron (BSE) and in-lens imaging detectors as well as Oxford Instruments 7430 energy dispersive X-ray spectrometer (EDX), was used at various accelerating voltages from 5 keV to 20 keV. During the SEM analyses to prevent surface charging of non-conductive samples, variable pressure (VP) option of microscope was used instead of conductive coating, which can hinder contrast differences and cause characteristic X-ray absorption during qualitative and quantitative EDX analyses. In VP mode sample chamber pressure increased up to certain pressure with N_2 gas and gas molecules are ionized to positively charged particles under electron beam. These positively charge ions can decrease the surface charging caused by negatively charged electrons by charge neutralization of surface.

SE and BSE imaging methods are commonly used SEM imaging techniques in order to obtain topographic and atomic number contrast, respectively; however, in-lens imaging is less frequently used technique. In lens detector is placed within the column of the SEM and electrons generated only from the surface of the sample are used for imaging. Because of this reason, direct surface information is collected. This imaging method become very important in the presence of any crystal structure that cause electron channeling effect such as graphite and hexagonal boron nitride. Electron channeling reduce the number of electrons generated from the scanned area and effects of this phenomena clearly visible in images obtained with in-lens detector since they are formed directly with scattered electrons from surface. Thus since the number of scattered electrons are decreased, any feature that cause channeling become black in this type of images [44-47].

3.2. TEM/STEM

In this thesis, JEOL™ JEM 2100F field emission transmission electron microscope (TEM) was used. The TEM was operated at 200 keV accelerating voltage and it is

equipped with Fischione 3000 STEM high angle annular dark field (HAADF) detector and Gatan™ bright field (BF) detector, as well as JEOL™ JED2300T energy dispersive X-ray spectrometer (EDX) and Gatan™ GIF Tridiem electron energy loss spectrometer (EELS). Precession electron diffraction unit from NanoMEGAS™ with Digistar P1000 scan generator and ASTAR V2 software package was retrofitted to this microscope.

3.3. Sample Preparation Methods

Sample preparation methods can be used into two distinct groups depending on the type of the electron microscope that used in this thesis. These are;

- Scanning electron microscopy sample preparation methods
- Transmission electron microscopy sample preparation methods

3.3.1. Sample preparation for sem analyses

In this thesis, SEM was used for mainly prior analysis of the samples before TEM to understand present microstructural features and for this purpose, flat and polished surfaces need to be used. Mainly SEM sample preparation steps can be divided into four distinct steps. First step is sectioning or cutting of the representative pieces from bulk and big sample, which was done by Buehler Isomet-1000 cutting equipment with diamond impregnated discs. Next step is mounting of small samples for better handling and to apply uniform pressure during polishing by using either cold mounting resins (e.g. epoxy or polyester) or bakelite hot mounting resin. Final step is the polishing of mounted samples by using Struers Tegrapol-25 automatic polisher with colloidal suspensions which contain various sizes (9, 3 and 1 μm) of synthetic diamond particles. In this step, polishing starts with the 9 μm diamond suspension followed by 3 μm and 1 μm suspensions with synthetic polishing felts to obtain mirror-like surfaces.

In addition to the conventional SEM sample preparation method, which is described above, advanced ion beam polishing by using accelerated Ar ions with Jeol SM-09010 cross-section polisher was used. Advantage of this method over the conventional preparation is no mechanical force and friction are applied to sample during polishing process, thus pull out of the grains or any other structural feature as well as any surface damage is prevented.

3.3.2. Sample preparation for TEM analyses

Sample preparation methods for TEM were completely different compared to SEM analyses due to the nature of TEM working principle. One and the most important pre-requisite for TEM samples is the sample thickness; that is, it must be thin enough to obtain electron transparency. And of course, representativeness of sample, that is analyzed small region should be represent the whole sample, is important. During sample preparation procedures, an additional care must be taken in order not to produce any additional defect or structural changes. Electron transparency of the bulk samples were obtained with conventional mechanical thinning followed by Ar+ ion beam milling.

This procedure starts with the cutting of bulk samples (at least 3x3x3 mm^3) into smaller pieces which has a thickness between 500 μm to 1 mm by using Buehler Isomet 1000 high precision disc cutter with diamond embedded cutting disc. These pieces then thinned down to ≈250 μm thickness by using SiC grinding papers or diamond embedded grinding discs. In this step, it is important to maintain the parallelism of both surfaces for further procedures. Next step is the cutting of samples into circles with 3mm diameter, which is the only geometry that TEM sample holder allow to be inserted into microscope, by using South Bay Technology-Sonicut 380 ultrasonic disc cutter with the help of B_4C abrasive particles. Even though geometrically sample is ready for TEM, thickness is still not enough for ion beam milling. For ion milling, sample thickness should be decreased down to ≈ 25 μm and for this purpose Gatan Disc Grinder and diamond embedded lapping films with 30, 15, 9, 6, 3 and 1 μm diamond particles were used under flowing water lubricant. In this step both side of the samples were also polished. After this step, electron transparency was obtained with Bal-Tec Res 101 Ar^+ ion beam milling which uses ionized Ar gas and ions are focused and accelerated towards sample with various accelerating voltages (from 2 kV to 8 kV) by using two ion guns located at each side of the sample with angles from 4° to 8°. During this process, accelerated Ar^+ hit the sample and cause the removal of surface atoms and as a result, electron transparent region with a thickness below 100 nm is obtained. At the start of ion milling highest accelerating voltages with high angle were used to increase the material removal rate and milling angle as well as accelerating voltages were decreased gradually after the semi-transparent sample was obtained.

Electron transparent samples were also prepared by focused ion beam (FIB) method that is basically like a modified SEM with a Ga ion gun inside the column. Instead of Ar

ions in ion beam milling, Ga ions are used for material removal. This configuration allows site specific samples to be prepared while observing with SEM. In this thesis, FIB samples from polished bulk samples were also prepared with JEOL JIB-4501 FIB located at Sabancı University, Istanbul.

Preparation of powder samples are easier compared to bulk sample preparation methods. Powder particles were dispersed in pure ethanol with ultrasonic bath to break the agglomerates. In this step, concentration of the particles should not be high to obtain an even dispersion. A drop of "ethanol + particle" suspension was dripped onto carbon (either Lacey or Holey) coated 3 mm cupper grid with micropipette then dried prior to TEM investigations.

3.4. Precession Electron Diffraction (ASTAR) Investigations

ASTAR system includes four different software named as;

- TEMDpa: used for data acquisition,
- DiffGen2: used to create diffraction templates,
- Index2: used for the diffraction pattern solution via template matching algorithm,
- MapViewer2: used for visualization of solutions.

Phase and orientation mapping studies were carried out by using these software packages. In the following section, the details about the PED investigations will be given.

3.4.1. Results obtained from ASTAR

Results from ASTAR system are presented in Map Viewer software as virtual bright and dark field images, pole figures, orientation, index, reliability and phase maps. These images and maps are described in detail.

3.4.1.1. Virtual bright field

Virtual bright field (VBF) images (Figure 3.1) are formed by placing a virtual aperture around the central spot and diffracted spots are excluded from the image. By doing this only intensity variations of central spot are measured to form an image [48] and this image looks like BF-TEM images however it is not safe to interpret directly as BF-TEM images, thus it is mostly used to visualize general appearance of scanned ROI.

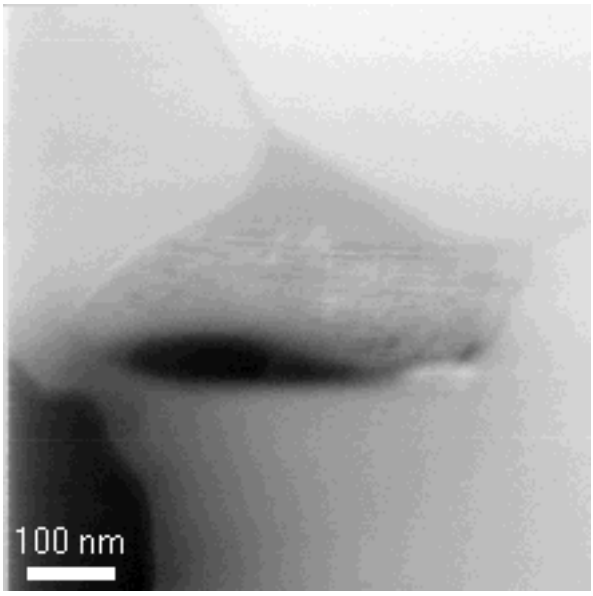

Figure 3.1. *The VBF image of hBN/SiC composite sample*

3.4.1.2. Virtual dark field

Virtual Dark Field (VDF) images are formed with a same principle with VBF images but with one difference, that is; VDF images are calculated by using a virtual aperture with user specified size placed any diffraction spot. VDF image is created by intensity measurement of diffracted spot within the virtual aperture for every pixel and intensity variations converted to an image. This method comes with several advantages compared with the conventional DF-TEM imaging method. In conventional DF-TEM imaging, user is limited to choose an objective aperture with several different sizes (for our microscope 5, 15, 30, 50 μm) that cannot be changed however VDF imaging in ASTAR have virtual aperture radius size ranges from 1 pixel to 74 pixels and this allows users to make different experiments. Additionally, software allows users to use more than one virtual aperture to combine or extract selected diffraction spot intensities for different purposes. For example, it can be used to discriminate the different phases like hBN in SiC matrix and even liquid phases within the matrix with the careful diffraction pattern/ring selection as shown in Figure 3.2.

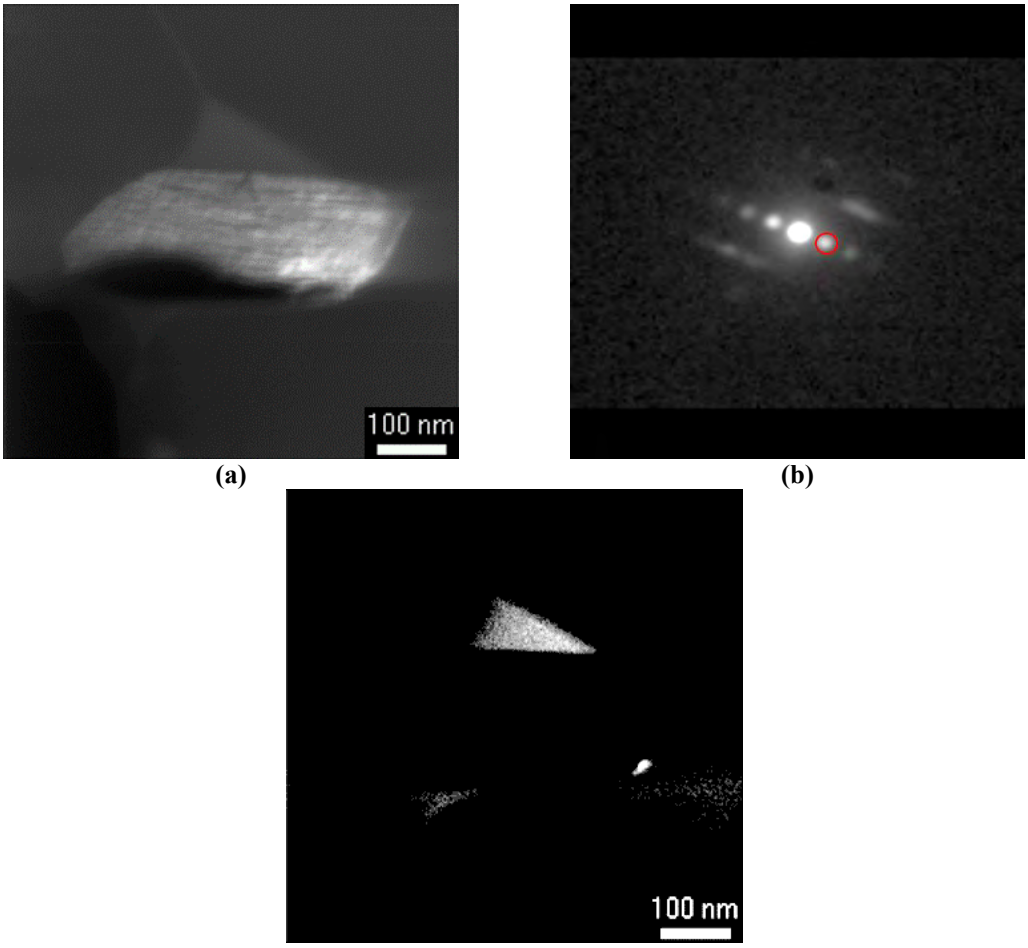

Figure 3.2. *(a) VDF image of hBN (please note that VBF image is given in Figure 3.1) (b) virtual aperture position and (c) VDF image of liquid phase (virtual aperture is placed on the ring pattern, not given in here)*

3.4.1.3. Orientation map (inverse pole figure)

The orientation map displays the different crystal orientations within the scanned area and all different orientations are visualized with a color code. The color code is associated with standard triangle that is every corner of the triangle have discrete directions and the area within the triangle has all the combinations of directions between corners. The angles of the corners vary with different crystal systems. There are three different axes in orientation maps; x, y and z axes. The three directions are;

- x: that is the horizontal axis towards the right,
- y: that is the vertical axis towards the top
- z: that is the axis normal to the screen.

The main advantage of visualization with different axes is the discrimination of orientations, which may not be revealed in one orientation map but may appear in another

one. The orientation maps (x, y and z) and the standard triangle is given in Figure 3.3. All the orientation maps in this thesis is combined with index maps for better representation unless otherwise is stated.

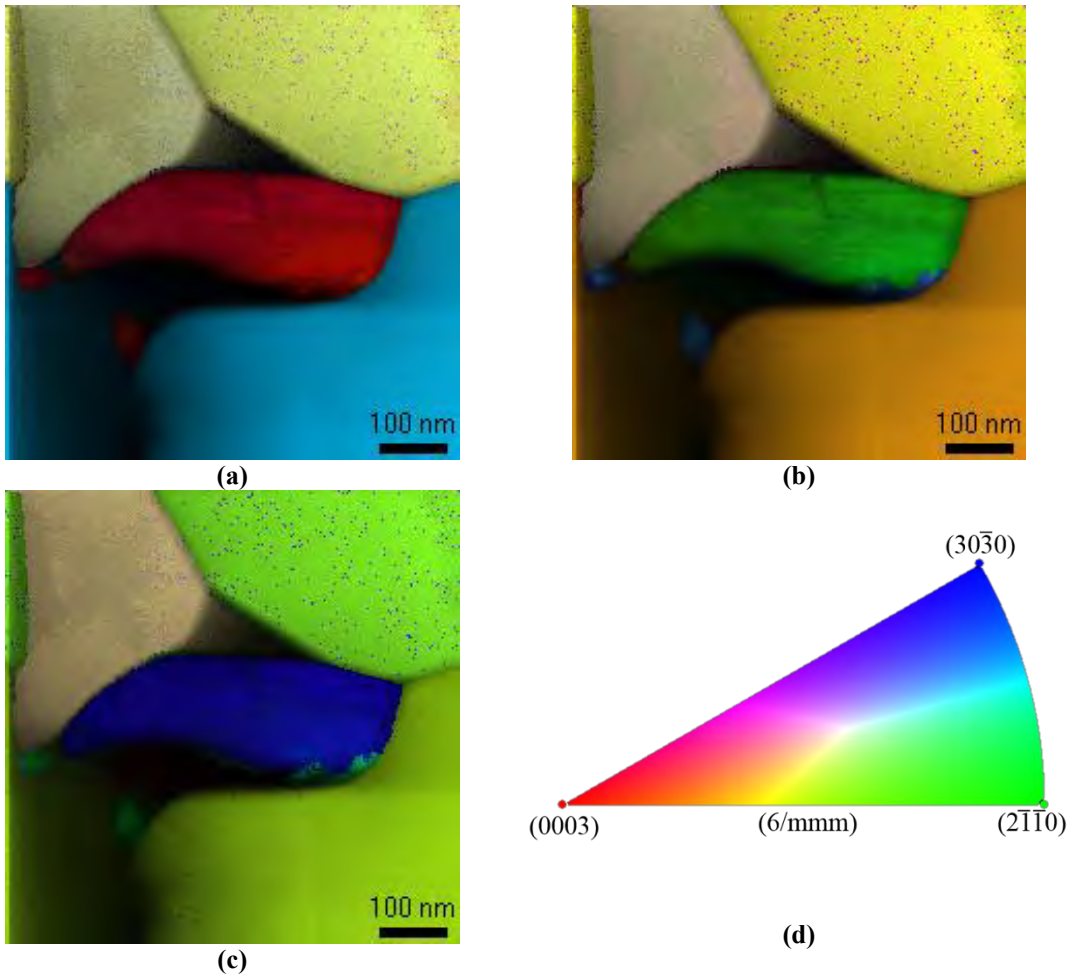

Figure 3.3. *Orientation maps for (a) x, (b) y, (c) z axes and (d) standard triangle*

3.4.1.4. Index map

Index map (Figure 3.4) is the combination of index value of each scanned pixel and index value (also named as correlation index) is the goodness of similarity between experimental diffraction pattern and template, thus higher the index score resulted in better template matching. The index score is calculated with the Equation (3.1). According to this equation, index is calculated with comparison of position (x, y) and intensity of spots between experimental and template data. In this equation P(x,y) and T(x,y) are intensity functions of observed and template, respectively. With this equation index is turned into a quantifiable information and index maps are formed by different

grey levels. In this map, higher index score appears brighter whereas lower index score appears darker.

$$Q(i)=\frac{\sum_{j=1}^{m} P(x_j,y_j)T_i(x_j,y_j)}{\sqrt{\sum_{j=1}^{m} P^2(x_j,y_j)}\sqrt{\sum_{j=1}^{m} T_i^2(x_j,y_j)}} \quad (3.1)$$

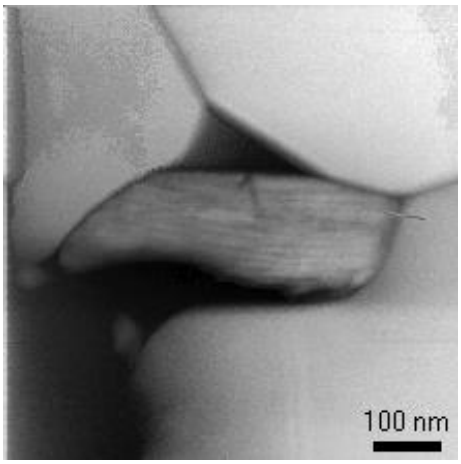

Figure 3.4. *Index map of the orientation map given in Figure 3.3*

3.4.1.5. Reliability map

According to the indexing method described above always find a solution that match with a template even if it is not he correct phase. In order to control the quality of the solution, additional parameter is required and that is the reliability. Reliability map is basically the goodness of the template matching process and it is formed by reliability value (as shades of black levels) of each pixel. Reliability of each pixel is calculated according to Equation (3.2), after indexing each diffraction pattern with full set of templates (bank file). In this equation, Q_1 and Q_2 are the index scores of the best solution and the second-best solution, respectively. According to this calculation, higher the reliability score, the more reliable template matching result is obtained for a given pixel. The value of the reliability ranges within 0 to 100, i.e. from unsafe to unique solution, respectively. According to the literature, reliability value about 15 is good for the validity of the result and above 40 is accepted as an excellent result, in contrast reliability below 5 is accepted as unsafe result [49, 50]. This value is also decrease with overlapping grains.

$$R=100\left(1-\frac{Q_2}{Q_1}\right) \tag{3.2}$$

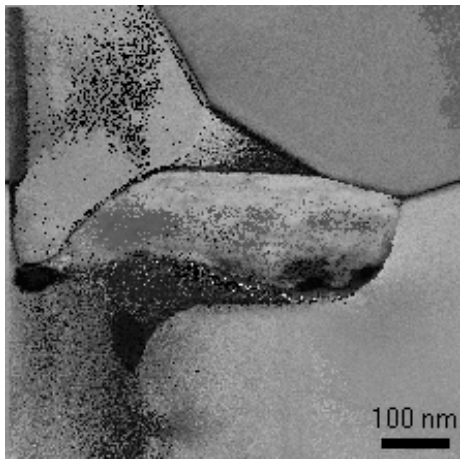

Figure 3.5. *Reliability map of the orientation map given in Figure 3.3*

3.4.1.6. Phase map

Phase maps are formed with best matching template of multi-phase systems and they are used to identify or separation of different phases within the ROI. For example, hBN and SiC phases are represented as red and green color, respectively in Figure 3.6.

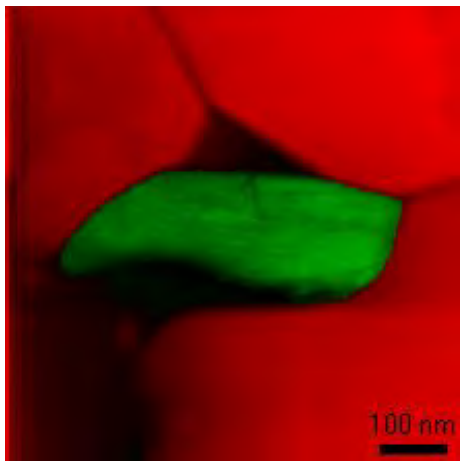

Figure 3.6. *Phase map of hBN/SiC composite combined with index map*

3.4.1.7. Pole Figure

It is possible to display stereographic projection of an orientation to the selected direction of crystal for a point, across a line or the complete map area. The colors in the

pole figure represents the selected directions or grain/particle. For example, set of points in the pole figure with a given color in Figure 3.7 represents the grain or particle with the same color in the orientation map.

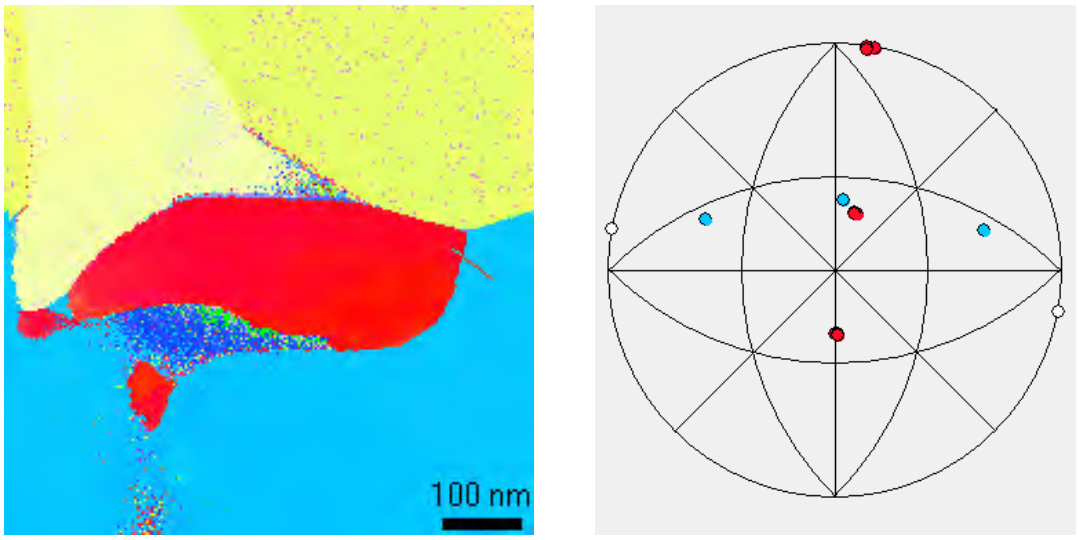

(a) (b)

Figure 3.7. *(a) Orientation map and (b) (11$\bar{2}$0) pole figure of the grains crossing with the line in orientation map. Different colors in pole figure is color coded with the orientation map*

3.4.2. Experimental parameters-process parameters during analysis

During data acquisition, there are several important parameters such as microscope variables, precession angle, alignment, scan step size, spot size and acquisition time.

3.4.2.1. Microscope variables

In JEOL JEM2100F TEM there are several imaging modes for different conditions like TEM, CBED, NBD, EDX and each mode has unique electromagnetic lens configurations. PED experiments are carried out in NBD mode and calibration of ASTAR system was done for NBD spot size 1 and alpha 5 at 15 cm camera length by the NanoMEGAS engineer.

3.4.2.2. Precession angle

One of the key advantage of the ASTAR system is the formation of precession movement around the optical axis during scanning and this precession angle is limited to

1° for the TEM (JEOL JEM2100F with UHR pole piece) used in this thesis, however due to the decrease of resolution around the maximum angle 0.7° is used as the highest angle. The application of precession is not a must for some cases, however, precession of electron beam help to increase template matching reliability due to excitation of diffraction spots from higher order Laue zones as shown in Figure 3.8. New spots revealed as the effect of precession is marked with arrows.

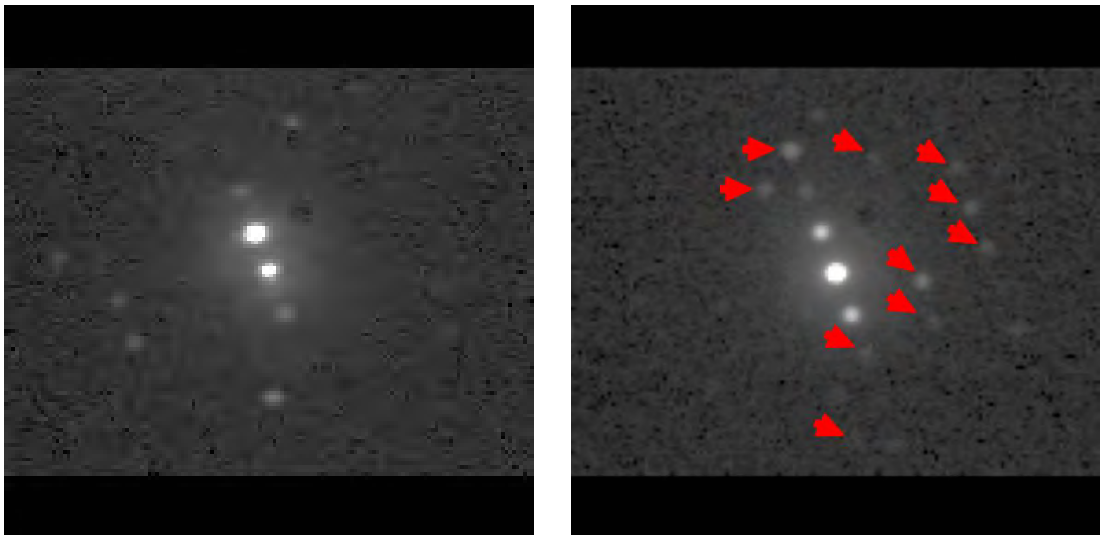

(a) **(b)**

Figure 3.8. *Diffraction spots obtained from the same region (a) without and (b) with 0.7° precession*

For the precession angle selection, there is no written rule, thus it is optimized by application of different angles by trial and error mostly depending on the sample studied. The optimum range for precession angle is given by Viladot et al. [51] (shown in Figure 3.9) according to the electron spot broadening with increased precession angle. According to this figure, more than 1.5° of precession, degrades the spatial resolution of this method and beyond that angle is only applicable for large grains.

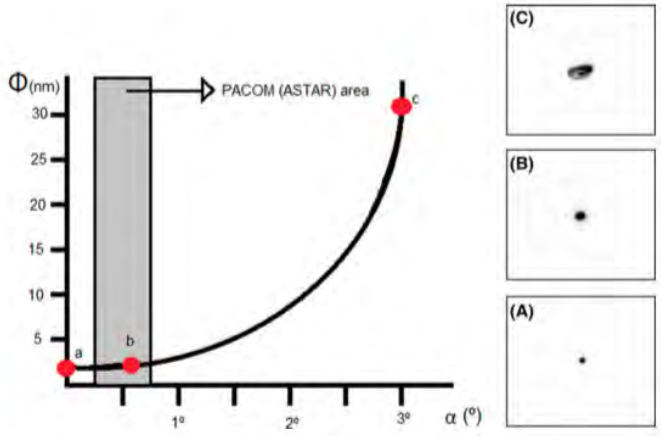

Figure 3.9. *Electron beam spot size (Φ) change with respect to precession angle (α) (after [51])*

3.4.2.3. Alignment

There are several important alignments for precession electron diffraction in order to obtain reliable, representative results with the best possible resolution. These are image pivot point and beam pivot point alignments. Even though the TEM basic alignments are perfect these alignments are crucial for ASTAR system. Image pivot point and beam pivot point alignments are done to obtain a stationary probe over the sample at a point and transmitted and diffracted beams after the sample, respectively. Figure 3.10 show the effect misaligned beam pivot point in gold nano particles. In the case of misaligned beam pivot point, electron beam that diffracted from the sample does not form a spot diffraction pattern and thus post-field descan coils form a diffraction ring instead of spots. Due to the misaligned beam pivot point spherical particles imaged as hollow core particles.

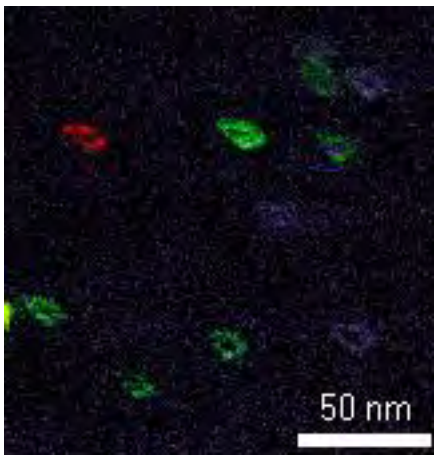

Figure 3.10. Effect of misaligned beam pivot point in gold nano particles. Particles imaged as hollow core instead of spherical particles

3.4.2.4. Scan step size

Scan step size in ASTAR is defined as the distance between two different scanned point that create two pixels and it is a tunable acquisition parameter depending on the sample studied. ASTAR system allows users to adjust step size from 1 nm to a hundred (?) of nanometers which is not a very practical step size in TEM. A small step size is an essential for nano sized grains or particles to separate from each other and create fine grain boundaries however it comes with a longer scanning times for large ROI. Fine grain boundaries are good for especially for determination of mean grain or particle size. On the contrary large step size decrease the scanning times however grain boundaries become thick and small sized grains or particles (that are smaller than step size) cannot be captured or partially captured. For the rule of thumb, minimum step size should be at least twice of the spot size of the electron beam in order to avoid oversampling, that is 2 nm for JEOL JEM2100F since calibration was made for 1 nm electron spot. The optimum step size is chosen according to size of the features present in the sample studied.

3.4.2.5. Spot size

In JEOL JEM2100F TEM, ASTAR system is used at nano beam diffraction (NBD) mode to form a nano sized probe over the sample. To form the probe NBD mode 1nm spot with α5 was calibrated by NanoMEGAS for this microscope and different spot size other than this is not possible. Only variable is the condenser aperture size that defines the probe size. In order to obtain smallest probe 5 μm aperture, which is the smallest for our configuration, was used.

3.4.2.6. Acquisition time

The last variable before scanning the sample to obtain diffraction patterns is the acquisition time that is the time spend on every pixel during scanning and defines the total scanning time. Total scanning time is calculated simply the multiplication of total number of pixels (number of pixels in x direction multiplied with number of pixels in y direction) with the acquisition time. In order to decrease the scanning time shorter acquisition times are preferred however, for the samples that have faint diffraction spots on the phosphorus screen with the help of increased acquisition time spots will become more apparent. This is important because faint spots cannot be distinguished from noise

and template matching will become complicated, thus with increased acquisition time better template matching results can be obtained.

In ASTAR system, there are several discrete acquisition times that can be used, they are 10, 20, 40, 50 ms because of the 100Hz precession frequency. To avoid non-complete precession turns these discrete values needs to be used otherwise there will not be full circle like 2.5 turn around the optical axis. Acquisition times of 10, 20, 40, 50 ms resulted in 1, 2, 4, 5 full turns of precession movement are obtained, respectively.

3.4.3. Data processing parameters

During data processing, there are several important parameters such as diffraction pattern generation, camera length, diffraction pattern centering, polar image, noise threshold and gamma correction.

3.4.3.1. Diffraction pattern generation

In this thesis, all obtained data were taken with JEOL JEM2100F operated at 200 keV and all diffraction spot templates were generated at this accelerating voltage and stored in bank files. The diffraction patterns are generated all possible orientations and need to be done for every possible phase in the sample.

During pattern generation, there are few parameters that have great influence on template matching process. Excitation error is the main variable for the pattern generation and depending on the sample thickness and/or lattice constants it needs to be changed before template generation procedure and this will change the number of diffracted spots in the template. For example, if one of the lattice constants is bigger than about 10 Å, excitation error needs to be decrease roughly below 0.5 however optimum excitation error is found by trial and error.

Step count is the last variable that defined as angle between two zone axes divided how many steps. In order to obtain 1° of angular resolution bank files have to be created with a step count of 50 and 90 for cubic and hexagonal crystals, respectively.

3.4.3.2. Camera length

Camera length is one of the most important data processing parameter during indexing. Even though diffraction patterns were taken with a specific diffraction camera

length of microscope, during data processing it needs to be optimized to get the best reliability from template matching process for every single scan. During installation of the ASTAR system diffraction patterns acquisition was calibrated at 15 cm camera length however, there could be some deviations from 15 cm to get the best reliability score after template matching. The optimized camera length varies for every scan however, camera lengths are in between 14 and 16 cm. Figure 3.11 shows the orientation maps with 15 cm camera length and optimized to 16 cm. The quality of the orientation maps increase drastically with camera length optimization. For optimization of the camera length various camera length in a user specified range is scanned and compared with the template for a given pixel (scan result is given in Figure 3.12) and user select the camera length that gives the highest index score and optimum camera length is chosen after few iterations at different pixels, preferably from different phases if present.

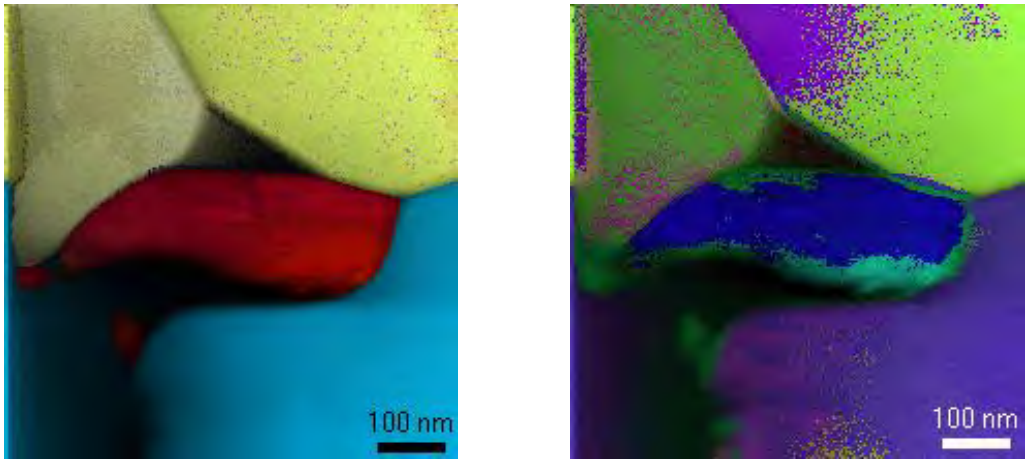

(a) **(b)**

Figure 3.11. *Orientation map of hBN/SiC orientation map with (a) 15 cm and (b) 16 cm*

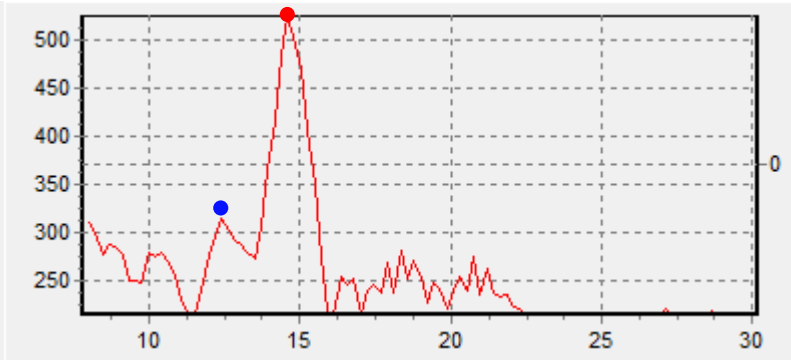

(a)

Figure 3.12. *(a) Camera length optimization scan result, (b) uncorrected template matching (12.4 cm, blue dot) and (c) corrected template matching result (14.9 cm, red dot)*

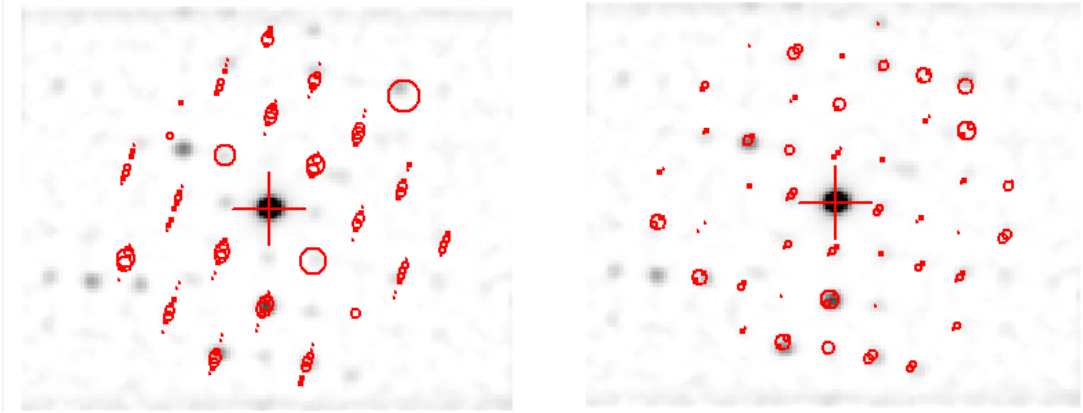

(b) (c)

Figure 3.12 (Continued) *(a) Camera length optimization scan result, (b) uncorrected template matching (12.4 cm, blue dot) and (c) corrected template matching result (14.9 cm, red dot)*

3.4.3.3. Diffraction pattern centering

Even though the central spot is very well aligned during microscope alignment procedure, due to the variations of sample thickness within the ROI, position of the central spot can change and this change lead to misindexing of the diffraction spots. In order to solve that problem automatic central spot detection option can be used and additionally it can be optimized automatically according to the template matching, however this process requires few iterations for optimization that cause increase of indexation times about two or three folds.

It is worth to note that template matching always find a solution if centering, camera length is wrong and even diffraction template bank belongs to completely different material. The differences between correct and wrong parameters are orientation/phase reliabilities and index score that affect the quality of the results.

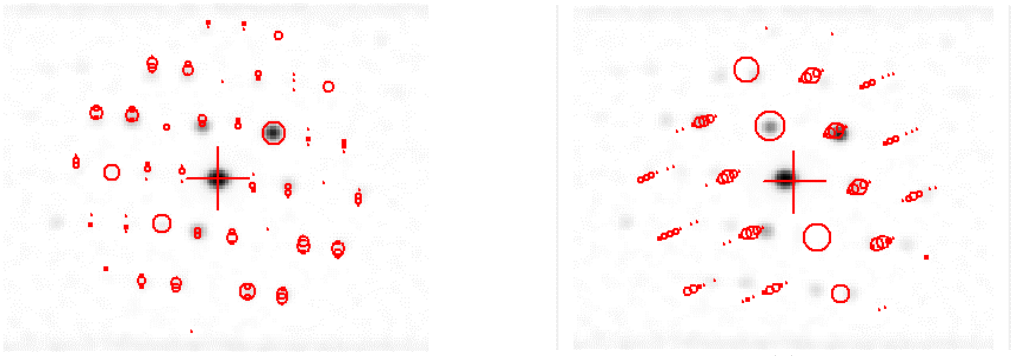

(a) (b)

Figure 3.13. *Effect of (a) correct and (b) wrong diffraction pattern centering on template matching (Reliability is changed from 30 to 2 and index from 350 to 210 with wrong centering)*

3.4.3.4. Polar image

Polar image is the rectangular transformed image of 144x144 pixel diffraction pattern that has polar coordinates. This polar coordinate system has two components; R and θ as shown in Figure 3.14 (a). R is the radius of polar coordinate and θ is angle between axis and diffraction spot. This polar image is used during image processing to control maximum distance; controlled with R, which is indexed during template matching. This is somewhat important to eliminate the noise present in the four corners (marked with a-d in Figure 3.14 (a)) of the 144x144 pixel image and additionally used to eliminate very faint diffraction spots that interfere with the noise at the outermost region in diffraction pattern to use higher intensity spots close to central beam for increasing reliability index. For example, decreasing polar radius from 120 to 50 changes the number of used diffraction spots during template matching and this change is marked with red and blue dashed circles in diffraction pattern as shown in Figure 3.14 (c), with the help of this reliability index score of the respective pixel is changed from 5 to 22 for same orientation.

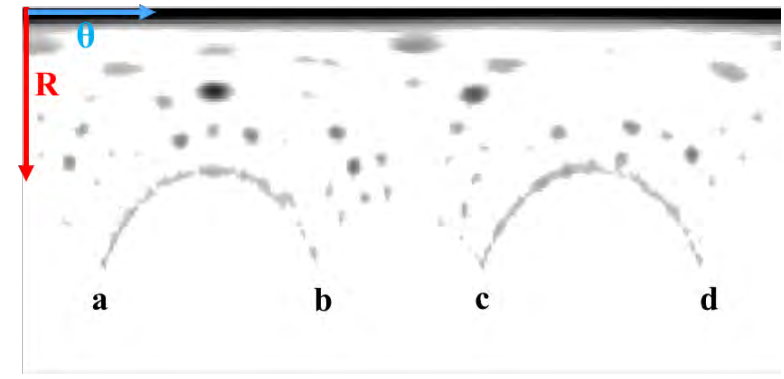

(a)

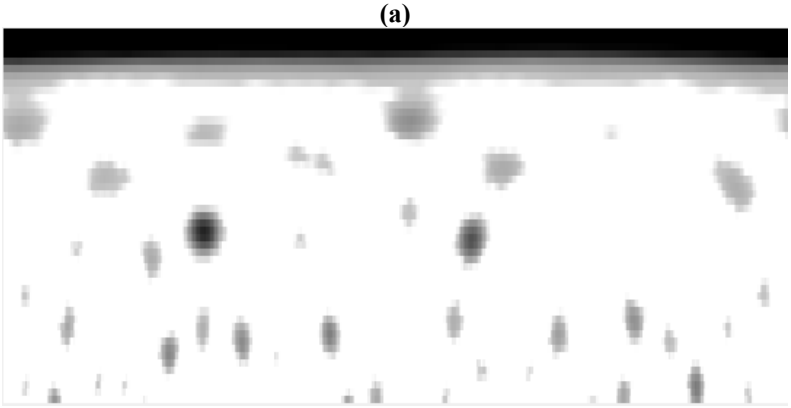

(b)

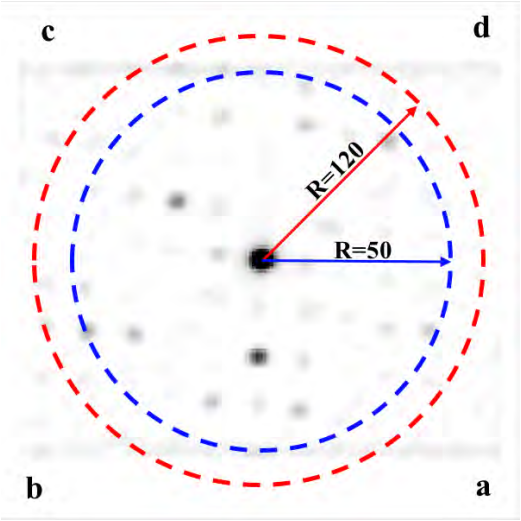

(c)

Figure 3.14. *(a) Polar coordinate system of a diffraction pattern, (b) Polar transformed image of a diffraction pattern; R is unchanged (default value is 120), (b) R is set to 50 (c) diffraction pattern used for polar transformation*

3.4.3.5. Noise threshold and gamma correction

Intensities of the experimental diffraction pattern spots can be enhanced by changing gamma correction and the separation of noise from the diffraction spots can be done with adjusting the noise threshold values. Gamma correction option enhances the intermediate spot intensities while noise threshold is used to zero all intensities below certain value. In this thesis used gamma correction values between 0.33 and 1, and noise threshold values between 8 to 12.

3.5. Calibration between image and diffraction modes

The Orientation maps obtained with PED technique contains orientation information, Euler angles, for every pixel, however in order to obtain absolute orientation information the rotation between image and diffraction patterns needs to be calibrated. Even though this is not necessary for relative orientations because both orientations contain the same rotation that cancel out each other, however this is required for absolute orientation of the grains or particles.

Because of the different lens settings between image and diffraction modes, there is a rotation between these modes at different magnifications and camera length of 15 cm (that camera length is used for orientation mapping acquisitions). The rotation between these modes are calibrated by α-MoO_3 sample. This sample has distinct growing direction

along [001] direction to form high aspect ratio nano particles. By the help of the elongated structure of this sample, long direction that is [001] direction is easily recognized in TEM images. These crystals have a=0.3963nm, b=1.3856nm and c=0.3697nm lattice parameters. With the help of smallest lattice parameter along c axis, [001] direction is easily recognized in diffraction pattern that has the highest d spacing in reciprocal space. Figure 3.15 shows the rotation between image (at 30k magnification) and diffraction pattern (at 15cm camera length). Because of JEOL JEM2100F has different lens settings at different magnifications, there is also a variation between images taken at different magnifications (and even at different magnification modes). Rotation between images at different magnifications are calibrated by using image taken at 30k magnification as a reference. Rotation angles are given in Table 3.1. According to these measurements, highest rotation is 4.1° however, rotations for most of the magnifications are negligible.

Table 3.1. *Rotation angles between image and diffraction pattern at different magnifications*

Magnification	***Rotation Direction[1]***	***Rotation Angle (A)***
8000	Ccw	1.1
1000	Cw	1.1
12000	Ccw	2.2
15000	Ccw	4.1
20000	Ccw	1.5
25000	Ccw	0.9
30000	-	0
40000	Ccw	1.9
50000	Ccw	2.3
60000	Ccw	0.6
100000	Cw	0.1
120000	Ccw	0.3
150000	Ccw	1.2
200000	Ccw	0.7

[1] Cw and Ccw stands for clockwise and counter-clockwise, respectively.

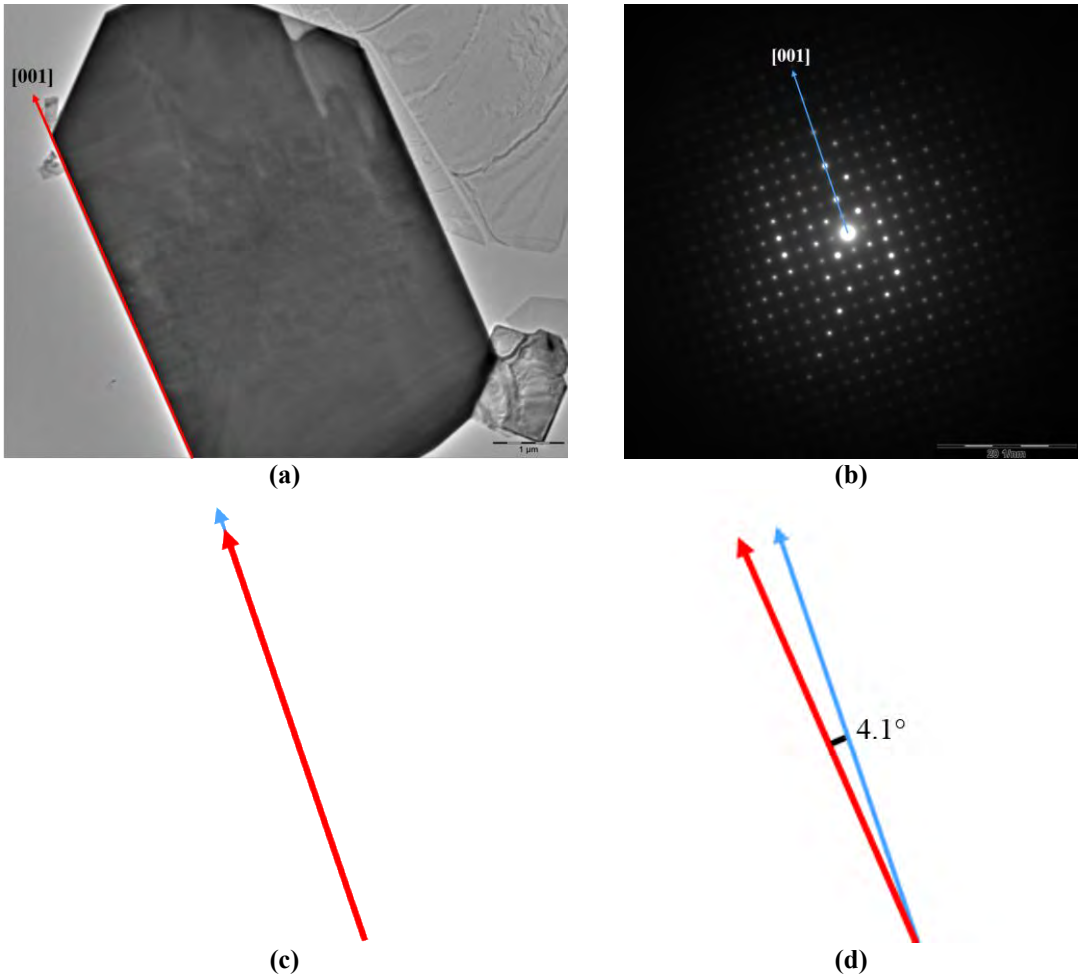

Figure 3.15. *(a) BF-TEM image of MoO_3 particle, (b) diffraction pattern obtained from particle in (a), rotation between image and diffraction modes for (c) 30k and (d) 15k magnifications*

3.5.1. 180° ambiguity problem

In addition to the rotation calibration between image and diffraction pattern, 180° ambiguity problem needs to be solved to obtain absolute orientation of a given particle or grain. Ambiguity issue is caused by the use of symmetric nature of diffraction patterns in TEM.

Even though ambiguity and rotation between image and diffraction spaces is not that important for the comparison within a same scan or map because of the fact that same rotation is applied to both orientations and relative comparison of them cancel each other. However, they become important for orientation comparison between different scans especially if they are taken at different magnifications.

In order to solve whether 180° ambiguity is present or not, first TEM bright field image with characteristic feature needs to be taken as shown in Figure 3.16. Then, same feature is imaged within the central spot of under focused diffraction pattern. Under focus

conditions in diffraction mode is obtained with counterclockwise rotation of focus knob in JEOL microscopes. The rotation angle between BF-TEM image and under focused diffraction image reveals the approximated is 187° that is the angle needs to be applied to any bright field image to coincide with the under focused diffraction image. Since this measured angle is greater than 180°, rotation angle that needs to be is 180°+A°, where A is the rotation angle measured in Section 3.5 for different magnifications. This rotation angle is applied to the first component (ϕ_1) of the Euler angle set in Map Viewer software.

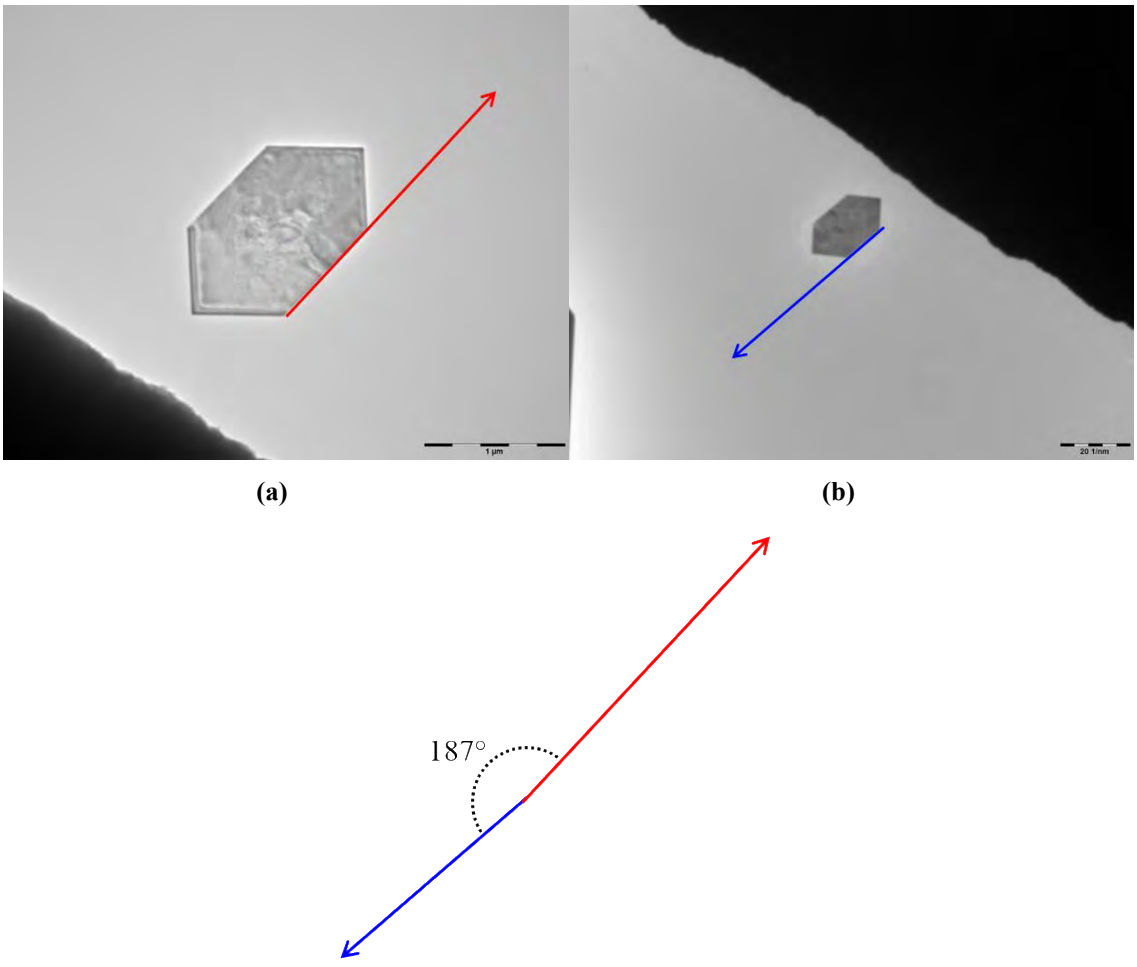

Figure 3.16. *(a) BF-TEM image of MoO_3 particle, (b) underfocused image of (a) in diffraction mode, (c) rotation between (a) and (b)*

Even though ambiguities are solved by the method described above, still ambiguities can be present due to the template matching procedure because of the symmetric nature of the templates. This type of ambiguity is mostly present in the orientation maps in the form of a pixel or combination of few pixels with different

orientation. These insignificant orientations can be solved by the ambiguity resolver option of Map Viewer software. During this procedure pixel, having an ambiguity is compared with the neighboring pixels and the software corrects ambiguity. In Figure 3.17 (a) pixels with ambiguities can be seen clearly at the upper right SiC grain and some of these ambiguities are corrected with the help of software as shown in Figure 3.17 (b).

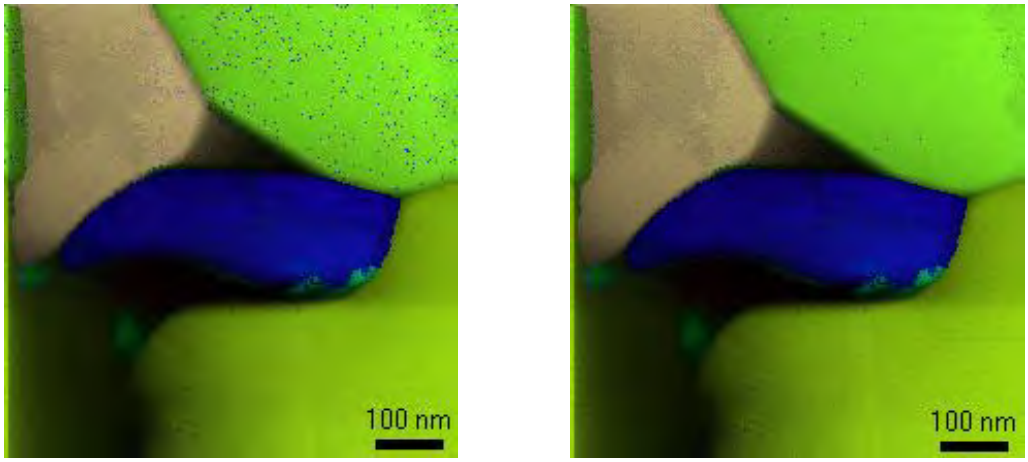

(a) **(b)**

Figure 3.17. *An orientation map (a) before and (b) after the ambiguity correction*

3.6. In-Situ Heating Experiments

In-situ heating experiments were conducted by using DENSSolutions brand Wildfire D6 double tilt in-situ heating holder that use MEMS based heating chips covered with $SiN_{(x)}$ supporting film. Sample preparation of powder samples were same with conventional powder preparation routes that is particles dispersed in ethanol and a small drop of mixture was place onto reverse side of the heating chip. Then chip was inserted to the holder and contact points were tested with contact tester in order to make sure that electrical connections of heating and temperature sensing were correct.

3.7. Other Techniques Used In This Thesis

(i) X-ray Diffraction

X-ray diffraction (XRD) analyses for bulk and powder samples were done by using Rigaku MiniFlex 600 X-ray diffractometer with Cu-K_α X-ray source.

(ii) Hardness and Toughness Measurements

Hardness and indentation toughness values were measured by EmcoTest M1C hardness tester by using Vickers indenter with an application of 10 kg force for 15 seconds. Vickers hardness values were calculated after measuring diagonal lengths of indenter marks and indentation toughness were calculated by Niihara Equation after measuring crack lengths formed at the tip of the indenter marks by using an SEM to obtain precise values.

(iii) Density Measurements

Densities of the bulk samples were measured with the Archimedes principles by weighing samples in air and in water after boiled for 3 hours in water. Relative densities were calculated by using theoretical densities.

(iv) Thermodynamic Calculations

Thermodynamic calculations in order to find out the Gibbs- free energy change of a reaction at a specific temperature range were calculated with thermodynamic data compiled with HSC Chemistry 5.0 software. Theoretical phase diagrams were calculated with FactSage software package in order to investigate phase changes with respect to temperature and TEM vacuum pressure, which is around 10^{-6} Pa.

(v) Identification of principal directions for directional properties

In this thesis some of the properties such as, hardness, electrical and thermal conductivity measured and phase identification with XRD were done for different directions with respect to uniaxial pressing direction of production method, i.e. hot press and spark plasma sintering, that can affect the microstructure and material properties for different directions. The terminology used in thesis is schematically given in Figure 3.18, but to summarize, surface means that the normal direction (along z-direction) of that surface parallel to pressing direction (along z-direction) and vice versa, plane normal of cross section (along x-direction) is perpendicular to the pressing direction (along z-direction). Measurements mentioned above done from these surfaces labelled as *"surface"* and *"cross section"*.

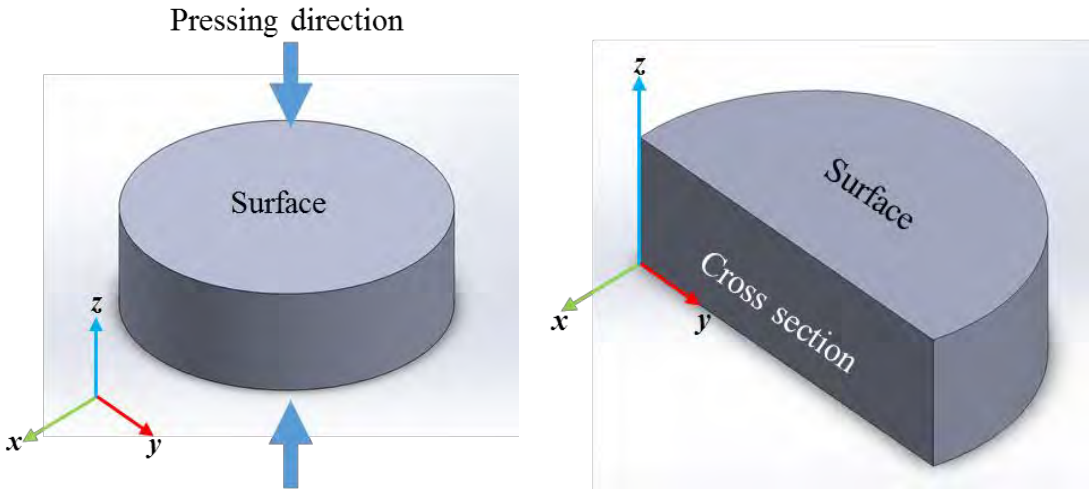

Figure 3.18. *Schematic drawing that shows two principal directions*

4. CHARACTERIZATION OF SIC & hBN COMPOSITE

4.1. Why SiC & hBN Composite

Silicon carbide (SiC) is one of the important and widely used high temperature ceramic due to its outstanding properties such as; high elastic modulus, high strength at high temperatures, chemical and thermal stability. In addition to the high temperature applications, it is also used in electronic applications due to its semiconductor properties. Outstanding mechanical properties of SiC cause the machinability problem to obtain complex geometries. In order to increase the machinability of SiC, there are several different approaches available and one of them is to produce of SiC composite containing a different particle or phase that can increase the machinability. Hexagonal boron nitride (hBN) is one of the possible candidate as a second phase due to its high thermal shock resistance, high temperature stability and machinability. Even though hBN can provide increased machinability, there are also several drawbacks of using hBN for example decreased hardness due to delamination and inherent hardness of hBN. In the literature, it was reported that hBN addition to SiAlON and Si_3N_4 [52] successfully increased their machinability. There were several different studies to obtain SiC-hBN composite structures. One of the main challenges during SiC-hBN composite production is the homogeneous mixing of SiC and hBN powders with conventional mixing methods. To solve non-homogenous distribution of hBN particles, in-situ hBN synthesize approach during sintering process can be used. In this approach, SiC and hBN forming raw materials are mixed and sintered. During sintering, in-situ hBN formation occurs between SiC grains [53].

The mechanical properties of materials can be improved by forming composite structure with the addition of secondary phases which can be particles, fibers or whiskers. Mechanical properties (as well as other properties like thermal conductivity) of composite structure can be controlled with the properties of reinforcement phase; however, in the literature it is also reported that mechanical properties may change not only with properties of secondary phase but also how reinforcing phase is bonded with the host phase [2, 3]. Depending on the bonding character between phases in the composite electrical properties or mechanical properties might be improved. This improvement maybe related to special misorientations that can change the grain boundary energy. For example; fracture resistance and fracture mechanism of ZrB_2-ZrC composite was found

to be varied by using different sintering method that can change the number of special grain boundaries [1].

In the composite structures, which were produced by in-situ synthesizing methodology, there may be special orientation relationship between in-situ synthesized phase and the host structure. In the literature, Al_2O_3 in Al [54], WC in Co [3], Ti_2AlN in TiB_2 [55] and hBN in SiC [16] can be given as examples with a special orientation relationship between in-situ synthesized structures and the matrix phase. These orientation relationships may correspond to a low energy special grain boundaries, which can enhance the mechanical properties. Therefore, in addition to the conventional TEM methods, composite samples were also investigated with a novel TEM-PED technique to answer the question of *whether there are any specific orientation relation present between SiC and hBN phases?*

4.1.1. Production of SiC-hBN composite

Sample that is used in this study was produced by Zuhal Yılmaz [53]. Briefly, production of the sample was started with mixing of α-SiC with boric acid (H_3BO_3) and urea ($CO(NH_2)_2$) in ethanol with Si_3N_4 balls in a planetary ball mill for 90 minutes. Dried mixture was calcined under N_2 atmosphere at 850°C for 16 hours. 5 % sintering additives of Al_2O_3 and Y_2O_3 mixture with a 7:3 ratio by weight, respectively, was mixed with ball milling in ethanol for homogenization prior to spark plasma sintering (SPS). SPS process was conducted at 1850°C for 17 minutes under 50 MPa pressure. Readers should refer to reference [53] for the detailed information about the production and effect of hBN addition on the machinability. According to the XRD analysis given in a previous study [53] the samples were found to be mainly contain hBN (7%), 6H-SiC and small amount of 4H-SiC phases.

4.2. Characterization of the Composite

Microstructural characterizations of the samples were carried out by using various TEM and STEM methods. According to STEM images given in Figure 4.1, hBN particles distributed homogeneously between SiC particles. Higher magnification TEM image of one of the black regions in the STEM-HAADF image of hBN particle shows the hBN $d_{(0002)}$ planes as well as the delamination of these planes. This phenomenon will be

discussed in detail in Section 4.3.1. In the STEM-HAADF images, liquid phase, formed by sintering additives, were found between SiC-hBN and SiC-SiC interfaces as thin layer as well as at triple pockets between SiC and hBN particles. Based on the STEM-EDX analysis, liquid phase contains Y, Al, O and Si elements, where Si is coming from worn Si_3N_4 mixing balls due to the wear during milling. It was also found that Ni, Fe, Cr and Ti impurity elements were present, which were originated from stainless steel container used during milling.

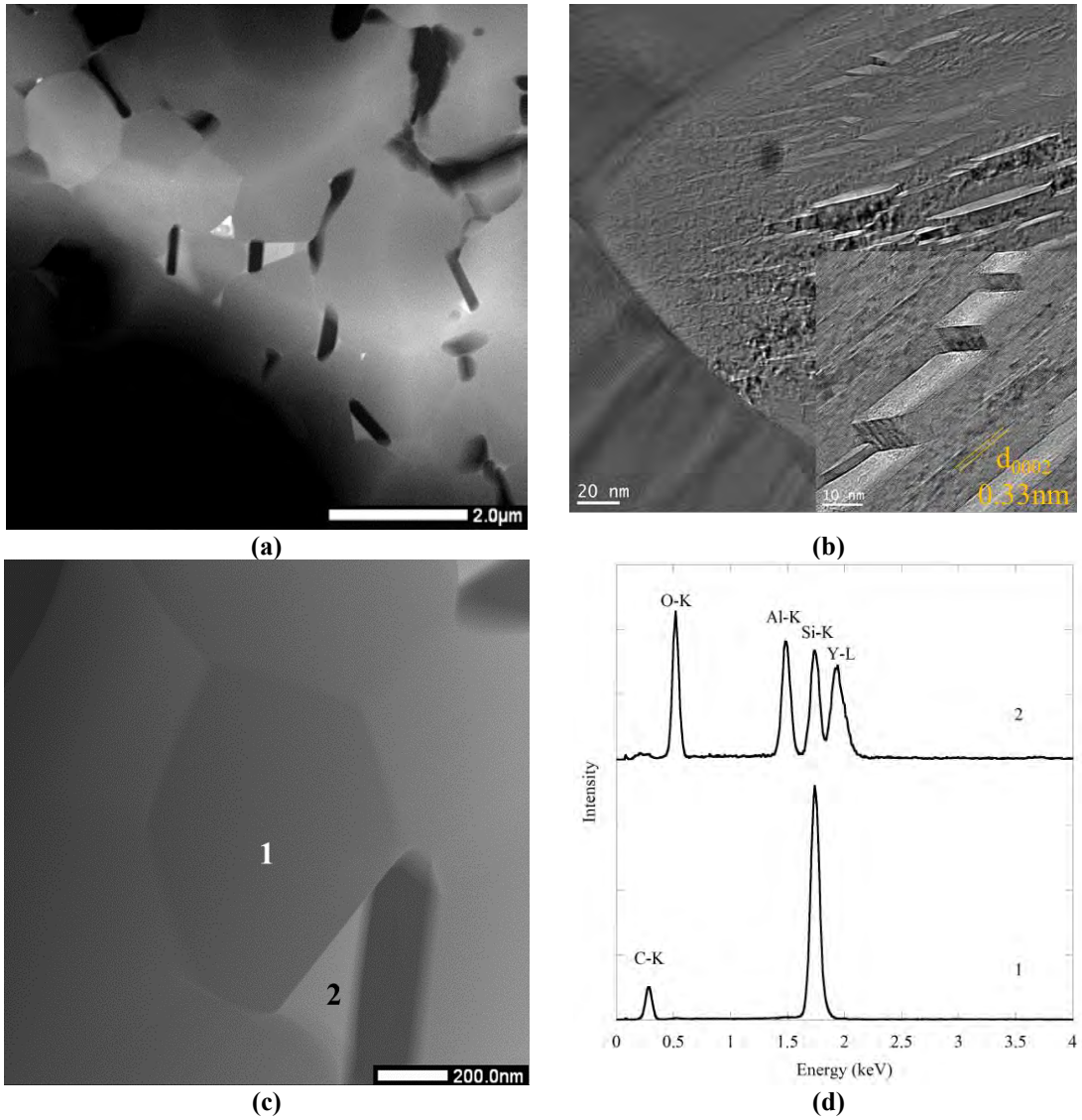

Figure 4.1. *(a) STEM-HAADF image showing general overview of the sample, (b) TEM-BF image of in-situ formed hBN, (c) STEM-HAADF image showing liquid phase and respective EDX spectra of labelled regions in (d), (e) STEM-HAADF and (f) STEM-BF images showing hBN particles with different morphologies as well as impurity phase between particles and (g) STEM-EDX spectra obtianed from regions labelled in (e)*

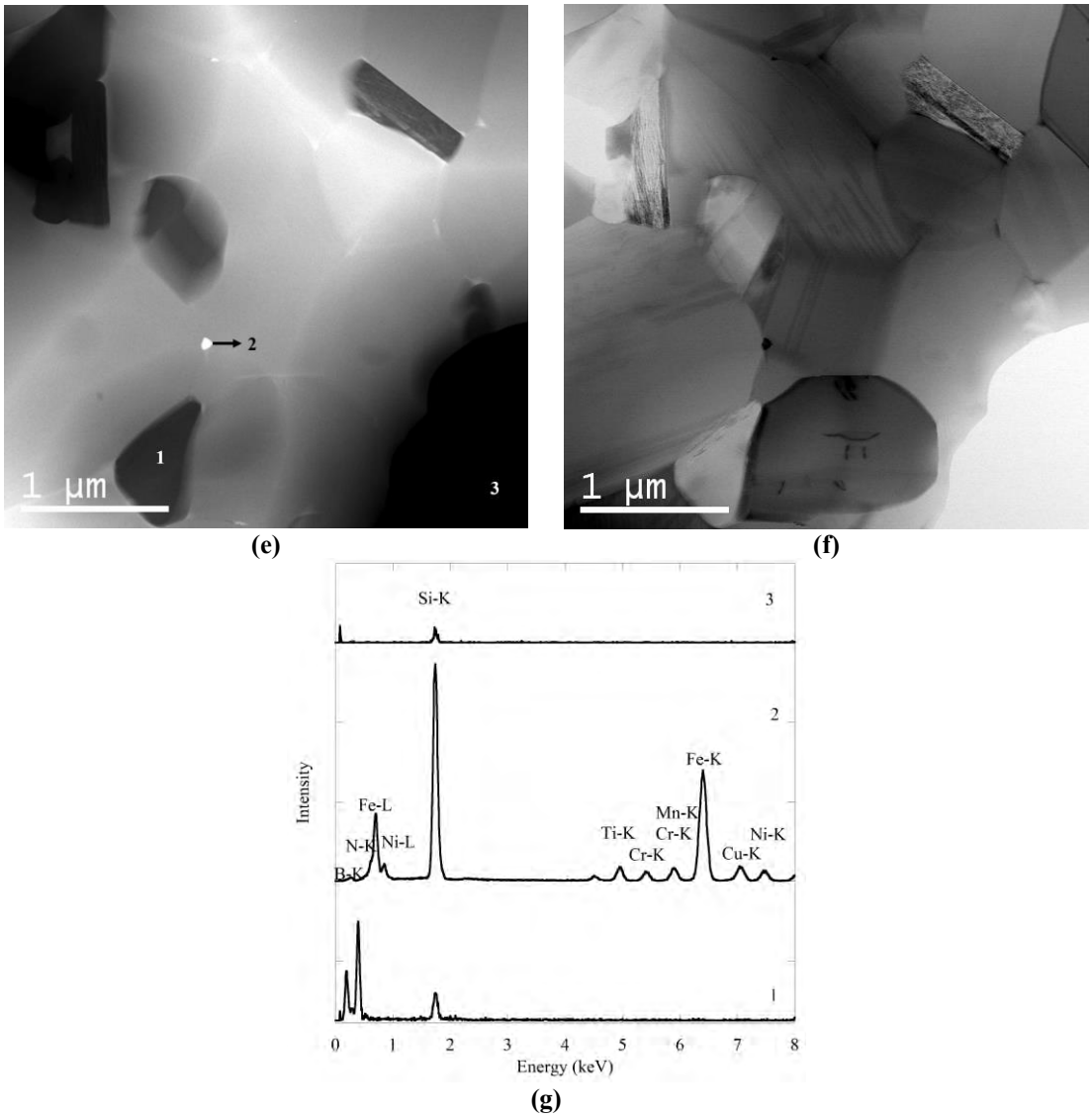

Figure 4.1. (Continued) *(a) STEM-HAADF image showing general overview of the sample, (b) TEM-BF image of in-situ formed hBN, (c) STEM-HAADF image showing liquid phase and respective EDX spectrums of labelled regions in (d), (e) STEM-HAADF and (f) STEM-BF images showing hBN particles with different morphologies as well as impurity phase between particles and (g) STEM-EDX spectrums obtianed from regions labelled in (e)*

In the EDX spectra, it was found that Si-K peak was present in the hBN particles even though it was not supposed to. This peak was also present in the vacuum region; therefore, it is possibly the Si escape or fluorescence peak due to Si crystal present in the detector, which is a common spectral artefact for Si(Li) type detectors [56].

In the literature [16] it was reported that there is a special orientation relation between in-situ formed hBN and α-SiC, that is $[11\bar{2}0]$ directions and (0001) planes of both SiC and hBN particles are parallel and expressed as follows;

$$[11\bar{2}0]_{\alpha\text{-SiC}} \,//\, [11\bar{2}0]_{hBN} \text{ and } (0001)_{\alpha\text{-SiC}} \,//\, (0001)_{hBN}$$

In order to investigate the presence of orientation relation mentioned above, TEM-PED studies were conducted. For this purpose, orientation maps of neighboring hBN and SiC grains were obtained and analyzed via [11$\bar{2}$0] and (0001) pole figures. Additionally, visualization of the neighbors were done by CrystalMaker software by using absolute orientation of each particle, calculated by Equations (2.3) and (2.4) from Euler angles.

An example TEM-PED result is given in Figure 4.2 with TEM-BF image and respective phase and orientation maps with pole figures. In the pole figures, it was observed that there is no common point for both particles, which points out that special orientation found in the literature was not present in this sample. Similar results were also observed for other orientation maps (not given in here), thus it can be concluded that hBN and SiC particles oriented randomly in this sample. Visualization of the absolute orientation of the particles supports given pole figures, Euler angles and calculated absolute orientations are given in Table 4.1. In the orientation maps, it was also found that hBN particles have band-like structure with different orientations but they have common point in (0001) pole figure. Details of this bands with different orientations will be given in Section 4.3.2.

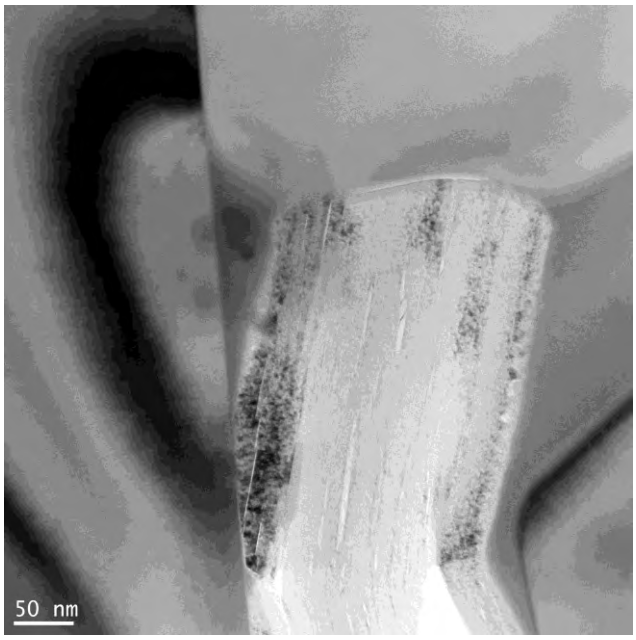

(a)

Figure 4.2. *(a) TEM-BF image and respective (b-d) orientation maps for x, y and z directions (e) phase map (green: SiC, red: hBN), (0001) and* [*11$\bar{2}$0*] *pole figures for orientations labelled as (f, g) hBN-SiC-1 and (h, i) hBN-SiC-2 (j, k) absolute orientations and (l, m) (0001) and* [*11$\bar{2}$0*] *pole figures for different orientations found in hBN particle*

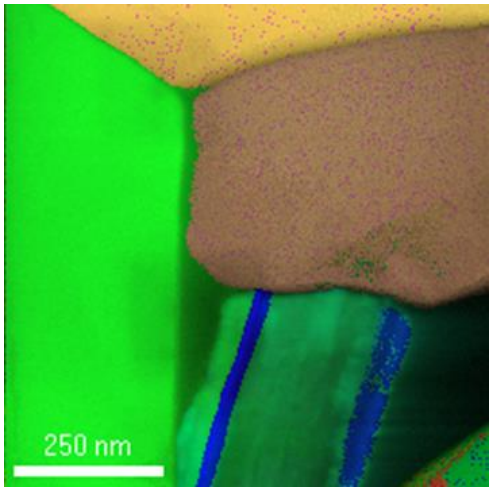

(b)

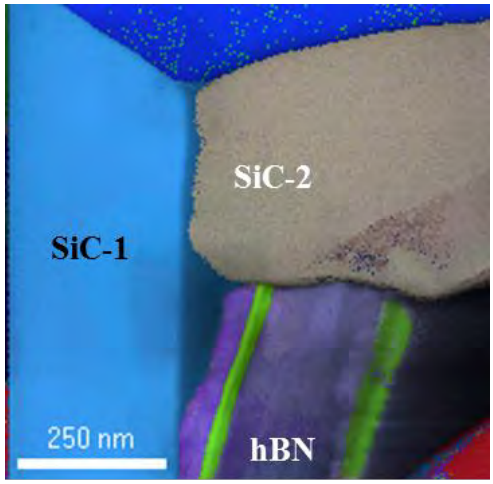

(c)

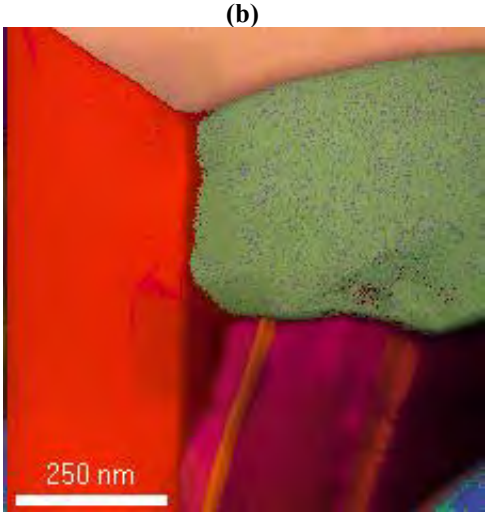

(d)

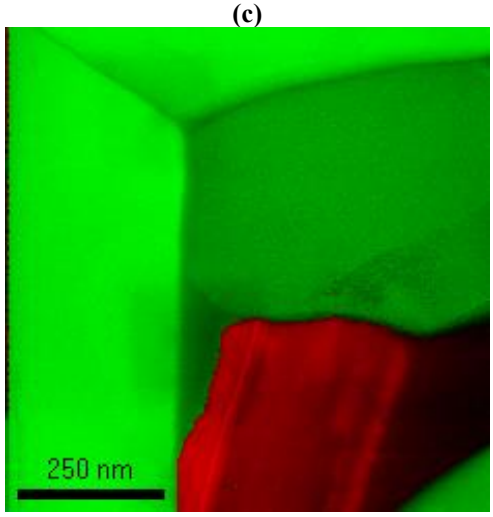

(e)

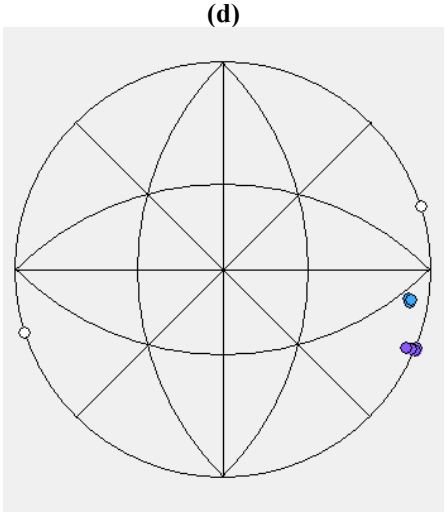

(f)

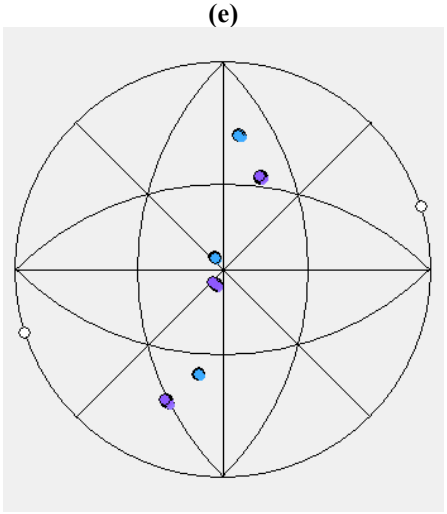

(g)

Figure 4.2 (Continued)*(a) TEM-BF image and respective (b-d) orientation maps for x, y and z directions (e) phase map (green: SiC, red: hBN), (0001) and* $[11\bar{2}0]$ *pole figures for orientations labelled as (f, g) hBN-SiC-1 and (h, i) hBN-SiC-2 (j, k) absolute orientations and (l, m) (0001) and* $[11\bar{2}0]$ *pole figures for different orientations found in hBN particle*

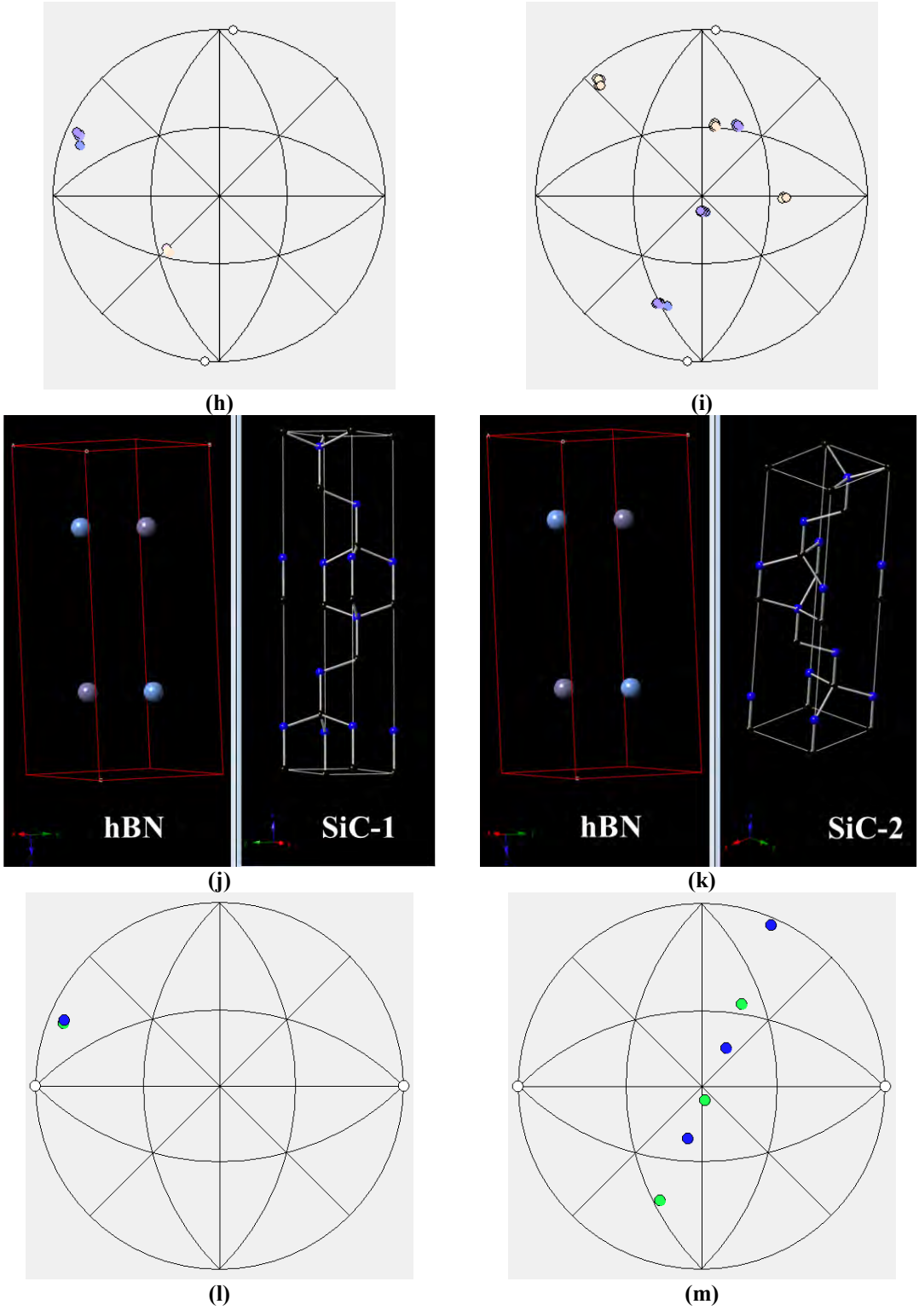

Figure 4.2. (Continued) *(a) TEM-BF image and respective (b-d) orientation maps for x, y and z directions (e) phase map (green: SiC, red: hBN), (0001) and* $[11\bar{2}0]$ *pole figures for orientations labelled as (f, g) hBN-SiC-1 and (h, i) hBN-SiC-2 (j, k) absolute orientations and (l, m) (0001) and* $[11\bar{2}0]$ *pole figures for different orientations found in hBN particle*

Table 4.1. *Euler angles and calculated orientations of SiC and hBN particles*

	Euler Angles										
	ϕ_1	ϕ	ϕ_2	< h	k	i	l >	{ u	v	t	w }
hBN	246.00	84.92	84.26	0.808	0.099	-0.908	0.235	-0.011	0.275	-0.164	-2.421
SiC-1	82.00	84.75	83.71	0.802	0.109	-0.911	0.448	-0.001	-0.098	0.099	4.832
SiC-2	136.00	130.88	246.36	-0.448	-0.303	0.751	-3.206	0.195	-0.569	0.365	2.573

According to the TEM-PED results, it can be concluded that hBN particles were formed independently from SiC particles, and growth of both phases occur independently. The proposed sintering mechanism is given schematically in Figure 4.3

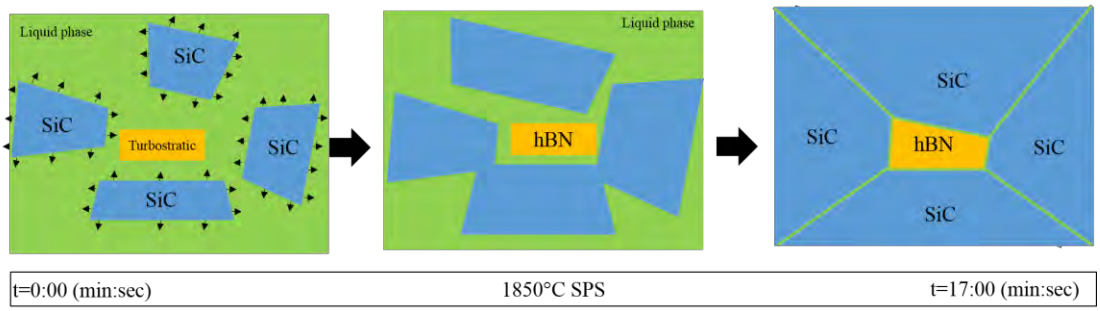

Figure 4.3. *Proposed sintering mechanism during SPS*

4.3. Characterization of Defects in hBN

During TEM imaging and TEM-PED analyses of hBN-SiC composite system, it was found that there are two distinct defects present as delamination and misorientation within (0002) planes in the hBN particles, respectively.

4.3.1. Delamination in hBN particles

During TEM analysis of hBN particles, it was found that there was delamination of (0002) basal planes associated with cracks between matrix and delamination bands (Figure 4.4). Because of the delamination, hBN appeared as fibrous texture. These delamination bands are inclined or tilted strands of (0002) planes from the matrix, which is again (0002) planes with an angle. Delamination bands consists of various numbers of strands (basal planes) from 3 to 15 (0002) planes oriented away from the matrix.

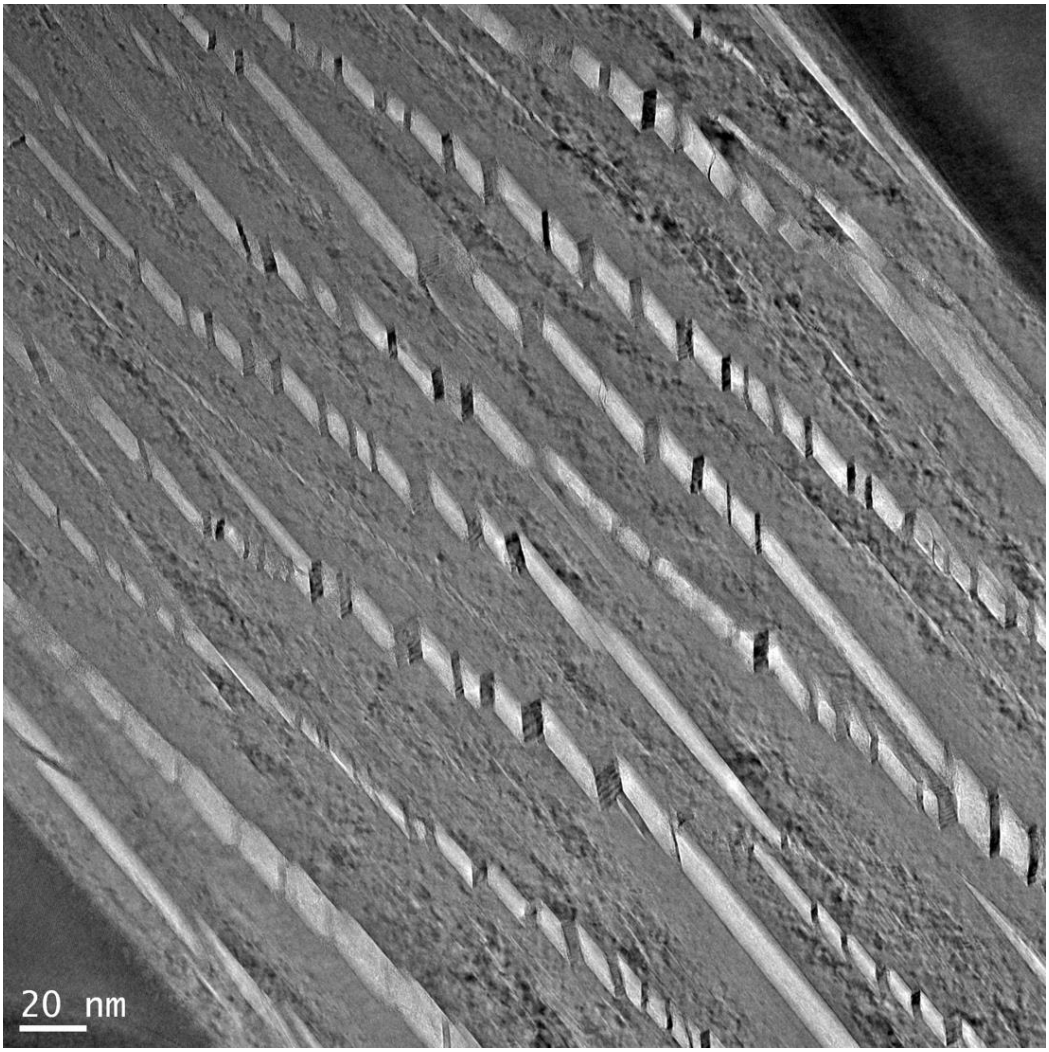

Figure 4.4. *TEM image of delamination bands seen in hBN particle*

These delamination bands can be either deformation bands, kink bands or twin bands according to the specific morphology and angle between band the and the matrix. Deformation bands defined as differently oriented regions in crystal due to the inhomogeneous deformation process. They can be observed in both single and polycrystalline materials and they are elongated along principal strain direction; however, they are poorly defined [57].

Twin band is another possibility, which occur due to the twinning of a crystal with a specific orientation with the rest of structure. Twinned structure appears as mirror of parent structure around the defined twinning plane under specific shear directions and there are specific direction and anglular relations between twins. Twinning can be occurred both in graphite and hBN structures. In graphite, twinning occurs as 20.48° rotation of structure around an axis parallel to $[1\bar{1}00]$ direction with $(11\bar{2}1)$ twinning plane

and under shear parallel to (0001) planes. However, in hBN twinning angle was reported as 139° rotation of (0001) planes from the matrix with $(1\bar{2}12)$ twinning plane under shear parallel to (0001) planes. According to this specific description of deformation twin, angle between delamination strands and matrix should be equal to 139°. Additionally deformation twins are visualized as changes in orientation with sharp twin boundaries [16, 58].

In hexagonal crystals, it is difficult to deform when stress is applied parallel to the basal planes of crystal. In the literature, it was found that when compression applied parallel to basal planes of cadmium and zinc crystals, localized deformation of crystal occurs as tilting of basal planes and shortening of crystal [59] and this is called as kinking. Kink bands can be found in f.c.c., b.c.c. and h.c.p. structures as well as layered structures under deformation especially compression parallel to the layered planes. Kink geometry is defined with kink inclination angle (α) and kink boundary orientation angle (β, ranging between 20° and 30°) and in this definition α should be twice of β as shown in Figure 4.5. Another characteristic feature of Kink bands is the gradual and continuous change of orientation [58].

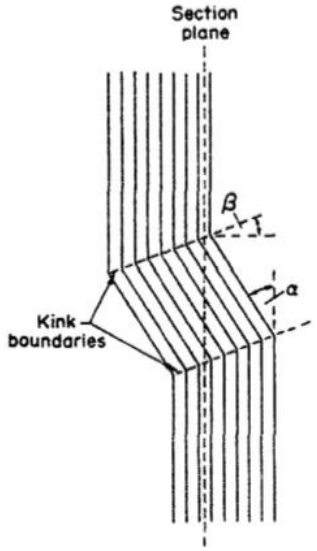

Figure 4.5. *Geometry of lattices after kinking [60]*

Deformation bands are more pronounced in f.c.c. and b.c.c. materials; however, kink and twin bands are more pronounced in hcp materials like graphite and hBN. The ideal kink band, deformation band and twin band is given in Figure 4.6.

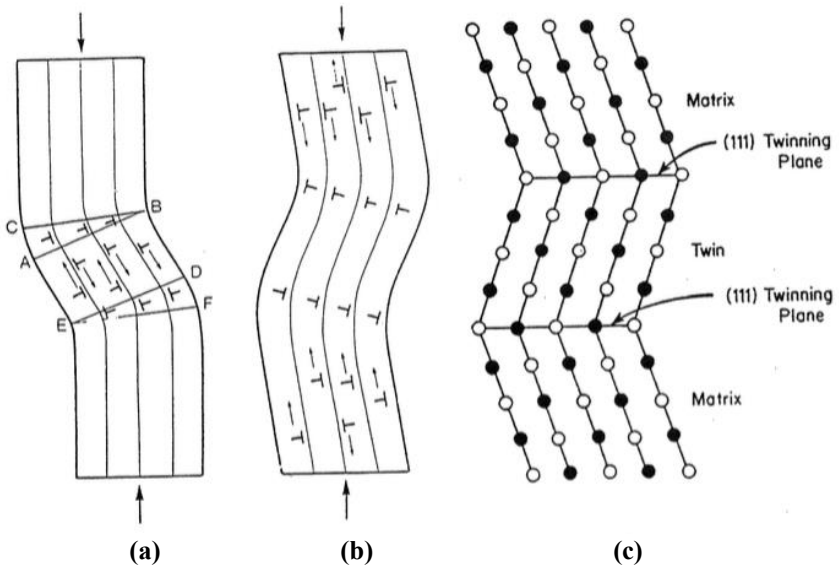

Figure 4.6. *Ideal schematics for (a) a tilt, (b) a deformation bands and (c) a deformation twin [16]*

In the literature, there are several studies reporting the delamination of hBN particles. In a study, ball milling of hBN particles resulted in the formation of delamination bands, one of them is defined as kink band but the other one do not satisfy the kink angle requirements [61]. In another study, unintentionally added hBN particles in hBN-SiC composite, delamination bands are appeared as kink band and deformation twins [16]. In the same study, theoretical kink angle is also calculated as 41°, which is same with deformation twin angle.

According to this information, detailed analysis of the delamination bands were carried out. The inclination angle of deformation bands in hBN particles were measured and it was found that angles vary between 136° and 163°; however none of them is 139° which is a criteria for deformation twin. Thus, none of the delamination bands were characterized as deformation twin. Considering the possibility of kinking, in most of the images it was not possible to determine the kink boundary to measure orientation angle of kink boundary. In the delamination band images, only one of them (given in Figure 4.7) was close to satisfy $\alpha=2\beta$ criteria (α=36.4° and β=18.6°) angles and only this one can be considered as kink band; however, all the others have randomly distributed angles as shown in Figure 4.8.

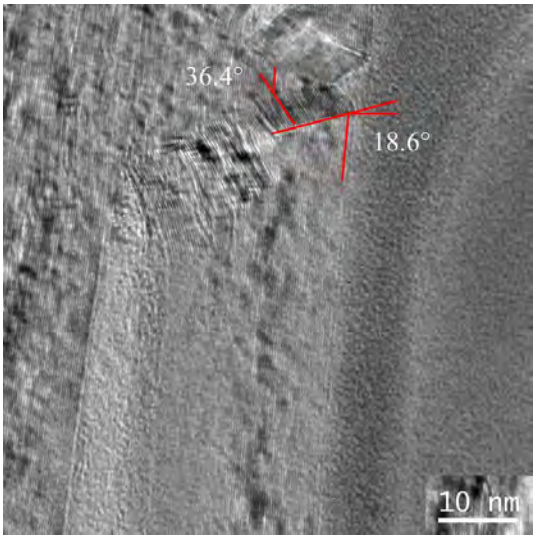

Figure 4.7. *TEM image of possible kink band in hBN particle*

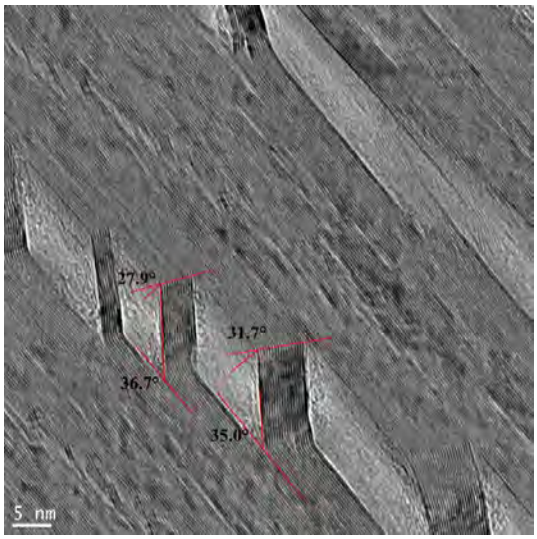

(a)

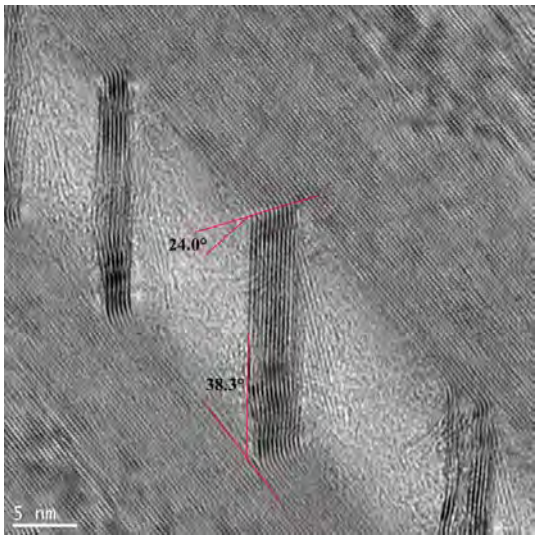

(b)

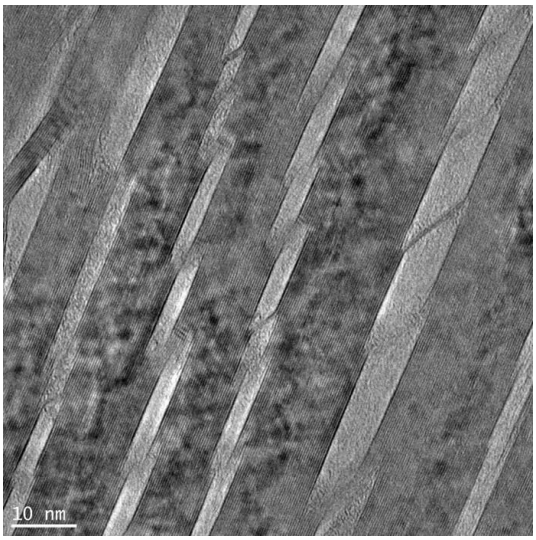

(c)

Figure 4.8. *(a-c) TEM images of selected hBN deformation bands*

The reason for the formation of delamination bands in hBN can be explained with formation of compression/shear stresses during composite production due to the thermal expansion coefficient differences between 6H-SiC and hBN during cooling from 1850°C to room temperature. Thermal expansion coefficient of 6H-SiC reported as 4.2 and $4.7x10^{-6}$ K^{-1} between 0-423°C for a and c-axes, respectively. Thermal expansion coefficient of hBN reported as anisotropic and 0 K^{-1} for a axis and $40.5x10^{-6}$ K^{-1} for c-axis at 770°C [16]. This anisotropic thermal expansion behavior of hBN cause significant shrinkage along c-axis, which resulted in tension stress along c-axis; however, along a-axis there was no compression/tension/shear stress due to zero thermal expansion coefficient of hBN during cooling, but there could be a tension stress due to the shrinkage of surrounding 6H-SiC particles during cooling from SPS sintering to room temperature.

Since there was no compression on crystal parallel to basal planes (and along any axis), delamination could only occur during cooling due to the tension perpendicular to the (0002) planes (in other words parallel to c-axis). This might be the reason for the observation of deformation bands without specific angles.

Another reason for characterization of delamination bands as deformation bands could be the unstable nature of them under electron beam. Even though these bands were originally kink or twin bands, their orientation might be changed during the TEM analyses. In our study, it was found that this band structure changed with the influence of electron beam. Change of the band structure under the electron beam is given in Figure 4.9 (taken with few seconds of intervals) and according to this, these bands can be changed from a kink to deformation band during TEM imaging. This could be the reason why kink or twin bands were not observed in this study. According to these results, delamination bands have randomly distributed tilt angle with the basal plane and this random distribution can be interpreted as deformation band due to tensile stresses along c-axis during cooling.

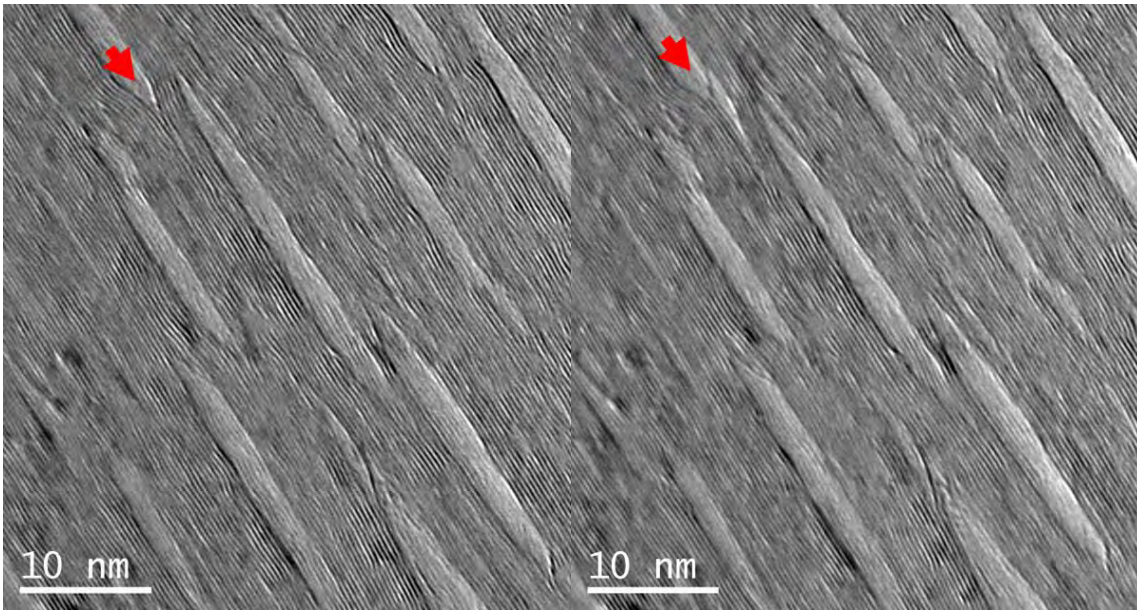

(a) (b)

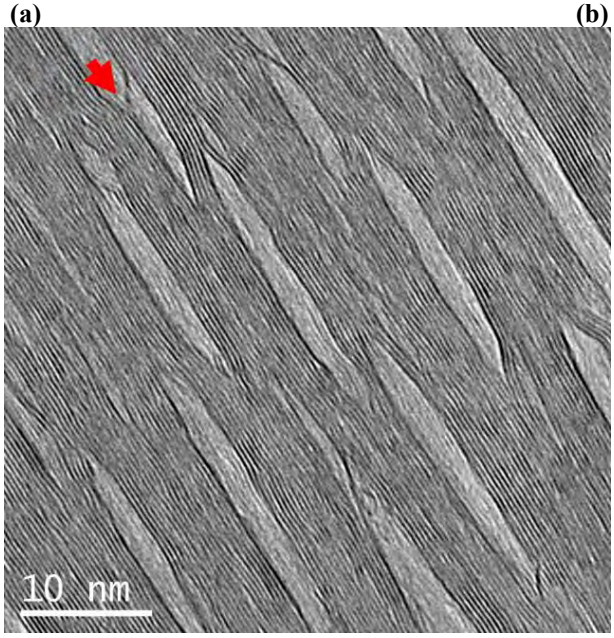

(c)

Figure 4.9. *Change of delamination bands under electron beam. (a), (b) and (c) images taken by few seconds intervals*

4.3.2. hBN twist boundaries

Another feature found in the TEM images was the local variation of contrast in basal planes, which characterized as twist boundaries within hBN (0002) planes as shown in Figure 4.10 and it means that (0002) planes rotated along a common axis, which cause orientation variation on (0002) planes on this common axis.

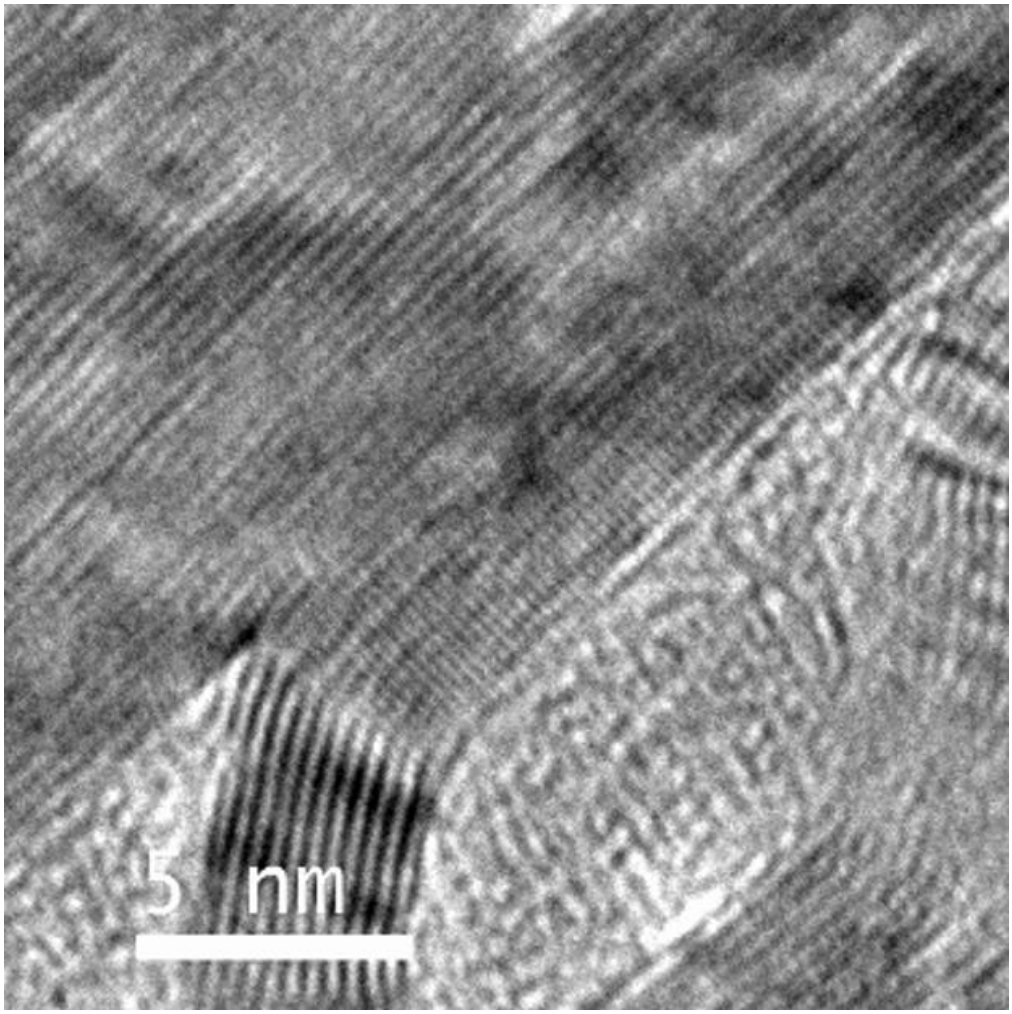

Figure 4.10. A t*wist boundary in hBN grains*

There are several different classes of special grain boundaries in polycrystalline materials and one of them is twist boundaries. In twist boundary, rotation axis between two grains is perpendicular to the boundary plane. Twist boundary is defined with rotation axis and rotation angle θ [62]. If the rotation angle is smaller than 15°, then, it is called as low-angle twist boundary otherwise high-angle twist boundary. The schematic view of [0001] twist boundary for hexagonal bicrystal is given in Figure 4.11. As seen in the scheme, given below, two hexagonal crystals with (0001) planes parallel to each other as well as [0001] directions but they are rotated with θ angle, thus $(01\bar{1}0)$ and $(10\bar{1}0)$ planes are no longer parallel to each other.

Table 4.2. *Four classes of grain boundaries [5]*

Boundary Type	*Interface Plane*	*Twist Angle*
Symmetrical Tilt Boundary	$\{h_1k_1l_1\} = \{h_2k_2l_2\}$	$\theta = 0$
Asymmetrical Tilt Boundary	$\{h_1k_1l_1\} \neq \{h_2k_2l_2\}$	$\theta = 0$
Twist Boundary	$\{h_1k_1l_1\} = \{h_2k_2l_2\}$	$\theta \neq 0$
Random Boundary	$\{h_1k_1l_1\} \neq \{h_2k_2l_2\}$	$\theta \neq 0$

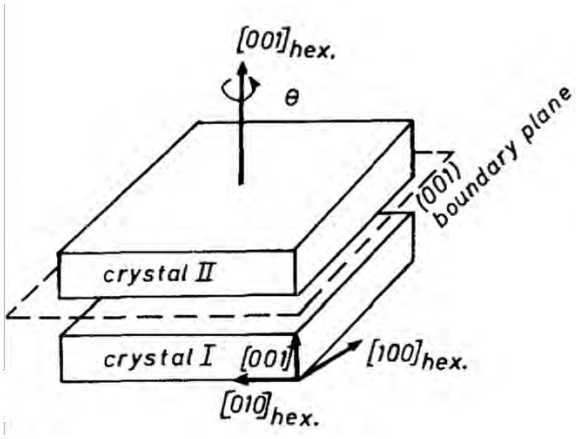

Figure 4.11. *Schematic explanation of [0001] twist boundary in hexagonal bicrystal [63]*

Low angle twist boundaries can be characterized with conventional HRTEM technique coupled with image simulations [58] and electron diffraction [64] method for twist direction that is perpendicular and parallel to the electron beam direction, respectively. It means that grains containing twist boundary must be tilted perfectly to correct zone axis for imaging of twist grain boundaries. Additionally, double diffraction can be a serious problem for electron diffraction method. TEM images taken along the $[11\bar{2}0]$ direction showed that even 10 mrad (0.57°) rotation around [0001] can cause contrast variation in (0002) planes of hBN [58, 61]. Twist boundaries in polycrystalline materials can also be identified in SEM-EBSD method [65].

TEM-PED method could offer a new methodology for twist boundary characterization no matter what is the orientation of twist direction with respect to electron beam with high resolution, in theory. In this method, there is not any requirements for grain orientation with respect to electron beam. In this study, TEM-PED method was used for twist boundary characterization and detailed orientation analysis of twist boundaries was done by using orientation maps and pole figures.

TEM-PED analyses were conducted for different hBN particles with 0.7° precession angle and orientation mapping results showed that some of the hBN particles contains band type structure within a single hBN particle which can be identified as hBN bicrystal. However, not all the inspected hBN particles have this kind of orientation bands; an example of this type of orientation band is given in Section 4.2. Orientation difference between bicrystals can be measured by using misorientation tool in MapViewer2 and it has been seen that misorientation angle varies between 9.5° to 29° and given in Table 4.3. Selected hBN bicrystals with 23°, 29°, 12°, 9.5° and 25° of misorientations are given in Figures 4.12-4.16, respectively. Even though misorientation tool gives the misorientation angle between differently oriented particles, it does not provide in which axis or planes are oriented with a given angle directly. In order to get this information, pole figures of possible misoriented planes needs to be examined and extracted.

Visualization of the absolute orientations in bicrystals was done by using CrystalMaker software and {hkil}<uvtw> parameters used during this process were calculated according to Equations (2.3) and (2.4). According to these results, (0001) planes of crystals are parallel to each other and it looks like crystals are rotated along [0001] direction on common (0001) plane. It means that, there should also be a rotation angle between $(11\bar{2}0)$ planes.

Table 4.3. *Misorientation angles between orientation bands in hBN bicrystals (Bold results are given in here)*

Sample	***Misorientation Angle (θ°)***	***Sample***	***Misorientation Angle (θ°)***
14/070	12	29/070	24
15/070	22	34/070	25
16/070	22	39/070	26
17/070	23	44/070	27
20/070	29	45/070	22
21/070	23	**46/070**	25
23/070	29	50/070	25
25/070	9.5	54/070	22

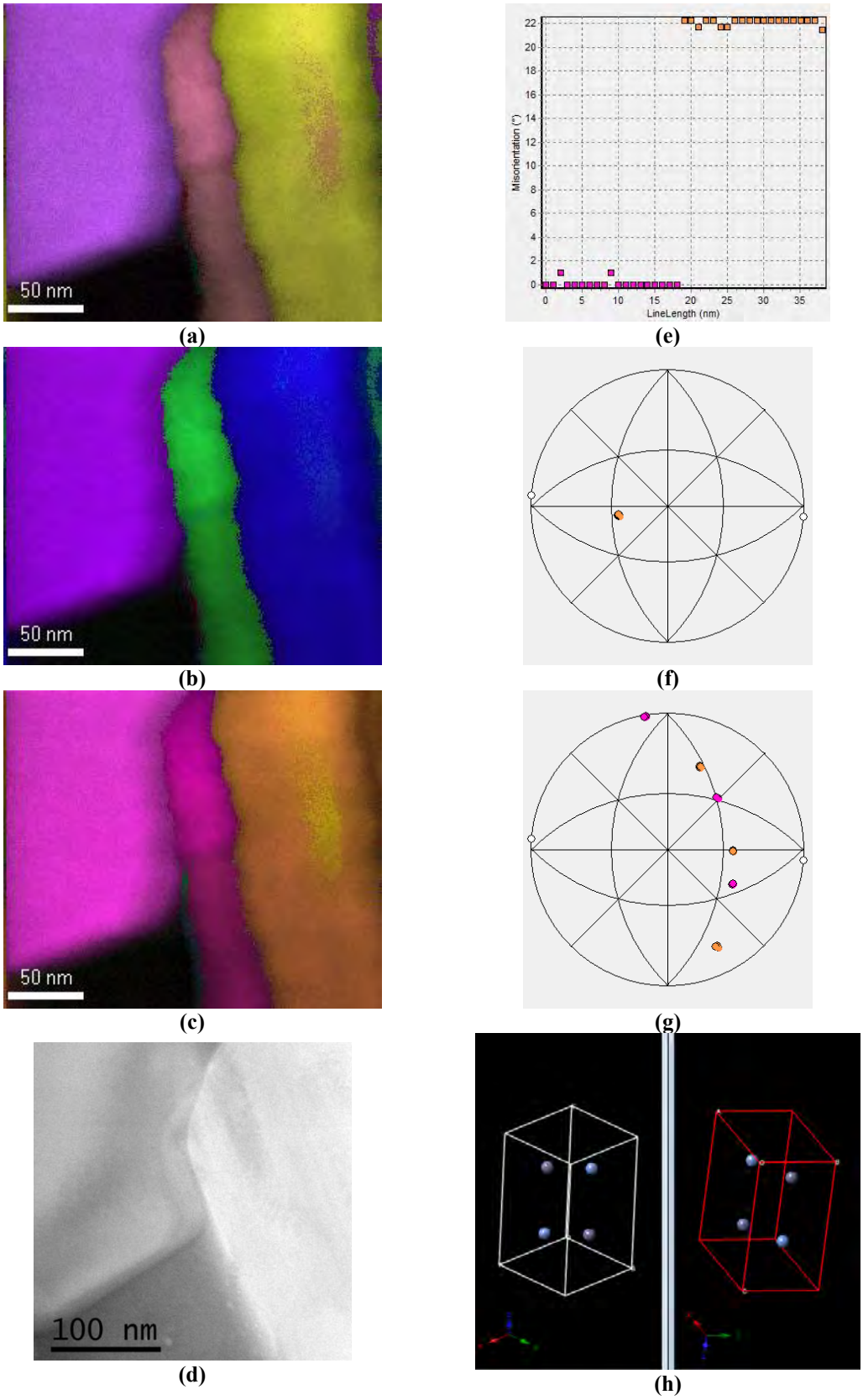

Figure 4.12. *TEM-PED orientation mapping results (a) x, (b) y, (c) z directions, (d) TEM image of analysed region, (e) misorientation chart, (f) (0001) pole figure, (g) [11$\bar{2}$0] pole figure, (h) absolute orientations of rotated hBN bicrystal with 22° (∑7) (0001) twist boundary*

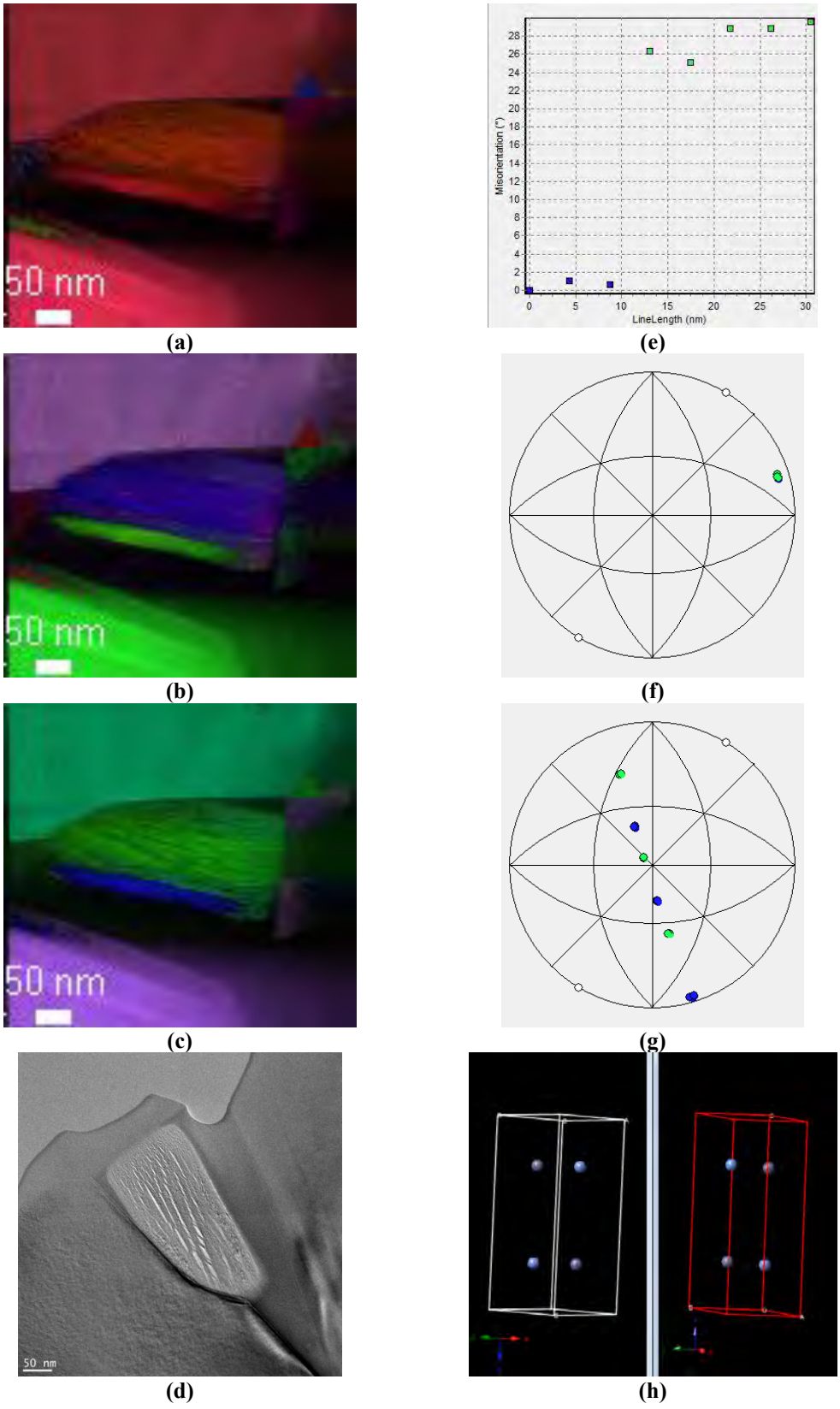

Figure 4.13. *TEM-PED orientation mapping results (a) x, (b) y, (c) z directions, (d) TEM image of analysis region, (e) misorientation chart, (f) (0001) pole figure, (g) [11$\bar{2}$0] pole figure, (h) absolute orientations of rotated hBN bicrystal with 28° (∑13) (0001) twist boundary*

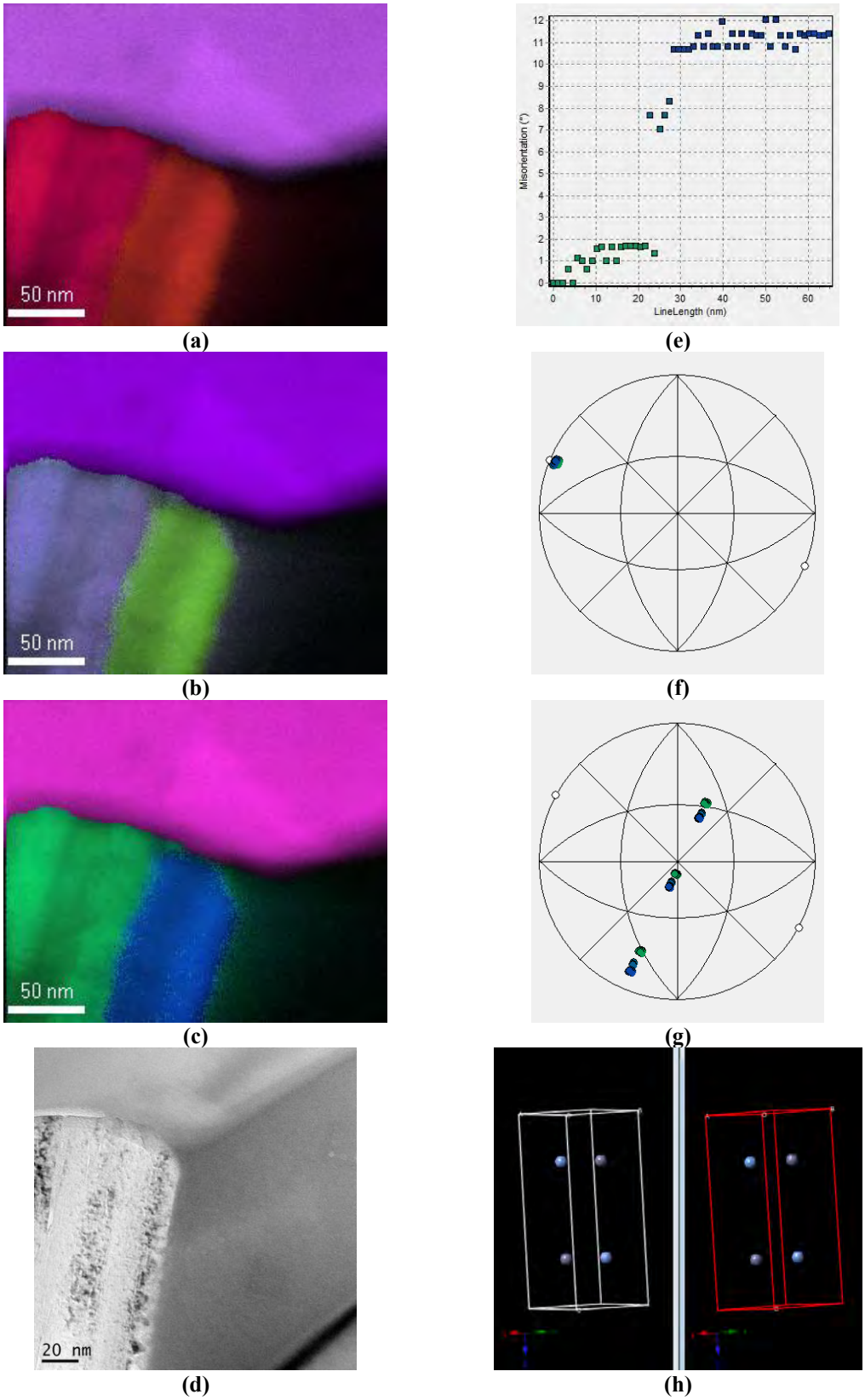

Figure 4.14. *TEM-PED orientation mapping results (a) x, (b) y, (c) z directions, (d) TEM image of analysis region, (e) misorientation chart, (f) (0001) pole figure, (g) [11$\bar{2}$0] pole figure, (h) absolute orientations of rotated hBN bicrystal with 13° (∑19) (0001) twist boundary*

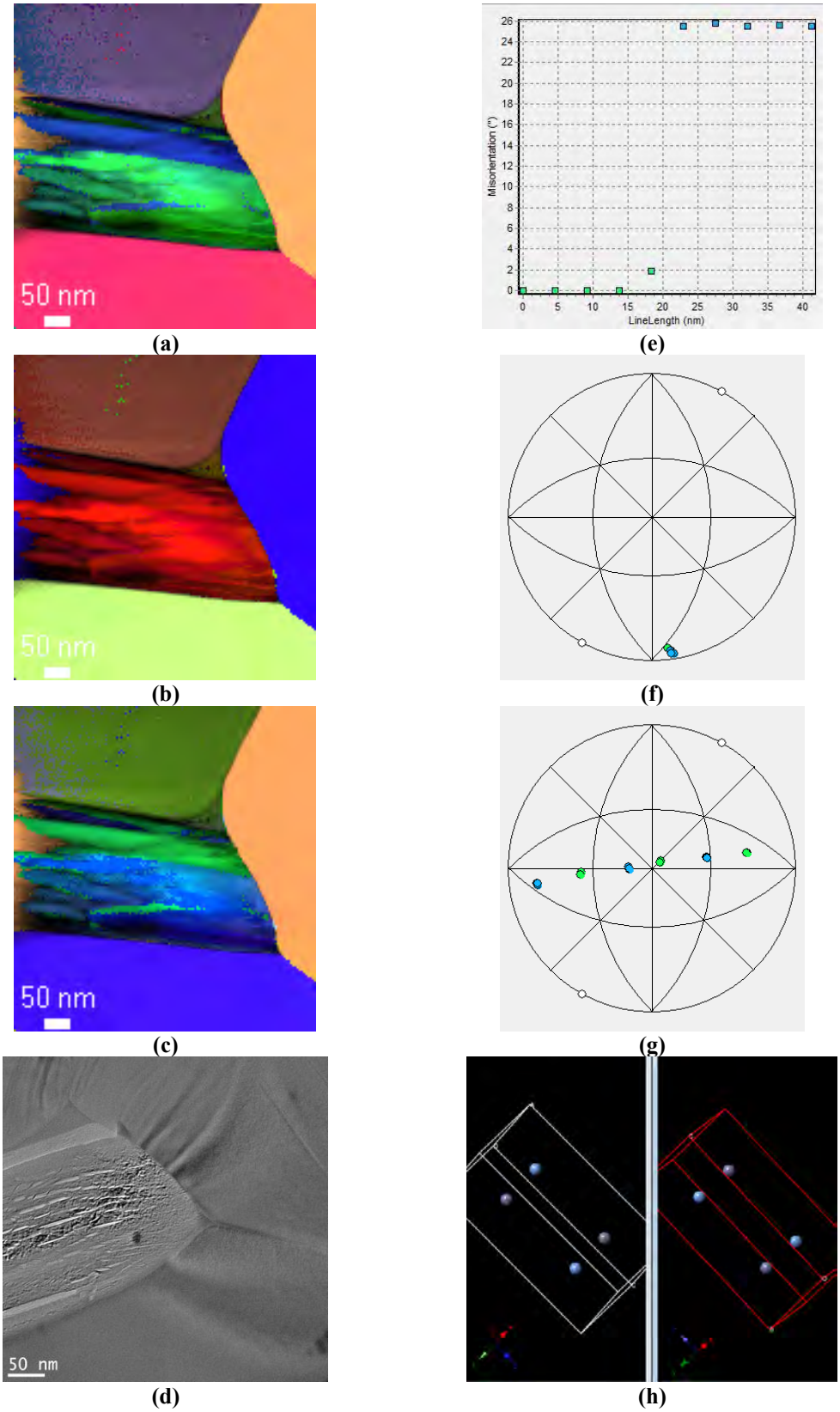

Figure 4.15. *TEM-PED orientation mapping results (a) x, (b) y, (c) z directions, (d) TEM image of analysis region, (e) misorientation chart, (f) (0001) pole figure, (g) [11$\bar{2}$0] pole figure, (h) absolute orientations of rotated hBN bicrystal with 26° random high angle (0001) twist boundary*

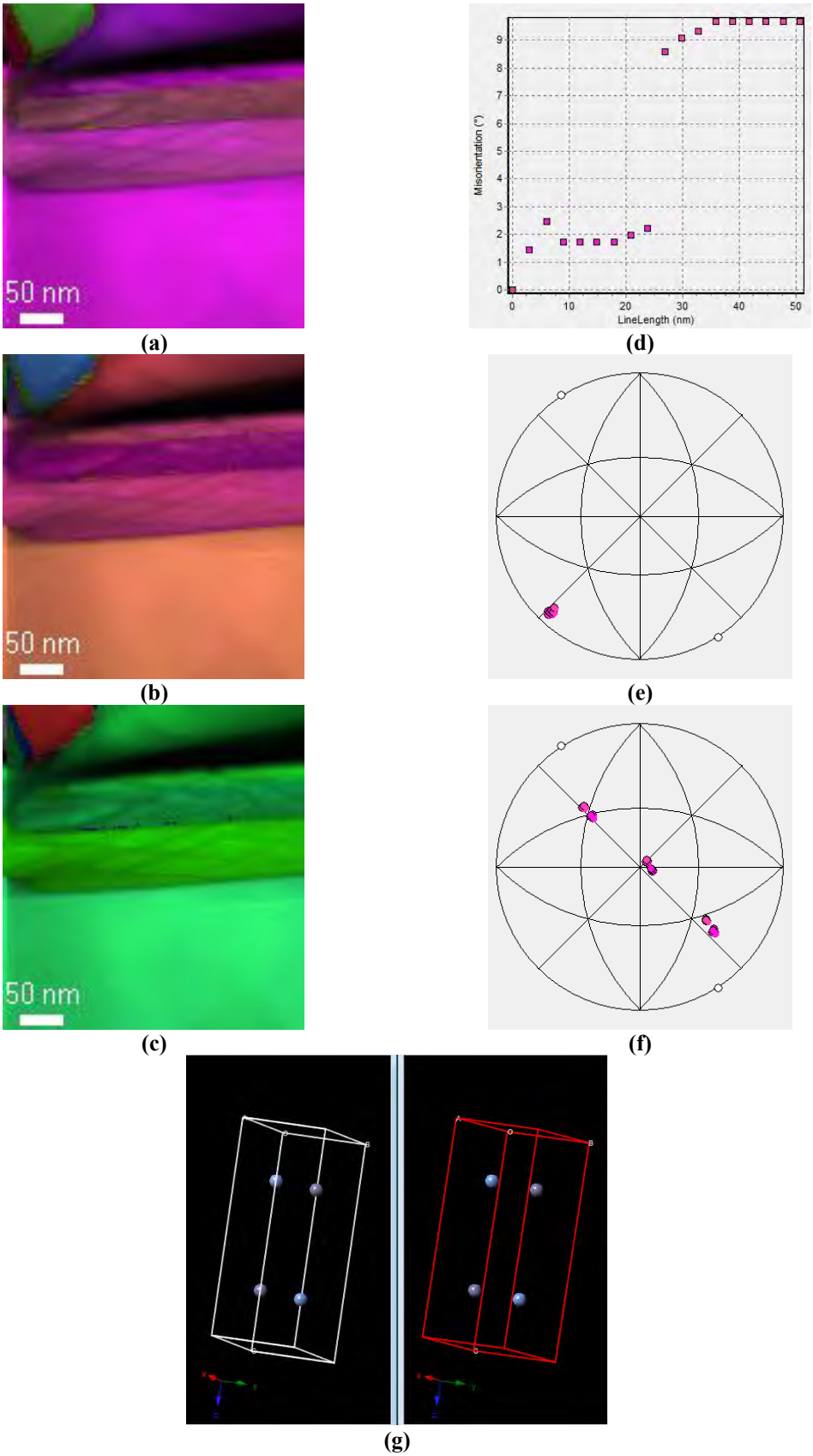

Figure 4.16. *TEM-PED orientation mapping results (a) x, (b) y, (c) z directions, (d) misorientation chart, (e) (0001) pole figure, (f) [11$\bar{2}$0] pole figure, (g) absolute orientations of rotated hBN bicrystal with 9.5° (0001) random low angle twist boundary*

For the characterization of these bands, having different orientations in accordance with orientation maps, pole figures were used. Pole figures can be used to show the relative orientations of specified plane for different crystals. In the pole figures, for example (0001) pole figure, all the (0001) plane normals cross at the same point on the reference sphere. That means all (0001) planes are parallel to each other. The principle is the same for $(11\bar{2}0)$ pole figure, however as seen in the figures (given above) plane normal of $(11\bar{2}0)$ planes of different bands in the hBN particle crosses at different points in reference sphere and the angle between these points gives the rotation angle around common axis, which is [0001]. In hexagonal crystals Miller indices of many crystallographic planes and their normal directions are not the same; however, Miller indices are the same for (0001) and $(11\bar{2}0)$ planes and their normal directions ([0001] and $[11\bar{2}0]$), therefore, it is safe to use these planes in pole figures.

All these results proved the presence of (0001) high angle twist boundaries in hBN bicrystals with various angles smaller than 30°. After these results, then a question of *"Do these misorientation angles mean any specific boundaries or they are just random twist boundaries?"* can be raised. In order to search for an answer of this question, coincidence site lattice theory and grain boundary energies needs to be understood.

Coincidence site lattice (CSL) theory is a straightforward method to apply and it is used to identify special grain boundaries, especially the high angle ones. CSL theory based on the geometrical relationship between the lattices of two grains and coincidence periodicity of atoms in these lattices. When two lattices rotated with respect to each other, atoms which create the lattice rotate as well and due to the rotation atoms of both lattices are coincides with a periodic fashion and this periodicity is defined with CSL theory. Figure 4.17 shows the schematic view of the CSL description [62, 66, 67].

Periodicity of CSL is characterized by the value of $\sum$ (calculated as in (4.1) which is the reciprocal of density of coincidence sites between two lattices meaning that lower the value of $\sum$, increase in number of coincidence sites. Resulted CSL boundaries with different numbers of coincidence atoms exhibit different properties than random boundaries [62].

$$\sum = \frac{\text{number of coincidence sites in an elementary cell}}{\text{total number of all lattice sites in an elementary cell}} \tag{4.1}$$

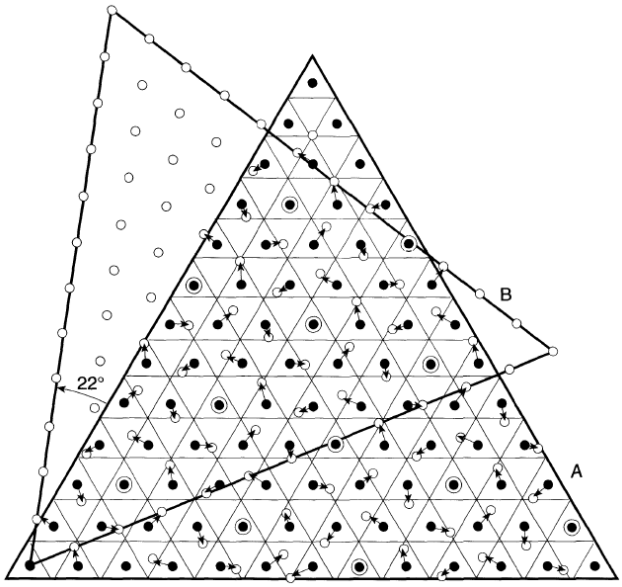

Figure 4.17. *Schematic view of CSL ∑7 boundary with 22° rotation [66]*

In an ideal grain boundary between bicrystal, there is 0° or no misorientation and all the atoms will coincide itself meaning that ∑ = 1 and interfacial energy is zero since there is actually no interface present. For a rule of thumb, grain boundaries having low value of ∑, are accepted as special boundaries. Smallest angular deviation from the ideal grain boundary cause significant change in ∑ value due to change in geometry of two lattices.

In the literature, (0001) twist boundaries can also present in SiAlON [63], bicrystal α-Fe_2O_3 nanoblades [68], Mg-alloys [69] in addition to the hBN [70] and in these studies, (0001) twist boundaries with some specific rotation angles are defined with CSL theory.

TEM study of baked hBN nanoparticles [70] revealed that great majority of the overlapped hBN grains have common rotation axis of [0001] with 13°, 22° and 28° of rotation as a result of electron diffraction pattern analyses and grains having these rotation angles are related with ∑19, ∑7 and ∑13 according to the CSL theory. It means that 1/19, 1/7 and 1/13 of atoms of new (rotated) orientation are coincident with atoms in old (stationary) orientation. Same CSL grain boundaries are also found in bicrystal α-Fe_2O_3 nanoblades and SiAlON.

According to these results, hBN twist boundaries present in this thesis can be classified as CSL twist boundaries and random twist boundaries according to the CSL theory. The samples having rotation angles of 12°, 23° and 29° can be defined as CSL ∑19, ∑7 and ∑13 boundaries, respectively, even if they are not in exact CSL angles due

to the angular resolution of TEM-PED method, which can give ±1° deviation. Schematic view of CSL ∑19, ∑7 and ∑13 (0001) twist boundaries are given in Figure 4.18.

In hexagonally structured materials, there is a prerequisite for the presence of CSL boundaries, unlike the cubic structure. Presence of different CSL boundaries depend on the c/a ratio. For example, ∑11 CSL boundary can be observed for c/a = 1.58 and 1.63 but not present for c/a = 1.55, 1.60 and 1.46 [71]. However, CSL ∑7, ∑13 and ∑19 grain boundaries do not depend on to the c/a ratio and they can be present any hexagonal structured crystals [72].

In this study CSL ∑7, ∑13 and ∑19 grain boundaries were found in hBN but in order to find out the answer for *"are these boundaries energetically favorable or not?"*, grain boundary energy variation for different CSL boundaries needs to be explained. According to CSL theory by Kronberg and Wilson, increase in the number of coincident atoms or in other words increase in the ratio of coincident atom number to non-coincident atom number, energy of the grain boundary decreases [67]. Same CSL grain boundaries are also found in bicrystal α-Fe_2O_3 nanoblades and these boundaries are classified as the lowest interfacial energy according to the CSL theory.

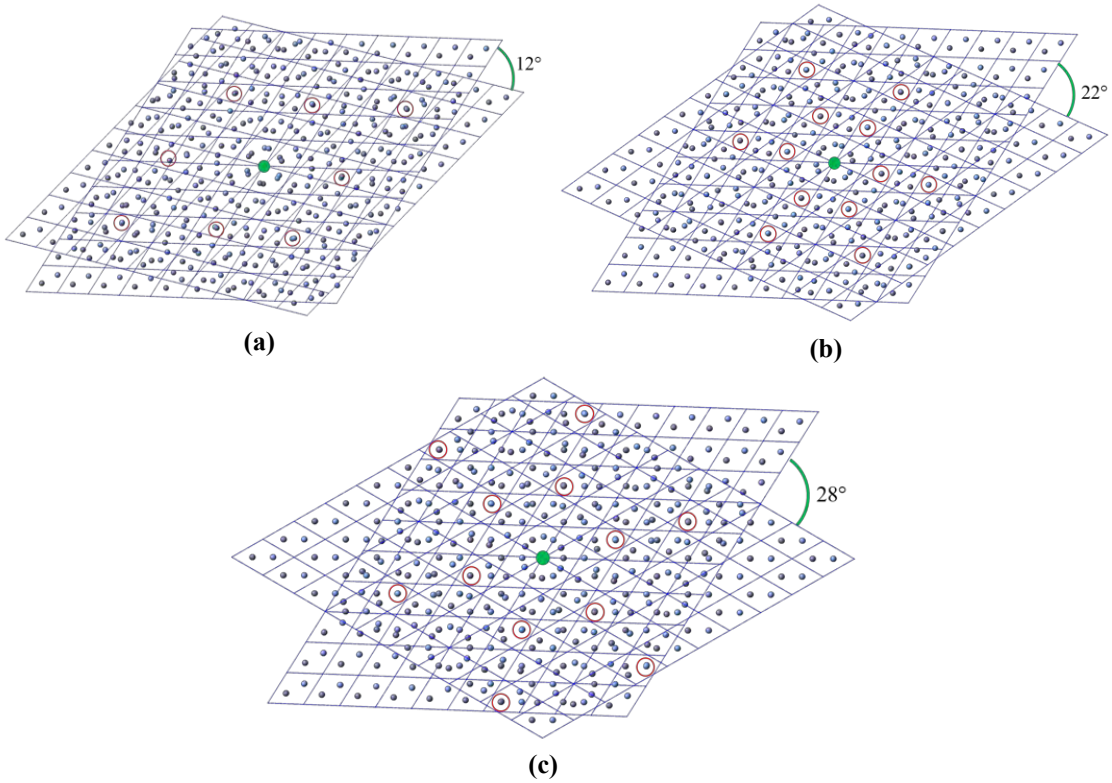

Figure 4.18. *Schematic view of hBN (0001) (a) ∑19 (12°), (b) ∑7 (22°) and (c) ∑13 (28°) twist boundaries*

According to this theory, same CSL boundaries resulted in same grain boundary energy for the same structure and this theory accepts atoms only as hard spheres. However, in reality, grain boundary energies vary even if they have the same CSL values. Another study also revealed that variation of grain boundary energies are not directly related with the CSL index and it can be vary for different CSL indexes [62].

In the literature, grain boundary energy changes with respect to twist rotation angle are reported and shown in Figure 4.19 for h.c.p. SiAlON [63] and Mg [69] structures. One of the most important result obtained from these plots is the variation of grain boundary energy at the same rotation angle for different compositions but same structure. Grain boundary energy is not only dependent to the twist angle but also the composition.

If the grain boundary energy change of SiAlON is considered, hBN CSL twist boundaries found in this thesis can be defined as energetically favorable and other random high angle twist boundaries are high energy boundaries. This assumption is done according to the SiAlON grain boundary energy change and it is not correct when Mg boundary energy change is taken into account. Furthermore, in order to validate whether our theory is correct or not, change of grain boundary energy for hBN needs to be known.

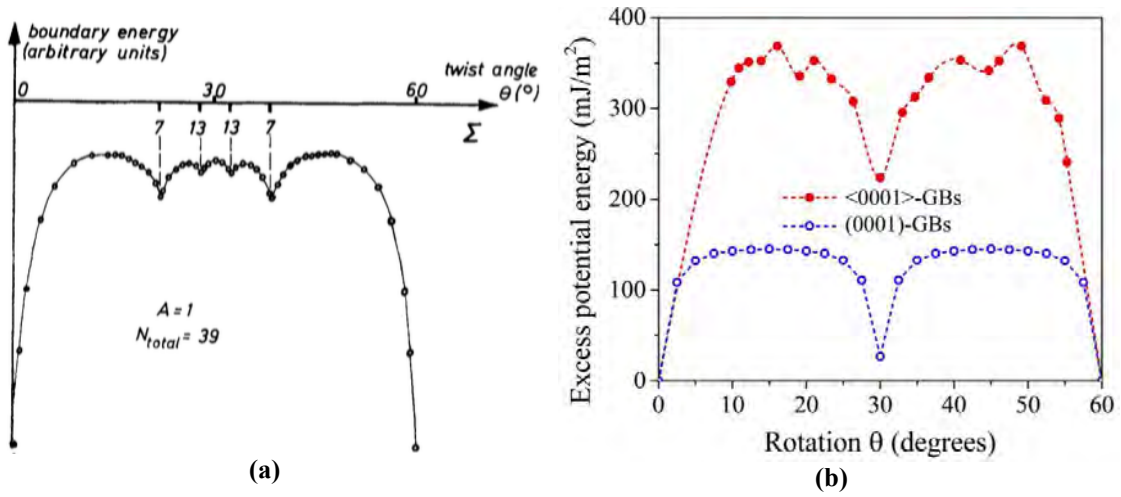

Figure 4.19. *Twist boundary energy change for (a) SiAlON [63] and (b) Mg (blue dotted line) [69] h.c.p. structures*

Change of energies for the same CSL value for the different materials with the same structure is one of the downside of CSL theory, even if they are same from geometrical point of view. Because of the variation in grain boundary energy with respect to misorientation angle between grains for different materials with same crystal structure, grain boundary energy measurements and theoretical calculations needs to be studied. In

the literature, there is no reported study about (0001) twist grain boundary energy change for hBN, thus it needs to be measured. Since this measurement is beyond scope of this thesis, it will remain as a future study.

Even though TEM-PED technique has 1° angular resolution, which can be very important for CSL theory, this method can be used for the grain boundary characterization due to the its flexibility on characterization without sample tilting. In other grain boundary characterization methods like HRTEM and SAED, sample must be tilted to proper zone axis in order to characterize the grain boundaries; however, TEM-PED eliminates this requirement in exchange for angular resolution compared with other methods, e.g. SAED method can provide angle with 2 significant figures such as 21.79°. Angular resolution can be the drawbacks of TEM-PED method for the grain boundary characterization.

4.4. Conclusions

Characterizations of SiC composite with in-situ formed hBN phase was done by various TEM and STEM methods in order to reveal overall microstructure as well as special orientations between hBN and SiC particles, if any present. TEM and STEM images showed that hBN particles were distributed between SiC particles and liquid phase is present between them. In order to investigate orientation relation between particles TEM-PED studies were conducted however, no special relation was found between them, rather they were aligned randomly. However, TEM-PED studies revealed that in the hBN particles band type regions with different orientation were found and according to their pole figures, they were characterized as (0001) twist boundary in hBN bicrystals. Based on their misorientation angles with matrix, grain boundary between them were defined as special $\sum 7$, $\sum 13$, $\sum 19$ (0001) twist boundaries as well as random high angle boundaries. In TEM images, it was seen that (0002) planes of hBN particles were delaminated due to anisotropic thermal expansion coefficient of hBN during cooling and deformation bands were formed.

5. CHARACTERIZATION OF B_4C-TiB_2 CERAMIC COMPOSITES

5.1. Introduction

Boron carbide (B_4C) is one of the important non oxide ceramic material due to its superior physical and chemical properties such as extreme hardness, low thermal conductivity [73]. Even though most of superior properties coming from its highly covalent bonding characteristics between boron and carbon atoms, it also comes with a major disadvantage, that is the difficulty in densification and sintering as pure material by pressureless sintering methods [74]. In order to improve the sinterability of B_4C, sintering additives such as C, Al, SiC, TiB_2 phases are added as sintering aid and also these additives improves mechanical properties as well [75]. Beside the sinterability difficulties due to its properties, it is also hard to obtain complex geometries by the machining. Improving the electrical properties of B_4C with an addition of electrically conductive phases may improve the machinability with introducing new methods like electrical discharge machining (EDM). Titanium diboride (TiB_2) is one of the candidate material for the composite production due to its high electrical and thermal conductivity as well as high hardness. Additionally TiB_2 is a suitable material because of the binary eutectic formation with B_4C. Binary phase diagram of B_4C- TiB_2 is given in Figure 5.1 [73]. Pressureless sintering of pure B_4C is very difficult and require very high temperatures in order to get 93% of relative density. Sintering additives can improve the densification however; it still requires very high temperatures like 2250°C. In order to decrease the sintering temperatures, while obtaining high relative densities, pressure assisted sintering methods like spark plasma sintering (SPS) [76] or hot pressing [77] can be used.

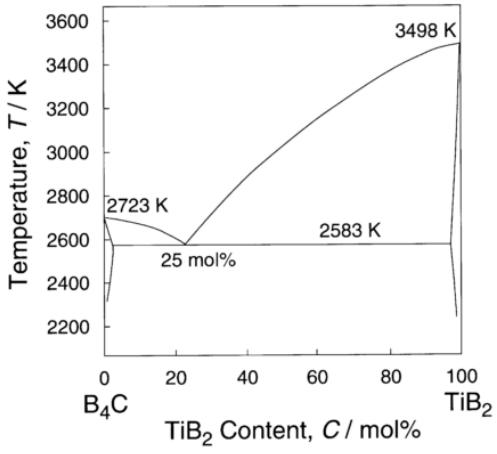

Figure 5.1. *Binary phase diagram of TiB_2-B_4C [73]*

5.2. Samples Used in This Study

In this study, two different production routes were used in order to obtain B_4C- TiB_2 ceramic composites. First production method was the reaction spark plasma sintering (R-SPS) at Anadolu University, Turkey. In this method B_4C- TiB_2 composites were prepared by mixing TiC and B_4C powders (9/91 by mass, respectively) with SiAlON balls for homogenization and then reaction spark plasma sintered at 1980°C for 15 min at 30 MPa pressure under vacuum. During sintering TiC was reacted with B_4C and form TiB_2 according to the (5.1. In the literature carbon is used as sintering additive in order to help the densification of pure B_4C [75], also in this study carbon is formed according to this equation and it acts as sintering aid for the composite system.

$$2TiC_{(s)} + B_4C_{(s)} \rightarrow 2TiB_{2(s)} + 3C_{(s)} \ (T>0K, \Delta G<0) \qquad (5.1)$$

The other production method was hot pressing (HP) at Institute of Science and Technology for Ceramics, Italy. In this method three different samples were mixed in ethanol as follows;

- 50/50-BM: (50 % B_4C – 50 % TiB_2) powders were soft ball milled with WC balls
- 50/45/5-BM: (50 % B_4C – 45 % TiB_2 – 5% WC) powders were soft ball milled with WC balls
- 50/50-HEM: (50 % B_4C – 50 % TiB_2) powders were high energy ball milled with WC-Co balls

Dried and sieved powders then sintered by using hot press at 1930°C for 20 minutes with 30MPa pressure under vacuum.

5.3. Characterization of the B_4C-TiB_2 Composites

5.3.1. Reaction spark plasma sintered b_4c-tib_2 composites

Characterization of the sample prepared by reaction spark plasma sintering was carried out by SEM, and (S)TEM techniques.

Samples for SEM were prepared by using conventional mechanical polishing method with diamond solutions and polishing discs as well as Ar^+ ion cross-section polisher (CP). Mechanical polishing caused pull out of particles from the polished surface due to weakly bonded TiB_2 phase and in addition to that, surface was not free from scratches due to the very high hardness of B_4C. The composite is mainly composed of

two different phases with a different hardness values and because of that reason sample surface is polished non-uniformly. To overcome the mechanical polishing disadvantages, cross-section polisher that use accelerated Ar^+ ions parallel to polished surface was used. Sample polished at CP has free from the scratches and pull out was significantly reduced. TEM sample preparation was done with conventional mechanical thinning followed by ion beam milling.

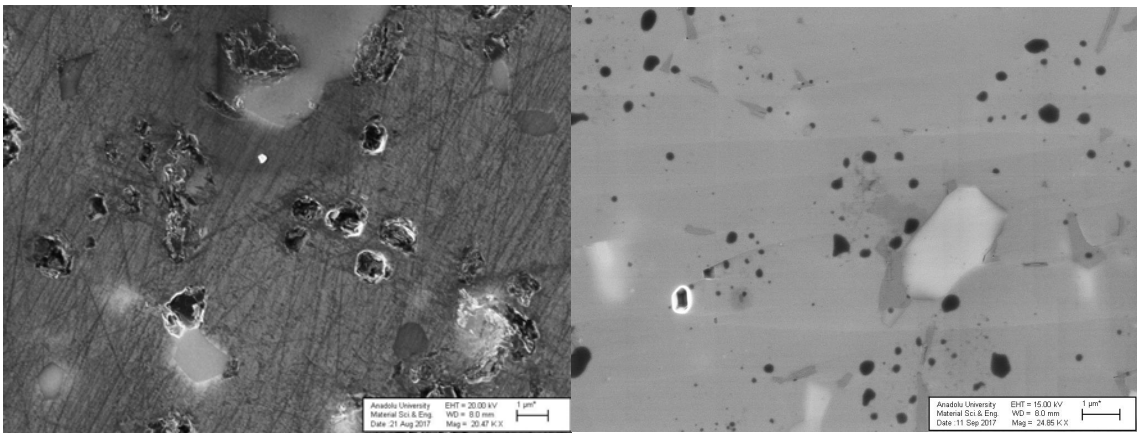

(a) **(b)**

Figure 5.2. *Scratches and pulled out particles can be easily seen from SEM-in-lens images for (a) after mechanical polishing and (b) after CP, free from scratches and pullout was significantly reduced*

5.3.1.1. Scanning electron microscopy results

SEM investigations were done at 15 and 20 keV accelerating voltages and SE, BSE and in-lens detectors were used to obtain different information from the same area. Since samples were polished, SE images did not provide much information other than pores. In BSE images, samples are mainly composed of three different phases with white, gray and black contrast as TiB_2, SiC and B_4C, respectively. Compositions of these samples were confirmed by EDX analyses (Figure 5.3). In the SEM-EDX results, due to the interaction volume of electrons, X-rays were generated from both B_4C and SiC phases and because of this reason SiC spectrum contains signal of both phases. In order to separate SiC spectrum, B_4C spectrum was subtracted from SiC spectrum, both processed and unprocessed spectra (labelled as SiC (B_4C subtracted) and SiC (raw), respectively) were given in Figure 5.3. SiC phase was not intentionally added to the composition but formed during sintering as a reaction product from C and worn out mixing ball composition, which formed according to (5.1).

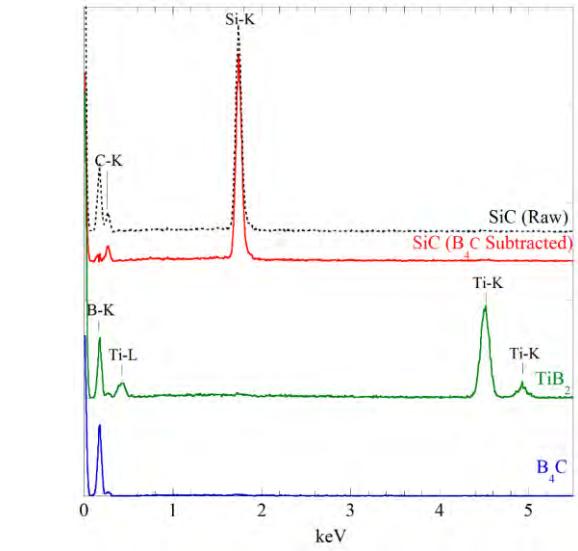

(a)

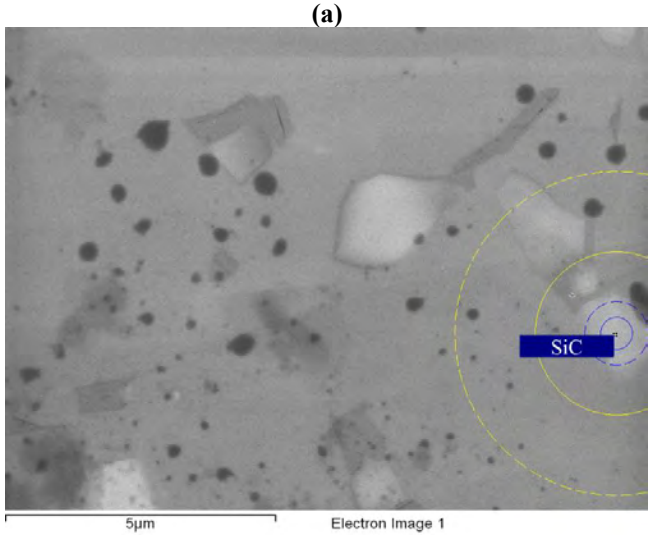

(b)

Figure 5.3. *SEM-EDX (a) spectra of TiB_2, SiC, B_4C and (b) X-ray generation region for analysed grain at this accelerating voltages*

In-lens imaging method provided much more detail about the sample, which were not present in BSE and SE images; such as carbon particles as graphite like and free carbon forms. There was significant amount of graphite like and free carbon formation according to the in-lens images. For the in-lens imaging of the graphite particles 15 keV was chosen due to the lower interaction volume of electrons, thus contrast of these particles improved. One of the major findings from the in-lens images is; graphite like carbon was found next to TiB_2 phase, which is quite reasonable when sintering reactions are considered. During sintering TiC phase reacts with B_4C and reaction products are TiB_2 and carbon.

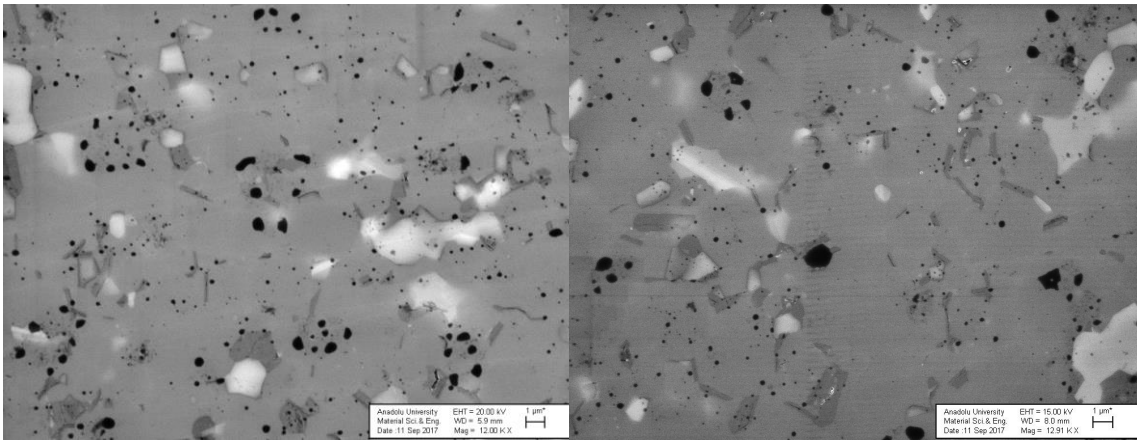

(a) **(b)**

Figure 5.4. *SEM in-lens images obtained with (a)20 keV and (b)15 keV acceleration voltages*

The composition of the graphite like carbon was confirmed with EDX analyses. SEM-EDX results showed that graphite like regions attached to TiB_2 phase consists of carbon but EDX spectrum also contains B element due to the e^- interaction volume, and X-rays are collected from both B_4C and C regions. To distinguish whether carbon signal is originating from B_4C or C, both spectra are compared in Figure 5.5. According to this comparison, B_4C spectrum (obtained from red point in Figure 5.5 (a)) showed 0.07 C/B intensity ratio; however, spectrum that was obtained from graphite like carbon region (as shown with yellow point in Figure 5.5 (a)) has 0.7 C/B intensity ratio. This clearly showed that X-rays collected during graphite like carbon region did not only belong to C but also B_4C due to the interaction volume of electrons. EDX results additionally showed that there was no residual TiC present in the structure, thus all TiC was consumed during sintering.

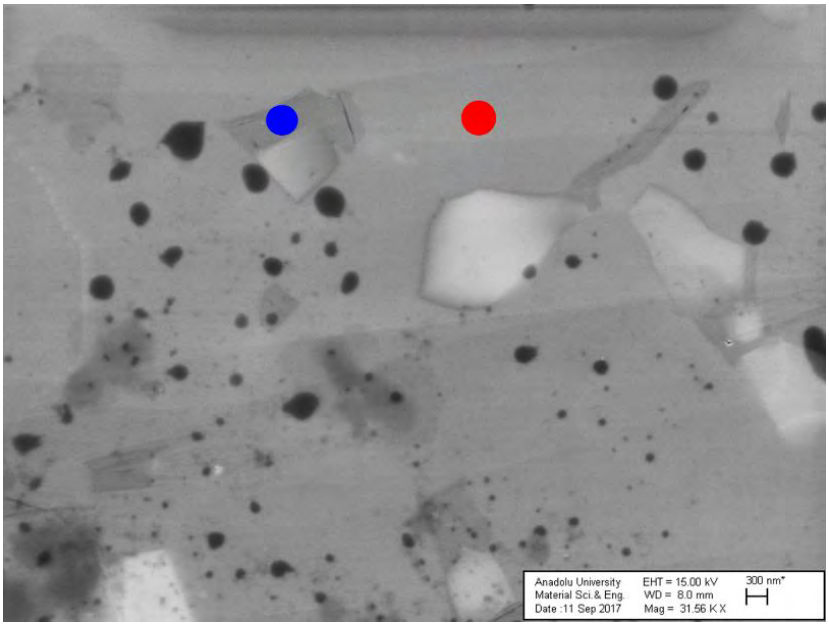

(a)

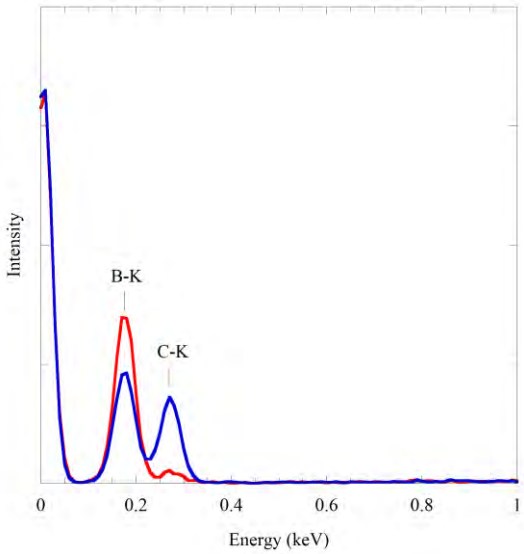

(b)

Figure 5.5. *Comparison of EDX spectra collected from graphite like carbon and B_4C phases. For the comparison, zero peaks of both spectra were scaled and spectra are color coded.*

The free carbon as black roundish regions in the in-lens images are also confirmed with the EDX-line scan analyses. Figure 5.6 shows the result of line scan analysis. In order to confirm the composition and structure of graphite-like and crystallinity of free carbons and relation between graphite like carbon and TiB_2, TEM studies needs to be conducted.

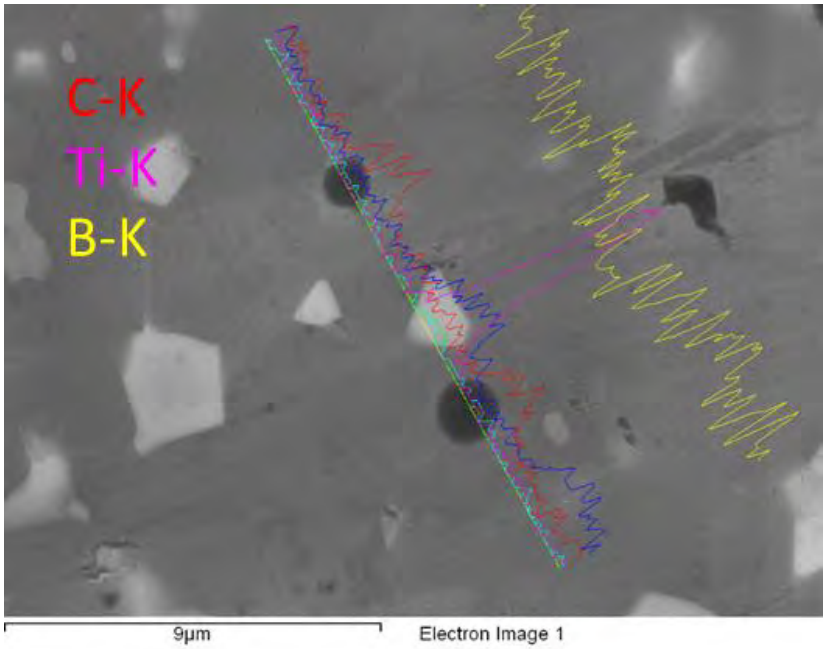

Figure 5.6. *Line scan analysis result of the free carbon*

5.3.1.2. Transmission electron microscopy results

TEM analyses showed that, there are four different phases as in SEM results in the TEM-BF images. The contrast difference between TiB_2, SiC and B_4C is significant due to the mass contrast mechanism, therefore, they can be easily differentiated. However, due to the very close mass of graphite like carbon with B_4C, it is hard to differentiate these phases in TEM-BF images at low magnifications. Higher magnification TEM imaging can differentiate graphite like carbon and lattice image of this phase (Figure 5.7(c)) confirms that particles with graphite like morphology are graphite. Due to the anisotropic linear thermal expansion coefficients ($1.0x10^{-6}$/C normal to c-axis and $27x10^{-6}$/C parallel to c-axis [78]) of graphite, during cooling of the sample, graphite basal planes were delaminated similar to the hBN particles given in Section 4.3.1. which can decrease the strength of the composite. TEM analyses also revealed that free carbons found in SEM were not present in TEM sample; this indicates that free carbons might formed during cross section polishing process as an artefact due to high energy Ar^+ ions.

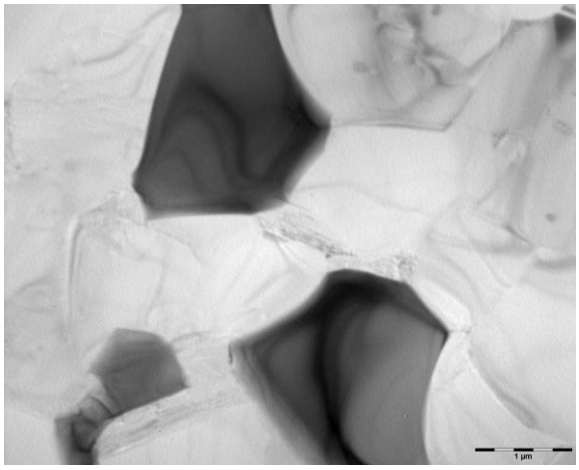

(a)

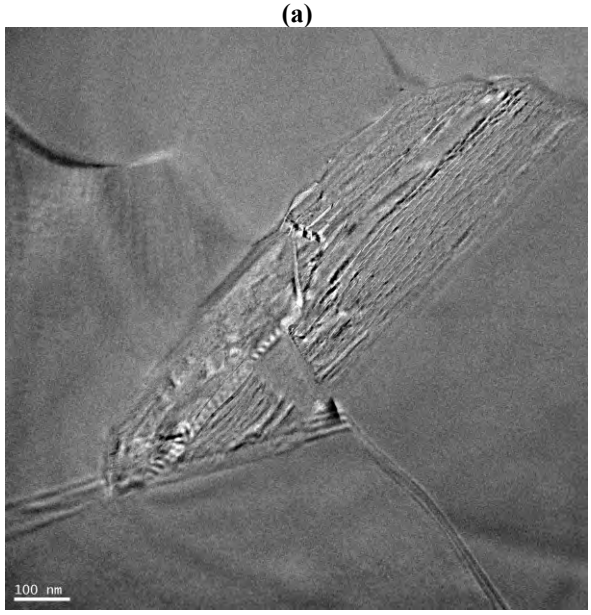

(b)

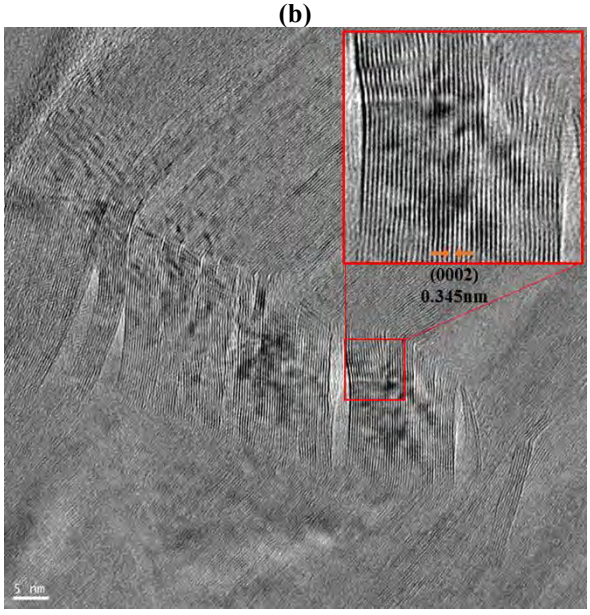

(c)

Figure 5.7. *BF-TEM images at (a) low and (b, c) higher magnifications. High magnification image (c) confirms the graphite structure*

5.3.1.2.1. Inter and intragranular particles

TiB_2 particles can be classified as inter and intragranular according to where it's located within the structure. Intragranular TiB_2 was located only within the B_4C phase but not within SiC, the reason for this could be the TiB_2 formation reaction starts from the surface of B_4C with limited amount of TiC (e.g. nanoparticle due to mixing) attached to B_4C surface and after TiC consumed, nano TiB_2 particle was formed while B_4C grain growth occur. Morphology of intragranular TiB_2 particles also supports suggested formation mechanism. Intragranular TiB_2 particles can also be formed by the reaction between TiO_2 layer found on TiB_2 particles with B_4C as given in (5.4. TiB_2 is a hexagonal structure (a: 3.033 nm and c: 3.23 nm) and composed of alternately stacked Ti and B layers along c-axis with the fastest growing plane family is $\{11\bar{2}0\}$ which is resulted in plate like growth of TiB_2 [79]. Unlike the in-situ synthesized TiB_2 particles found in the literature [79, 80] none of the above TiB_2 particle types found in the TEM possess platelet morphology. Morphologies of both types of TiB_2 particles were similar to those found in hot pressed B_4C-TiB_2 composite structure [81].

SiC particles were also present as intergranular and intragranular within the B_4C phase. SiC phase was formed during the sintering by the reaction of Si (coming from the grinding media) and C (from the (5.1). This is an indication of wear of SiAlON mixing balls during process since there was not any intentionally added Si or SiC into composition. The size of the intragranular SiC varies from 50 nm to 300 nm with a round-like morphology, however the intergranular particles were bigger in size (about few microns) with irregular morphologies that were confined by the surrounding particles. In case of intergranular SiC particles, they were mostly next to TiB_2 particles which is reasonable, because C is formed from TiC according to (5.1 next to TiB_2 and SiC was formed by this C. Due to relatively small amount of Si element in composite, all Si consumed to form SiC in contact with TiB_2 and graphite neighbors as shown in Figure 5.8.

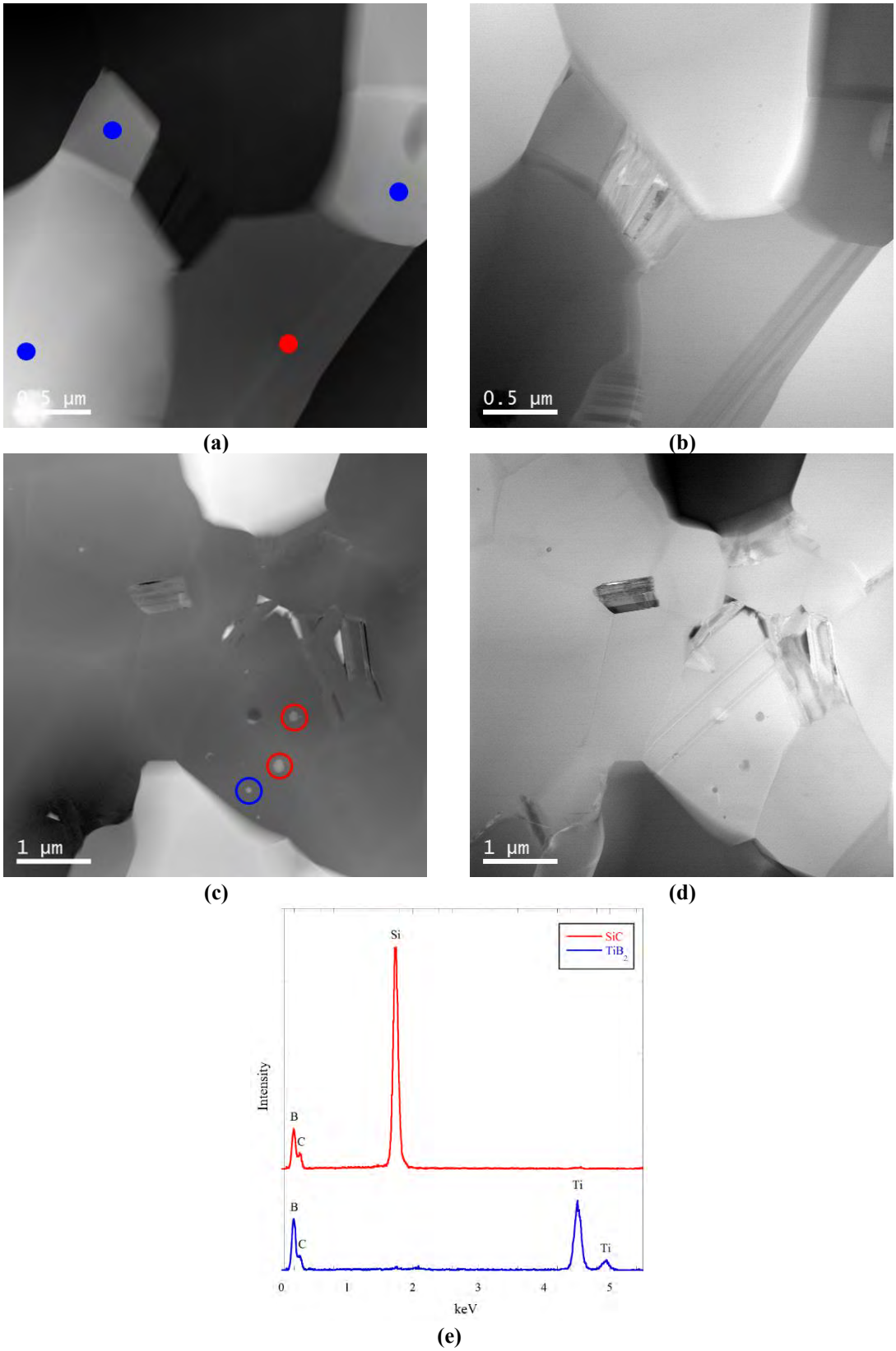

Figure 5.8. *(a) STEM-HAADF and (b) STEM-BF image of intergranular SiC and TiB_2 particles, (c) STEM-HAADF and (d) STEM-BF image of intragranular SiC and TiB_2 particles (e) EDX spectra obtained from two phases. (Please note that in all images TiB_2 and SiC phases are color coded with blue and red, respectively*

5.3.1.2.2. Graphitic structures

TEM and STEM images revealed that in the microstructure various graphitic structures were present. Graphitic structures can be divided into two categories depending where its located within the composite microstructure. One type of graphitic structure was found in direct contact with TiB_2 as shown in Figure 5.8 (a, b). Graphitic carbon produced with a reaction between TiC and B_4C according to (5.1) thus the ones in contact with TiB_2 phase formed simultaneously during sintering reactions.

Second group of graphitic structures were found between B_4C particles as shown in Figure 5.9 and there could be several reasons for the formation of this type of structure. According to the XRD and TEM analyses of B_4C starting powders, graphite was already present in the composite mixture and during sintering, clusters of graphite particles around the B_4C particles can be combined to form single graphite particle due to high diffusion rate of carbon [80] and also aid of liquid phase found at interface between B_4C and graphite. Detailed analyses of the second group of graphitic structures revealed that they are not only graphite but also contains hexagonal boron nitride, as shown in Figure 5.9, which is coming from starting B_4C powders. Formation of this kind of graphitic hybrid structure can be explained as follows. In the literature, it is well known that SPS processing of graphite [82] and hBN [83] containing ceramic composites resulted in orientation of these anisotropic crystals along c-axis parallel to pressing/current flow direction. Combination of carbon diffusion around the hBN particle and external forces that cause orientation change of graphite and hBN (both in same direction) during SPS might be resulted in the formation of this type of hybrid structure. Last but not least, it is also possible that hBN particles can be formed during SPS according to reactions given in Section 5.3.1.3.

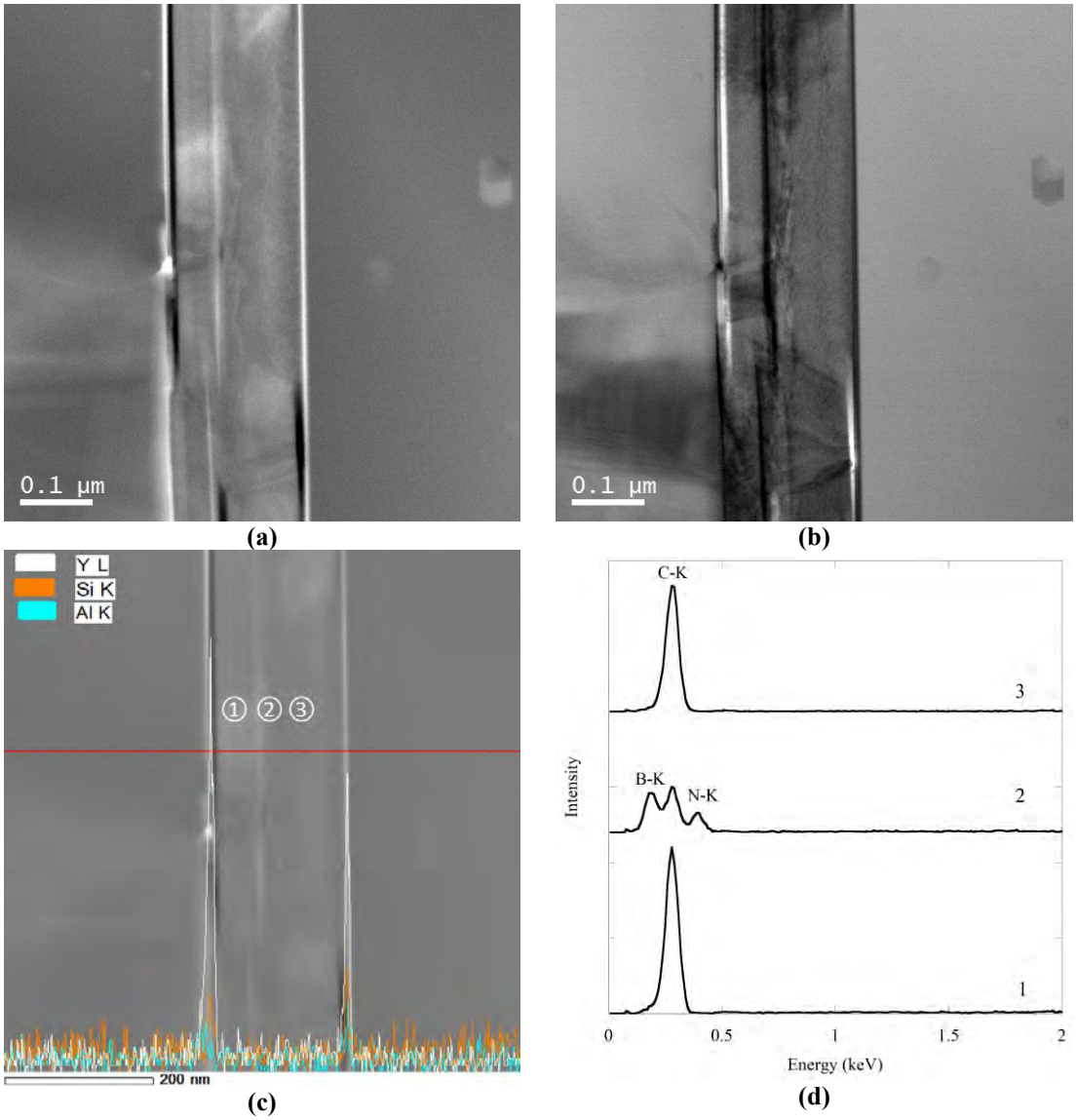

Figure 5.9. *(a) STEM-HAADF, (b) STEM-BF image of graphitic hybrid structure surrounded by B_4C particles, (c) EDX line scan analysis showing liquid phase at the interface, (d) EDX spectra obtained from points given in (c)*

XRD results taken from different directions of the sample, given in Figure 5.10, are in a good agreement with the literature that is at the surface of the sample (0002) plane intensity of graphite and hBN (located at 26.4° and 26.5°, respectively) is increased which means that quantitatively higher number of (0002) planes are present at the surface, which has a normal parallel to pressing direction. XRD results also revealed that peak intensities of TiB_2 and B_4C phases are almost identical which means that sintered sample, except graphite and hBN phases, is isotropic in microstructural manner.

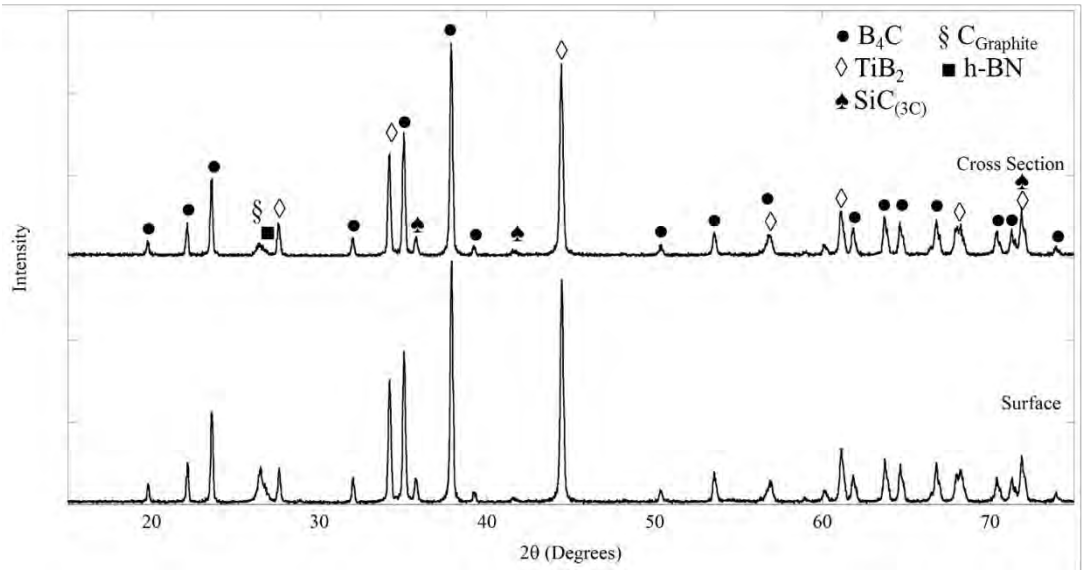

Figure 5.10. *XRD results for two principal directions with respect to SPS pressing direction*

5.3.1.2.3. Expect the unexpected

In the STEM-HAADF images, it was found that, there was a higher atomic number phase within the B_4C-B_4C and B_4C-graphite grain boundaries. EDX analysis revealed that this phase is rich in Si and Y elements (Figure 5.11). The only known source for these elements is the mixing balls that were made from SiAlON that contains Y_2O_3 as sintering aid. That is also another indication that the grinding balls worn out during homogenization procedure due to the very high hardness of B_4C. According to this result, in this liquid phase composition in addition to the Si and Y elements, there should also have been Al, O and N elements if worn out particles were only melted. However, EDX analysis showed that these elements were not present at the grain boundary phases, and this indicated that SiAlON-Y_2O_3 particles were not only melted but also decomposed at sintering temperatures. Decomposition reaction of SiAlON will be discussed in Section 5.3.1.3. Additionally, similar composition with Al, Y, O and Si (without any N) were found as pockets at some C-C-B_4C triple junctions (Figure 5.12). Main reason for this could be the wetting behavior of liquid phase on C and B_4C phases but not TiB_2 phase.

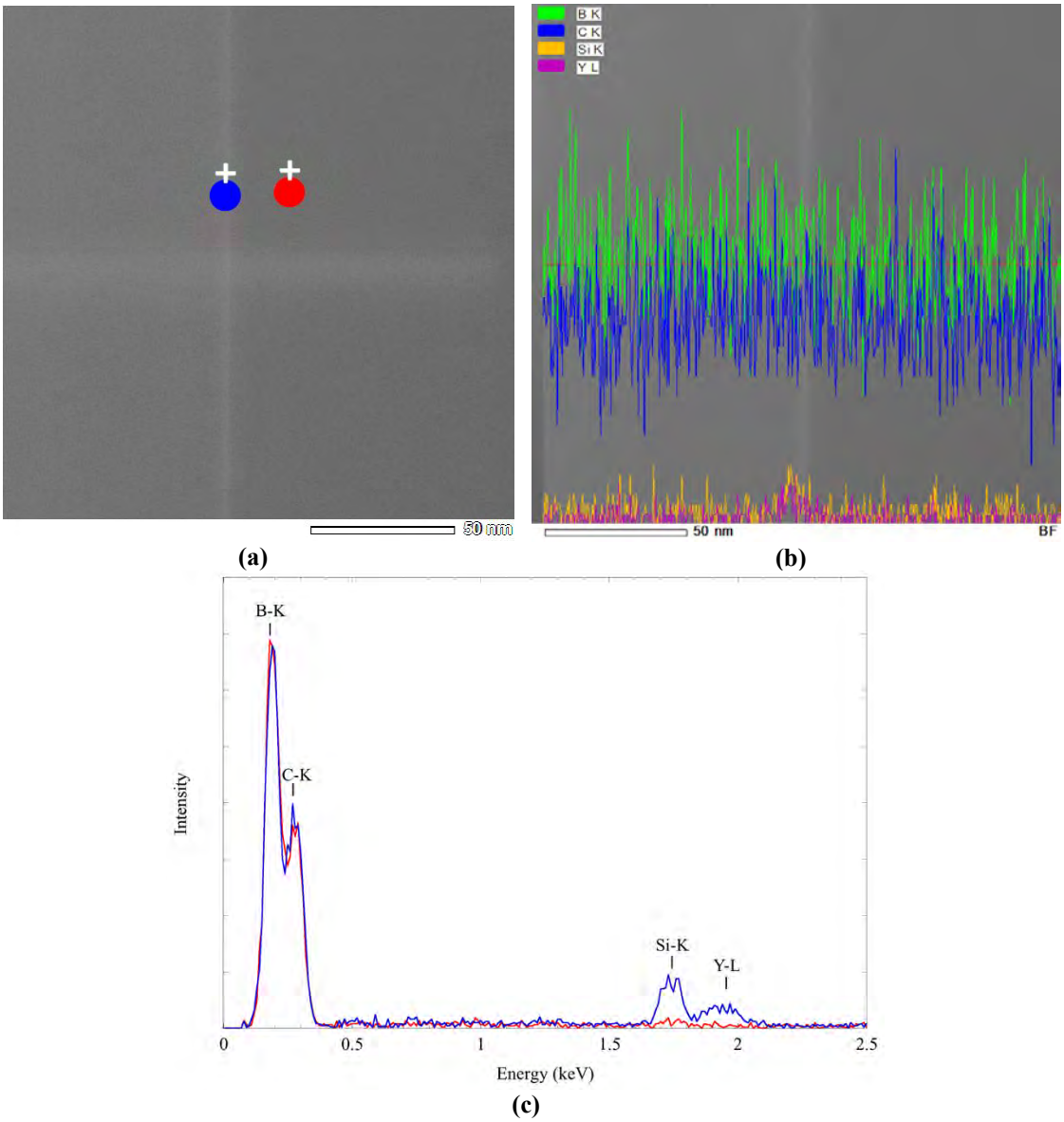

Figure 5.11. *(a) STEM-HAADF image and respective point and (b) line scan analyses of grain boundary phase (c) EDX spectra of points in (a) (note that analysed points are color coded)*

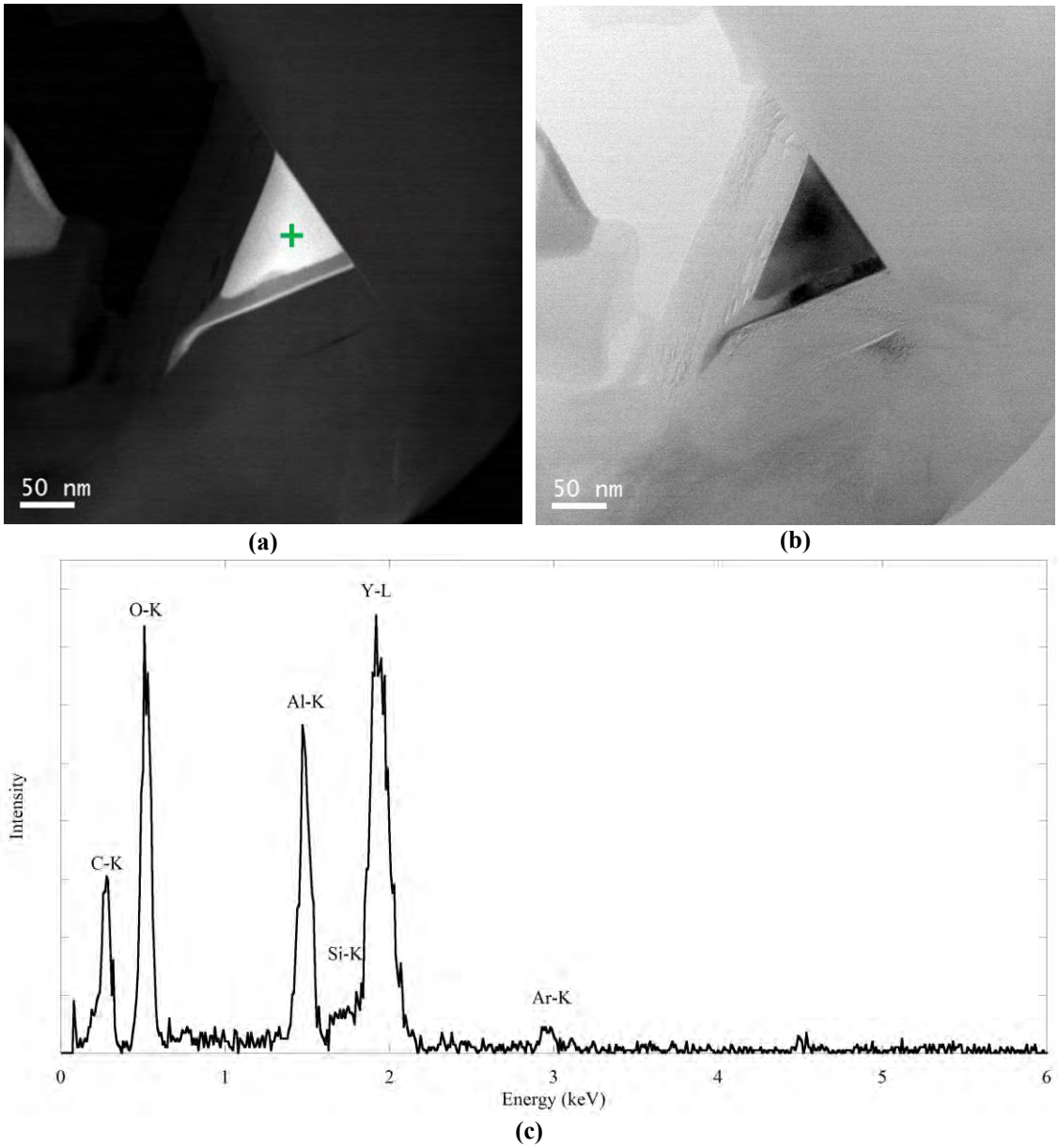

Figure 5.12. *STEM (a) HAADF, (b) BF images of a triple junction phase and (c) the EDX spectrum*

5.3.1.2.4. Orientation relationship between TiB_2 and graphite

TiB_2 and graphite are both hexagonal and their interplanar distance between basal planes are close to each other i.e. $d_{(0001)\text{-}TiB2}$: 0.325 nm and $d_{(0002)\text{-}Graphite}$: 0.34 nm. Therefore this plane may act as a template during growth of graphite and cause epitaxial relation between them. In the literature [84], according to the TEM images it was found that this small interplanar distance difference (<5%), resulted in orientation relation between in-situ synthesized graphite and TiB_2 particles and this relation can be expressed as $(0001)_{TiB2}$ // $(0002)_{graphite}$. Due to this special relation found in the literature, orientation

relation between graphite and TiB_2 particles in R-SPS'ed B_4C-TiB_2 composite sample were investigated with TEM-PED method (with 0.7° precession angle).

The orientation mapping of TiB_2 and graphite particles, which are in contact, were done with TEM-PED method. Characterization of the suggested orientation relation was done by using $(10\bar{1}0)$, (0001) and $(11\bar{2}0)$ pole figures. One of the orientation maps is given in Figure 5.13. According to the orientation maps obtained from several different TiB_2 and graphite neighbors and respective pole figures, in-situ formed TiB_2 and graphite particles were randomly oriented.

One possible reason for random orientation between phases could be simultaneous formation and growth of particles. During sintering, both TiB_2 and graphite formed simultaneously during sintering according to the reactions given in Section 5.3.1.3, therefore it was likely to have graphite grow over any surface of growing TiB_2 particle.

Another reason for random orientation between TiB_2 and graphite particles could be the presence of Si and Y containing liquid phase (as shown in Figure 5.14) during sintering, this liquid phase may prevent contact of graphite with planes of so called "template phase" thus resulted in a random orientation.

There were several challenges to obtain good orientation map with high reliability due to delamination in graphite. One was the local orientation change in graphite particle as shown in Figure 5.15 (b) and the other problem was multiple diffraction spots due to overlapped strands of graphite, which was again a result of delamination, as shown in Figure 5.15 (d-g). Overlapped diffraction patterns reduce the orientation reliability during template matching process.

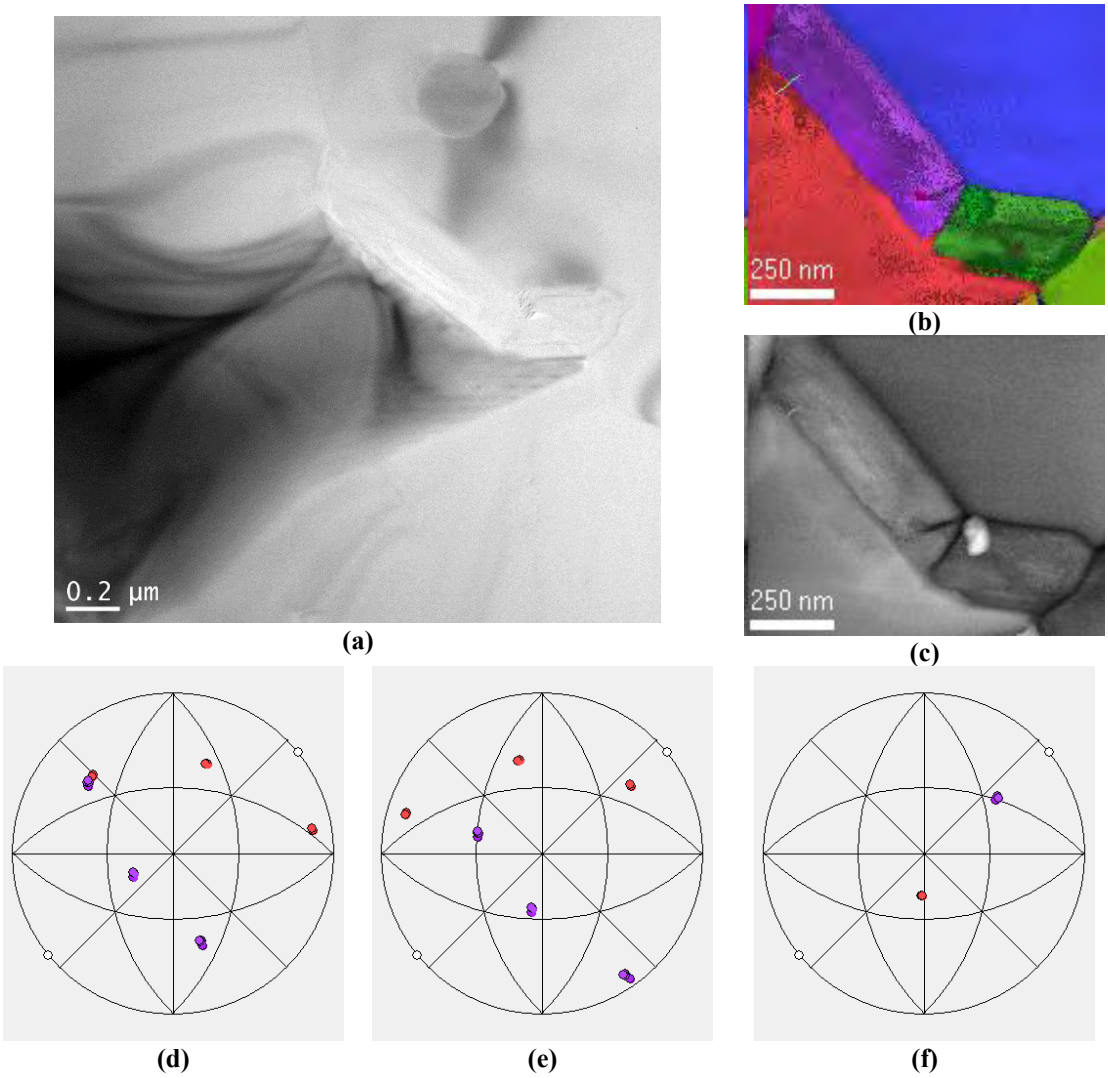

Figure 5.13. *(a) TEM-BF image, (b) Orientation map (z), (c) index map and (d) ($10\bar{1}0$), (e) ($11\bar{2}0$), (f) (0001) pole figures between TiB_2 and graphite phases*

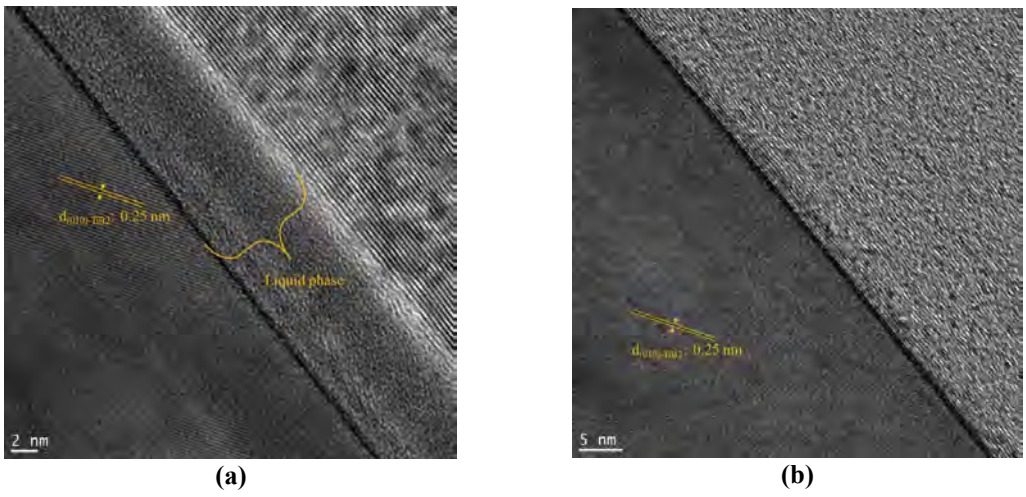

Figure 5.14. *TEM-BF images showing TiB_2 and graphite interface (a) with and (b) without presence of liquid phase*

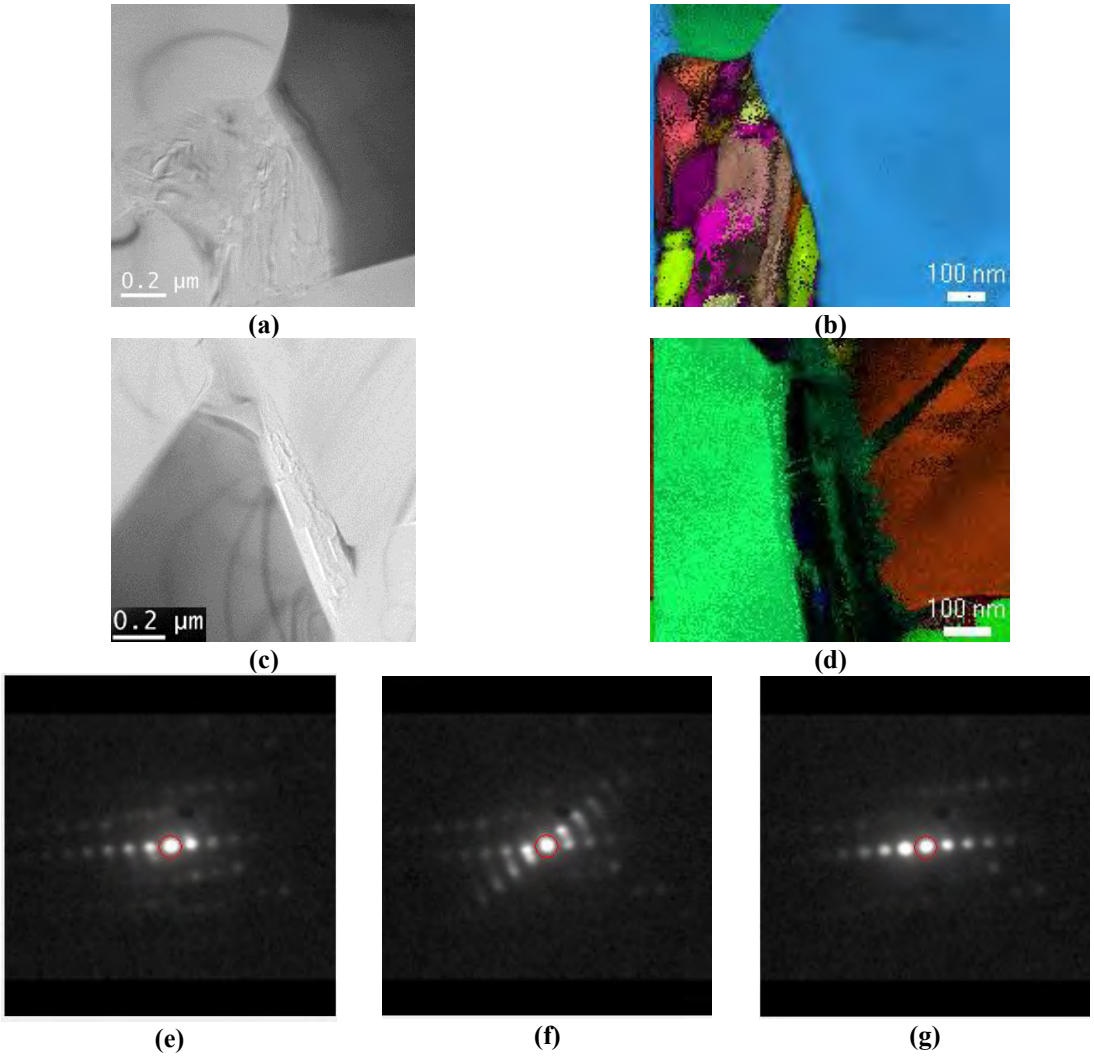

Figure 5.15. *(a) TEM-BF image of TiB_2 and graphite neighbors and (b) respective orientation map showing local orientation change within graphite, (c) TEM-BF image of another neighbors and (d) respective orientation map showing low reliability due to overlapped diffraction patterns from different strands as shown in (e-f)*

5.3.1.2.5. Characterizations of starting powders

TEM and STEM results showed that there are several different and unintentionally added phases, such as hBN, present in the composite system. For the search of an answer for *"Do they come from starting powders or are they products of reactions occur during sintering?"* question, characterization of starting powders were carried out.

(S)TEM images of TiC starting particles showed that they are micron sized particles, with irregular morphologies, contains graphitic carbon particles at its surface as well as non-continuous oxide layer. In TEM-BF images there was not any continuous

oxide layer around TiC particles in contrast to the literature [80]. However, STEM-EDX analyses showed that surface oxide as TiO_2 was present without showing a continuous distribution. Graphite found in TEM images was not present in the XRD results, which could possible due to its very low amount.

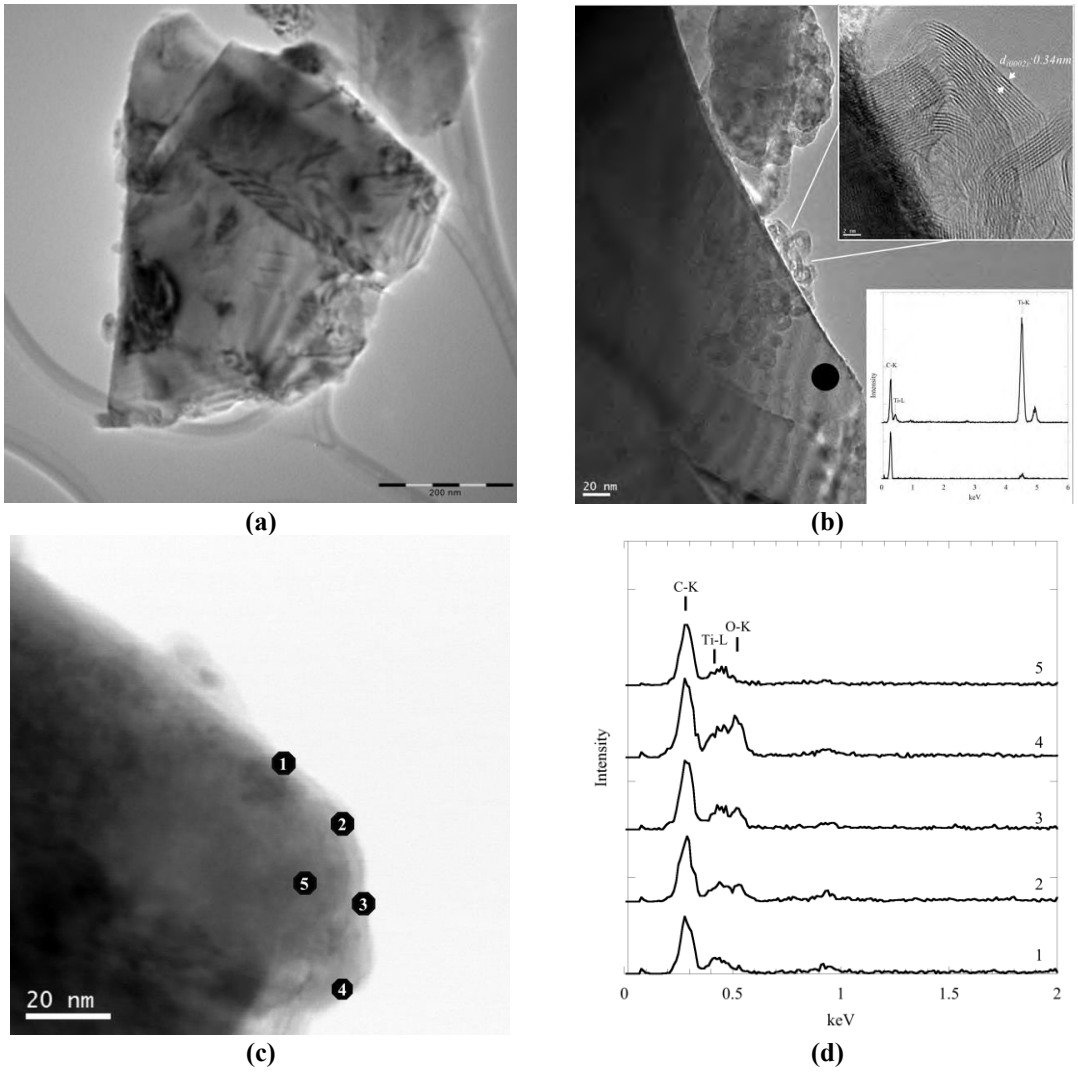

Figure 5.16. *(a) TEM-BF image showing TiC particle, (b) TEM-BF and STEM-EDX results of the TiC and graphitic particle at its' surface, (c) STEM-HAADF image and (d) STEM-EDX results taken from points in (c) showing non-continuous surface oxide*

(S)TEM analyses also showed that B_4C powders have non-continuous B_2O_3 surface oxide layer and additionally graphite as well as hBN particles are present at its' surface (Figure 5.17). XRD results, given in Figure 5.18, showed that B_4C starting powder contains graphite and hBN impurities which in a good agreement with TEM results.

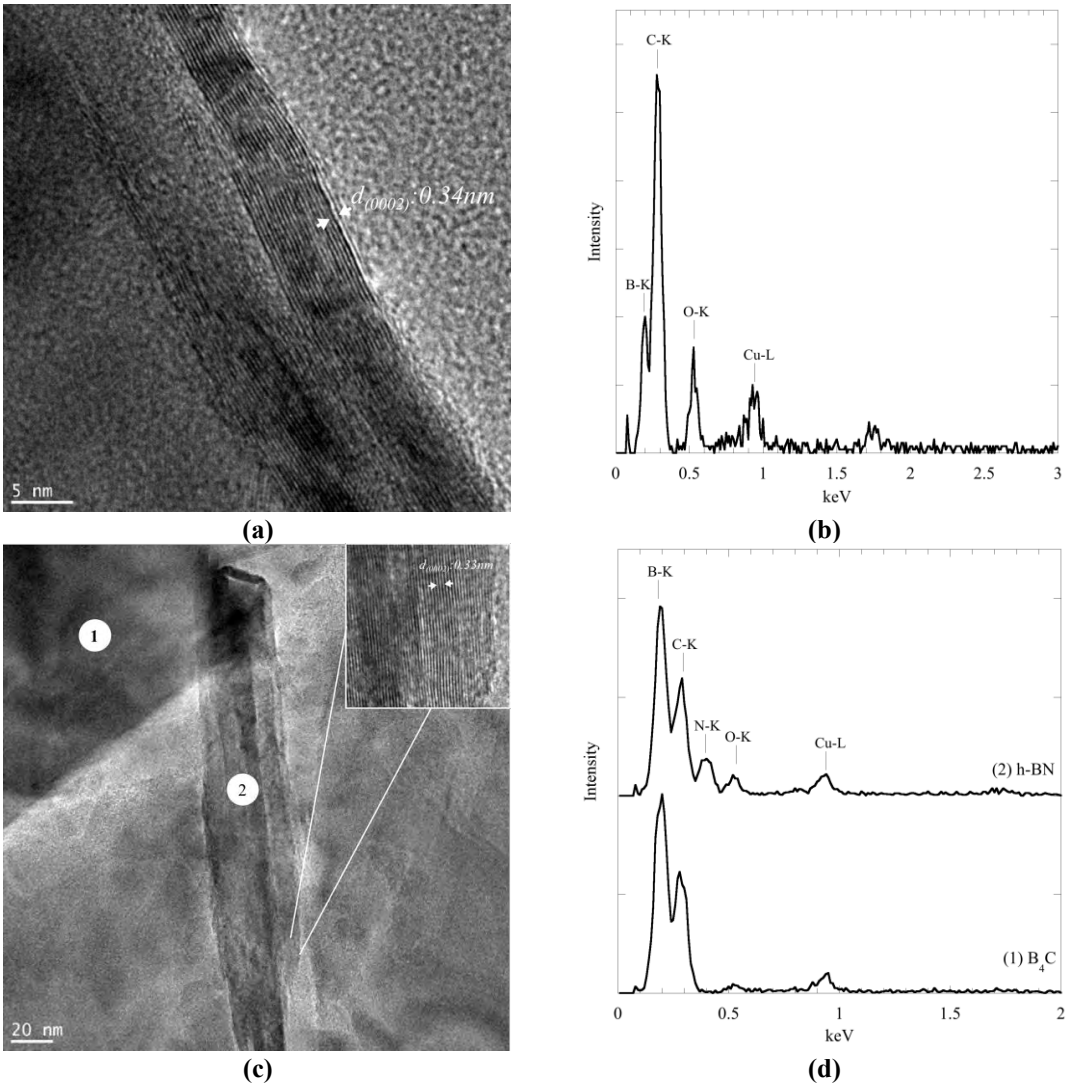

Figure 5.17. *(a) TEM-BF image showing surface graphite, (b) STEM-EDX result of graphite structure given in (a), (c) TEM-BF image of hBN particle and (d) STEM-EDX results from points (1-B_4C and 2-hBN, respectively) given in (c)*

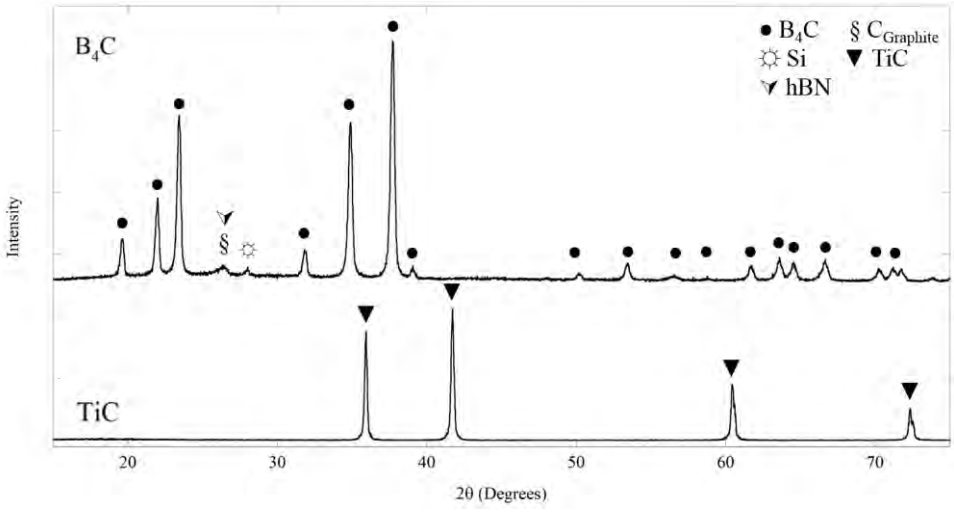

Figure 5.18. *XRD results of starting raw materials*

5.3.1.3. Sintering reactions

During sintering of in-situ formed TiB_2 - B_4C (with SiC) composites there are several different reactions occurred to form present phases from the starting powders. These reactions can be investigated in three sections; (i) TiB_2 formation, (ii) SiC and liquid phase formation and (iii) hBN formation reactions.

(i) TiB_2 Formation Reactions

During the sintering in SPS, reactions between starting raw materials and impurities can be resulted in TiB_2 formation. The list of possible reactions and their respective Gibbs-free energy changes are given in Equations from (5.2) to (5.6). The main reaction to form TiB_2 phase occur between TiC and B_4C phases as given in (5.3). As a result of this reaction, beside TiB_2 phase, carbon is also formed. In this study, carbon as a reaction product was identified as graphite structure from the TEM images.

In addition to the reaction stated above, TiB_2 phase may also formed by the reaction between B_4C and TiO_2 surface oxide found on TiC as given in (5.4) until surface oxide consumed. Since the amount of surface oxide is low, only a small amount of TiB_2 particles may be formed by this reaction and may be the ones observed as intragranular TiB_2, given in Figure 5.8.

Another possible reaction (given in (5.5) occurred between B_4C, TiC and Si (from milling media) during sintering and this reaction resulted in the formation of TiB_2 and SiC phases. Details of the SiC formation are given in the following section.

$$TiC_{(s)} + 2B_{(s)} \rightarrow TiB_{2(s)} + C - \Delta G<0,\ T<2000°C \quad (5.2)$$

$$2TiC_{(s)} + B_4C_{(s)} \rightarrow 2TiB_{2(s)} + 3C_{(s)} - \Delta G<0,\ T<2000°C \quad (5.3)$$

$$4B_4C_{(s)} + 5TiO_{2(s)} \rightarrow 5TiB_{2(s)} + 4CO_{(g)} + 6BO_{(g)} - \Delta G<0,\ T>1600°C \quad (5.4)$$

$$B_4C_{(s)} + 2TiC_{(s)} + 3Si_{(s)} \rightarrow 2TiB_{2(s)} + 3SiC_{(s)} - \Delta G<0,\ T<2000°C \quad (5.5)$$

$$4TiC_{(s)} + B_4C_{(s)} \rightarrow 4TiB_{(s)} + 5C_{(s)} - \Delta G>0,\ T<2000°C \quad (5.6)$$

(ii) SiC and Liquid Phase Formation Reactions

In the literature, it is reported that thermal decomposition of Si_3N_4 starts at 1880°C according to (5.7) [85], whereas Y-SiAlON decomposition starts at 1700°C under 1 atm of N_2 pressure and as the N_2 pressure increase decomposition is suppressed and instead

of decomposition, phase transformation occurs or in other words reducing the N_2 pressure resulted in reduced stability of SiAlON [86]. The decomposition reaction in the literature is given in (5.8). In this study, at the SPS temperature, which was 1980°C, under vacuum, worn out SiAlON particles were decomposed and decomposition products were in liquid and gaseous forms. The decomposition product, $Si_{(l)}$ can react with C, which is a byproduct from TiC with B_4C reaction or existing as a remnant impurity in the starting powders and form SiC phase in the composite as shown in (5.9). According to the (5.8), there should also be AlN phase in the system; however, AlN phase was not observed during TEM analyses. Instead of AlN, Al was found in Al-Y-O-Si liquid phase pockets between graphite structures.

One of the reason not to find AlN phase might be the decomposition of AlN into Al and N (according to (5.10) at sintering temperature under vacuum and other reason might be the reaction of AlN with other element(s) in the system. Considering the possibility of AlN decomposition, in the literature [87], it was found that AlN decomposes above 1300°C that is lower than TiB_2-B_4C sintering temperature under vacuum, which was an SPS atmosphere during sintering. This could be the reason of absence of AlN phase in the structure. Considering the reaction of AlN with other element (s) in composition, according to the literature AlN can react with B_2O_3 (formed during TiB_2 formation) at 2100°C to form Al_2O_3 and BN according to (5.11; however, Al_2O_3 was not present in the composite structure. The reason of the absence of Al_2O_3 could be the decomposition due to its reaction (according to (5.12 at 1500°C in Ar) with C present in the composition, resulted in Al_2O and CO gases [88].

The raw materials and composition of the SiAlON mixing balls are not known exactly to interpret amorphous phase composition between SiAlON particles; however, it is a well-known fact that sintering additives in SiAlON ceramics are found in liquid phase regions. The Y-Si-Al-O containing phase, which is found at triple junction of graphite structures, is qualitatively same with the composition of triple junction amorphous phase found in Y-SiAlON ceramics [89]. Only difference found in composition of triple junction phase in our sample is the N content. In R-SPS'ed sample, N element was not found in the composition; however, in the literature [89] it is also reported that presence of N element in triple junction phases vary depending on the SiAlON starting composition. The N deficiency in our triple junction phase composition could be due to the fact that SiAlON sintering is almost always associated with some

extent of N_2 use. Amorphous phase in SiAlON can be found as in liquid state during sintering at 1940°C [90], thus, it is likely to be in the liquid form during TiB_2-B_4C composite sintering at 1980°C.

SiC formation and liquid phase found in the TiB_2-B_4C composite can be explained by using the reactions given below.

$$Si_3N_{4(s)} \rightarrow 3Si_{(g,l)} + 2N_{2(g)} - \Delta G<0,\ T>1820°C \quad (5.7)$$

$$Y_{0.6}(Si_{9.3},Al_{2.7})(O_{0.9},N_{15.1})_{(s)} \rightarrow 7.2Si_{(l)}+0.6YSi_{2(l)}+2.7AlN+0.9SiO_{(g)}+6.2N_{2(g)} \quad (5.8)$$

$$Si_{(l)} + C_{(s)} \rightarrow SiC_{(s)} - \Delta G<0,\ T<2000°C \quad (5.9)$$

$$AlN_{(s)} \rightarrow Al_{(g)} + \tfrac{1}{2}N_{2(g)} - \Delta G>0,\ T<2000°C \quad (5.10)$$

$$2AlN_{(s)}+B_2O_{3(l)} \rightarrow Al_2O_{3(s)} + 2BN_{(s)} - \Delta G<0,\ T<2000°C \quad (5.11)$$

$$Al_2O_{3(s)}+2C_{(s)} \rightarrow Al_2O_{(g)}+2CO_{(g)} - \Delta G<0,\ T>1980°C \quad (5.12)$$

$$TiC_{(s)} + Si_{(s,l)} \rightarrow SiC_{(s)} + Ti_{(s)} - \Delta G>0,\ T<2000°C \quad (5.13)$$

(iii) hBN Formation Reactions

In the hybrid graphitic structures beside graphite, it was found that hBN also present and if hBN was formed instead of coming from the starting powders, there are several different reactions for hBN formation.

The boron source for hBN can be B_2O_3 oxide layer around the B_4C particles or B_4C itself. The reaction of these boron sources with $N_{2(g)}$ originating from decomposition of Si_3N_4/SiAlON phase resulted in hBN formation and change of Gibbs free energies of these reactions are below zero within the process temperatures. hBN formation reactions are summarized below.

$$B_2O_{3(l)}+N_{2(g)}+3C \rightarrow 2BN_{(s)}+3CO_{(g)} - \Delta G<0,\ T>1100°C \quad (5.14)$$

$$3B_4C_{(s)}+B_2O_{3(l)}+7N_{2(g)} \rightarrow 14BN_{(s)}+3CO_{(g)} - \Delta G<0,\ T<2000°C \quad (5.15)$$

$$B_2O_{3(l)}+3C_{(s)}+N_{2(g)} \rightarrow 2BN_{(s)}+3CO_{(g)} - \Delta G<0,\ T>1100°C \quad (5.16)$$

$$B_4C_{(s)}+2N_{2(g)} \rightarrow 2BN_{(s)}+C_{(s)} - \Delta G<0,\ T<2000°C \quad (5.17)$$

5.3.2. Hot pressed B_4C-TiB_2 composites

In this section, in addition to the microstructure analyses done by SEM and TEM, mechanical properties such as hardness and toughness of the composite structure depending on the pressing direction during hot press will be given and discussed.

Sintering conditions and resulted density values of the samples used in this section is given in Table 5.1. Theoretical densities for 50/50-BM, 50/45/5-BM and 50/50-HEM samples were calculated as 3.52 g/cm^3, 4.08 g/cm^3 and 3.70 g/cm^3, respectively and measured values, according to Archimedes method, were 3.33 g/cm^3, 3.95 g/cm^3 and 3.61 g/cm^3, which resulted in 94.6 %, 96.7 % and 97.5 % relative densities, respectively.

Table 5.1. *Sintering conditions and density values of samples used in this section*

Sample	*Sintering Temperature (°C)*	*Bulk Density (g/cm^3)*	*Theoretical Density (g/cm^3)*	*Relative Density (%)*
50/50-BM	1920	3.33	3.52	94.6
50/45/5-BM	1930	3.95	4.08	96.7
50/50-HEM	1860	3.61	3.70	97.5

5.3.2.1. SEM and XRD results

SEM results revealed the microstructural differences between the samples depending on the composition as well as milling method. In the SEM-BSE images B_4C particles characterized as dark contrast due to the lowest atomic number combination, in contrary, W containing phases appeared as the brightest contrast due to the highest atomic number and depending on the amount of W in respective phase, contrast changed accordingly. TiB_2 phase characterized as gray contrast in the images.

One of the most important difference between microstructures is the present phases. In the 50/50-BM sample, microstructure (given in Figure 5.19 (a, b)) mainly consists of TiB_2 and B_4C phases and very small amount of W containing contamination phase (according to EDX analysis given in Figure 5.19 (c)), around TiB_2 particles, originating from the WC grinding media. With the addition of WC to the sample before sintering resulted in a formation of solid solution having Ti-W-B elements (according to the EDX analysis) between B_4C and TiB_2 particles in 50/45/5-BM sample (Figure 5.19 (d, e)). Microstructure of high-energy milled 50/50-HEM sample, which is given in Figure 5.19 (g, h), showed significantly smaller B_4C and TiB_2 particles. Particle size difference between sintered samples were originating from the starting raw materials. Even though

B_4C and TiB_2 sources were the same for all samples, change of milling method resulted in different particle sizes for the samples 50/50-BM and 50/50-HEM prior to sintering and reported d_{50} values for B_4C-TiB_2 mixtures are ~3.1 μm and ~2.8 μm, respectively [91]. Particle size difference between three samples can be seen clearly in Figure 5.20, which were taken at the same magnification. Reported particle sizes for B_4C and TiB_2 phases for three different samples are given in Table 5.2.

In 50/50-HEM sample, in addition to the B_4C and TiB_2 phases, there was a solid solution composed of regions with different W content; W rich Ti-W-B and Ti-W-B regions, labelled as 1 and 2 in Figure 5.19 (h), respectively. Great majority of solid solution composed of Ti-W-B region and it was found almost everywhere in the microstructure; however W-rich Ti-W-B solid solution regions were only found around TiB_2 particles. This type of structure is called as core-rim structure where core is TiB_2 and rim is W-rich Ti-W-B solid solution phases. SEM-EDX chemical analysis results are given in Figure 5.19 (i) and according to these results, intensity of the W-M peak for W-rich Ti-W-B region is almost the double of Ti-W-B region. Additionally, Ti-K/B-K peak intensity for both solid solution regions are similar to TiB_2 phase which points out that solid solution could be $(Ti_{1-x}W_x)B_2$, however it should be confirmed with additional analyses. Similarity of the Ti-K and B-K peak intensity ratio between solid phase and TiB_2 could also be originating from the electron-solid interaction volume with the bulk sample. Therefore, SEM-EDX quantitative results of bulk samples can be misleading. These results needs to be confirmed with thin sample in TEM, where interaction volume effect is almost diminished.

Last but not least, in the SEM analyses, both intentionally and unintentionally added WC was not present in the microstructures and it was also confirmed with XRD results (Figure 5.21). It can be seen that WC phase was consumed to form solid solution during hot pressing. The amount of WC incorporation during milling is reported as ~ 0.1 vol % and ~ 1.4 vol % for 50/50-BM and 50/50-HEM samples, respectively [91].

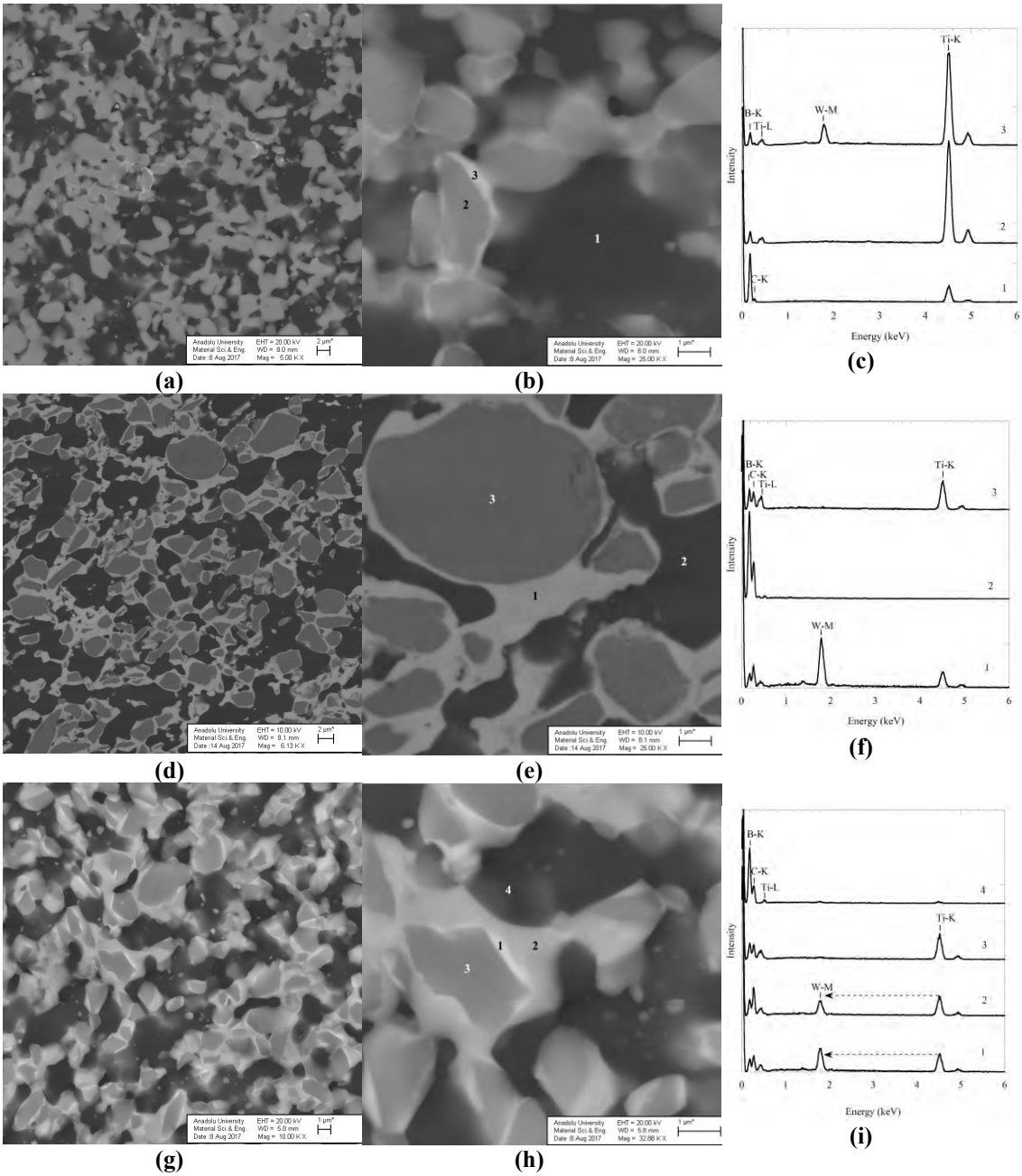

Figure 5.19. *SEM images showing overall microstructure and magnified image and respective EDX spectra obtained from the points labelled in the magnified image for (a-c) 50/50-BM, (d-f) 50/45/5-BM and (g-i) 50/50-HEM samples*

Table 5.2. *Reported average grain sizes for B_4C and TiB_2 for samples used in this study (adapted from [91])*

Sample	Average grain sizes (μm)	
	B_4C	TiB_2
50/50-BM	1.69	2.33
50/45/5-BM	1.70	1.65
50/50-HEM	0.89	1.00

As mentioned before, in any sintering processes that uniaxial pressure was applied in addition to heating, may end up with anisotropic microstructures in other words, texturing could be observed. In order to investigate the anisotropic effect of pressure during sintering on the microstructures, surface and cross section of the samples were both polished and analyzed with SEM and XRD.

SEM-BSE images showed that there is a slight texturing present when the surface and cross section microstructures are compared. Cross section and surface SEM-BSE images are given in Figure 5.20 (a-c) and Figure 5.20 (d-f), respectively for 50/50-BM, 50/45/5-BM and 50/50-HEM samples. Cross section images showed that TiB_2 and B_4C particles were slightly oriented along y-axis, which was perpendicular to the pressing direction, along z-axis, compared to surface microstructure. These results were confirmed with the XRD analyses of cross section and surface of the polished bulk samples, (Figure 5.21). Comparison of the peak intensities were used for the characterization of texture, in this case intensity of the planes related with TiB_2 phase was used, due to very low peak intensities from planes of B_4C, which are originating mainly from low atomic scattering factor compared to TiB_2 even though their volume fractions are close to each other.

Relative peak intensity values for TiB_2 planes are given in Table 5.3 and they were calculated as $d_{(hkl)}$ peak intensity divided by the intensity of $d_{(101)}$ peak which is the most intense peak in XRD results and multiplied with 100. Calculated values were then compared with the simulated theoretical powder XRD result of 50/50 vol % TiB_2/B_4C. It can be seen from this table at the cross section, peak intensities for $d_{(100)}$, $d_{(110)}$ and $d_{(200)}$ planes decreased while peak intensities of $d_{(001)}$, $d_{(002)}$ and $d_{(102, \bar{1}11)}$ planes increased, vice versa for peak intensities obtained from cross section. Average peak intensity of given $d_{(hkl)}$ plane obtained from surface and cross section is almost the same with the theoretical values. According to these results it can be concluded that there was no significant texture present for samples produced with hot pressing at this processing conditions. However, slight orientation of $d_{(001)}$ planes perpendicular to the pressing direction (in other words; TiB_2 <001> direction is parallel to the pressing direction) is present.

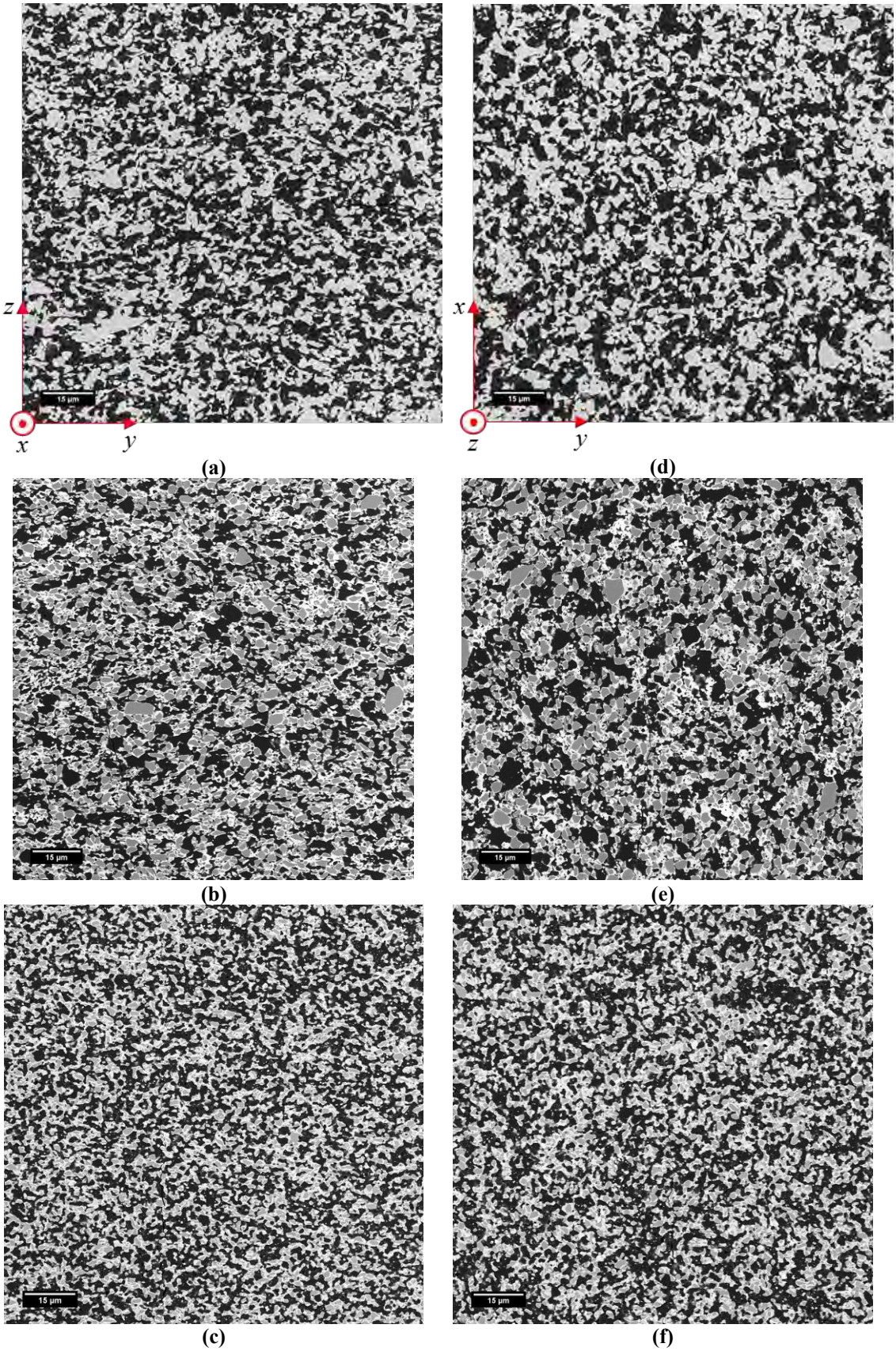

Figure 5.20. *SEM-BSE images showing the microstructures for cross section of samples (a) 50/50-BM, (b) 50/45/5-BM, (c) 50/50-HEM and surface of samples (d) 50/50-BM, (e) 50/45/5-BM, (f) 50/50-HEM (please note that all images are scaled to same magnification)*

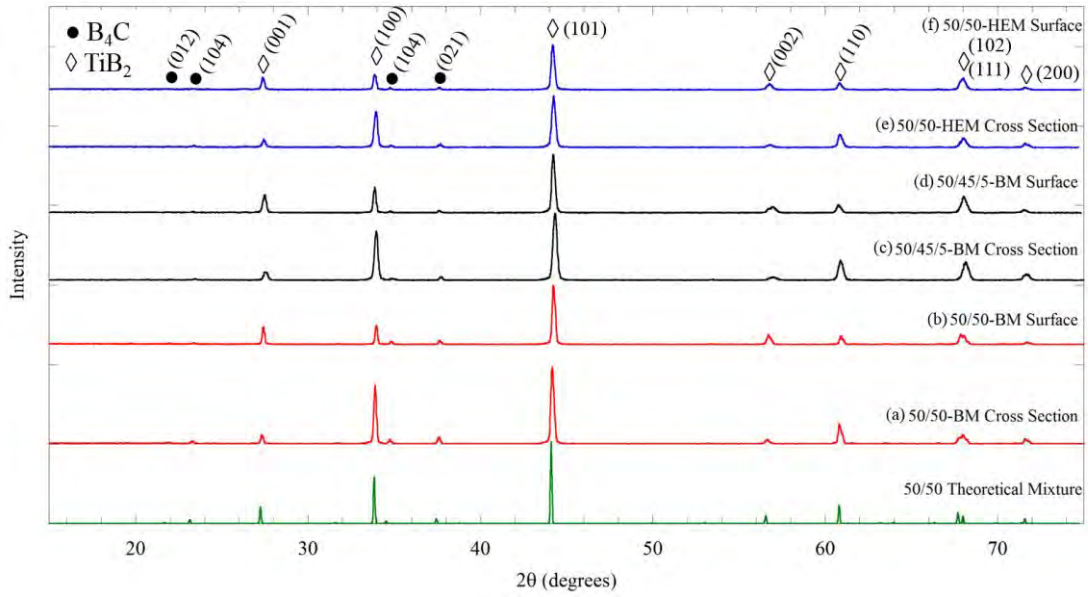

Figure 5.21. *XRD results of bulk samples from surface, cross section and theoretical powder mixture. Samples are coded with a thru f, which refers to images in Figure 5.20.*

Table 5.3. *Measured TiB_2 peak intensity percentages for surface and cross section obtained from XRD results*

	50/50-BM		***50/45/5-BM***		***50/50-HEM***		***50/50 Powder Mixture***	
	Surface	*Cross section*	*Surface*	*Cross section*	*Surface*	*Cross section*	*Theoretical*	*Planes*
TiB_2 Intensity %	30	12	31	14	28	17	22	*(001)*
	31	76	43	74	33	70	55	*(100)*
	100	100	100	100	100	100	100	*(101)*
	17	7	11	6	15	5	12	*(002)*
	14	27	13	31	17	26	27	*(110)*
	17	12	30	27	27	19	17	*(102, $\bar{1}11$)*
	4	6	6	11	6	6	7	(200)

There are several solid solution compositions in FIZ/NIST Inorganic Crystal Structure Database (2016-2) that contains Ti, W and B elements and they are $(Ti_{0.9}W_{0.1})B_2$, $(Ti_{0.7}W_{0.3})B_1$, $(Ti_{1.6}W_{2.4})B_4$. During the sintering, these solid solutions might be formed between TiB_2 and B_4C particles by the reaction between TiB_2 and WC. In the XRD results, there were no unidentified peaks, therefore it is highly possible to have peak overlapping between solid solutions and main phases. In order to find out peak overlapping, theoretical XRD results of possible phases and TiB_2 were simulated and results are given in Figure 5.22. According to these results, phases other than $(Ti_{0.9}W_{0.1})B_2$ have distinct peaks around 38° and 42°, which were not present in the experimental

results. According to the SEM images, volume fraction of solid solution is close to TiB_2 phase, thus highest peak intensities of these peaks should be similar considering in terms similar atomic scattering factors. However, in the experimental XRD results there was no peak for $(Ti_{0.7}W_{0.3})B_1$, $(Ti_{1.6}W_{2.4})B_4$ phases. In contrast, simulated peak positions and intensities for $(Ti_{0.9}W_{0.1})B_2$ phase, which is formed by incorporation of W into TiB_2, are very close to TiB_2 peaks due to similar atomic radius and scattering factors for Ti and W elements. The difference between TiB_2 and $(Ti_{0.9}W_{0.1})B_2$ peak positions are only 0.2°. In the light of these information, solid solution can be assumed as $(Ti_{0.9}W_{0.1})B_2$, however, it needs to be proved with spectroscopic methods.

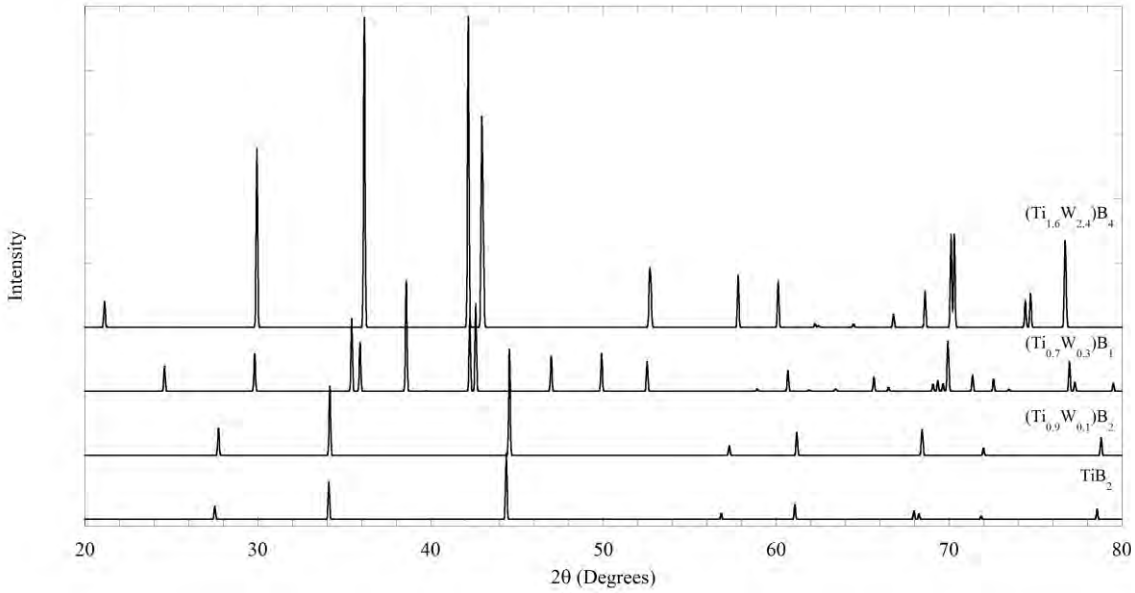

Figure 5.22. *Theoretical powder XRD results for possible solid solution phases*

Due to the significant contrast differences between present phases (bright: solid solution, gray: TiB_2 and dark: B_4C) in the SEM-BSE images, volume fractions of the phases can be calculated by contrast thresholding method from the SEM images, which gives the area percentage of respective phase within 2D image that can be deduced as volume fraction of 3D volume [92]. For this purpose, low magnification SEM images were used for the statistical significance and measured volume percentages of the phases are given in Table 5.4. According to these results with the presence of W, amount of TiB_2 phase was significantly reduced to form solid solution that contains Ti-W-B elements. The 50/50-BM sample also contains very small amount W, however, contrast difference of this small quantity was not high enough for the contrast thresholding, therefore, there

was small fraction of information from image was absent in the calculations. This could be the reason of deviation from theoretical phase ratio, which was 50/50 volume percentage.

As expected, amount of solid solution increases with the W content which is the main reason for solid solution formation. The calculated solid solution from the SEM-BSE images of 50/50-HEM sample include both W-rich and W-containing solid solution regions (labelled as 1 and 2 in Figure 5.19 (h)) because of the fact that contrast sensitivity, was not enough to differentiate these two phases.

It should also be noted that pull out of particles, during mechanical polishing due to the difference in the coefficient of thermal expansion (CTE) of B_4C and TiB_2 phases [91], may change the calculated volume percentages. The reason for miscalculation is the regions where pulled out particles originally located appear as dark contrast in the SEM-BSE images, therefore, the quantity of B_4C phase might be calculated higher than it is real content.

Table 5.4. *Calculated volume fractions from 2D SEM-BSE images*

Sample	*B_4C (area%)*	*TiB_2 (area%)*	*Solid Solution (SS) (area%)*	*Average (vol%)*
50/50-BM Surface	51.3	48.7	-	B_4C:51.20
50/50-BM Cross section	51.1	48.9	-	TiB_2: 48.80
50/45/5-BM Surface	44.6	26.8	28.6	B_4C:44.40
50/45/5-BM Cross section	44.2	27.6	28.2	TiB_2: 27.20 SS:28.40
50/50-HEM Surface	50.1	27.8	22.1	B_4C:50.80
50/50-HEM Cross section	51.5	26.5	22.0	TiB_2: 27.15 SS:22.05

5.3.2.2. Transmission electron microscopy results

5.3.2.2.1. Characterization of the starting powders

STEM and TEM characterizations of the starting powder mixtures after different milling conditions revealed that TiB_2 particles surrounded with continuous amorphous layer for all powder mixtures. Composition of the amorphous phase varies depending on the starting mixture content. Amorphous phase mainly composed of Ti and O elements; however, the one found around the TiB_2 particles within ball milled 50/45/5-BM powder mixture, contains higher amount of W element compared to other mixtures. According to these results, it can be concluded that amorphous layer around TiB_2 particles contains Ti-

W-O elements for the 50/50-HEM and 50/45/5-BM samples. This result also showed that there is no significant effect of milling energy on the amorphous layer composition.

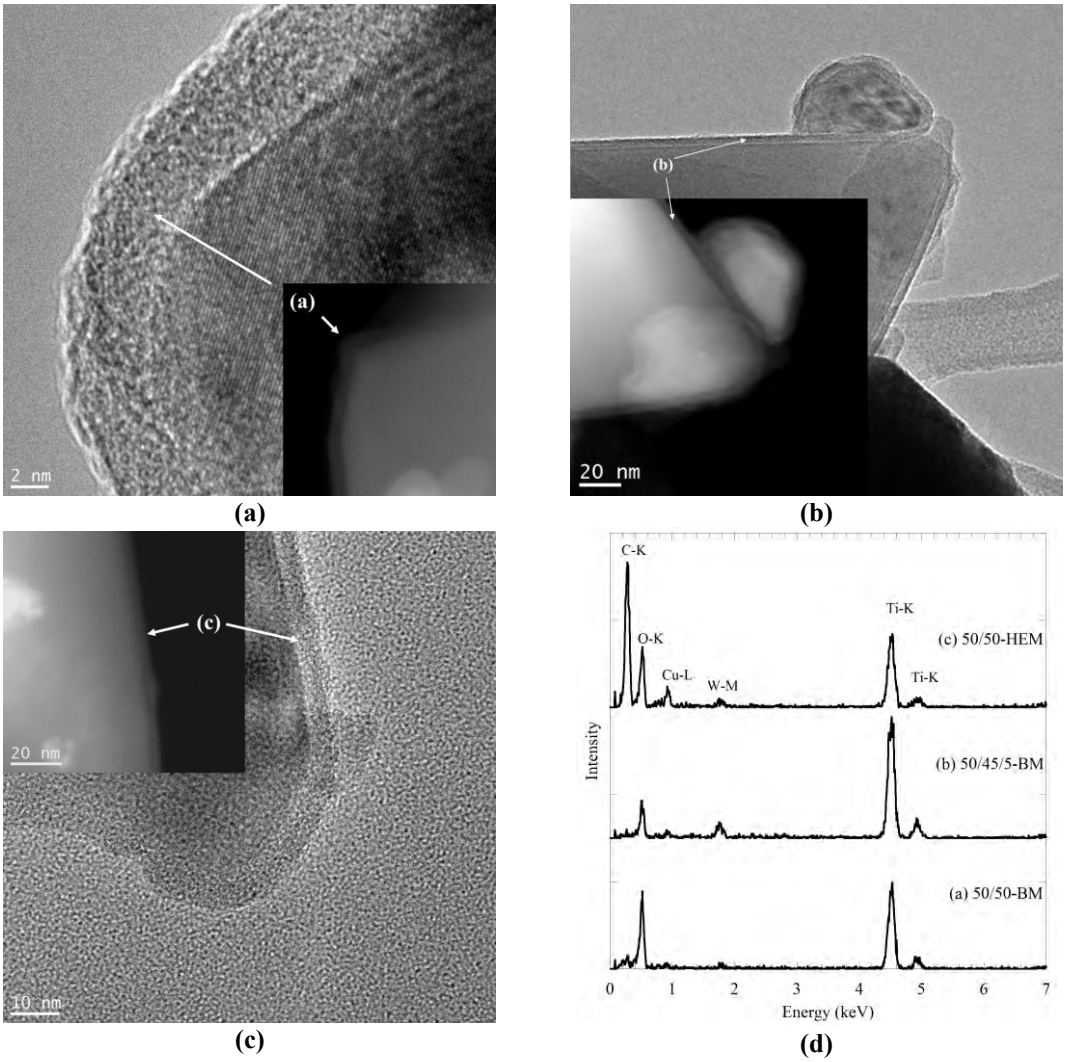

Figure 5.23. *TEM-BF and inset STEM-HAADF images of amorphous layer found on the surface of TiB_2 particles (a) soft milled, (b) Soft milled with WC addition, (c) High energy milled and (d) respective STEM-EDX spectra of these amorphous layers*

S/TEM analyses of 50/50-BM (given in Figure 5.24) showed that particle sizes distributed within a wide range from few hundreds nanometers to few microns after milling as well as WC contamination due to milling media. Addition of 5 vol% WC resulted in the presence of both micron and nano sized WC particles for 50/45/5-BM sample (as shown in Figure 5.25). Nano sized particles were found mostly on the surface of B_4C, which possibly caused by the grinding of WC balls by the hard B_4C particles. In this sample, WC was added as metallic powder without any other additive, because of this reason, no additional elements were present.

High energy milling resulted in smaller particle sizes and in this mixture, in addition to the WC, WC/Co-Cr and Ti-W-(B-C) containing nano particles were found (Figure 5.26). Addition of Co/Cr elements to WC is widely used production method to obtain better mechanical properties. Therefore, source of these elements was wear of WC-Co balls. One of the interesting feature on the surface of B_4C particles was the nano sized Ti-W-(B-C) containing particles. It is known that high-energy milling might be resulted in mechanical alloying, therefore, Ti-W-(B-C) containing alloys could be formed. B and C elements are written within brackets because presence of these elements could not be confirmed due to the underneath B_4C particle and carbon support film. The reason of these particles were found only on the surface of B_4C can be related to the WC nano particles on the surface of B_4C and during milling, impact of these particles with TiB_2 may cause the formation of this alloy.

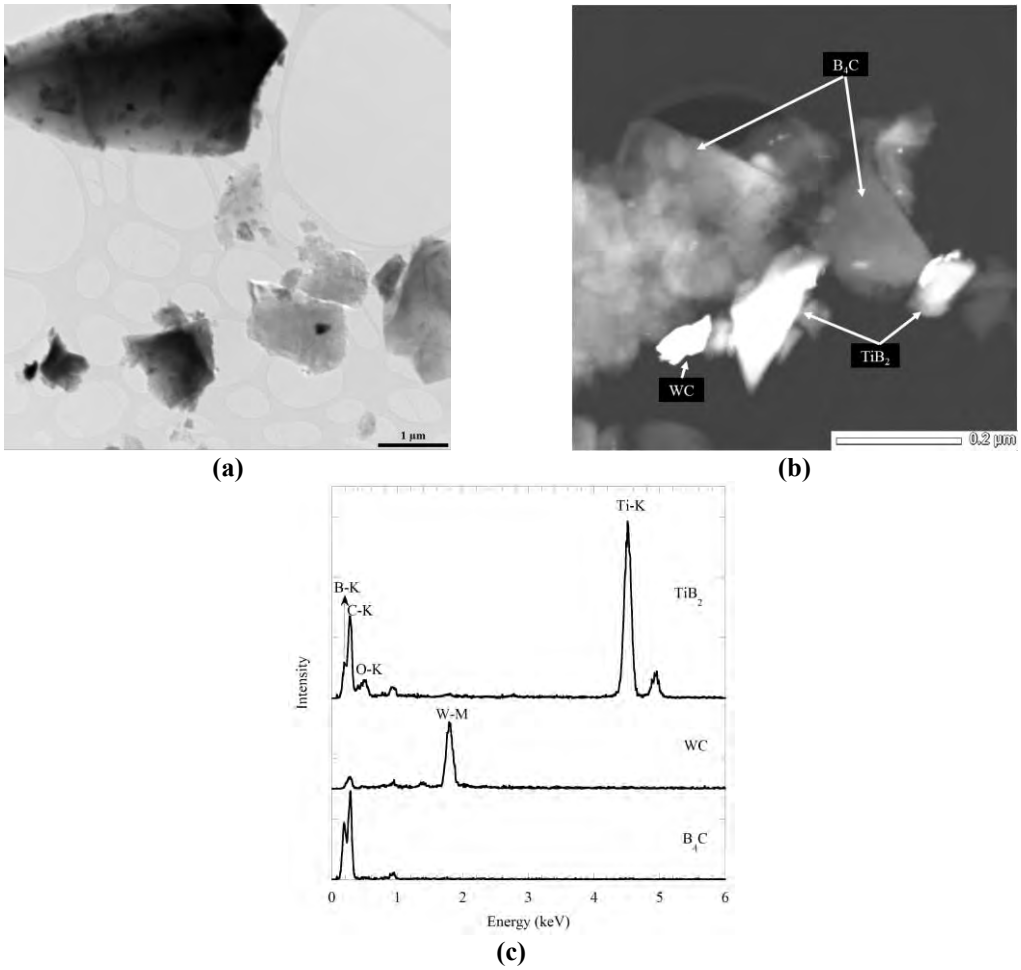

Figure 5.24. *(a) TEM image of 50/50-BM showing general overview, (b) STEM-HAADF image showing present phases and (c) STEM-EDX spectra obtained from particles in (b)*

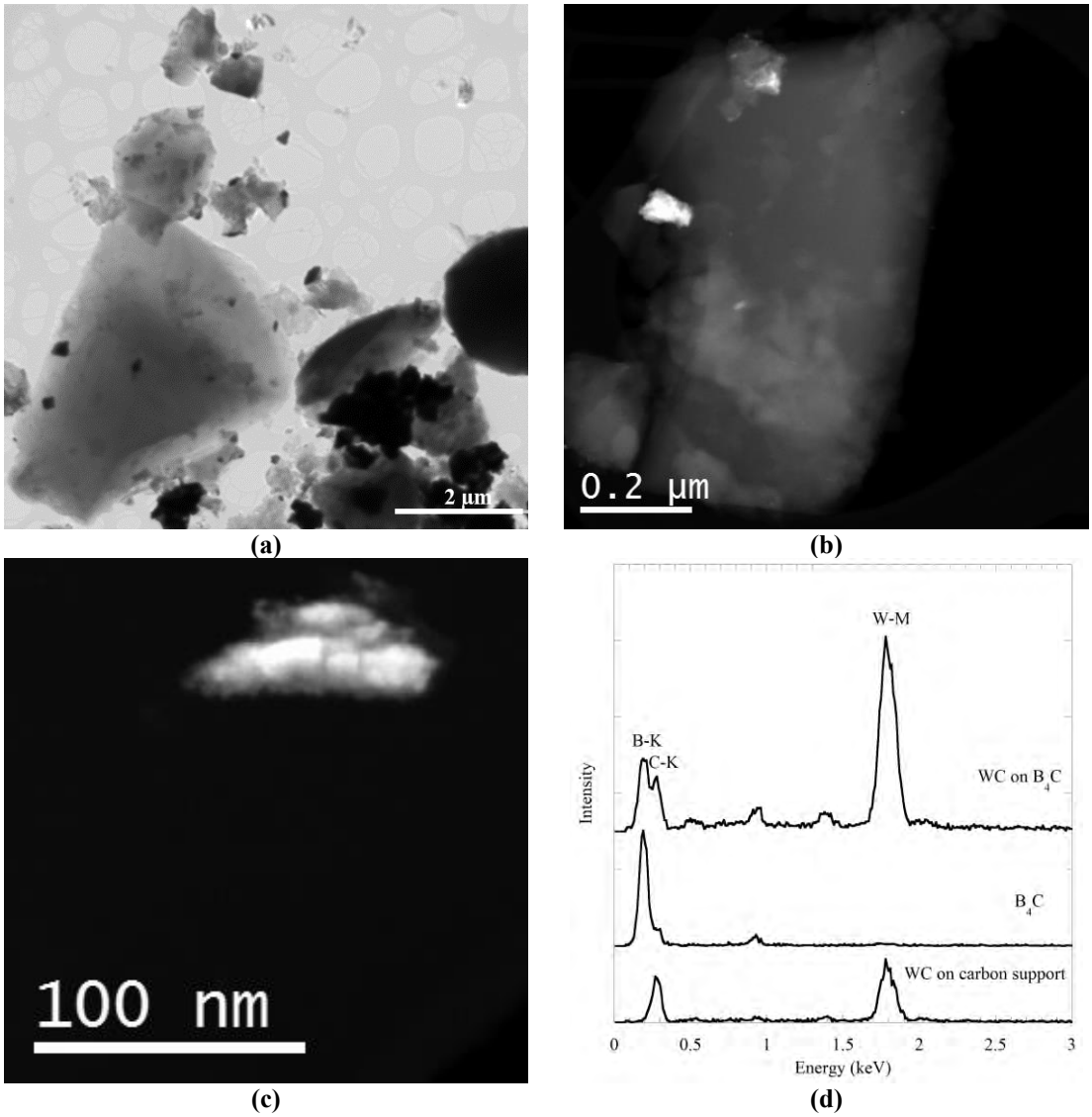

Figure 5.25. *(a) TEM image of 50/45/5-BM showing general overview, STEM-HAADF images showing (a) WC particle on B_4C, (c) WC on carbon support film and (d) STEM-EDX spectra obtained from particles in (b) and (c)*

Phase analysis of the powder mixtures was done with XRD analyses. During these analyses to calibrate scanning errors like peak shifts, pure silicon powder was added to powder mixtures and then necessary calibrations were done. This is an important step to separate the very close TiB_2 and $Ti_{0.9}W_{0.1}B_2$ peaks, if it is present. According to the XRD results, all powder mixtures were composed of B_4C, TiB_2 and WC phases; however, $Ti_{0.9}W_{0.1}B_2$ phase was not resolved from these measurements. There could be several reasons for that; one could be the overlapping of the peaks or amount of this phase may be very small or Ti-W-(B-C) phase found in TEM analyses may not be crystalline.

Additionally, peak broadening of ground WC peaks was observed due to very small size of the particles after milling.

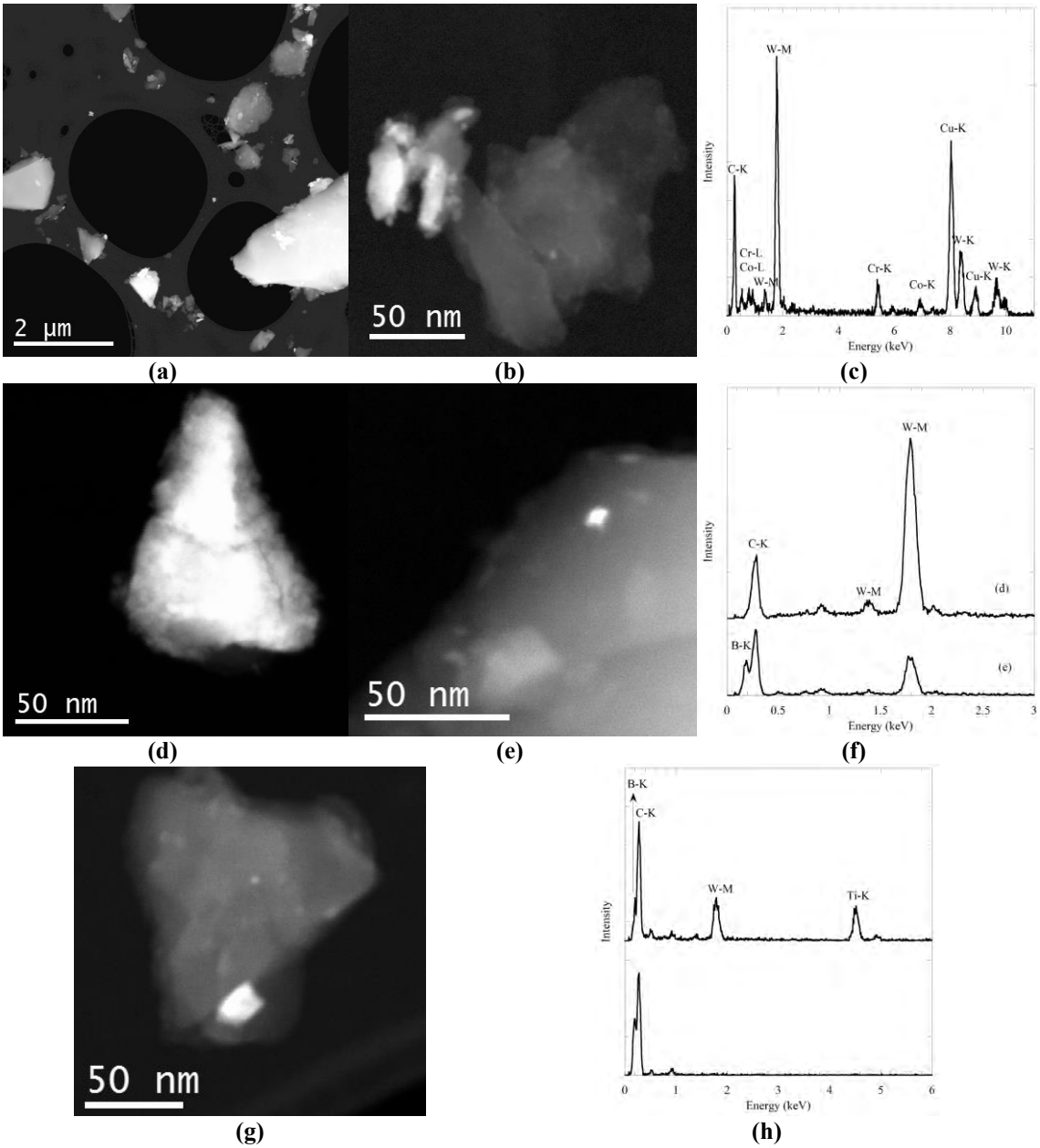

Figure 5.26. *STEM-HAADF images of (a) general overview, (b) Co-Cr containing WC, (c) STEM-EDX result of particle in (b), STEM-HAADF images of (d) WC on support film, (e) WC attached to surface of B_4C, (f) STEM-EDX results obtained from WC particles in (d) and (e), STEM-HAADF image of Ti-W-(B-C) particle attached to B_4C and (h) respective STEM-EDX spectra*

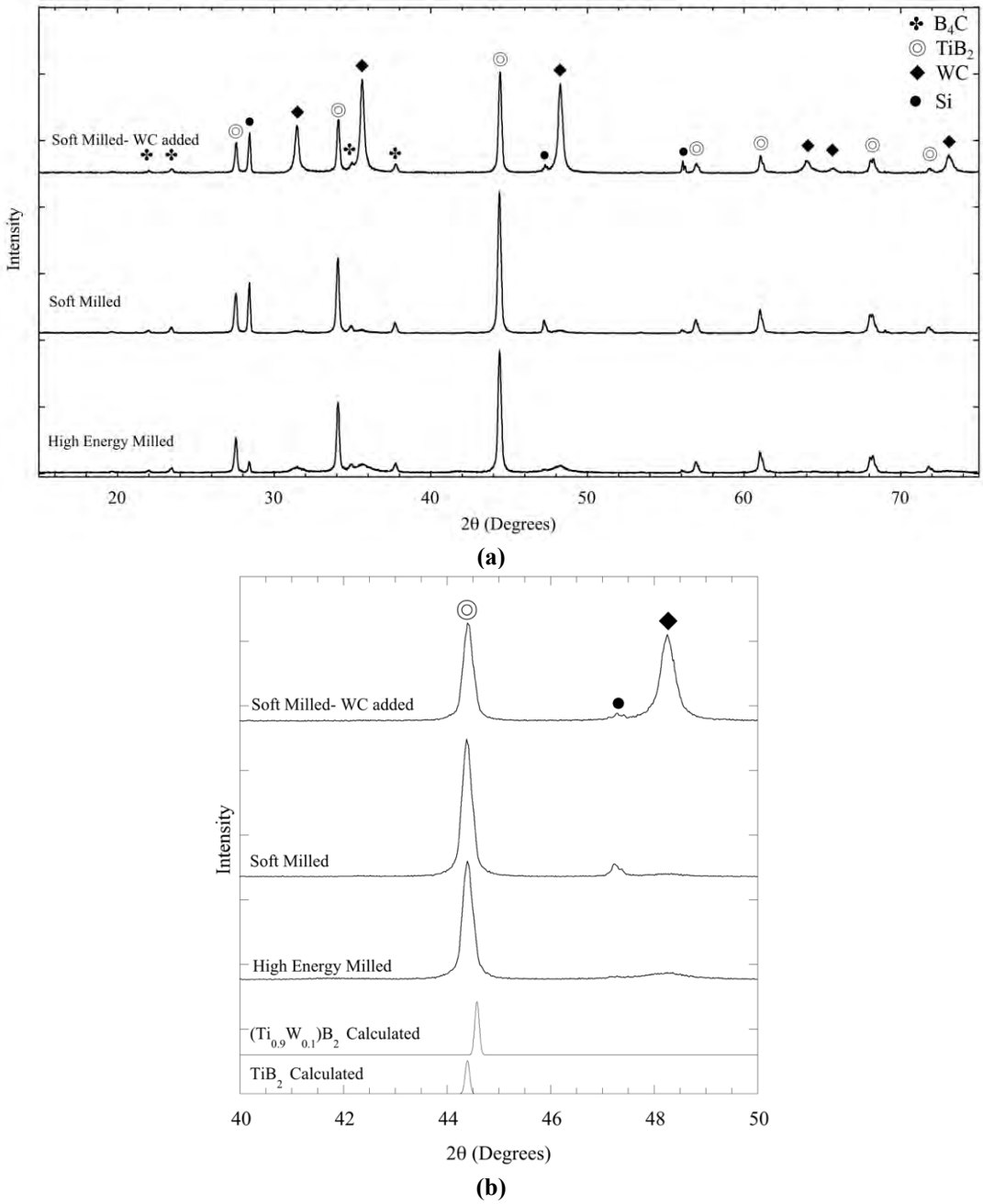

Figure 5.27. *(a) XRD results for starting powder mixtures after milling and (b) zoomed view between 40° and 50°*

5.3.2.2.2. Characterization of sintered composites

Sintered composite samples were investigated with various TEM and STEM methods and the obtained results will be given and discussed in this section.

STEM characterizations of 50/50-BM sample support SEM results of the respective sample. As shown in Figure 5.28, sample mainly composed of B_4C and TiB_2 particles however, there are regions around TiB_2 particles with W content due to the WC

contamination from milling media. It can be seen that regions with W content are localized and found in a small fraction of sample. Possibly, ground fragments of WC balls melted during hot pressing and wets the TiB_2 particles, because they were found only around TiB_2. In this sample, submicron TiB_2 particles were found within and in between B_4C particles as intra and intergranular particles, which are given in Figure 5.29, same as R-SPS'ed sample. During sintering, ground TiB_2 particles were surrounded by growing B_4C and become intragranular TiB_2. The convex grain morphology is also supports this possibility.

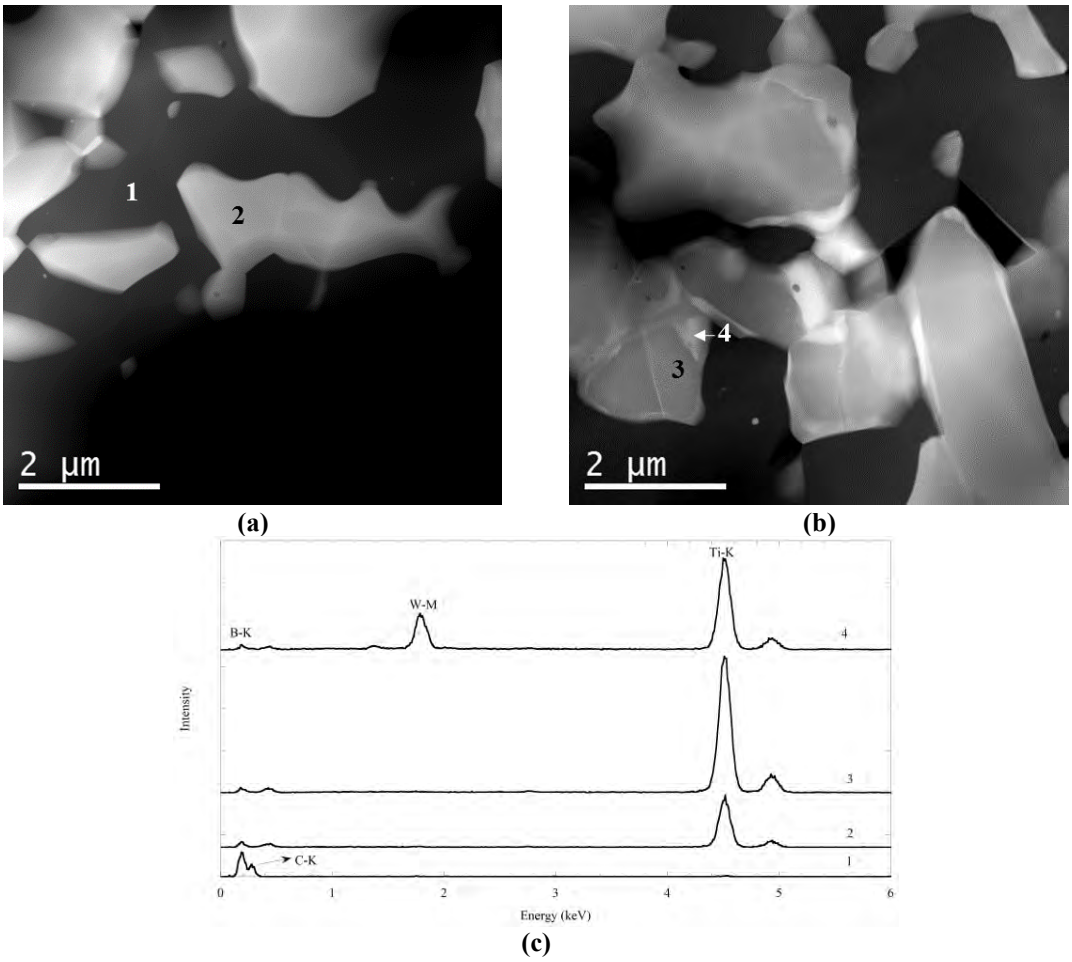

Figure 5.28. *(a, b) STEM-HAADF images showing general overview of 50/50-BM microstructure and (c) respective STEM-EDX spectra obtained from regions labelled in (a) and (b)*

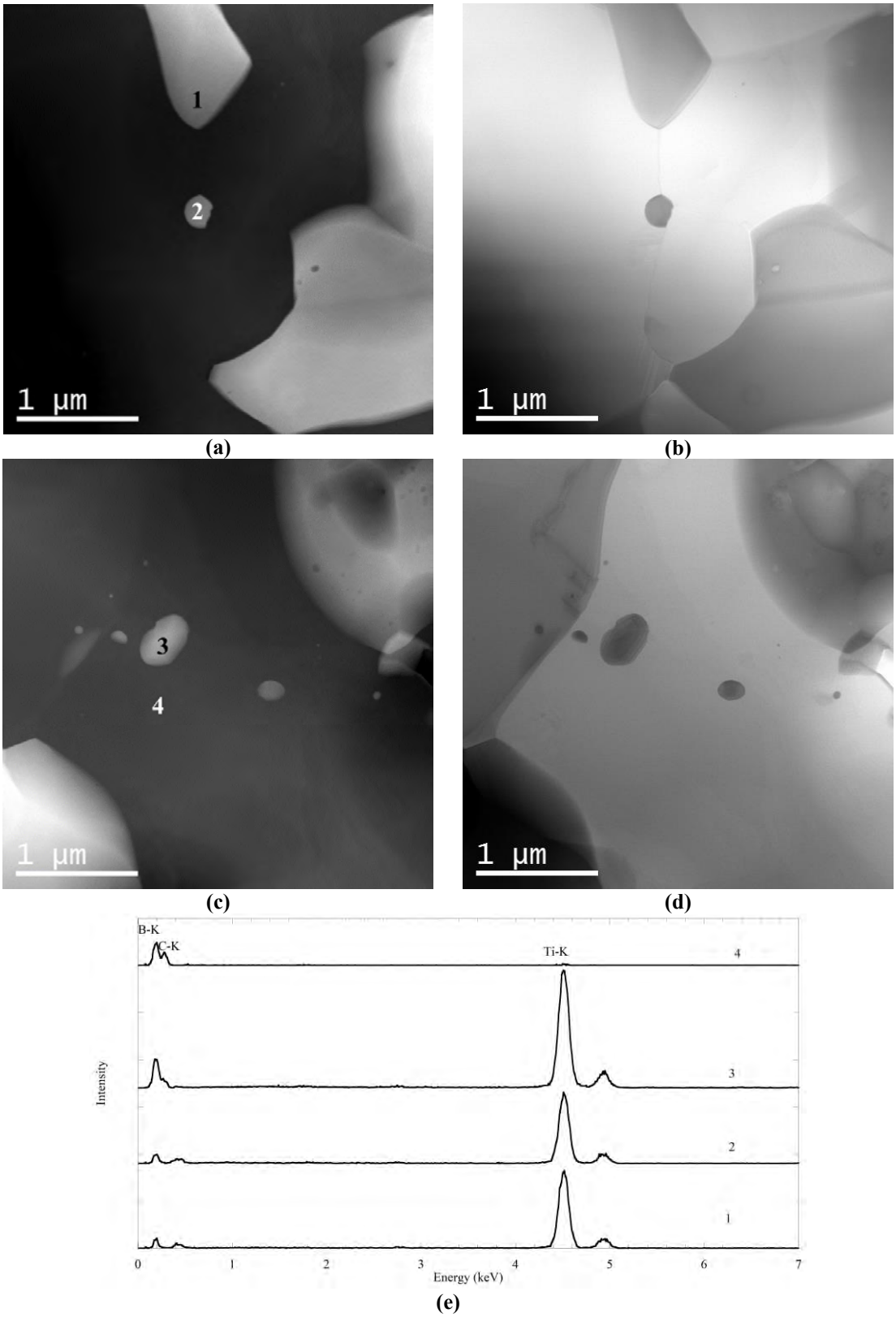

Figure 5.29. *(a, c) STEM-HAADF, (b, d) STEM-BF images showing intergranular and intragranular TiB_2 particles within 50/50-BM sample and (e) STEM-EDX spectra obtained from points labelled in (a) and (c)*

An interesting core/double rim type structures were observed around TiB_2 particles that were covered with W containing phase. (Figure 5.30), In this type of structures, inner core is TiB_2 and it was covered with two different rims having different contrasts in STEM-HAADF images, which indicates the presence of compositional difference. STEM-EDX analyses (Figure 5.30) clearly showed the compositional variation in core/double rim structure and they are labelled with 1, 2 and 3 for core, inner and outer rims, respectively. Quantitative STEM-EDX results are given in Table 5.5. The core was identified as TiB_2; however, both rims composed of Ti-W-B elements with different W content. The inner rim has higher W content compared to the outer rim. At the inner rim, amount of W increased while Ti decreased compared to the outer rim.

STEM-EDX line analysis (Figure 5.30(d)) also showed that amount of boron is almost constant in overall core/rim structure; however, titanium content is highest at core and decreased in the rim having a small difference between the inner and outer rims. All these data, indicate the formation of $(Ti_{1-x}W_x)B_2$ solid solution that formed by substitution of Ti element in TiB_2 structure with W element from surrounding phase. Details about $(Ti_{1-x}W_x)B_2$ solid solution will be discussed in Section 5.3.2.2.3.

Table 5.5. *Quantitative STEM-EDX results for regions found in core/rim structure*

Region	***B (at%)***	***Ti (at%)***	***W (at%)***
Core (1)	70.30	29.70	0
Inner Rim (2)	63.98	31.01	5.01
Outer Rim (3)	60.22	38.29	1.49

STEM analyses of 50/45/5-BM sample showed that in the microstructure there are three main phases; TiB_2, B_4C and surrounding W containing phase, which is similar to SEM analyses. In addition to the main phases, graphite particle was present as an impurity phase, possibly formed by the C from WC or most probably comes from B_4C starting powder. The W containing phase also has B and Ti elements in its composition and the amount of W is the highest for this solid solution among all the samples investigated. Average composition of this solid solution is; 45.54 at% B, 41.94 at% Ti and 12.52 at% W elements.

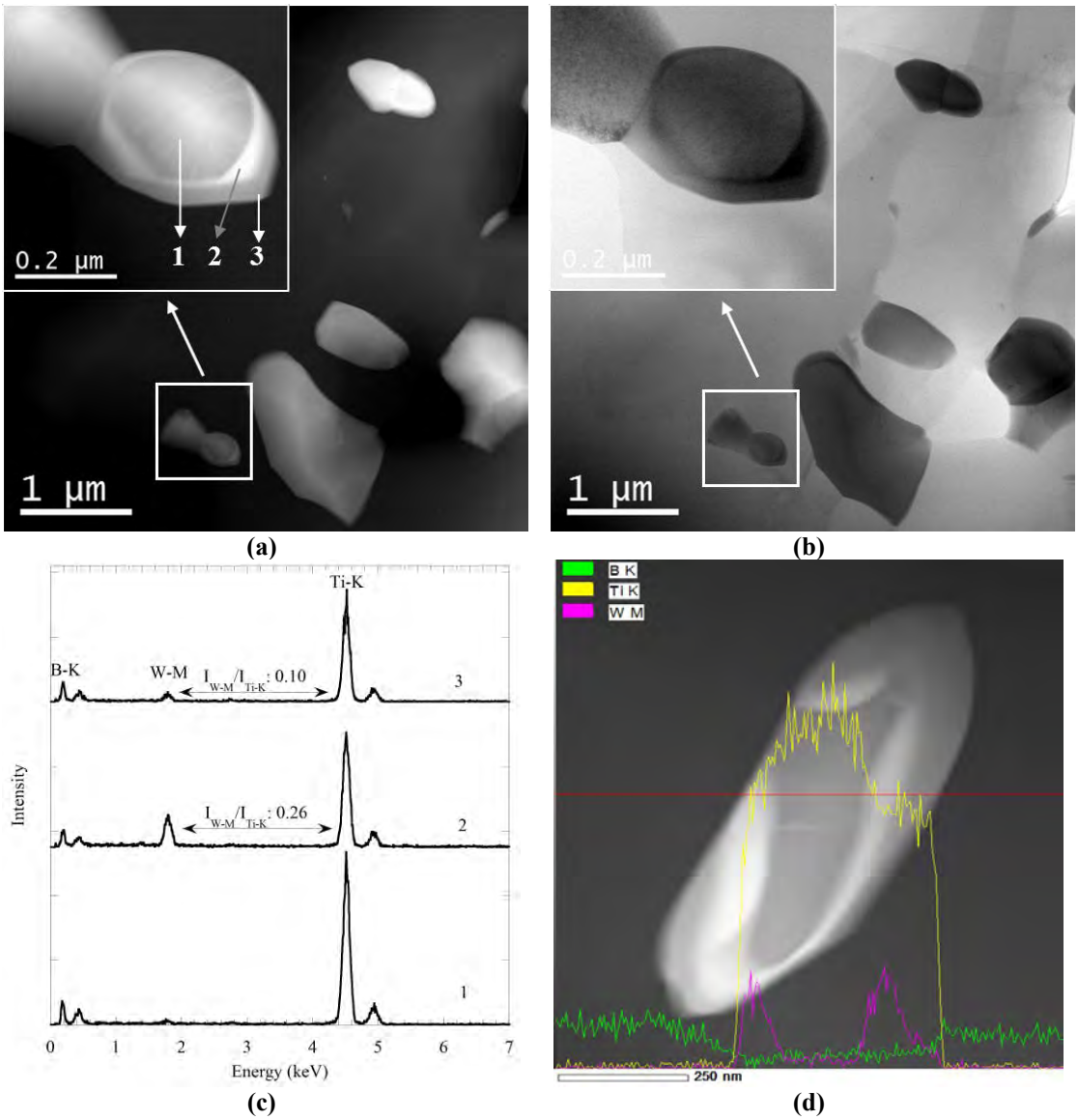

Figure 5.30. *(a) STEM-HAADF, (b) STEM-BF images showing core/rim type structure, (c) STEM-EDX spectra of core/rim regions labelled in (a) and (d) STEM-EDX line scan analysis showing distributions of Ti, B and W elements*

STEM images that shows general overview and impurity particle and respective STEM-EDX spectra are given in Figure 5.31. According to this result, increased W amount in the starting composition resulted in the $(Ti_{1-x}W_x)B_2$ phase with homogeneous W distribution compared to other samples that have double rim around TiB_2 particles.

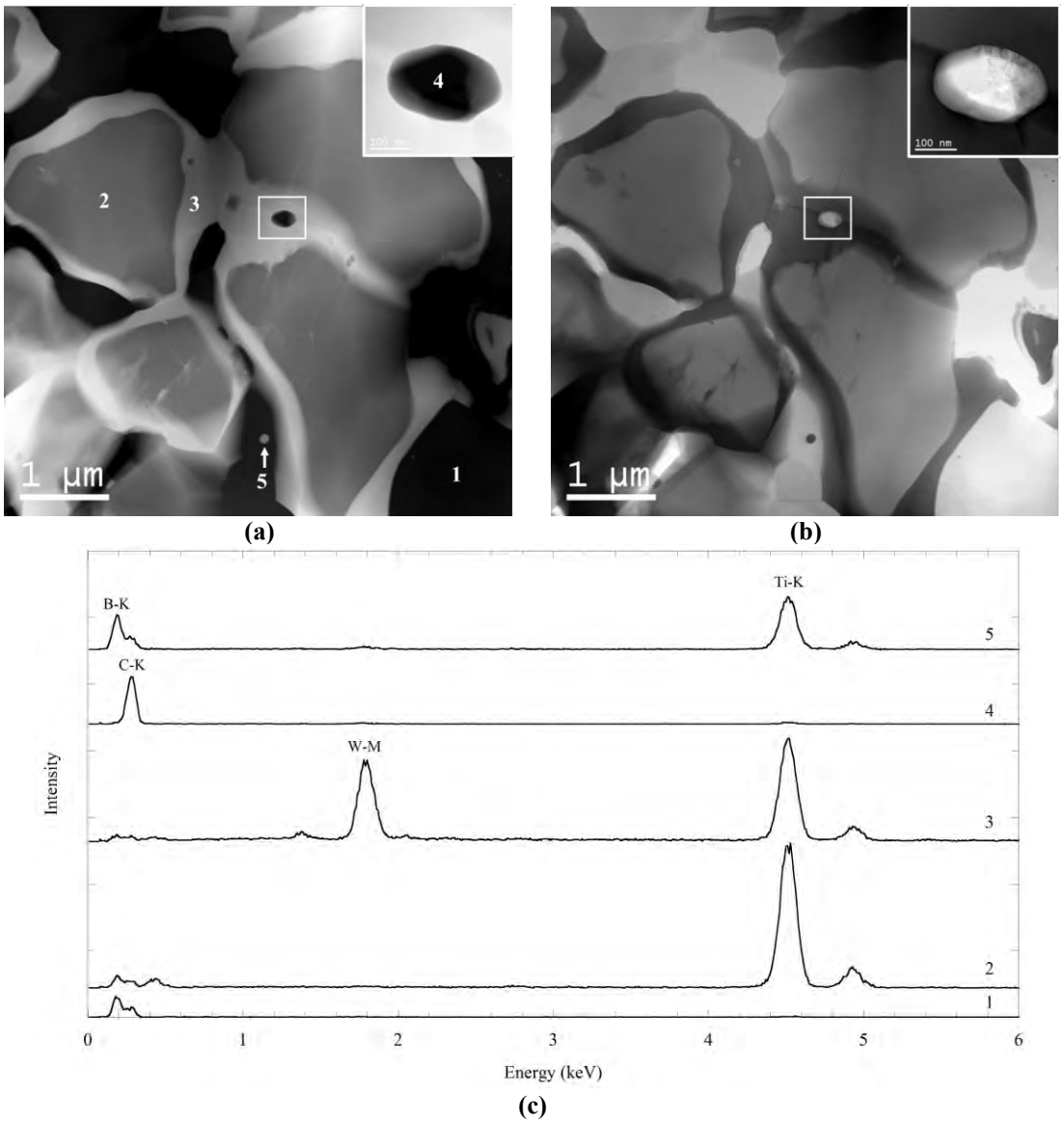

Figure 5.31. *(a) STEM-HAADF, (b) STEM-BF images showing microstructure of 50/45/5-BM sample and STEM-EDX spectra from regions labelled in (a)*

High energy milled 50/50-HEM sample showed similar behavior with 50/50-BM in terms of core/rim structure, both have double rim around the core. The chemical composition of inner and outer rims were qualitatively similar to 50/50-BM; W content was higher at the inner rim compared to the outer rim. In Figure 5.32, STEM-HAADF and BF images showing general overview and detailed core/rim structure with respective STEM-EDX point and line scan analyses. As it can be seen from STEM-EDX analyses; the core (labelled as 1) is TiB_2 and the rims (labelled as 2 and 3) are $(Ti_{1-x}W_x)B_2$, where x varies for inner to outer rims. STEM-EDX spectrum comparison of rims was done with scaling both spectra to the Ti-K peak, and this revealed that intensities of Ti-K and B-K

peaks were the same but W-M peak intensity almost doubled at the inner rim. Line scan analysis supports this result and additionally shows that the B content almost constant for both core and rims similar to results obtained from 50/50-BM sample. Average compositions for inner and outer rims are given in Table 5.6. STEM-BF (Figure 5.32) images also provide an important information about crystallinity of the rim; between outer rims of different core/rim structures, grain boundaries exist, which indicates that rims are in crystalline form.

Table 5.6. *Quantitative STEM-EDX results of the inner and outer rims present in 50/50-HEM sample*

Region	***B (at%)***	***Ti (at%)***	***W (at%)***
Inner Rim	74.48	20.60	4.51
Outer Rim	74.26	23.04	2.69

In the 50/50-HEM sample, there are several impurity phases; one of them is the graphite and it is present in all the samples. However, the other phase that is containing, Co-Ti-W-B due to the WC-Co grinding balls was found between particles as shown in Figure 5.33. Same figure also shows the unreacted Co from WC-Co during sintering.

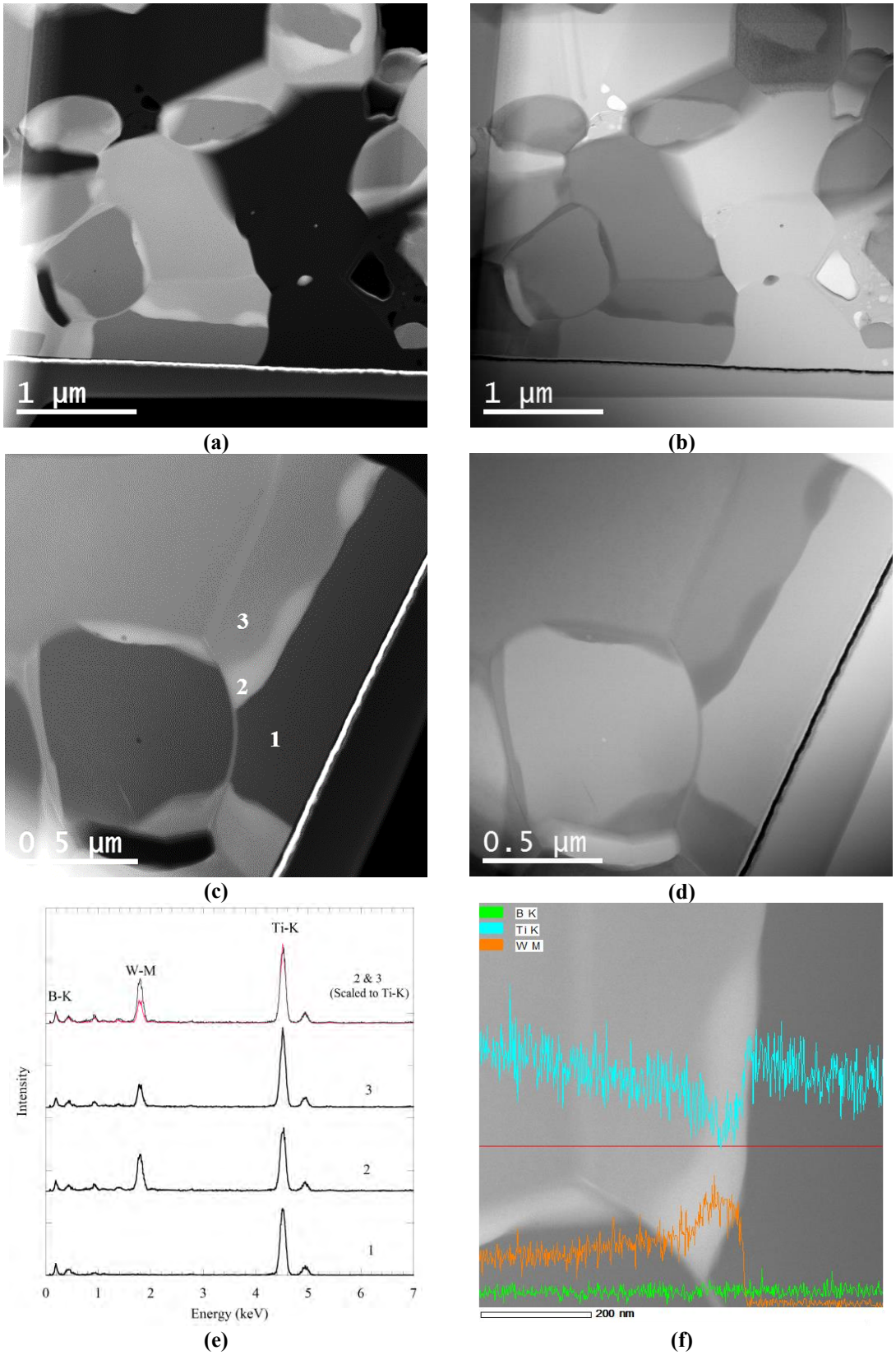

Figure 5.32. *Low magnification (a) STEM-HAADF, (b) STEM-BF images showing general overview, higher magnification (c) STEM-HAADF, (d) STEM-BF images showing detailed view of core/rim structure (e) STEM-EDX spectra taken from points labelled in (c) and (f) STEM-EDX line scan analysis showing distribution of Ti, W, B elements along core/rim structure*

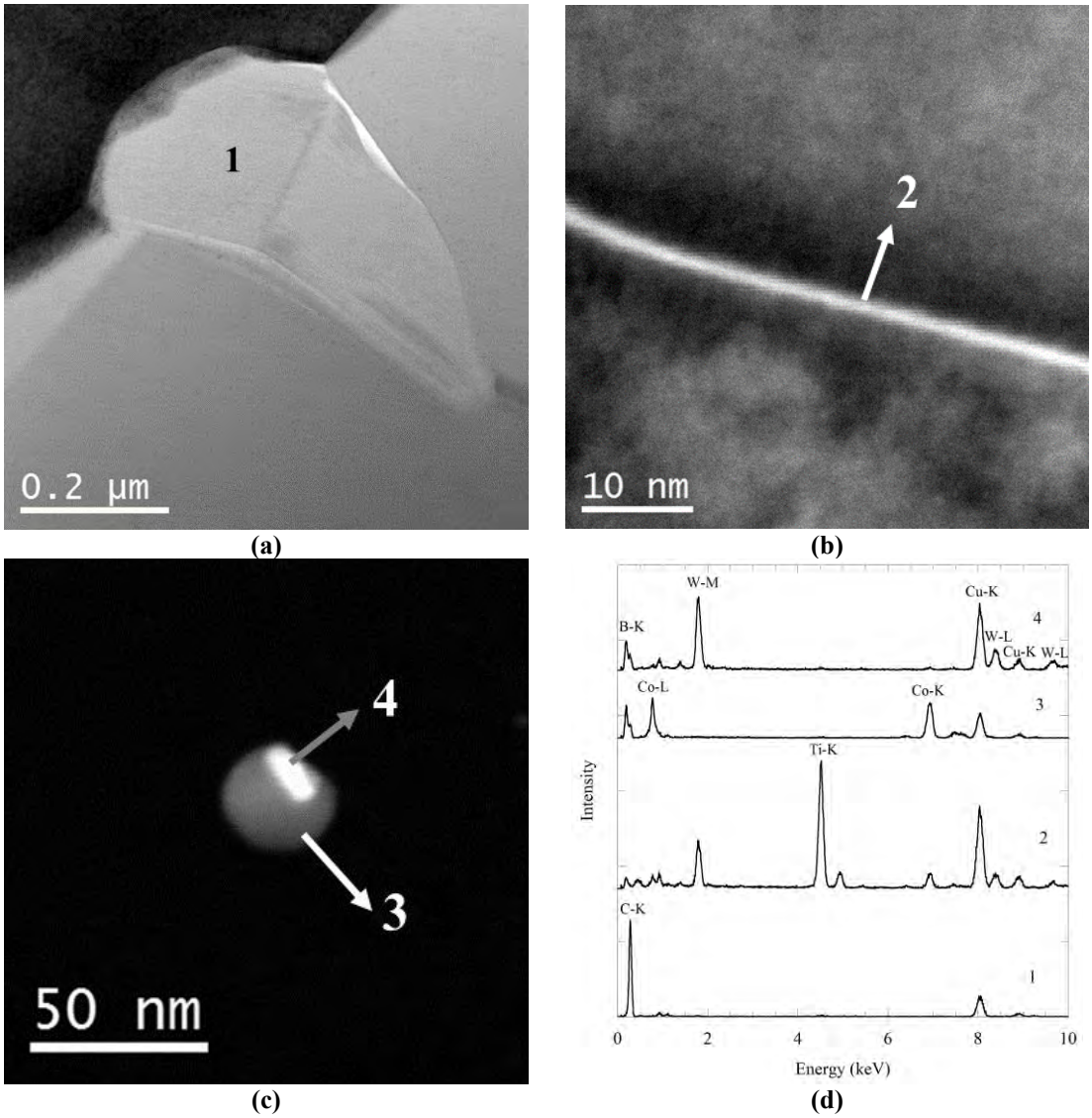

Figure 5.33. *(a) STEM-BF image of graphite particle, STEM-HAADF images of (b) Co containing grain boundary phase, (c) unreacted Co and WC phases and (d) respective STEM-EDX spectra of labelled regions*

5.3.2.2.3. TEM-PED results

Characterization of bulk samples showed that all the samples consist of three main phases; TiB_2, B_4C and $(Ti_{1-x}W_x)B_2$ as core/rim structure, where core is TiB_2 and rim is $(Ti_{1-x}W_x)B_2$. There is also significant difference in core/rim structure in terms of rim; there is a double rim structure in 50/50-BM and 50/50-HEM sample with different W contents; however, in the 50/45/5-BM sample there is only a single rim with homogeneous elemental distribution. The chemical composition and crystal structure of rim was found as $(Ti_{1-x}W_x)B_2$ according to the EDX and XRD analyses, however it needs to be supported with especially additional diffraction analyses.

According to the ICSD crystal information database, there are three possibilities for Ti-W-B containing rim phase with different crystal structures; they are $(Ti_{0.9}W_{0.1})B_2$, $(Ti_{0.7}W_{0.3})B_1$ and $(Ti_{1.6}W_{2.4})B_4$. The details of crystal structures are given in Table 5.7 and according to this information only $(Ti_{0.9}W_{0.1})B_2$ is similar to TiB_2 in terms of crystal structure and lattice parameters.

Table 5.7. *Details of crystal structures for TiB_2 and possible solid solutions*

Phase	*ICSD Number*	*Crystal Structure*	*a (Å)*	*b (Å)*	*c (Å)*	*α (°)*	*β (°)*	*γ (°)*
TiB_2	190893	Hexagonal	3.031	3.031	3.237	90	90	120
$(Ti_{0.9}W_{0.1})B_2$	108088	Hexagonal	3.026	3.026	3.213	90	90	120
$(Ti_{0.7}W_{0.3})B_1$	615603	Orthorhombic	5.984	3.049	4.532	90	90	90
$(Ti_{1.6}W_{2.4})B_4$	615602	Orthorhombic	3.187	8.395	3.075	90	90	90

TEM-PED method (with 0.7° precession angle) was utilized for crystal structure determination of rim(s) as well as orientation relation between core and rim(s) for 50/45/5-BM and 50/50-HEM samples. Figure 5.34 shows the STEM-HAADF image of core/rims structure for 50/50-HEM sample and orientation map (that is formed by using both TiB_2 and $(Ti_{0.9}W_{0.1})B_2$ banks) combined with virtual bright field (VBF) image of respective region. In the orientation map itself, core and rim regions cannot be distinguished because all three regions are oriented in the same direction, therefore, combination with VBF image used to highlight the core, inner and outer rim regions due to their formation mechanisms as explained in Section 3.4.1.1. Orientation map results revealed the heteroepitaxy between the core and rim structures and the diffraction patterns of these three regions were found identical with an exception of very small intensity variations. High orientation reliabilities for the core/rim sections and the similar diffraction patterns, validates the orientation results.

Phase map was used to differentiate TiB_2 core and $(Ti_{1-x}W_x)B_2$ rims, however as shown in the Figure 5.34 phase map could not provide the phase separation due to the very close crystal lattice parameters and also having almost identical theoretical diffraction spots (Figure 5.34) for this orientation of both phases. In the same phase map which was obtained with TiB_2, $(Ti_{0.9}W_{0.1})B_2$, $(Ti_{0.7}W_{0.3})B_1$ and $(Ti_{1.6}W_{2.4})B_4$ banks, they were colored with green, red, purple and turquoise, respectively. However there were not any regions colored with purple and turquoise. Orientation maps obtained with $(Ti_{0.7}W_{0.3})B_1$ and $(Ti_{1.6}W_{2.4})B_4$ phases also have very low reliabilities. With these

TEM-PED results, possibility of rim structure being $(Ti_{0.7}W_{0.3})B_1$ and $(Ti_{1.6}W_{2.4})B_4$ phases eliminated, which is in good agreement with XRD results.

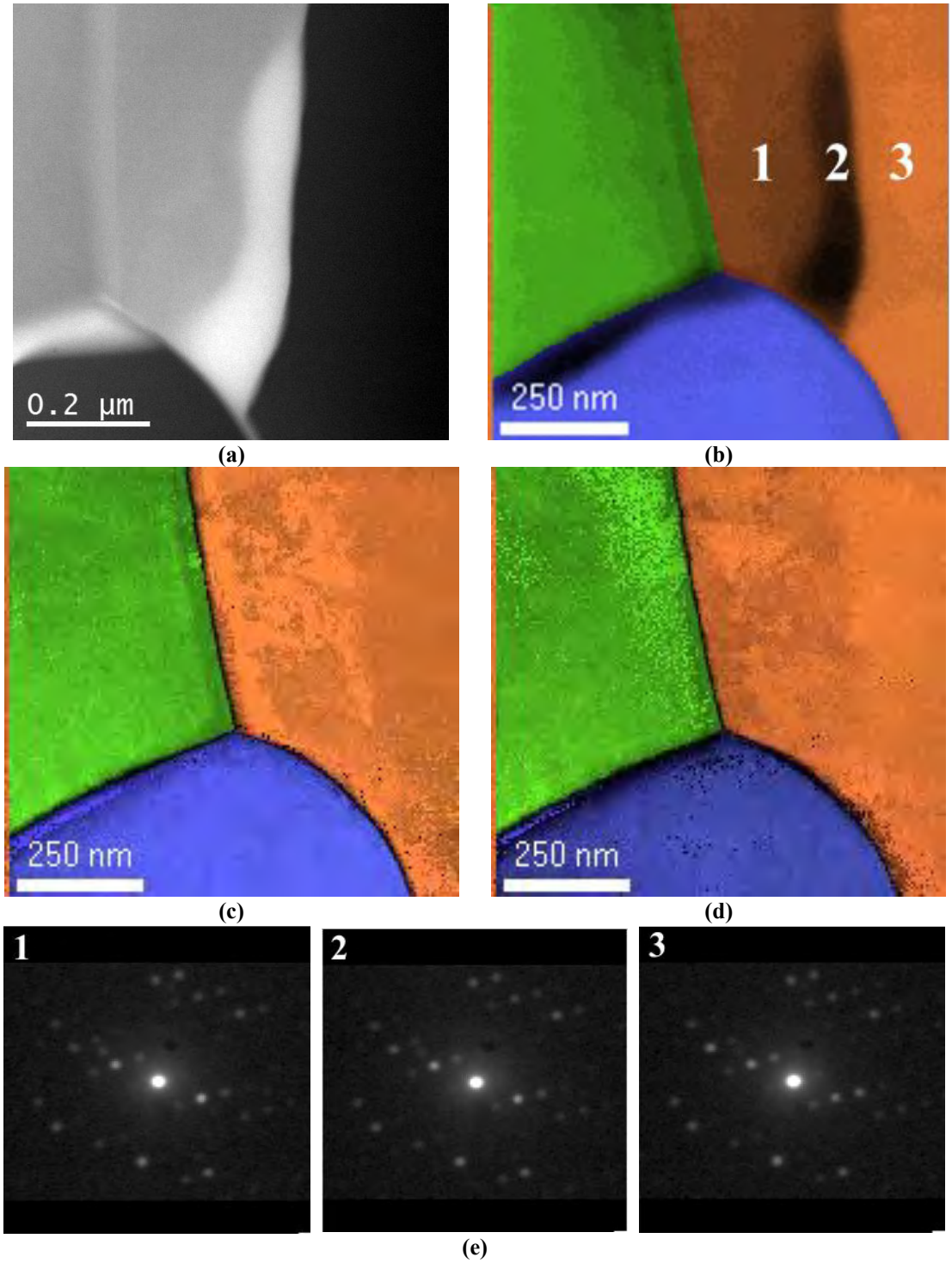

Figure 5.34 *(a) STEM-HAADF image of core/rim structure found in 50/50-HEM sample, respective (b) orientation map combined with VBF, orientation maps combined with reliability obtained with by using (c) $(Ti_{0.9}W_{0.1})B_2$ and (d) TiB_2 banks, (e) diffraction spots obtained from points labelled in (b), (f) calculated diffraction spots for present orientation, (g) phase map and orientation maps combined with reliability obtained by using (a) $(Ti_{1.6}W_{2.4})B_4$ and (i) $(Ti_{0.7}W_{0.3})B_1$ banks*

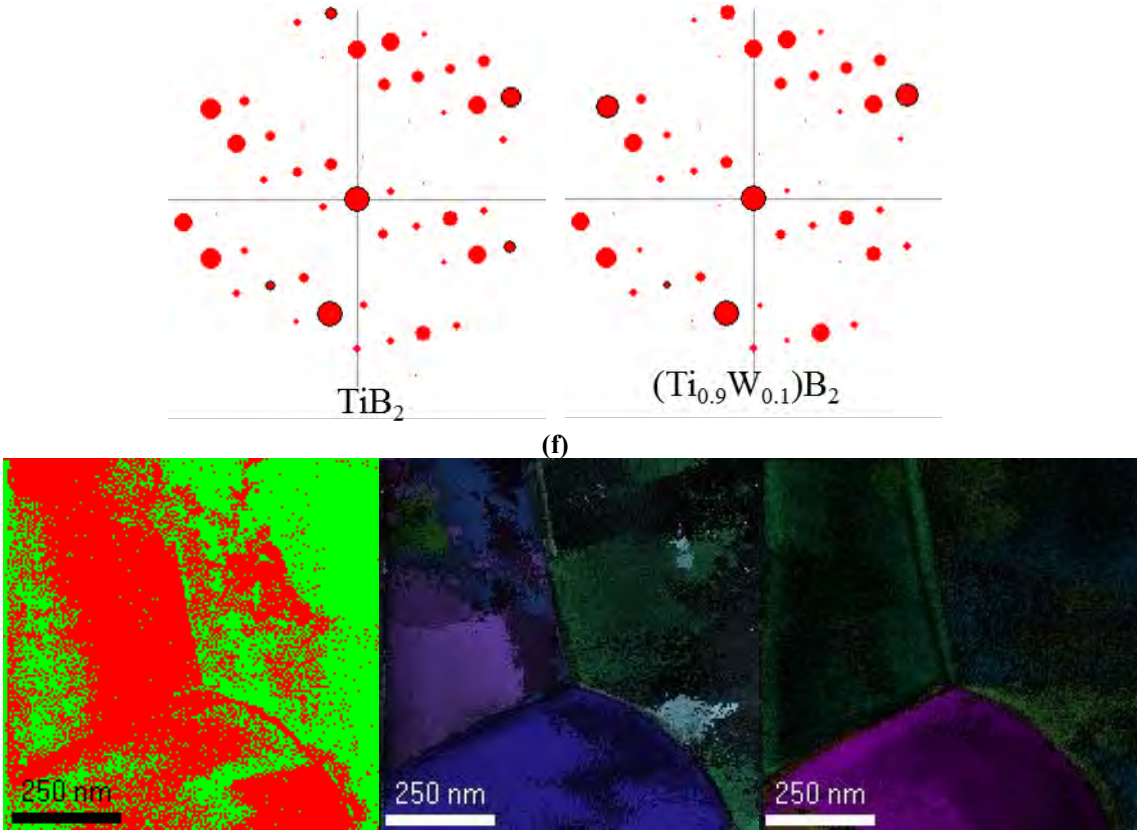

Figure 5.34. (Continued) *(a) STEM-HAADF image of core/rim structure found in 50/50-HEM sample, respective (b) orientation map combined with VBF, orientation maps combined with reliability obtained with by using (c) $(Ti_{0.9}W_{0.1})B_2$ and (d) TiB_2 banks, (e) diffraction spots obtained from points labelled in (b), (f) calculated diffraction spots for present orientation, (g) phase map and orientation maps combined with reliability obtained by using (a) $(Ti_{1.6}W_{2.4})B_4$ and (i) $(Ti_{0.7}W_{0.3})B_1$ banks*

Similar results (Figure 5.35) were also obtained from core/rim structure found in 50/45/5-BM sample, which has homogeneous and higher W content in a single rim. In this sample the rim phase was also found as $(Ti_{0.9}W_{0.1})B_2$.

In both samples, heteroepitaxy was observed between the core and rim phases independent of W content. Due to the heteroepitaxy, core/rim structure seen as single grain in the B_4C-TiB_2 composite microstructures. According to these orientation results, presence of heteroepitaxy and non-faceted/irregular boundary between core and rim(s) indicates epitaxial growth of rim with dissolution and precipitation. Formation of core/rim structure is discussed as follows.

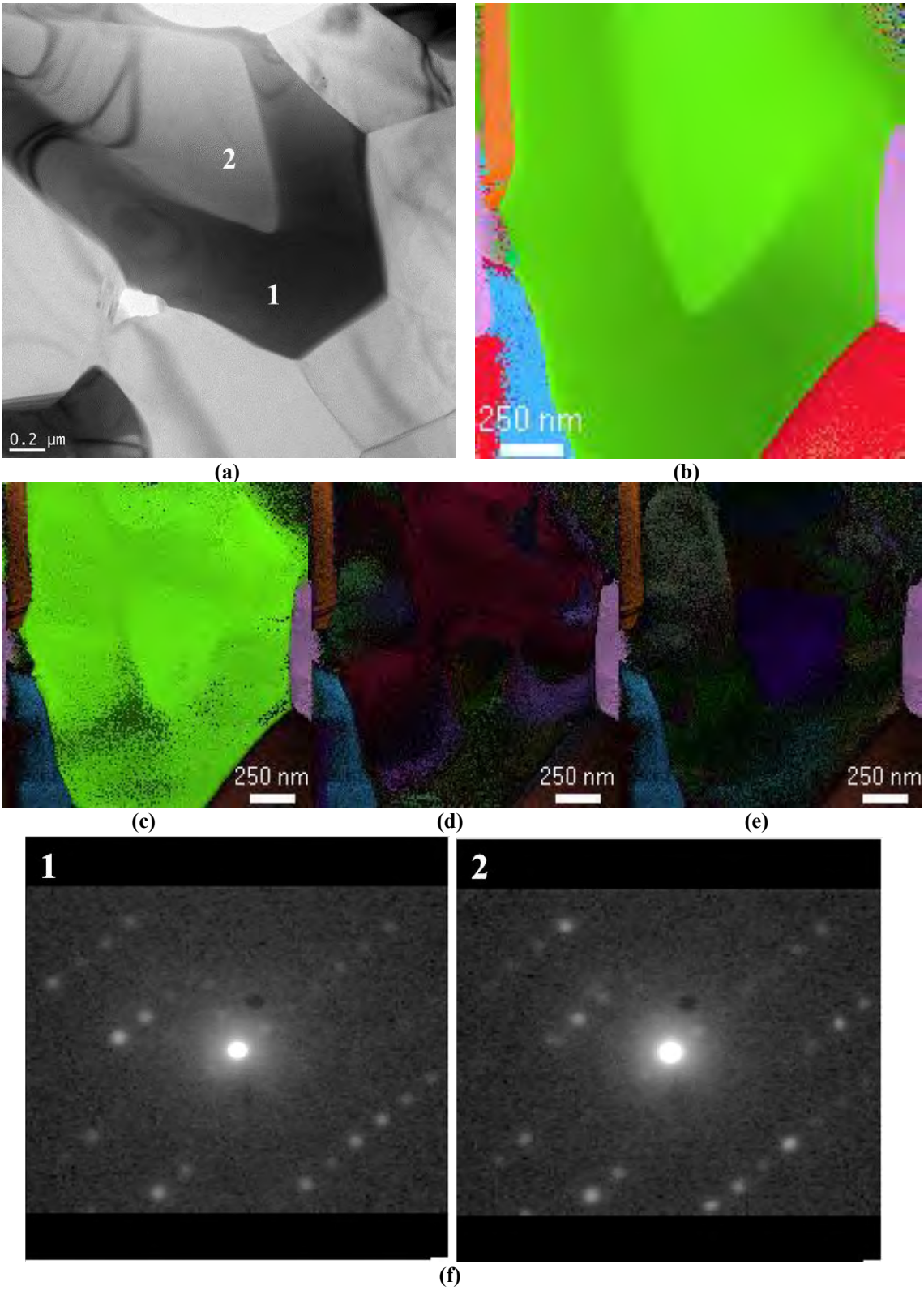

Figure 5.35. *(a) TEM-BF image of core/rim structure found in 50/45/5-BM sample, (b) orientation map combined with VBF, orientation maps combined with reliability obtained by using (c) $(Ti_{0.9}W_{0.1})B_2$ (d)$(Ti_{1.6}W_{2.4})B_4$ (e) $(Ti_{0.7}W_{0.3})B_1$ and (f) diffraction spots obtained from points labelled in (a)*

There are several different studies reporting that TiB_2 can dissolve 2 at % [93], 3 at % [94] and 5 at % [95] of W element without changing its crystal structure to form $(Ti_{1-x}W_x)B_2$ phase and its phase diagram is given in Figure 5.36. Based on this information, quantitative analysis results obtained from W-rich inner and outer rims present in 50/50-BM and 50/50-HEM samples are in good agreement with the literature, W content of both rims are lower than 5 at %. Similar core/double rim structure was observed in Ti(C,N)-WC composite that contains Ti(C,N) core surrounded by W-rich inner rim compared to the outer rim [96]. According to this study, W-rich inner rim is formed during heating of the sample with a formation of liquid phase, however, the outer rim formed at sintering temperature with dissolution-precipitation mechanism according to the observation of non-faceted boundaries between core and rims as well as inner and outer rims. With the formation of liquid phase, core material starts to dissolve from its surface and then precipitate over the undissolved core by nucleation when liquid phase reach saturation point.

Formation of double rim structure can also be explained with the same approach for 50/50-HEM sample. At the temperature of liquid phase formation, where sharp shrinkage observed during sintering, inner W-rich $(Ti_{1-x}W_x)B_2$ rim, then, at sintering temperature outer $(Ti_{1-x}W_x)B_2$ rim were formed [91]. TEM studies present in this thesis provide additional supporting information to the literature. The rim formation mechanism in the literature was done by guessing the crystal structure of rims as $(Ti_{1-x}W_x)B_2$ and without knowing exact chemical compositions, however additional TEM analyses in this study revealed the chemical compositions and crystal structures as well as orientation relations that prove the supposed dissolution-precipitation mechanism in the literature. In the same study, formation of core/double rim structure was related with high energy milling by using SEM images, however, TEM studies revealed that formation of this type of core/double rim structure might not be related with milling conditions because they are not only present in high energy milled sample (50/50-HEM) but also present in ball milled sample (50/50-BM).

WC addition into composite system resulted in core-single rim structure with higher amounts of W in the rim. The structure of the rim is found to be $(Ti_{1-x}W_x)B_2$, however, amount of W in the rim structure is above the solubility limit of core TiB_2 phase. The grain boundary morphology and TEM-PED results indicates, its formation mechanism should resemble core/double rim structure due to the microstructural similarities,

however, it cannot be explained by just dissolution-precipitation of TiB_2 in liquid phase. Hot pressing of B_4C and WC resulted in the formation of W_2B_5 about 1800°C [97] which is lower than sintering temperature of 50/45/5-BM sample. According to the TiB_2- W_2B_5 phase diagram (Figure 5.36) at sintering temperature of 50/45/5-BM sample, W_2B_5 dissolve in $(Ti_{0.9}W_{0.1})B_2$ to form single phase up to 14 at % W concentration. Possible formation mechanism of the single phase rim structure could be the epitaxial orientation of $(Ti_{1-x}W_x)B_2$ phase around TiB_2 core with the same crystal structure and fast cooling rate after sintering might prevent the phase transformation into $(Ti_{1-x}W_x)B_2$ and W_2B_5 phases, and form oversaturated $(Ti,W)B_2$. This oversaturated phase could be separated into $(Ti,W)B_2$ and W_2B_5 phases with post-sintering heat treatment.

Other possibility for W-rich rim formation could be deduced by using TiB_2–W phase diagram (as shown in Figure 5.36), according to this diagram at sintering temperatures between solubility limit of TiB_2 and 50 at% W content, τ and TiB_2 phases present. τ phase is CrB type orthorhombic crystal and its chemical formula is $(Ti_1W_1)B_2$. According to this phase diagram rim should be τ phase, however W content of the rim does not meet with the τ phase composition and TEM-PED results also showed that crystal structure of rim is hexagonal. With this information, rim formation with this route will not be possible.

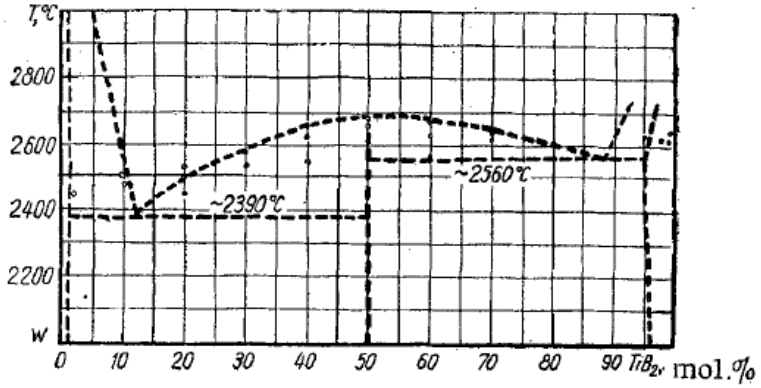

(a)

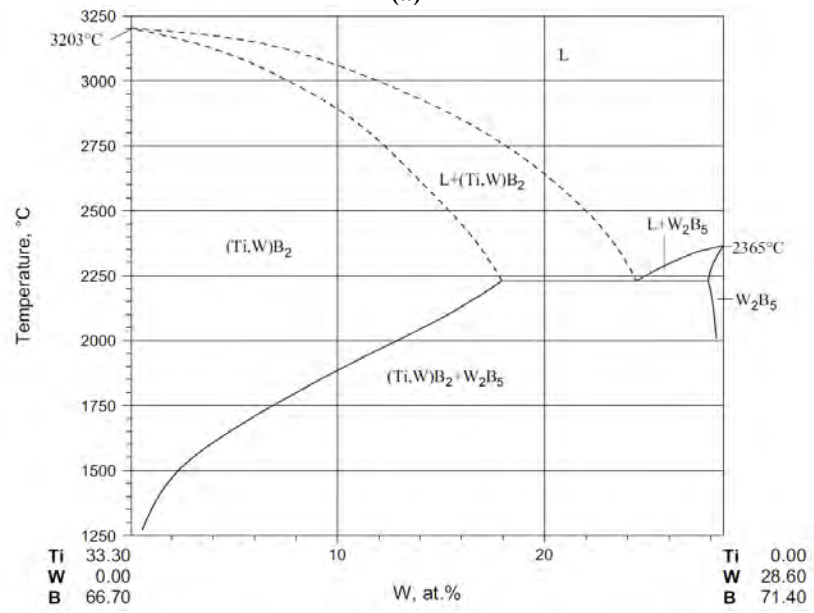

(b)

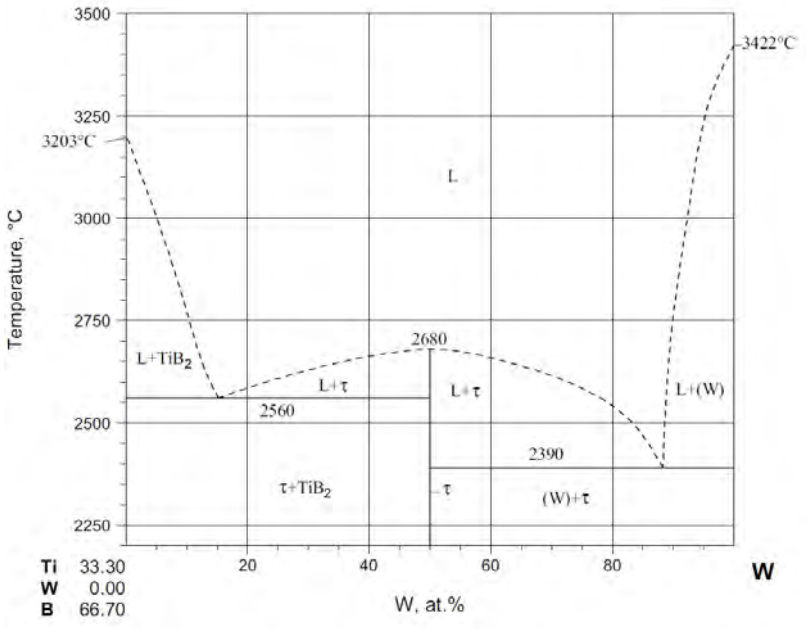

(c)

Figure 5.36. *Phase diagrams for (a) TiB_2-W [95], (b) TiB_2-W_2B_5 and (c) TiB_2-W [98]*

5.3.2.3. Directional properties of the B_4C-TiB_2 composite

SEM and XRD analyses showed that, hot pressing resulted in slight texturing in the bulk microstructure and this texture might cause a change in the mechanical properties of the composite depending on the pressing direction. To characterize directional variation, the mechanical properties such as hardness and indentation toughness were measured for both surface and cross section from the polished samples and results were summarized in Table 5.8.

According to this table, measured hardness and toughness values are very close to each other in different directions, therefore, there is no significant effect of slight texturing on these properties.

Table 5.8. *Measured mechanical properties with respect to hot pressing direction: (a) hardness and (b) toughness*

(a)	***Hardness (HV10-GPa)***		***Young's***
Sample	***Cross Section***	***Surface***	***Modulus (E-GPa) [91]***
50/50-BM	19.82±0.44	19.38±0.54	460
50/45/5-BM	19.58±0.77	21.33±0.96	406
50/50-HEM	16.08±0.33	16.93±0.56	407

(b)	***Indentation Toughness (MPa $m^{0.5}$)***	
Sample	***Cross Section***	***Surface***
50/50-BM	6.05±0.13	6.25±0.06
50/45/5-BM	5.74±0.17	5.83±0.17
50/50-HEM	5.97±0.13	6.18±0.1

TiB_2 addition into the B_4C resulted in a increase in the toughness of B_4C which is reported as ~ 2 MPa $m^{0.5}$ [91]. Thermal expansion coefficient difference between TiB_2 ($8.1x10^{-6}$ K^{-1})and B_4C ($4.5x10^{-6}$ K^{-1}) as well as anisotropic thermal expansion coefficient of TiB_2 (42% higher expansion along c-axis compared to a-axis up to 930°C [99]) can cause a residual stress toughening by crack bridging and deflection [100]. Fracture mechanism for both phases in monolithic state is transgranular, however it was reported that B_4C addition into the TiB_2 increased the intergranular fracture character possibly caused by weak bonding between phases [101]. According to the SEM images (Figure 5.37) of the cracks formed by indentation, transgranular fracture mode of monolithic TiB_2 and B_4C preserved in the composites that indicates a good bonding strength achieved between phases. The improved toughness can be related with crack deflection according to the SEM images due to residual stresses.

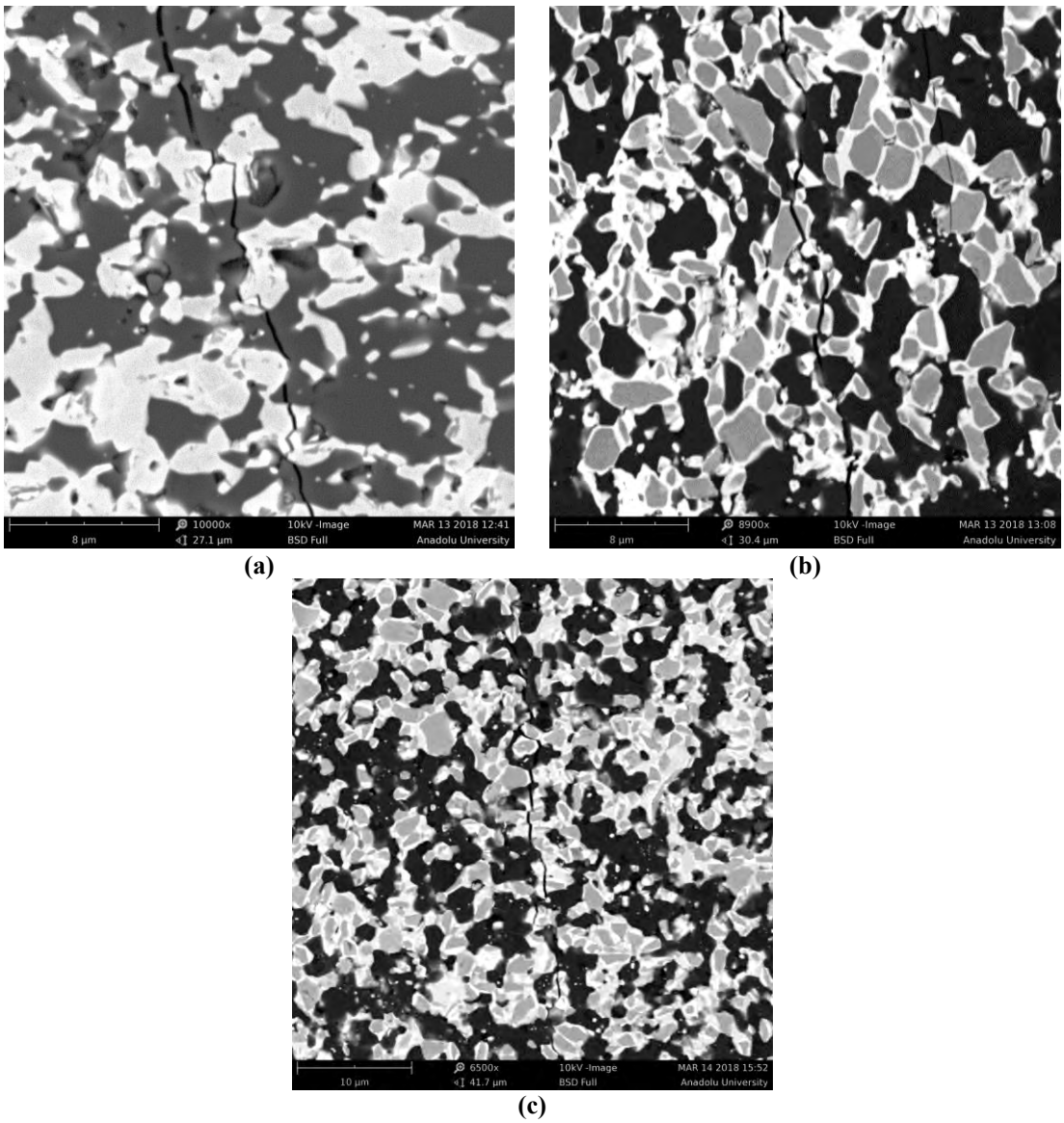

(a) **(b)**

(c)

Figure 5.37. *SEM-BSE images showing crack propagation for (a) 50/50-BM, (b) 50/45/5-BM and (c) 50/50-HEM samples*

5.4. Conclusions

Microstructural characterizations of R-SPS'ed and hot pressed B_4C-TiB_2 composites were carried out by various XRD, SEM and S/TEM analyses. In the R-SPS'ed sample, SEM analyses revealed the formation of SiC and graphite particles around TiB_2 phase as a reaction product in addition to main phases. Additionally, the effect of polishing method on the surface quality was shown. Scratch free samples cannot be prepared successfully due to the hardness variation between phases by using mechanical polishing method; therefore, ion beam polishing was utilized successfully.

S/TEM analyses of bulks samples as well as starting raw materials showed that there are several unintentionally added phases such as graphite, hBN and amorphous phase present in the structure. SiC and graphite were also observed in SEM analyses and TEM proved the presence of graphite around TiB_2 as intergranular particles. TiB_2 and SiC particles were also found as both intergranular and intragranular within B_4C. The use of SiAlON mixing balls resulted in the incorporation of Si, Al, O, N, Y elements as an impurity into the composite structure and these elements formed various additional phases such as SiC and Si-Al-O-Y containing amorphous phase between particles. Some of the additional phases; graphite and hBN were also found in the starting raw materials and their formation mechanism with other phases during sintering process were explained by means of chemical reactions and respective change in Gibbs free energies. The possibility of $(0001)_{TiB2}$ // $(0002)_{graphite}$ orientation relation between in-situ formed phases was analyzed with TEM-PED method but it was found that there was not any special relation present between phases, rather they were aligned randomly. One of the possible reason could be the presence of liquid phase between phases, which prevent direct contact of phases. During the TEM-PED analyses difficulties during indexing was experienced due to the delaminated and overlapped graphite layers, which lowers the orientation reliabilities of the results.

SEM results of hot pressed composite samples prepared by different mixing methods and compositions showed that there are various phases around the TiB_2 particles other than TiB_2 and B_4C phases. SEM studies revealed that TiB_2 particles surrounded with W containing phase, which is not present in the XRD results. In the 50/50-BM, very small and localized W containing phase increased with the addition of WC in 50/45/5-BM sample. High energy milled sample also contains two different layers with different W amounts. These analyses show the significant grain size reduction with high energy milling. SEM and XRD analyses of the samples were done for two principal directions with respect to pressing direction. These analyses showed that there is a slight texturing present in the hot pressed samples, which is not observed in R-SPS'ed sample. XRD results were used for determining possible Ti-W-B solid solution and present phase is determined as $(Ti_{1-x}W_x)B_2$, and this result is supported with different TEM analyses.

TEM analyses of starting powders after milling and sintered samples were done to reveal the composition and to understand the formation mechanism of W containing $(Ti_{1-x}W_x)B_2$ phases. According to these analyses core/double rim structure found to be

present in both the 50/50-BM and 50/50-HEM samples, but, there was a single rim present in the 50/45/5-BM sample with higher W amount compared to others according to EDX results. TEM-PED analysis used for the phase verification of rim structure and all rims were verified as $(Ti_{1-x}W_x)B_2$ with different x values and these results also showed that core and rim structure aligned in the same direction. According to these results core/rim structure formation mechanism was explained.

Mechanical properties were measured by hardness test for different directions in order to see the effect of texture, however, the mechanical properties were measured to be close to each other and can be concluded that samples have almost isotropic mechanical properties.

6. CHARACTERIZATION OF β-SiAlON/cBN COMPOSITES

6.1. Introduction

Silicon nitride (Si_3N_4) is one of the important engineering ceramic due to its superior mechanical properties and they used in wide range of applications such as ball bearing, nozzles, spark plugs, cutting tools etc. Properties of Si_3N_4 ceramics such as higher hardness and better sinterability can be improved with the formation of SiAlON solid solution with the substitution of Si and N with Al and O elements, respectively without changing Si_3N_4 crystal structure.

SiAlON ceramics can be divided into two groups depending on the chemical formula (and also starting composition), that is α and β-SiAlON. β-SiAlON chemical formula can be expressed as $Si_{6-z}Al_zO_zN_{8-z}$ ($0<z\leq4.2$) [102]. α-SiAlON is formed with incorporation of rare earth elements, which also act as stabilizer, into structure and general formula of its expressed as $M_xSi_{12-(m+n)}Al_{m+n}O_nN_{16-n}$ (x=m/v) and v is the valance of cation M^{+v} [103]. Difference between α and β-SiAlON ceramics is not only limited with chemical composition but also morphologies are different. α-SiAlON grains are mostly equiaxed and small, but β-SiAlON grains are elongated with high aspect ratio. Advantage of α-SiAlON ceramics is the higher hardness values compared with β-SiAlON ceramics; however, due to the grain morphology β-SiAlON ceramics have higher strength and toughness compared to α-SiAlON ceramics.

In order to improve mechanical properties and wear performance of SiAlON ceramics, several approaches are tried and one of them is the incorporation of various additives such as diamond, cBN, SiC, TiC, TiB_2, ZrB_2, etc. into SiAlON matrix [104-106]. Cubic boron nitride (cBN) is one of the promising additive for the SiAlON matrix due to its unique properties, such as superior hardness, excellent oxidation resistance, thermal conductivity and chemical inertness [103, 107]. In the literature, it was reported that cBN addition into SiAlON matrix provides improved hardness as well as fracture toughness due to weak bonding between phases that provides intergranular crack deflection [102, 103, 107]. One of the main drawback of using cBN additive is the sintering of composite structure. Sintering of cBN requires high temperatures and ultra-high pressures (above 5GPa) to prevent transformation of cBN into hBN phase while obtaining high density material. Sintering at moderate pressure values (<5 GPa) above 1300°C resulted in transformation into hBN phase [108]. Hot pressing and spark plasma sintering (SPS) method is used for densification of SiAlON and its composites; however,

due to rapid heating and short sintering times SPS can be preferred. Fast sintering is important especially for the cBN incorporated SiAlON composites to prevent/minimize formation of relatively softer hBN phase. Even though SPS provides fast sintering, phase transformation of pure cBN into hBN starts about 1550°C during SPS [102, 107].

In the literature, there are several studies about sintering of cBN added α and β-SiAlON and their properties. There are several studies about sintering and mechanical properties of β-SiAlON/cBN composite. According to these studies cBN phase transformation within β-SiAlON matrix starts at the similar temperature as pure cBN, however due to the liquid phase formation, as a result of eutectic reaction between SiO_2-Al_2O_3, phase transformation rate was increased [102, 107]. Promotion of phase transformation with the presence of liquid phase can be concluded as dissolution and precipitation is the main phase transformation. It should be noted that in these studies there were no additional liquid phase former sintering additives such as Y_2O_3 were added to the composite.

In the literature it was also found that relative density of β-SiAlON-cBN composite structure is dependent to the cBN content and above 40 vol% cBN addition relative densities significantly reduced due to low sinterability of cBN because of low self-diffusion coefficients and strong covalent bonding [102]. In all these studies in the literature, cBN addition increased the hardness of composite compared to pure SiAlON whether it is α or β-SiAlON. The advantage of the use of Y-α-SiAlON compared to β-SiAlON with cBN particles is improved hardness of composite structure [103].

Among Y-α-SiAlON/cBN and β-SiAlON/cBN composite systems, detailed microstructural analyses were done only for Y-α-SiAlON/cBN system by using SEM, TEM, Raman spectroscopy to try to understand the transformation mechanism and microstructure of composite.

About the phase transformation mechanism, two routes were proposed for Y-α-SiAlON/cBN system; one mechanism was the direct transformation of cBN into hBN phase at the surface of cBN particles and second mechanism was the dissolution and precipitation mechanism [108]. Due to the lack of evidence (and detailed studies) about the direct transformation (of cBN into hBN phase) mechanism and morphology of the hBN particles, that is an equiaxed instead of typical platelet morphology, supports the second proposed dissolution and precipitation mechanism [105]. According to this mechanism, metastable cBN phase is dissolved within the liquid phase formed during

sintering and precipitated as stable hBN phase according to the (6.1. These studies also revealed that increasing the sintering temperature resulted in thicker transformation layer.

$$Si_3N_4 + 2B_2O_{3(l)} \rightarrow 4hBN + 3SiO_{2(l)} \, (\Delta G \, @1600°C = -291 \, Kj/mol) \quad (6.1)$$

Recent study [109] about the stability of cBN revealed that B_2O_3 must be present around cBN particles for the hBN transformation if there is no any other liquid phase is present. Same study also investigated the effect of liquid phase with the same composition as SiAlON sintering additive liquid phase and it showed that with the melting of oxide mixture at 1400°C, hBN transformation starts and if B_2O_3 is added to this mixture transformation rate increases. This study clearly showed that even if there is no B_2O_3 present around the cBN particles or within liquid phase, hBN transformation occur with solution-precipitation mechanism within the Y-Si-Al-O liquid phase.

There are several aims for this study. One of them is the detailed characterization of β-SiAlON/cBN composite microstructure by using SEM, TEM and Raman spectroscopy. Other aim is the characterization and phase mapping of transformation layer since there is no direct evidence that the all the transformation layer around the cBN particle is hBN phase. Final one is the orientation characterization between cBN and hBN phases to search for the question of *"Is there any orientation relation between cBN and hBN?"* which might be an evidence for direct transformation of cBN.

For these purposes characterization of β-SiAlON/cBN sample was done with SEM and (S)TEM methods. The sample was produced at 1650°C (with 200°C/min heating rate) for 3 minutes under 50 MPa pressure in SPS. Before sintering, starting powders (Si_3N_4, Al_2O_3, AlN, Y_2O_3 and cBN) were mixed with 50 vol% in alcohol with planetary ball milling for homogenization then dried and sieved (with 300 μm sieve). Raman spectroscopy studies were conducted with WITec Alpha 300R with 532nm wavelength laser at 50mW power from SEM sample.

6.2. Results and Discussions

6.2.1. SEM investigations

Produced samples first investigated with SEM to understand the general microstructure with back-scattered electron (BSE) mode. During SEM studies, variable

pressure mode was used to prevent charging of non-conductive samples without having conductive coating e.g. gold/palladium, which can lead to contrast decrease between, phases. SEM samples were prepared with conventional mechanical polishing followed by low angle (4° at 6kV for 30 minutes) Ar ion beam milling for contrast enhancement. Figure 6.1 shows the overall microstructure and it can be seen that cBN particles are homogeneously distributed in the β-SiAlON matrix. It can be also seen that between some of the cBN particles large liquid phase pockets are located. During sintering liquid phase was forced to infiltrate between cBN particles with applied pressure. Higher magnification image of one of these liquid phase pockets showed that exaggerated grain growth of β-SiAlON grains was occurred due to lack of any solid constrained that limits the grain growth in both a and c axes.

According to the SEM images (Figure 6.2) it can be seen that transformation layer is present almost all of the cBN particles without any surface selectivity. In the literature it was reported that, phase transformation occurs only for non-flat, rough surfaces in α-SiAlON/cBN composites [108]; however, this is not true for samples investigated in this study. EDX analyses of the transformation layer around the cBN particles confirms the B and N content; however, due to the interaction volume of electron, X-rays were generated both from surrounding cBN, liquid phase and β-SiAlON phases. In addition to this spectrum obtained from cBN particles was also contains Si, Al, and O elements from underneath β-SiAlON. Therefore, chemical composition of this layer should be investigated with thin sample in TEM to prevent interaction volume effects.

Figure 6.3 shows the SEM-BSE and SEM-Inlens image of the same region, due to the electron channeling effect and surface signals visibility of the transformation layer is significantly improved. However, due to non-uniform sputtering occurred during ion milling surface of the sample was not perfectly parallel, sputter rate of very hard cBN particles was very low and this creates “hills” at the center of cBN particles. Presence of these cBN “hills” causes shadowing effect in SEM-Inlens images that is very sensitive to surface topography especially in VP mode. Further ion milling can reduce surface topography and improve the SEM-Inlens imaging quality.

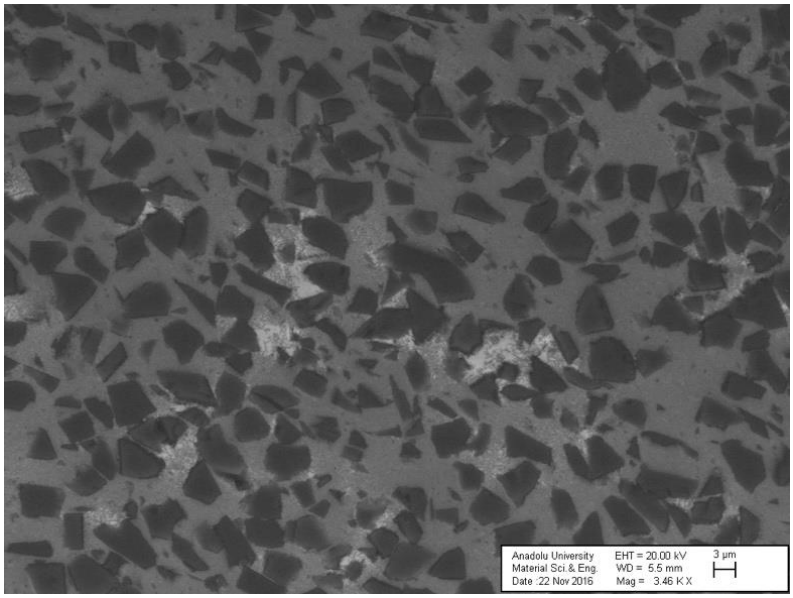

(a)

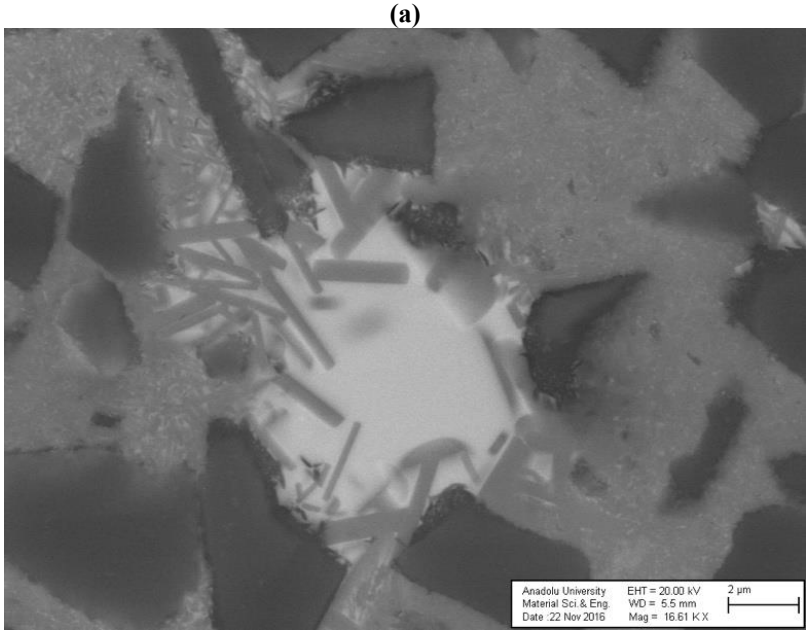

(b)

Figure 6.1. *(a) Low magnification SEM-BSE image for the visualization of overall microstructure and (b) higher magnification image of the liquid phase pockets trapped within reinforcement particles*

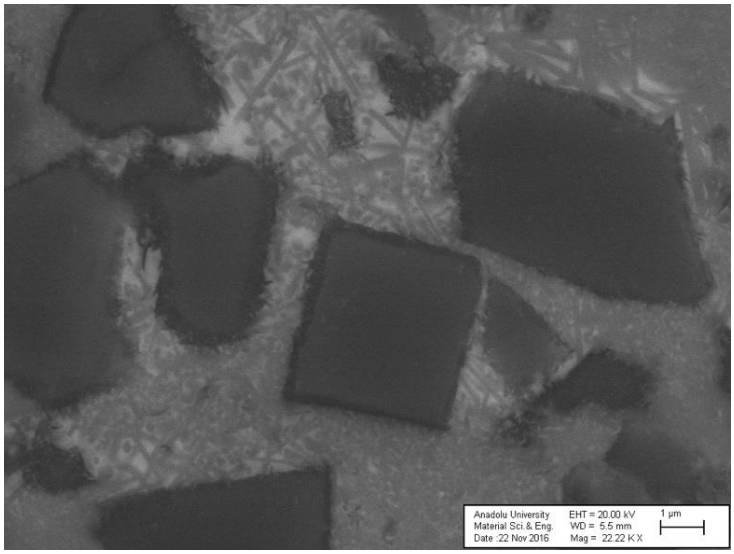

(a)

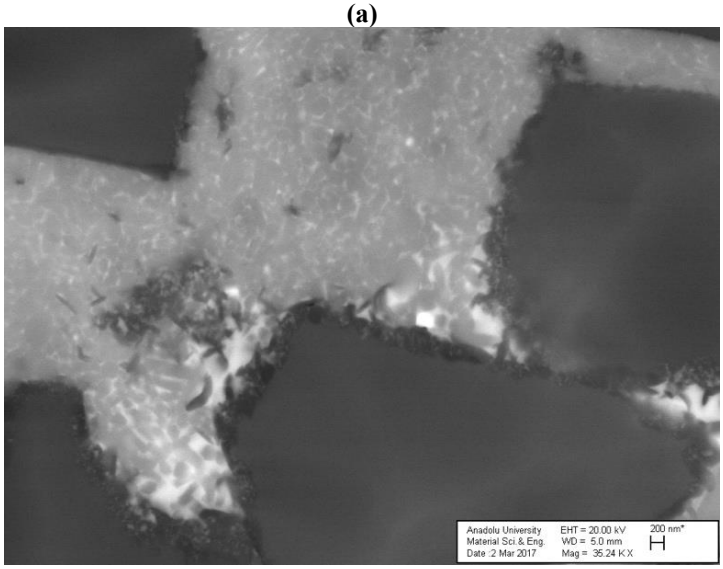

(b)

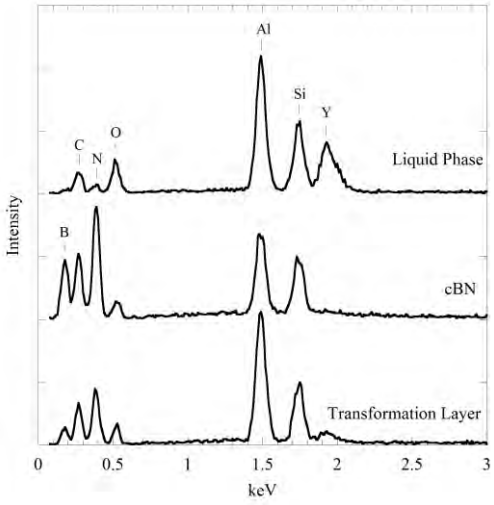

(c)

Figure 6.2. *Transformation layer around cBN particles from (a) mechanically polished sample, (b) mechanical polishing followed by ion beam processing and (c) EDX spectrum obtained from transformation layer, cBN and liquid phase*

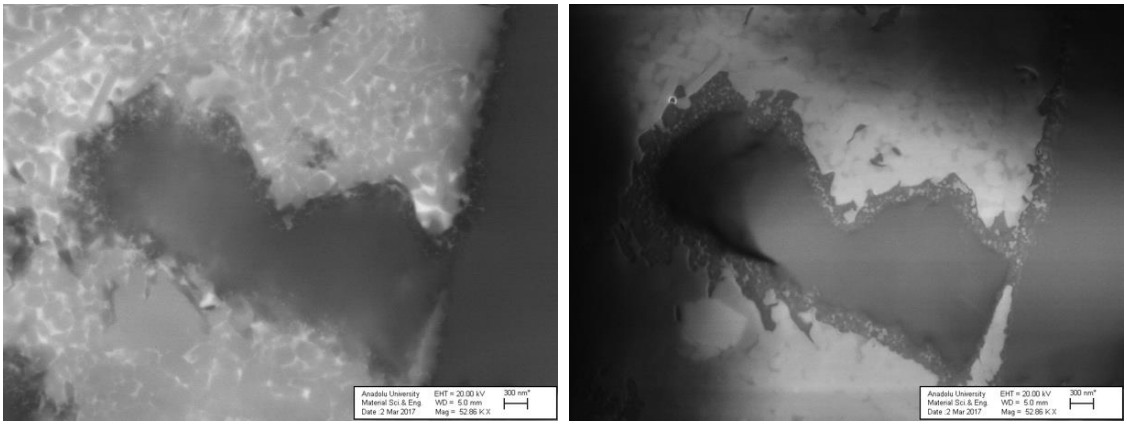

(a) **(b)**

Figure 6.3. *(a) SEM-BSE image and (b) SEM-Inlens image of cBN particle with surrounding transformation layer*

6.2.2. (S)TEM and PED investigations

TEM studies showed that there is a ~200-300 nm thick transformation layer around cBN particles and transformation layer is surrounded with liquid phase and β-SiAlON particles as shown in Figure 6.4. Morphology of the grains in transformation layer have two distinct characteristics according to its position within the layer. The grains, which are close to liquid phase (which are formed at the first) have conventional plate-like hBN morphology; however, as it closed to cBN particle morphology is transformed from plate-like to smaller and irregular, random morphology. This morphology change can be explained with the following theory; in the beginning of phase transformation there is only liquid phase around the cBN particle and formed hBN particles do not have any constrain around them and they can be grow into liquid phase freely. With time, more cBN transformed into hBN phase; however, hBN particles that are formed at the very beginning of phase transformation, constrain plate-like growth of newer particles. In addition to this, a volume expansion during cBN to hBN transformation [108] can be another constrain. Lastly, externally applied pressure during SPS can cause additional constrain which hinder growth of plate-like morphology.

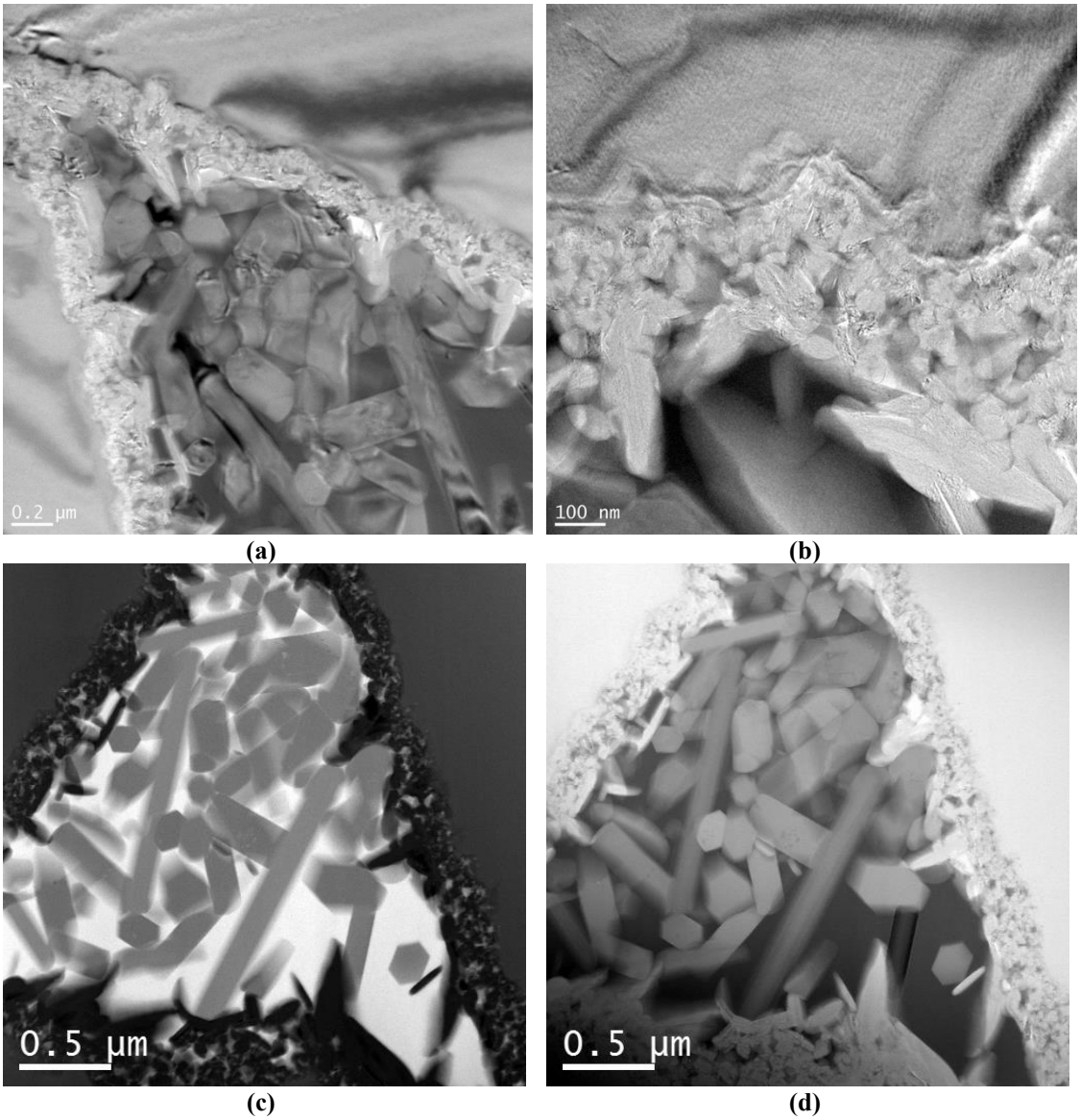

Figure 6.4. *(a) TEM-BF image showing overall microstructure, (b) higher magnification TEM-BF image showing two different morphology within transformation layer, (c) STEM-HAADF and (d) STEM-BF images of (a)*

Another approach could be the change of morphology during continuous growth. In the transformation layer, it was found that hBN grains, which were closest to the cBN particle, were in (0002)//e^- orientation as shown in Figure 6.5(b) and Figure 6.6(c). According to this finding, it can be concluded as; after precipitation, growth of hBN particles occur along the a-axis. However, during growth, due to volume expansion and limited space because of surrounding particles, which act as constrains, hBN particles were forced to be curled as they move away from starting point as shown in Figure 6.5(c). Based on these observations, following assumption can be concluded. If there is only liquid phase around cBN particle, hBN growth can be observed without any curling and

straight hBN planes can be observed. This assumption needs to be confirmed; however, these findings supports the first theory stated above for the morphology change within transformation layer. In the literature [105] it was mentioned that these particles could be turbostratic BN (tBN); however, tBN morphology was not present according to these images.

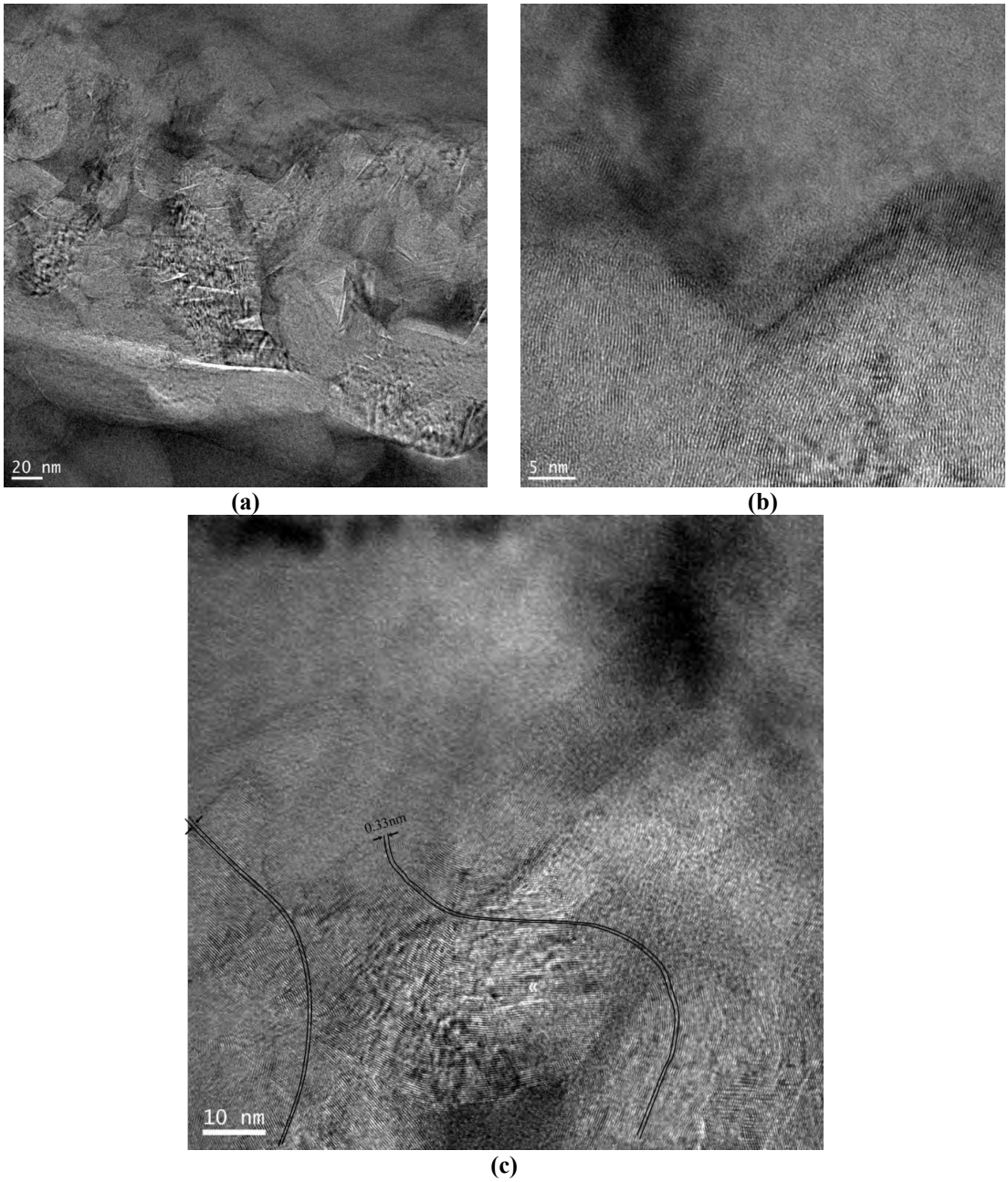

Figure 6.5. *(a) low magnification and (b) higher magnification TEM-BF images of transformation layer showing (0002)//e^- hBN planes at surface of cBN and (c) TEM-BF image showing continuous and curled hBN layers. Drawings show the hBN route but it should be noted that they are dramatized for better visualization*

The rough surface of cBN particles shows that there is a reaction front with “attack” of liquid phase and supports the theory of solution-precipitation for the hBN formation. During sintering surface of the liquid phase start to react with cBN and according to (6.1), hBN transformation starts. During phase transformation, liquid phase continues to penetrate between not only cBN and hBN layers but also transformed hBN particles with the application of pressure during SPS. Liquid phase in between hBN and cBN continues to “attack” cBN phase during sintering and resulted in phase transformation. Figure 6.6 shows the presence of liquid phase between cBN and hBN, and surface morphology of cBN supports the phase transformation theory stated above which is in a good agreement with literature. According to this theory, if enough time will be given during sintering, all cBN particles can be transformed into hBN phase vice versa shorter sintering times will reduce or prevent this transformation. The irregular shape of cBN-hBN interface point out that transformation does not have any preferential orientation, instead it can be random due to this morphology.

STEM-EDX analyses showed that chemical composition of transformation layer almost the same with cBN particle as shown in Figure 6.7. The only difference is the presence of very low amounts of Si, Al and O due to the surrounding liquid. Same figure also shows the spectra for Si-Al-O-Y containing liquid phase and β-SiAlON phase. According to these spectra, liquid phase is rich in Y element; on the contrary, β-SiAlON particle does not contain any Y element within its structure. STEM-EDX analysis also proved that liquid phase present around grains within transformation layer. Figure 6.8 also shows the STEM-EDX elemental map for B-K, N-K, Al-K, O-K, Si-K and Y-K peaks.

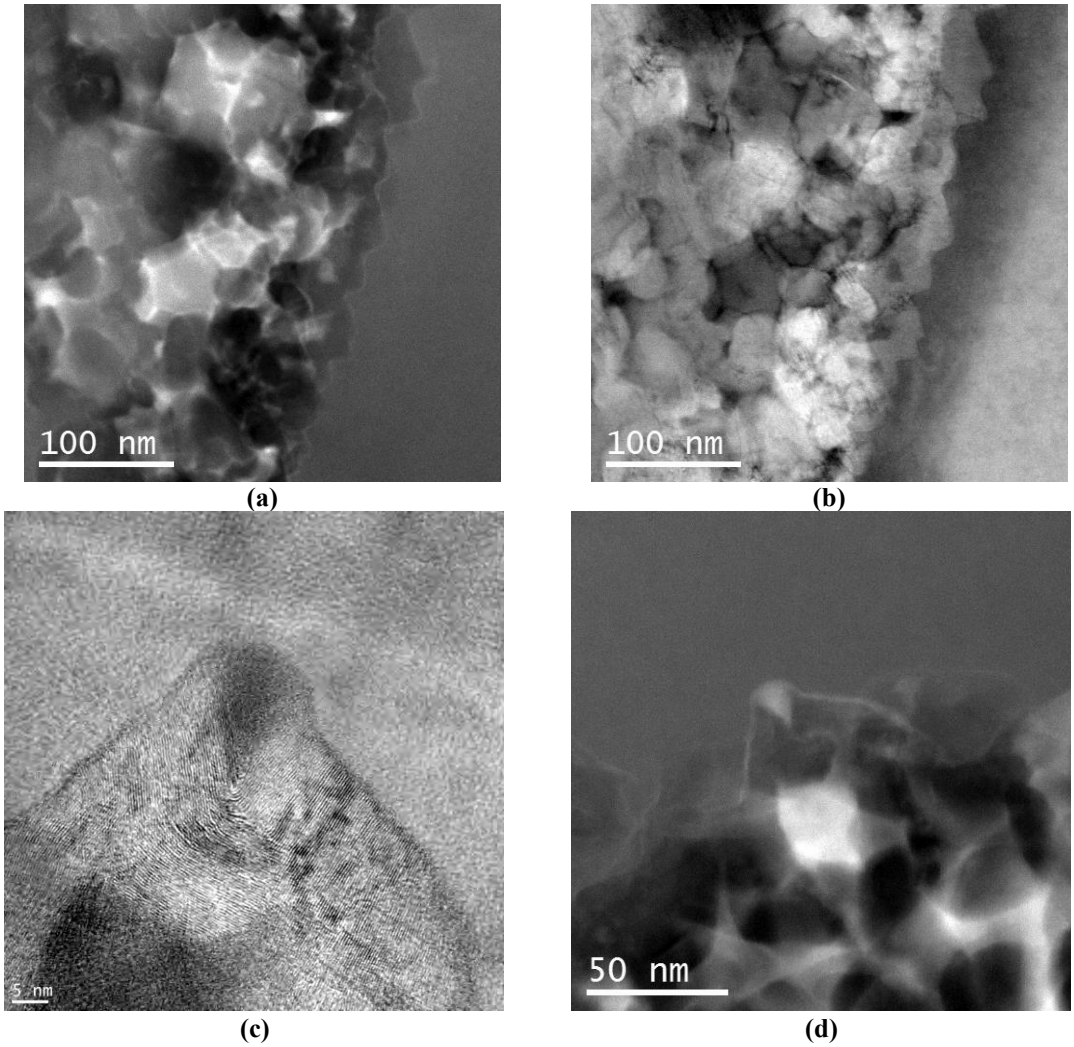

Figure 6.6. *(a) STEM-HAADF, (b) STEM-BF and (c) higher magnification TEM-BF and (d) STEM-HAADF images showing the cBN and hBN phases with liquid phase at their interface*

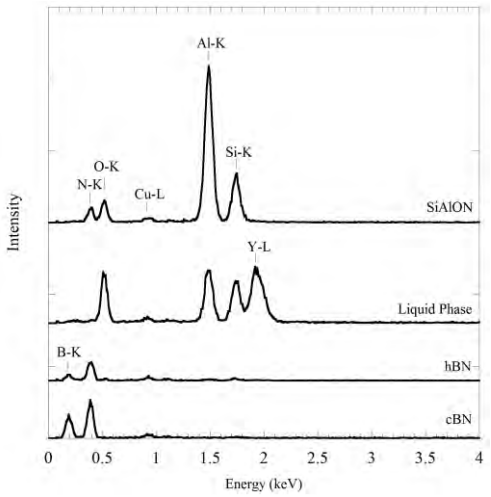

Figure 6.7. *EDX spectra taken from present hBN, cBN, SiAlON and liquid phases in the microstructure*

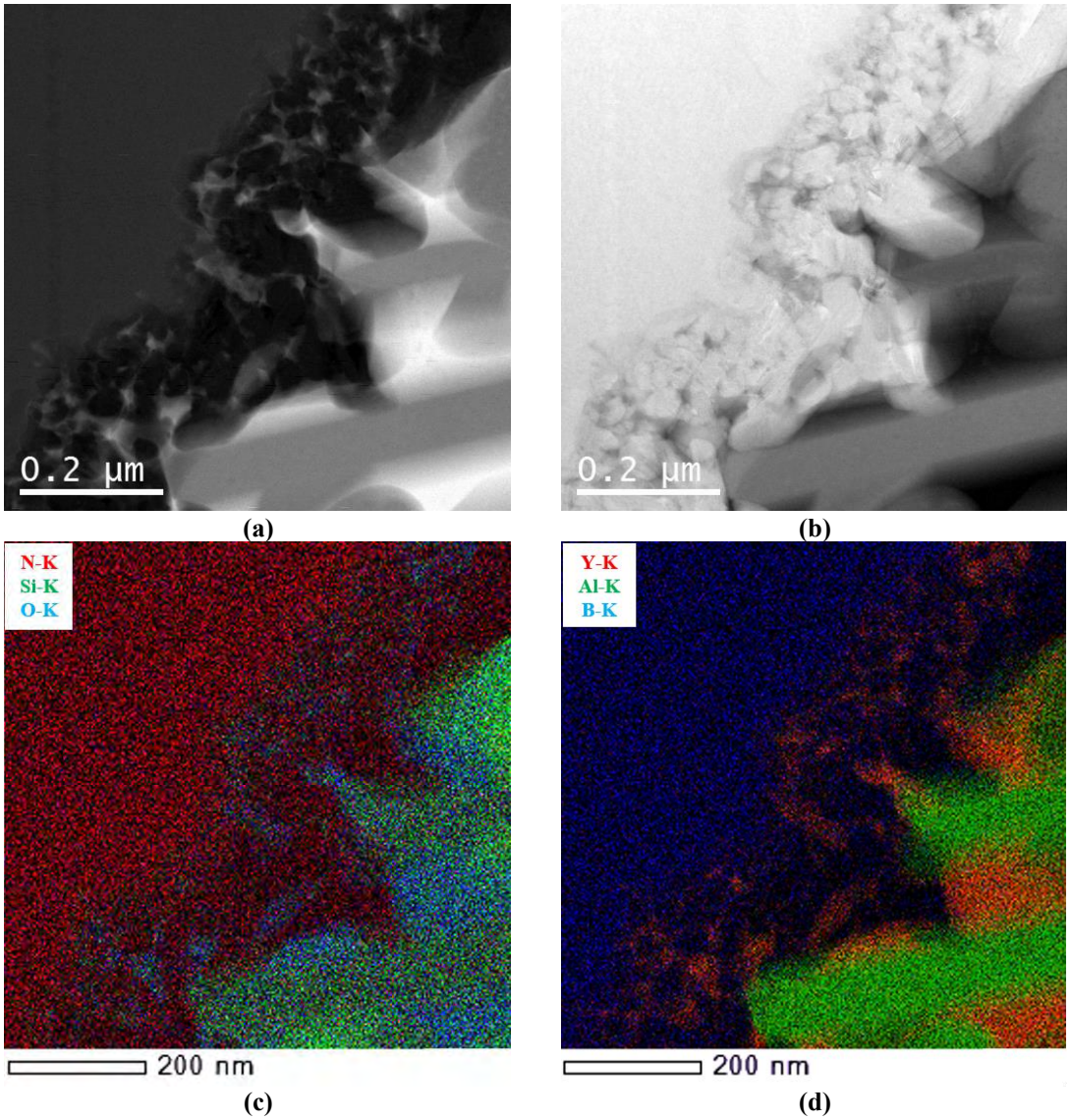

Figure 6.8. *(a) STEM-HAADF, (b) STEM-BF and RGB composite images for (c) N-K, Si-K, O-K and (d) Y-K, Al-K, B-K EDX maps*

EELS analysis can be used for the identification of phases with different crystal structure but the same composition like BN as explained in Section 8. hBN phase has characteristic peak at 190 eV belonging to π peak which is not present in cBN structure. EELS results (background subtracted signal) obtained from transformation layer and cBN particle is given in Figure 6.9. This figure clearly showed that transformation layer is hBN.

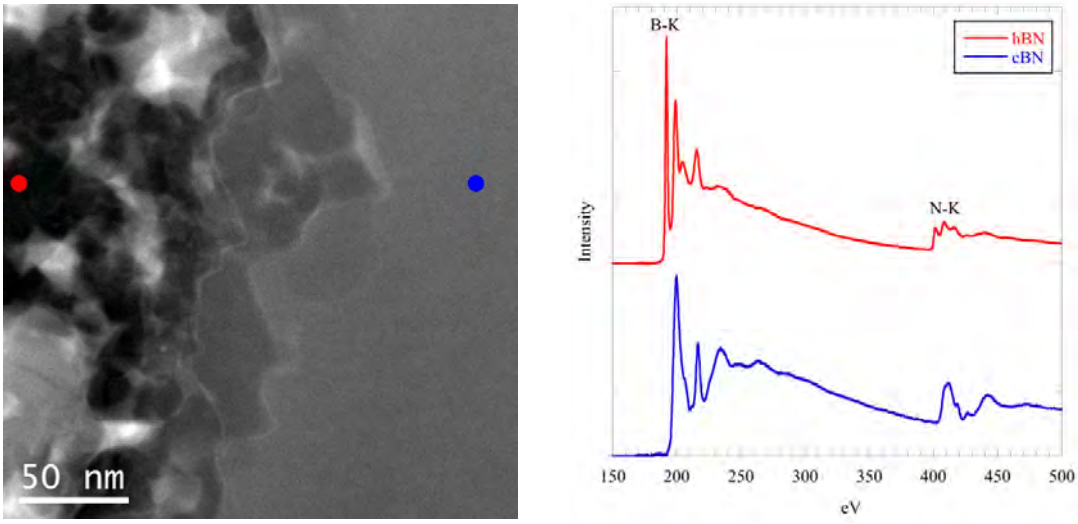

(a) (b)

Figure 6.9. *(a) STEM-HAADF image showing color coded EELS analysis points and (b) STEM-EELS results showing stripped B-K and N-K peaks obtained from cBN particle and surrounding hBN transformation layer*

Phase mapping was done with STEM EELS Spectrum imaging (STEM-SI) by using characteristic π peak of hBN by placing an energy window at 192eV with a width of 2eV (after background subtraction according to power law) for hBN mapping. Same process was also applied for cBN mapping by same energy window to 198eV. Figure 6.10(a) shows the STEM-SI region of interest (ROI) and spatial drift corrector ROI during analysis. The intensity variations in filtered STEM-SI images were caused by the non-homogeneous thickness of the sample; from top to the bottom of SI ROI sample thickness decrease and as a result of this EEL spectrum intensities were decreased.

Phase mapping was also done with TEM-PED method. In TEM-PED method during automated template matching process, software identifies the phase with highest indexing score at given pixel; however, this matching algorithm methodology starts to fail or unreliable for overlapping phases as in this hBN-cBN case, since indexing software was programmed to give only one solution. Figure 6.11 shows the phase map (obtained with TEM-PED method) for the same region given in Figure 6.10 and when these two figures are compared, overlapped region can be distinguished easily. In the phase map obtained with TEM-PED method, higher diffraction pattern intensities for cBN phase within overlapped region (outlined with white dashed line) resulted in higher index score, therefore this region was identified as cBN even if it also contains diffraction spots from hBN crystals. Figure 6.11 (c-e) shows the diffraction spots taken from cBN, overlapped region and hBN (from regions 1, 2 and 3), respectively. Advantage of the STEM-SI

imaging over TEM-PED phase mapping is the improved phase identification for overlapped cBN-hBN regions.

Due to the presence of characteristic EELS peak that belongs to hBN phase, STEM-SI phase mapping was successfully applied to distinguish hBN-cBN phase difference compared to TEM-PED method; however, the success of these methods could vary depending on different variables such as crystal and electronic structures, bonding type etc.

Based on Figures Figure **6.5** and Figure **6.6**, it was seen that hBN particles at the surface of cBN particle are in $c \perp e^-$ ($a // e^-$) direction and these hBN particles point out the possibility of growth in preferred orientation during phase transformation (it can also be said that during precipitation and growth process).

In the literature, it is reported that sintering methods involving application of uniaxial pressure with heating, like SPS or HP, hBN particles can be textured [83, 110]. According to these studies, randomly oriented hBN particles rotated during sintering and aligned as a-axis parallel to pressing direction. In addition to that, also grain growth occur along pressing direction. When this behavior is considered, it is possible to have an influence of applied pressure during SPS on hBN growth direction. However, there is a big difference between the works on literature and this study. In the literature, studies showed the effect of pressure on grain growth of existent hBN particles but in this study hBN particles are formed (by precipitation) during application of pressure and heat. Samples investigated in this study prepared without taking into consideration the effect of pressing direction, thus relative pressing direction on the sample was unknown. Therefore, to confirm the effect of pressure on the growth direction, extensive studies should be carried out with samples prepared from the different directions.

TEM-PED method was also utilized for the orientation mapping of cBN and hBN phases in order to investigate the presence of any orientation relation occurred during phase transformation. According to the orientation mapping results it was found that there was not a specific orientation relation between cBN and hBN phases. One of the reason for this was the overlapped region, which indexed as cBN, covers the cBN-hBN intersection. Another reason was the formation mechanism that was solution-precipitation from liquid phase cancel the effect of cBN orientation.

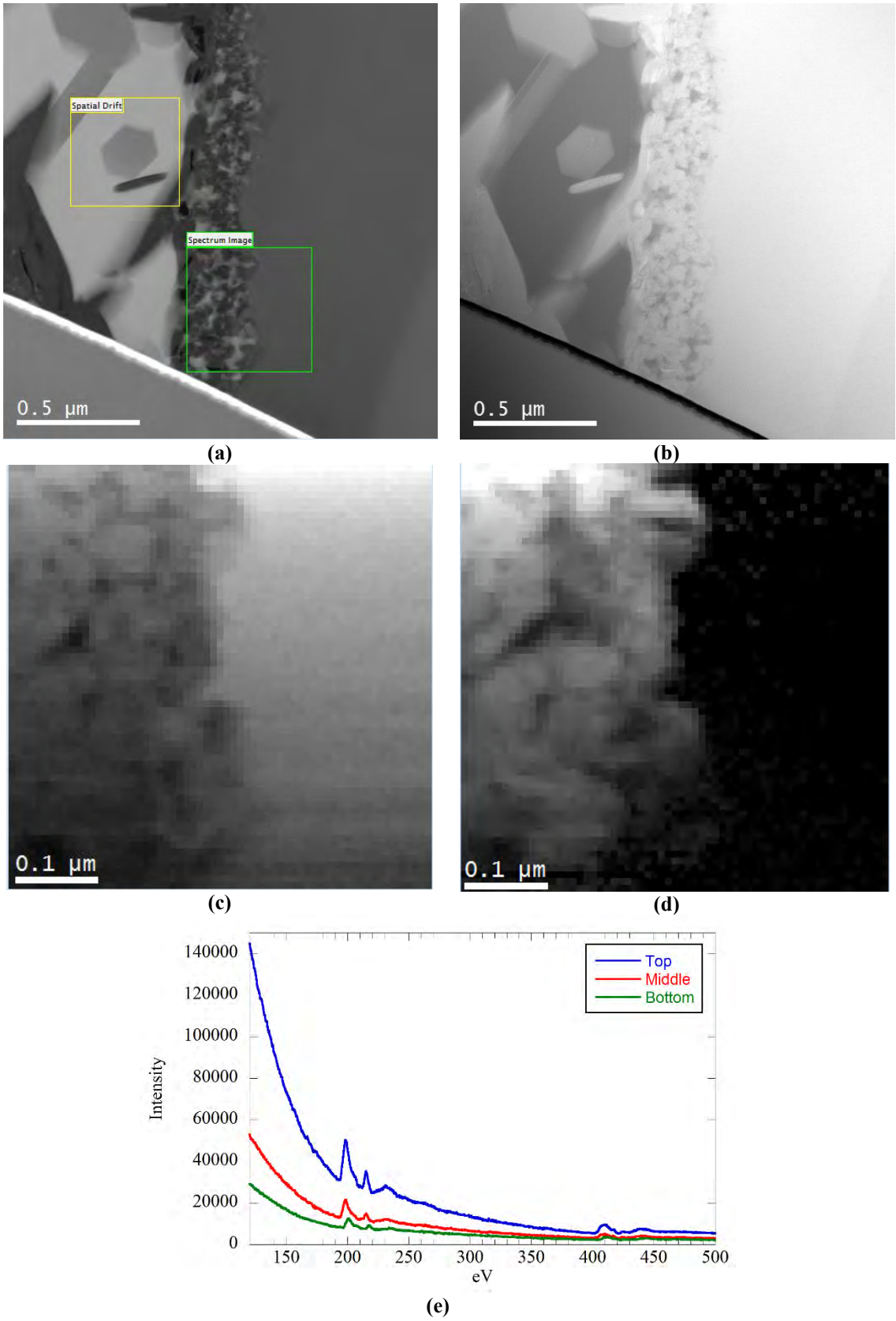

Figure 6.10. *STEM-HAADF image sowing SI ROI and spatial drift ROI, (b) STEM-BF, (c) energy filtered (c) cBN and (d) hBN maps and (e) EEL spectra taken from top, middle and bottom regions of cBN particle showing the intensity variation. (STEM-SI image was obtained with 7nm per pixel at 0.5s acquisition time per pixel)*

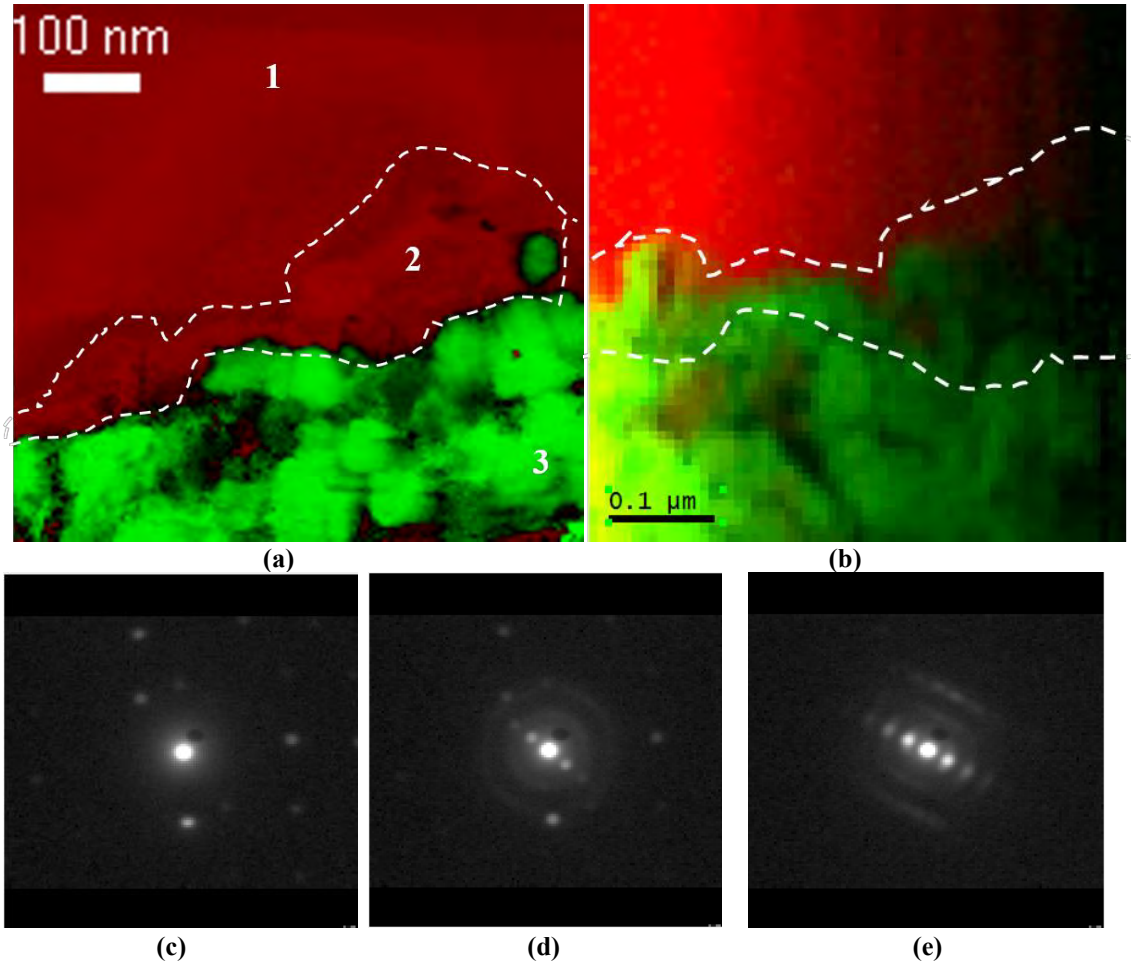

Figure 6.11. *(a) Phase map combined with phase reliability image obtained with TEM-PED method, (b) combined hBN and cBN map obtained from STEM-SI, diffraction patterns obtained from (c) region 1, (d) region 2 and (e) region 3*

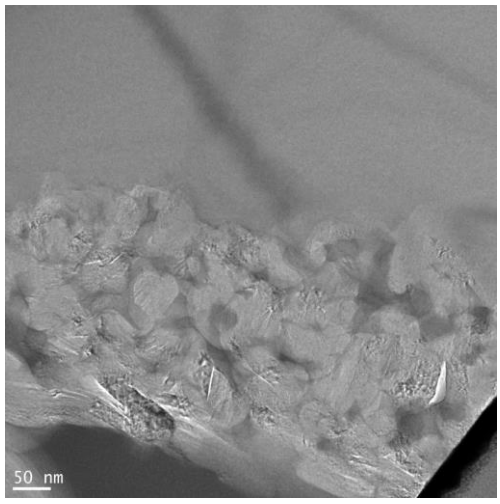

Figure 6.12 *(a) TEM-BF, (b) STEM-HAADF, (c) STEM-BF, (d-f) Orientation maps combined with reliability for x, y and z directions, respectively, (g) index and (h) reliability maps, (i) vdf for hBN and (j) vdf for cBN (phase map is given above)*

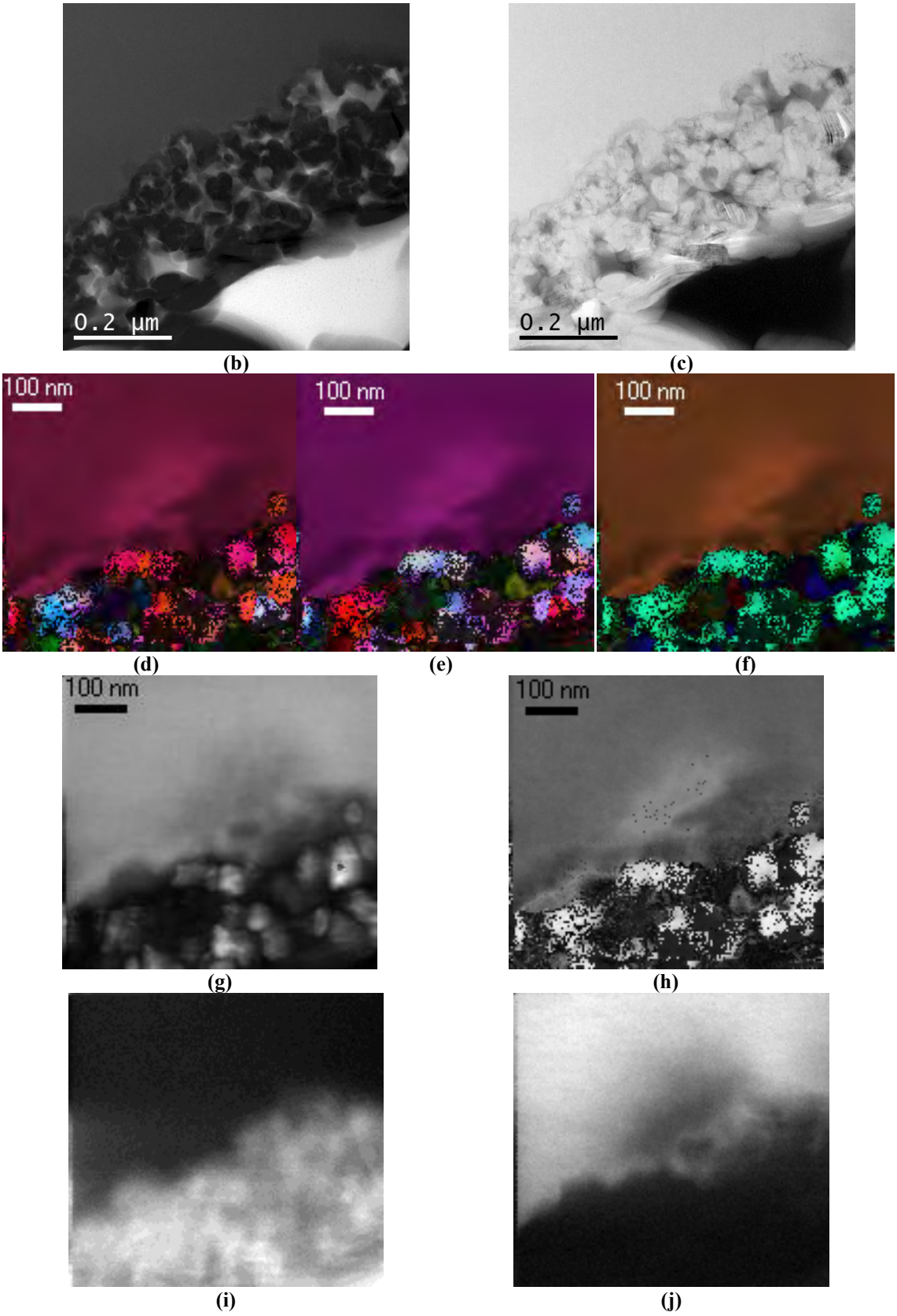

Figure 6.12. (Continued) *(a) TEM-BF, (b) STEM-HAADF, (c) STEM-BF, (d-f) Orientation maps combined with reliability for x, y and z directions, respectively, (g) index and (h) reliability maps, (i) vdf for hBN and (j) vdf for cBN (phase map is given above)*

Even though there was not any cBN-hBN relation, according to the hBN pole figures additional feature related to hBN orientations was obtained. The hBN ($11\bar{2}0$) and (0001) pole figures, given in Figure 6.13, support the orientation found in TEM images given in Figure 6.5 and Figure 6.6. As it can be seen from those images, (0002) planes of hBN are parallel to the electron beam direction (in other words ($11\bar{2}0$) plane normal is parallel to the e^- beam and (0002) plane normal is perpendicular to the e^- beam) and due to the buckling of these planes direction of c-axis (and of course (0002) plane normal) changes. It is worth to note that these pole figures are formed with hBN particles having reliability values above 15. Based on these pole figures and images, hBN growth occurs along a-axis from the surface of liquid phase and due to the constrain forced by surrounding particles, buckling of these layers occur during growth.

Orientation of hBN layers can be explained with the synthesis mechanism of hBN. Synthesis of hBN from boric acid and urea is a widely used method and in this method, hexagonal nucleus formed with NHBOH monomers and this reaction resulted in open H and OH groups around hBN ring. hBN growth occurs with attaching B and N atoms with replacement of H and OH groups along a-axis [111]. Similar hBN growth mechanism was also present on the surface of diamond with sputtered B and N. Once hBN nucleated at the surface of diamond, BN hexagonal ring formed by attached B and N atoms and it grows as nanosheet in a direction parallel to basal the plane, thus hBN grow occurs parallel to a-axis instead of c-axis [112]. In a-axis of hBN, there are B and N atoms present at the outer layer of BN ring with incomplete bonds along a-axis and growth occur with attaching B and N atoms to complete bonding, therefore growth in a-axis is energetically favorable compared to c-axis.

There is also a possibility of randomly oriented tBN formation within B-N-O containing liquid phase prior to hBN phase and then it can be crystallized as hBN since in the literature it was reported that tBN can be transformed into ordered hBN above 1500°C [113].

Based on these growth mechanisms and observations shown in Figure 6.5, Figure **6.6** and Figure **6.13**, hBN growth direction along a-axis from liquid phase can be explained in a same manner. Once hBN nucleation occur at the surface of liquid phase, hBN growth occurs by diffusions of B and N atoms from the liquid phase to the hBN nucleus. Since there is no direct evidence for nucleation and growth mechanism, for the observed hBN particles in this study, growth mechanism remains unclear.

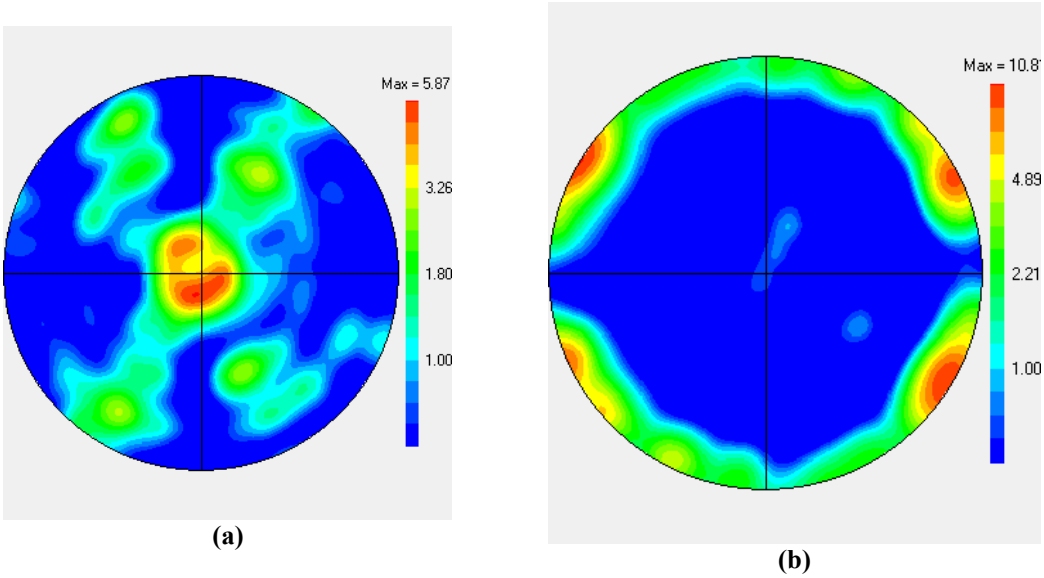

(a) **(b)**

Figure 6.13. *(a) (11$\bar{2}$0) and (b) (0001) pole figures of hBN particles in orientation map given in Figure 6.11*

Figure 6.14 shows the orientation mapping obtained from β-SiAlON region. It shows that elongated particles indexed with different orientations due to the change of intensities on diffraction spots within same grain. This orientation map does not provide any specific orientation related information; however, it clearly showed that TEM-PED method can be applied for the orientation characterization of SiAlON particles which do not have any microscopic orientation mapping study e.g. SEM-(t)EBSD, TEM-PED in the literature.

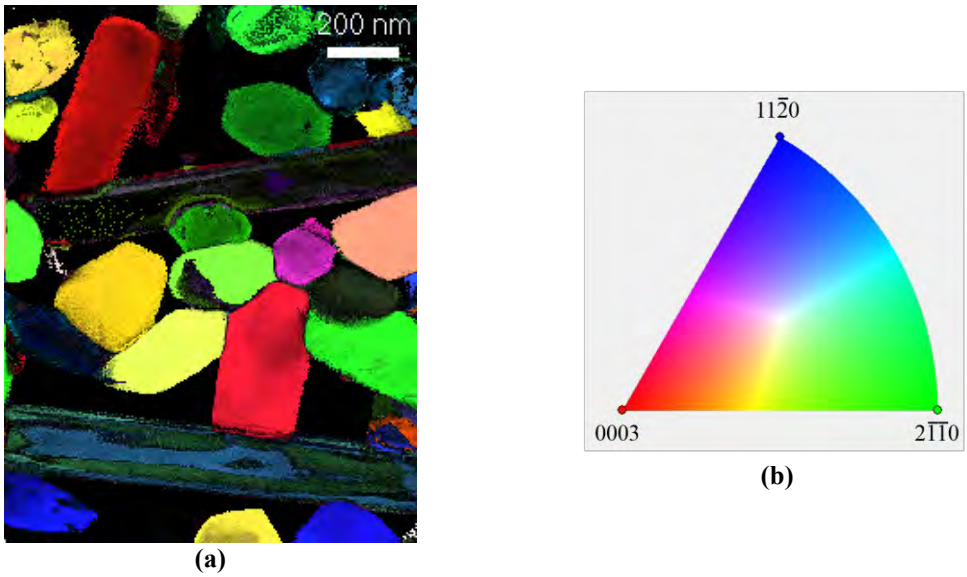

(a) **(b)**

Figure 6.14. *TEM-PED results: (a) Orientation map in x direction combined with orientation reliability and (b) standard triangle for β-SiAlON particles given in Figure 6.4*

6.2.3. Raman investigations

Raman spectrometer was also used for the supplementary phase identification of the transformation layer as [103]. In Raman spectrum, there are characteristic peaks for both hBN and cBN phases at ~1366 cm^{-1} and (~1056, ~1306) cm^{-1}, respectively. Figure 6.15(a) shows the Raman spectra obtained from TEM sample for both cBN and hBN phases. Same figure also shows the Raman line scan result from polished SEM sample. From this line scan hBN and cBN phase map along a line was extracted by filtering the spectra. Filtering process was similar to STEM-SI processing, filtering window with a width of 10 cm^{-1} was placed to 1056 cm^{-1} and 1364 cm^{-1} for cBN and hBN phases, respectively. Phase map along this line showed that hBN phase was formed at both sides of cBN particle. Due to the broad spot size of laser (~200-300nm) at the surface of cBN particle, peaks from both phases were present.

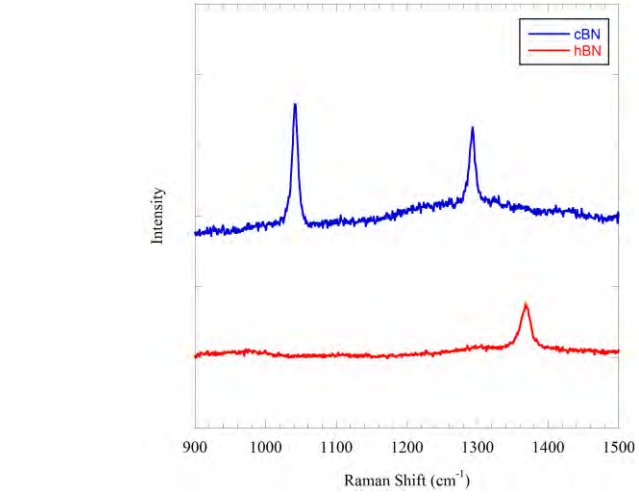

(a)

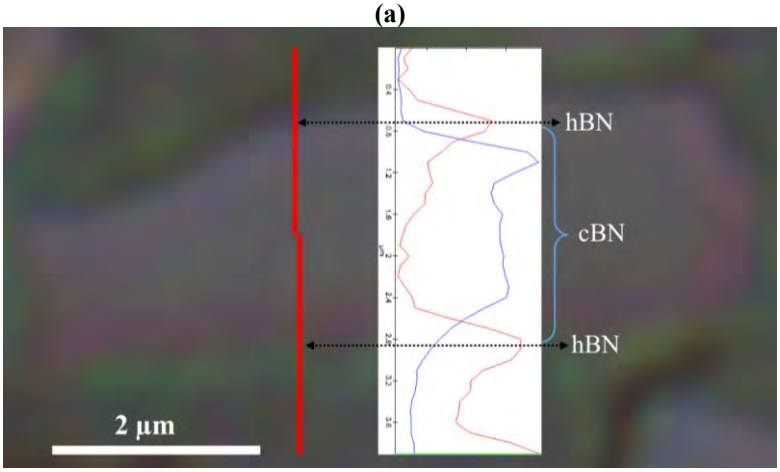

(b)

Figure 6.15. *(a) Raman (spot) spectra obtained from hBN and cBN phases and (b) Raman phase map along a line scan obtained after filtering process*

6.3. Conclusions

i. Phase transformation around cBN particles into low hardness hBN phase can resulted in decreased tool life due to the weak van der Waals bonding between graphitic hBN particles that can cause pull-out of cBN particles during machining process. Because of this reason optimum sintering conditions should be found to prevent phase transformation as well as to obtain high density.

ii. During SEM sample preparation, further ion beam milling can reduce the surface topography due to different sputtering rates in the present phases and SEM-Inlens imaging performance can be increased.

iii. Transformation layer is present at surface of all cBN particles without any surface selectivity. The transformation layer was confirmed as hBN with STEM-EELS, STEM-SI, TEM-PED and Raman techniques.

iv. hBN transformation assisted with liquid phase, from liquid phase hBN particles nucleate and grow along a-axis; however, due to the surrounding particles and volume change, hBN layers can be buckled as they grow and their morphologies changed. Buckling of hBN layers resulted in the overlapped grains in thin FIB lamella.

v. The main disadvantage of TEM-PED method was experienced during this study. Template matching of overlapped crystals can be resulted in unreliable or misleading results. Therefore, additional supplementary analyses should be done. In this section of the thesis, in order to support TEM-PED analyses STEM-SI method was utilized. According to this supplementary method, it was concluded as STEM-SI results were better in terms of phase mapping for the overlapped cBN-hBN phases.

vi. According to the TEM-PED results and TEM images, hBN growth occurs along a-axis of hBN. However, due to the buckling, [0001] direction changes randomly and this is showed by TEM-PED orientation maps.

vii. In this study, it was clearly showed for the first time that orientation mapping can be possible with TEM-PED method for submicron SiAlON particles due to scan area limitations.

viii. Raman spectroscopy can also be used for the phase mapping, however due to the broad spot size of the laser beam, this method is more applicable for microstructures having features bigger than laser spot size.

7. CHARACTERIZATION OF PRECIPITATES IN PETROLEUM STEELS

7.1. Introduction

Steel is one of the most commonly used material for engineering applications like constructions, ships, pressurized tanks, pipes, etc. Steel has wide variety of grades and properties and not every type of steel applicable for all applications. Due to that reason, correct type of steel needs to be selected for a specific application. For example, for the petroleum and natural gas pipeline applications where pressurized fluid is transported for long distances, American Petroleum Institute (API) X70, X80 or X100 steels are used due to their properties such as high strength, fracture toughness, weldability, corrosion resistance and deformability. API steels are ferritic steels and to obtain the desired properties like high strength, this type of steels are micro alloyed with elements such as Nb, Ti and V with precipitation hardening [114]. Properties of API steels, such as toughness, are modified by the thermo-mechanical rolling by tailoring the microstructure, in addition to the micro alloying. Thermo-mechanical rolling of metal is basically series of reheating and rolling processes and during this process grain refinement, which improves the mechanical properties, occurs [115]. During production and rolling processes several precipitates with different compositions can be formed. In the literature, (Ti,Nb)N [116], (Ti,Nb)C [117], Nb(CN) [118] (Ti,Nb)CN [116, 119] precipitates are reported in low carbon steels similar to API steels that are micro-alloyed with Ti and Nb elements. It is important to determine which precipitate is present in the produced steels, because mechanical properties of material may change with the type of the precipitate [120].

7.2. Results and Discussions

In this study API-X70 steel sample was used and it was produced by Ereğli Iron and Steel company with thermo-mechanical rolling, Turkey. The composition of that steel was taken from the company and given in Table 7.1. TEM sample was produced with conventional mechanical thinning followed by an Ar-ion beam milling. Characterizations of the precipitate particle were done by TEM/STEM imaging methods combined with EDX and PED.

Table 7.1. *Composition of API-X70 petroleum steel. The rest is Fe [121]*

Elements (wt %)						
C	***Mn***	***Si***	***P***	***S***	***Al***	***Ti***
0.08	1.6	0.15	0.01	60 ppm	0.01	0.008
Ca	***N***	***Cu***	***Ni***	***Nb***	***Mo***	
0.002	0.004	0.03	0.2	0.09	0.24	

7.2.1. TEM/STEM and TEM-PED results

TEM and STEM analyses showed that there is a precipitate particle with a non-equiaxed morphology with 2:1 (100 : 50 nm) aspect ratio within the ferrite grain. Figure 7.1 (a) shows the TEM-BF image of the precipitate particle. In TEM-BF images it is hard to distinguish the precipitate particles due to the lack of contrast compared with the ferrite matrix, however, STEM-HAADF images easily revealed the precipitate particles due to their different composition. The precipitate particle mainly composed of heavier atoms (like Nb) compared to Fe matrix and this provide significant contrast in STEM-HAADF imaging method.

STEM-EDX (Figure 7.2) analysis for this inclusion showed that it contains Ti, Nb, C and N however when the spectrum from precipitate compared with the matrix which is ferrite, it is hard to distinguish whether this precipitate contains C element or not due to the carbon content of the matrix. In addition, diffraction analysis (Figure 7.3) from the precipitate particle revealed that there are several diffraction spots coming from the matrix phase and this is an indication of overlapped phases. Thus, it is reasonable to have Fe and C peaks coming from ferrite in the EDX spectra of precipitate particle. In order to clarify whether this phase contains carbon or not, phase mapping to this precipitate was done with PED in TEM.

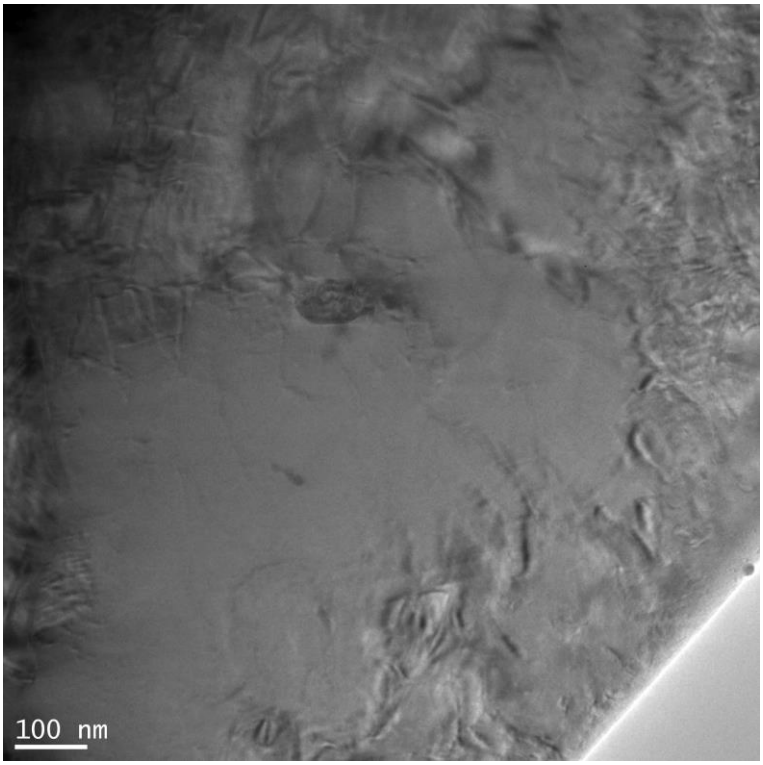

(a)

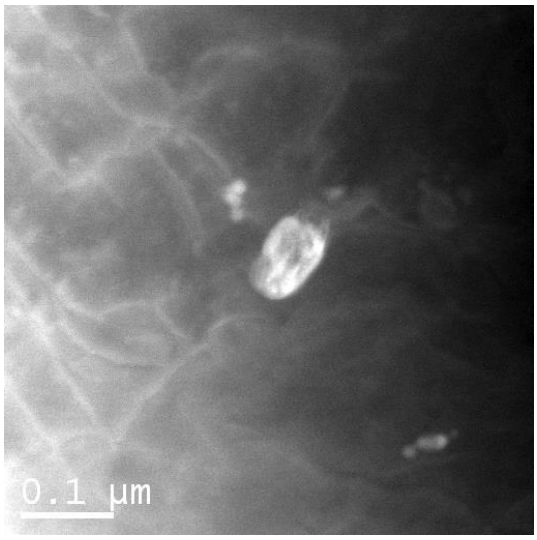

(b)

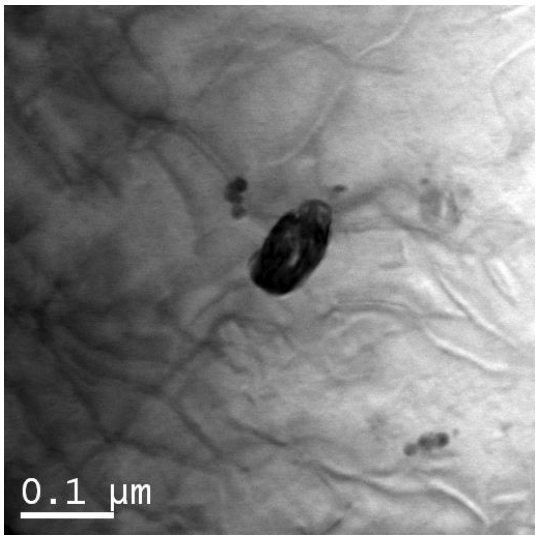

(c)

Figure 7.1. *(a) TEM-BF image of a region with a precipitate, (b) STEM-HAADF and (c) STEM-BF image of the same region*

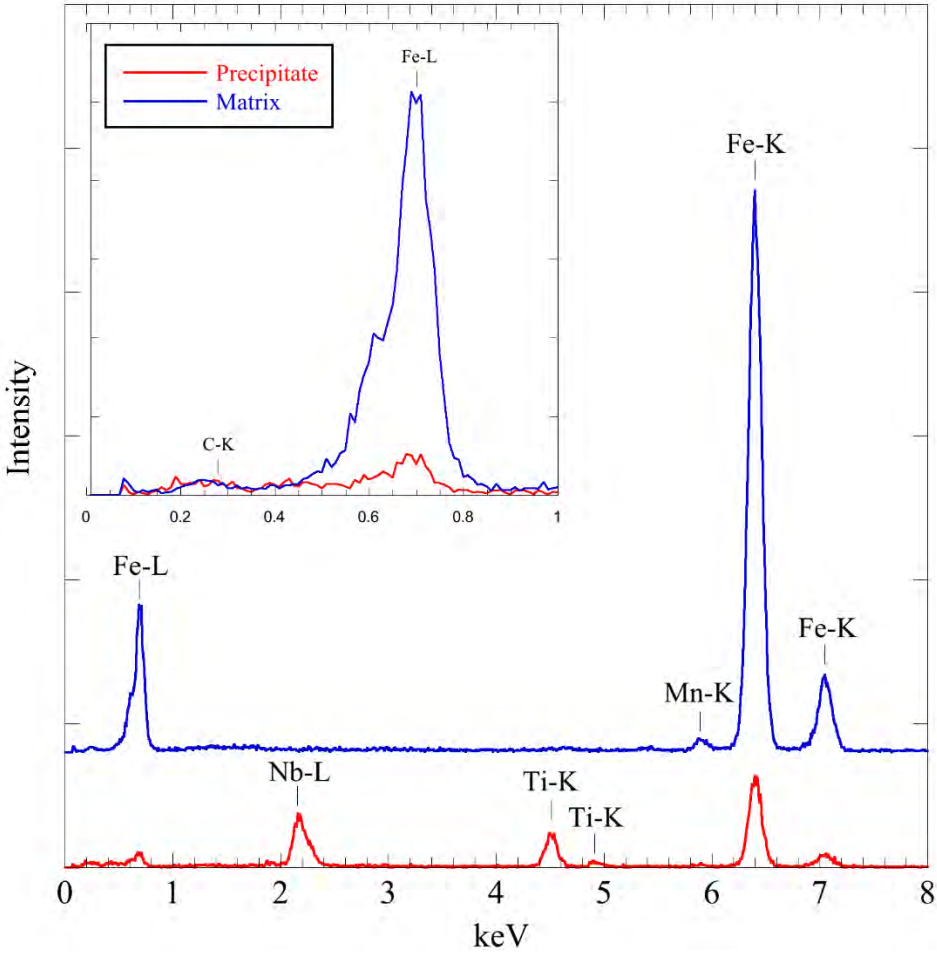

Figure 7.2. *EDX analysis results from the precipitate and matrix, inset figure shows the magnified spectrum for visualization of C-K peak*

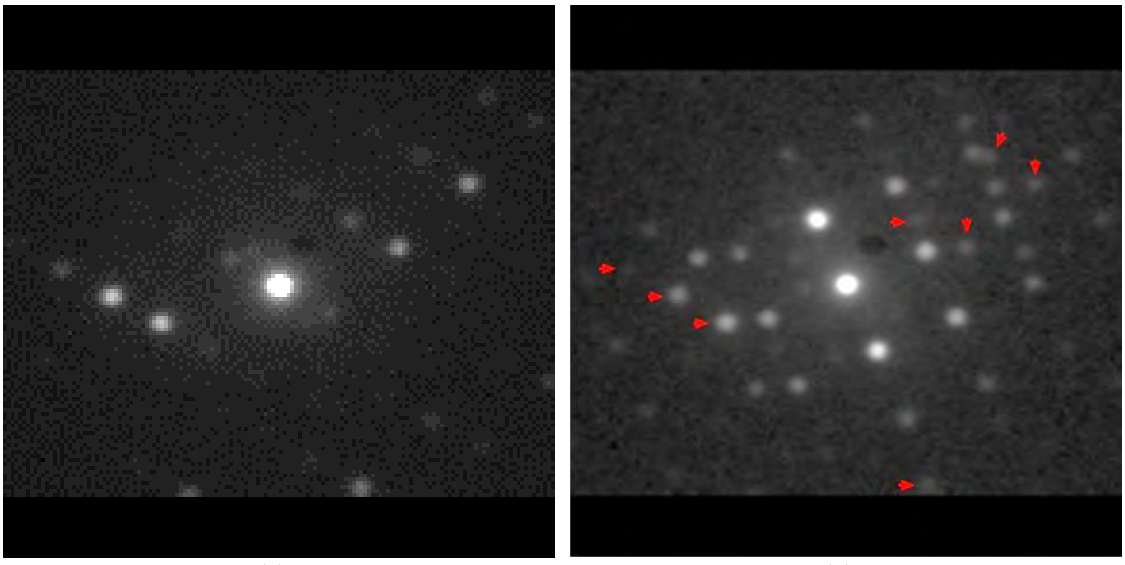

(a) **(b)**

Figure 7.3. *Diffraction pattern obtained from (a) matrix and (b) precipitate particle. Diffraction spots formed from matrix in the precipitate is marked with red arrows*

Phase and orientation mapping of a region containing a precipitate were also carried out with TEM-PED method. Phase maps were obtained without and with precession to see the effect of precession on the map quality. Result of phase mapping can be seen in Figure 7.4. According to these results, obtaining the maps with (0.7°) or without precession did not have an impact in the phase maps however, orientation, index and reliability maps were better with precession (Figure 7.4). This is mainly due to the variation of diffracted spot intensities as a result of non-uniform thickness of scanned area. Diffraction spots in thicker areas become faint and indexing quality degrades, however precession helps to improve diffraction spots in thicker areas. Because of these reasons, 0.7° of precession was used in PED analyses for the characterization of precipitate.

To determine whether this precipitate particle contains C element or not, indexing was completed with (Ti,Nb)C and TiNb data that were created by using ICSD # 77219 and ICSD # 105247 CIF files and results are given in Figure 7.5 and Figure 7.6, respectively. Lattice parameters and crystal structure is given in Table 7.2. According to these results, precipitate particle was identified as (Ti,Nb)C due to its better phase and orientation maps as well as index and reliability maps. The average reliability of (Ti,Nb)C phase was about 20; however, it was about 12 for TiNb phase which was below safety limit (15). Phase map of TiNb revealed that precipitate particle was not described completely and almost half of the pixels were identified as ferrite with TiNb phase data. In contrast to TiNb results, all pixels within precipitate was identified as (Ti,Nb)C with high reliability values. Phase and orientation maps also revealed that this particle is an intragranular precipitate and it has 47.5±0.5° of misorientation with the matrix phase. This angle is close to CSL ∑15 (48.19°), ∑19b (46.8°) and ∑29b (46.4°); however, it does not exactly match with them. Thus, this precipitate particle can be accepted as randomly oriented high angle grain boundary.

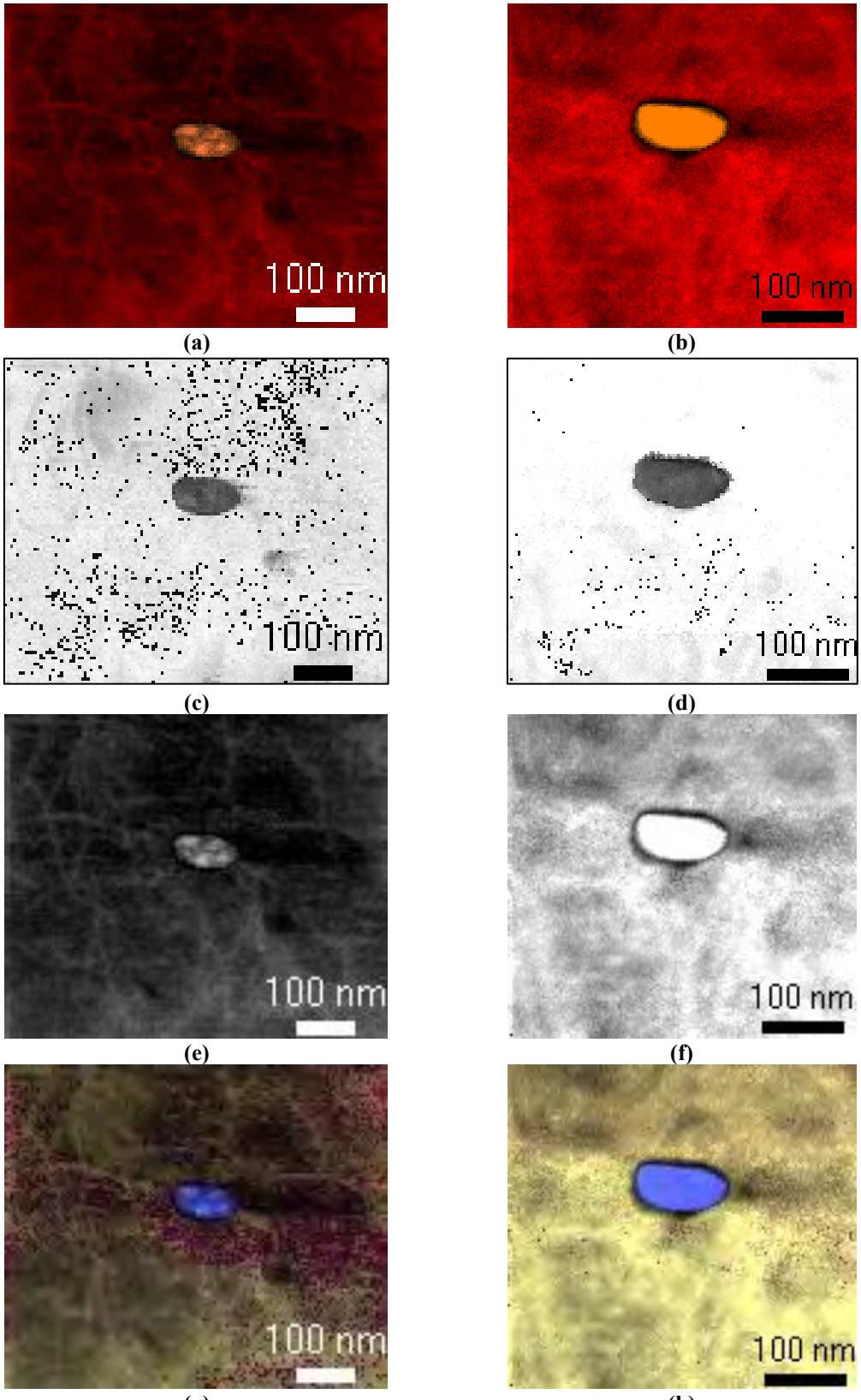

Figure 7.4. *Effect of precession on the phase, reliability, index and orientation (Y) maps for without precession (a, c, e, g) and for with 0.7° precession (b, d, f, h), respectively*

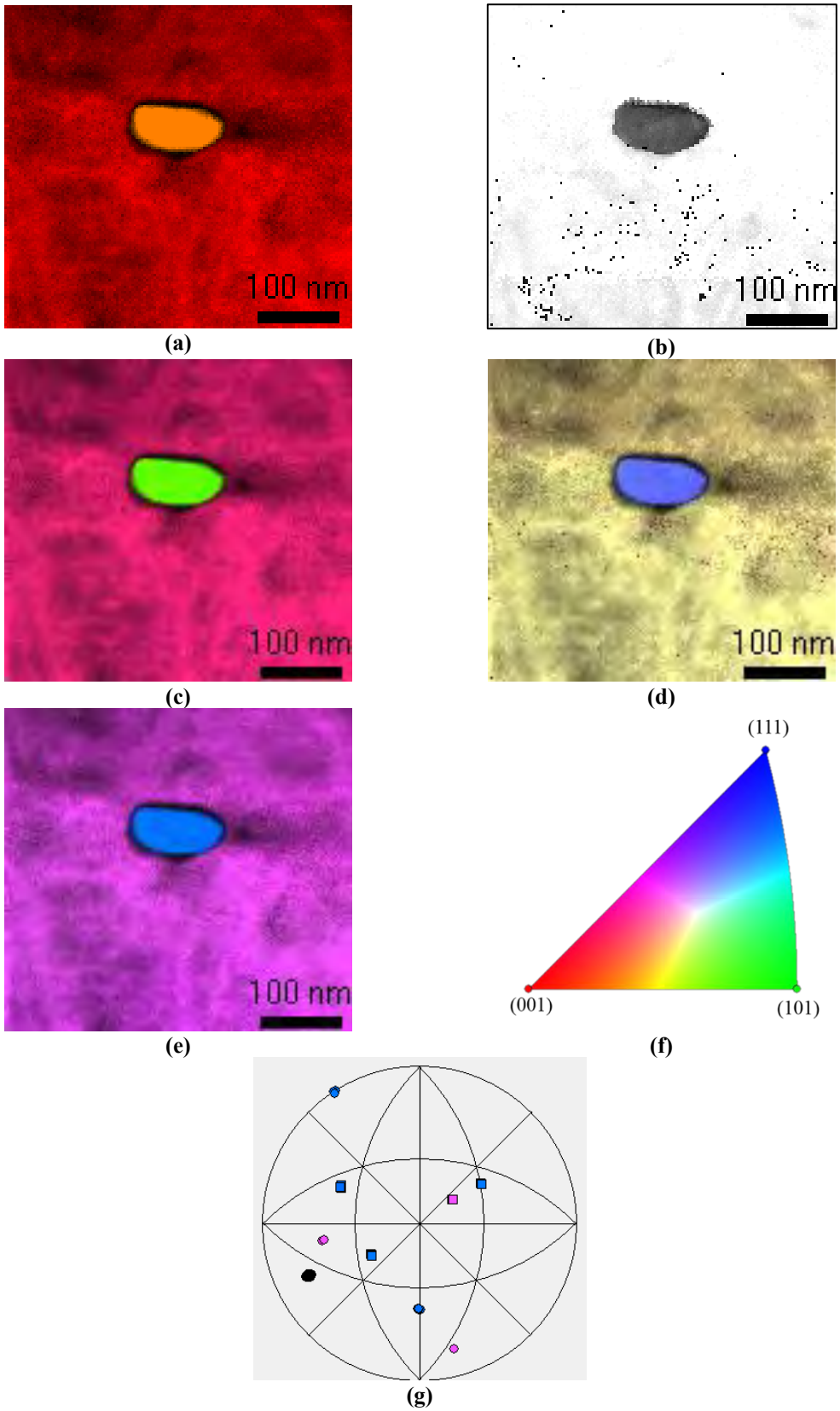

Figure 7.5. *Indexing results for (Ti,Nb)C (a) phase, (b) reliability, (c-e) orientation maps (X, Y, Z, respectively), (f) standard triangle and (g) inverse pole figure*

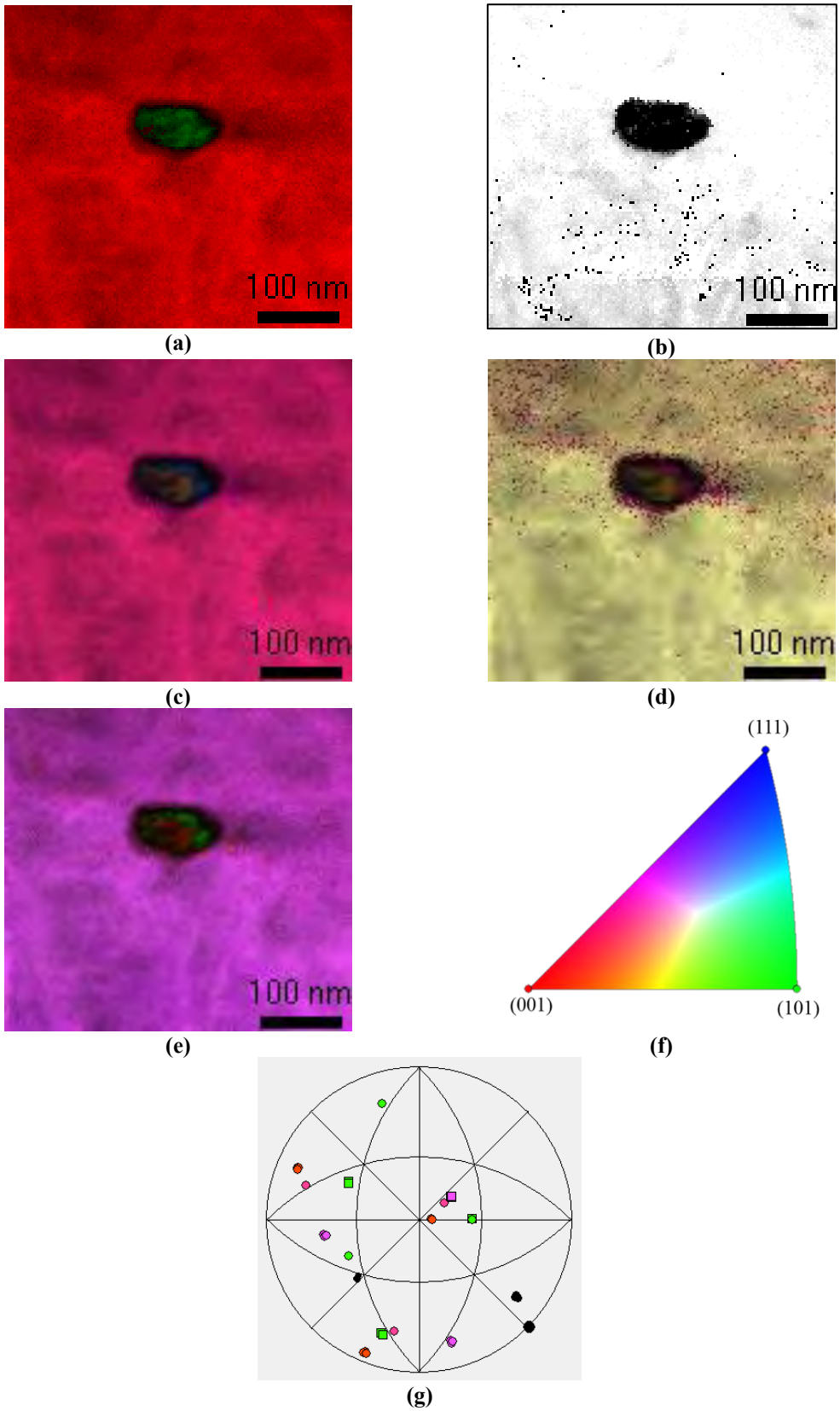

Figure 7.6. *Indexing results for TiNb (a) phase, (b) reliability, (c-e) orientation maps (X, Y, Z, respectively), (f) standard triangle and (g) inverse pole figure*

There is also a possibility for precipitate particles to be (Ti, Nb)CN according to the literature. To confirm whether this particle is (Ti, Nb)CN or not, indexing was done with (Ti, Nb)CN diffraction data created with only CIF file that contains Ti, Nb, C and N elements which is $Ti_{0.17}Nb_{0.83}C_{0.05}N_{0.77}$ (ICSD # 1549). Indexing results; phase, reliability and orientation maps with inverse pole figure is given in Figure 7.7. According to these results (index and reliability maps), this phase matched as good as (and even better than) (Ti,Nb)C and orientation maps are almost the same with (Ti,Nb)C; however, (Ti, Nb)CN phase should contain 9.33 at % Ti, 45.6 at % Nb, 2.7 at % C and 42.3 at % N, theoretically. The composition of this phase contains very high amount of N element and it should have a significant peak in EDX results; however, there is no evidence of N peak in the EDX result given in Figure 7.2. These findings are concluded as; only PED results do not enough for the characterization of unknown phase especially if lattice parameters and crystal systems are close to each other and that is why they should be supported with additional analyses like EDX, HRTEM etc.

Table 7.2. *Details of the phases used for characterization of the precipitate*

Phase	***ICSD #***	***Crystal Structure***	***Lattice Parameters (Å, °)***					
			a	***b***	***c***	***α***	***β***	***γ***
Ferrite	64998	BCC	2.861	2.861	2.861	90	90	90
TiNb	105247	BCC	3.286	3.286	3.286	90	90	90
(Ti,Nb)C	77219	FCC	4.396	4.396	4.396	90	90	90
(Ti,Nb)CN	1549	FCC	4.346	4.346	4.346	90	90	90

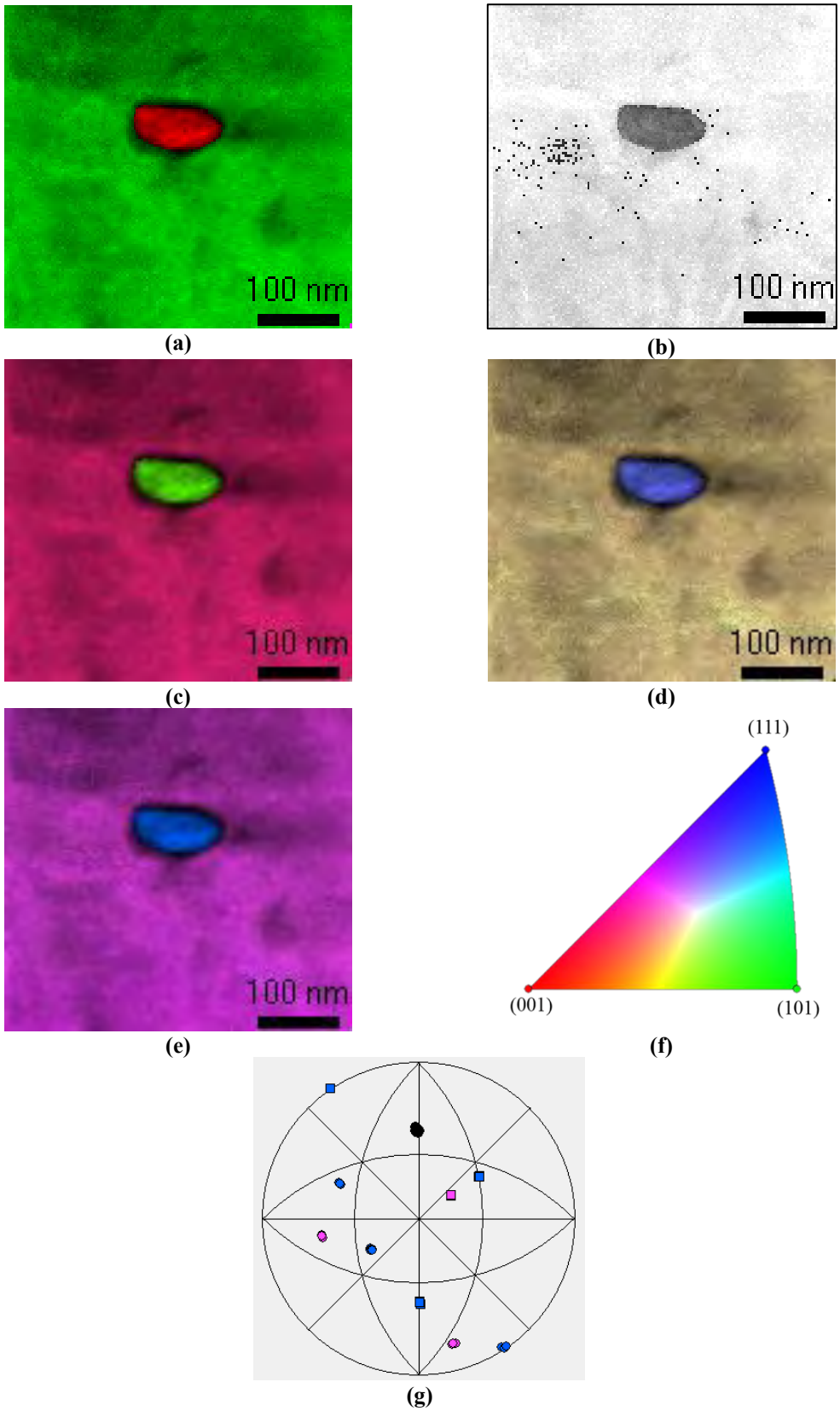

Figure 7.7. *Indexation results for (Ti,Nb)CN (a) phase, (b) reliability, (c-e) orientation maps (X, Y, Z, respectively), (f) standard triangle and (g) inverse pole figure*

7.3. Conclusions

In this part of the thesis, precipitate particle characterization within the ferrite matrix was carried out by using TEM-BF, STEM-HAADF, STEM-BF, STEM-EDX and PED techniques. Results obtained by using these methods are;

i. API-X70 steel contains non-equiaxed precipitate particle with 2:1 aspect ratio,
ii. STEM-HAADF images revealed that precipitate particle contains higher Z number elements than the matrix namely Nb and Ti elements,
iii. Precipitate particle can be TiNb or (Ti,Nb)C, due to STEM-EDX spectrum of the precipitate, that includes Fe and C peaks which may come from the matrix or from the precipitate particle,
iv. Characterization of precipitate was concluded with PED method whether it is TiNb or (Ti, Nb)C phase and this study showed that precipitate particle is (Ti, Nb)C,
v. PED results also showed that this precipitate may match to (Ti, Nb)CN even though STEM-EDX spectrum did not show any N peak. If cell parameters and crystal systems are close to each other for different phases, indexing can be quite similar and it is hard to distinguish which phase it is. In order not to make a mistake, supporting analyses (like EDX or any other) should be carried out.

Major advantages of PED for the phase analysis of precipitate particles over the EBSD method, experienced in this study, are;

i. The resolution limit of EBSD can limit the characterization of precipitate particles if their sizes are below EBSD limits, e.g. 50-200 nm. In PED method, resolution limit can be improved to few nanometers in FEG-TEM.
ii. Total scanning time is much shorter than EBSD.
iii. Other advantage of PED is the image processing. In EBSD method possible phase information e.g. CIF files needs to be provided before the scanning and it cannot be changed after scanning. This could be a disadvantage when additional phases wanted to be checked after scanning, however, in PED template matching strategy is done after getting the raw diffraction data. This provide offline data processing flexibility to the user such as additional phases can be provided to the software at any time and raw data can be processed at any time without any limitation if diffraction spot quality in a raw data is good enough for template matching.
iv.

8. ARGON IMPLANTATION INTO hBN PARTICLES

During the STEM analyses of the hBN containing composite systems, it was found that some of the hBN particles in the composite contain argon (Ar) element (Figure 8.1). The presence of Ar was also searched in the matrix particles, intergranular phases and other phases but it was found that none of them contains Ar.

In all of the hBN particles, silicone peak is also observed. It is known that in the EDX spectra, some of the peaks can be observed due to the overlapping, summation, escape peaks, etc. Especially in the 70's, Ar was observed in Al as a result of summation [56]. This unexpected inclusion of Ar and Si in the hBN grains raising a question whether these two elements observed as a result of microscope artefacts or not. Si was found as microscope artefact as found in Chapter 4. However, Ar element was found in multiple hBN particles having specific morphology, but Ar element was not present in hBN particles having random morphology. This observation revealed that Ar peak in the EDX spectra was not a microscope artefact; hence, this behavior raised a question of *"why only hBN particles and why only some of them contain Ar element which is not intentionally added to the materials?"*

In order to search for an answer of this question, first the source of argon should be found. During manufacturing processes of the composites, at none of the production steps Ar element has been used. Thus, if Ar was not introduced to the system during manufacturing, source of Ar must be from one of the sample preparation methods. Only the Ar ion beam milling process involves the use of Ar. In this procedure, energized (up to 8 keV) and ionized Ar atoms used for the material removal and thinning to obtain electron transparent samples. This procedure may explain the source and presence of Ar element, but it does not explain why hBN and why only some of the hBN grains contains Ar element. To search for an answer of this question extensive TEM and STEM studies were conducted.

Figure 8.1 shows the preliminary STEM-HAADF images of hBN particles and STEM-EDX results. According to the results, it was found that certain types of hBN particles contain Ar element. Specific hBN particles, which are elongated with high aspect ratio, contains Ar element but particles with non-specific morphologies did not have Ar element. These results showed that .only some of the hBN grains having certain orientations contained Ar ions. For the detailed analysis of this phenomenon, STEM-BF images of hBN particles both with and without Ar were obtained. Figure 8.2 shows the

STEM-BF and STEM-HAADF images of hBN particles with both with and without Ar labelled with green and red stars, respectively. In these STEM-BF images one significant detail was observed, that is hBN particles with Ar have different BF contrast compared with others. This contrast difference is caused due to the diffraction contrast and it means that these particles have (or close to) an orientation with significant electron diffraction, i.e. low index zone axis. For the detailed analysis of these particles, TEM images, coupled with STEM-EDX analyses were obtained. These TEM images confirmed that the contrast difference observed in the STEM-BF images, Ar containing hBN particles are not exactly in the zone axis but they are close to $[11\bar{2}0]$ zone axis, which means electrons are parallel to (0002) planes and they are visible in TEM images as shown in Figure 8.3. However, there was no specific orientation found in the particles that do not contain an Ar element in Figure 8.4.

The EEL spectra of each particle types stated above also showed variations with respect to each other. EELS analysis of particles with and without Ar element are given in Figure 8.5 and Figure 8.6, respectively. The first difference is the presence of Ar-$M_{2,3}$ peak at 12 eV, and this result is matched with EDX spectra that are obtained with the same particles. Other difference is the peak intensities in B-K and N-K ionization edges. First peak intensity in B-K edge is higher in particle with an Ar element compared with the one without having an Ar. The same is also true for the first peak of N-K edge.

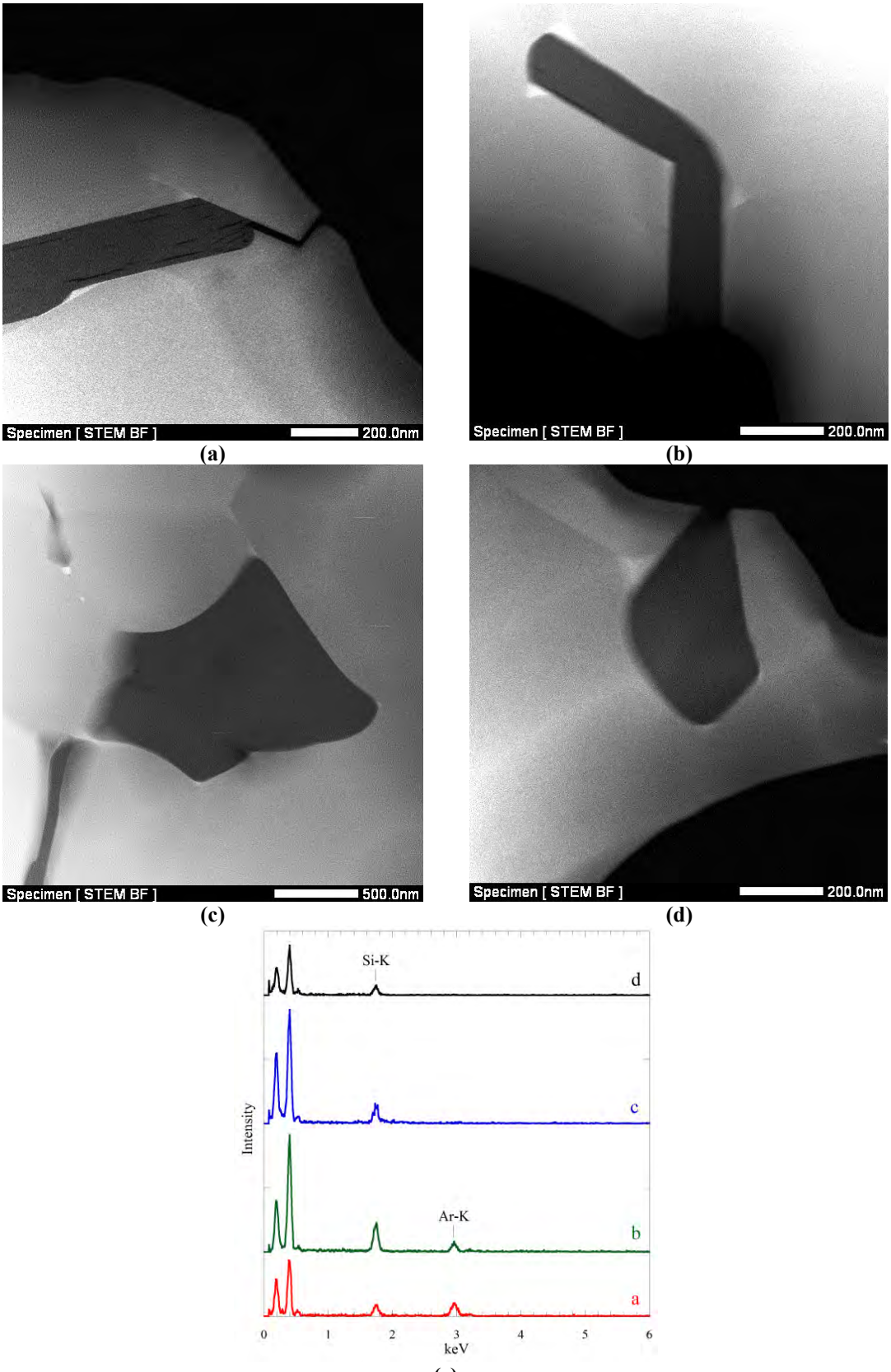

Figure 8.1. *Preliminary STEM-HAADF images of hBN particles (a, b) with Ar, (c, d) without Ar and (e) STEM-EDX results from these particles*

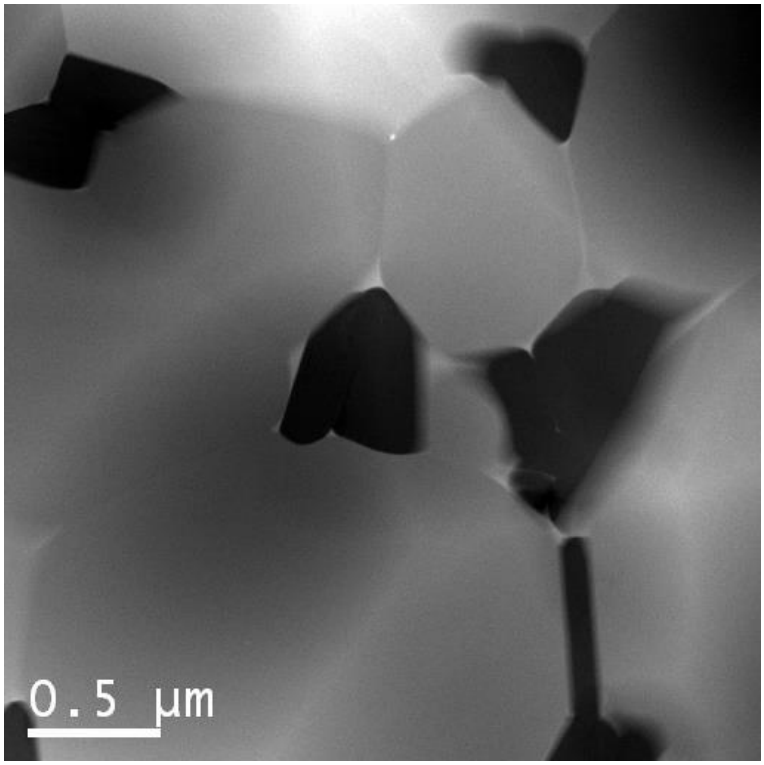

(a)

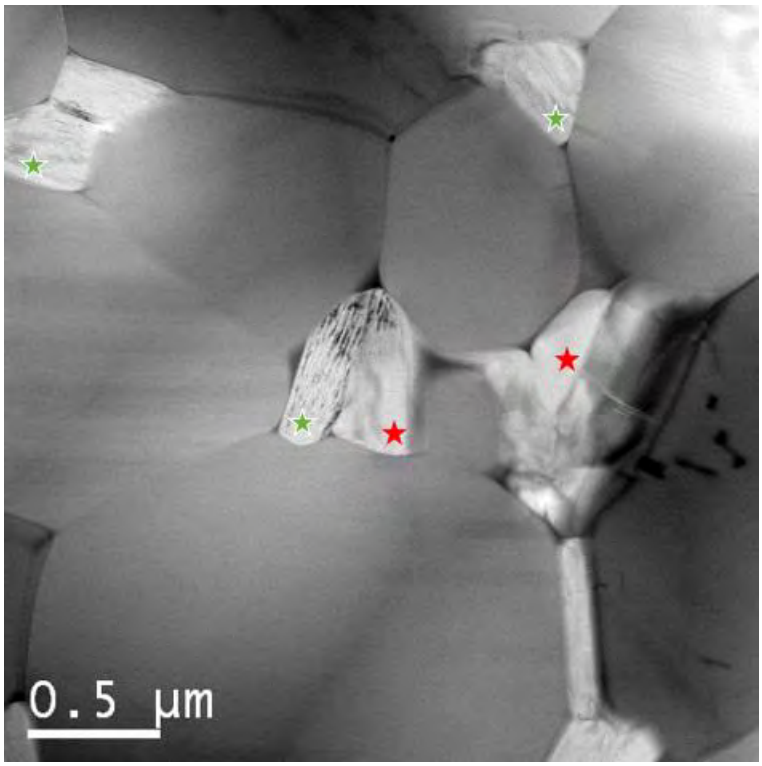

(b)

Figure 8.2. *(a) STEM-HAADF and (b) STEM-BF images of hBN particles. Ar containing particles are marked with green star and without Ar red star, according to the STEM-EDX results. Significant contrast difference in Ar containing particles is visible in the STEM-BF images*

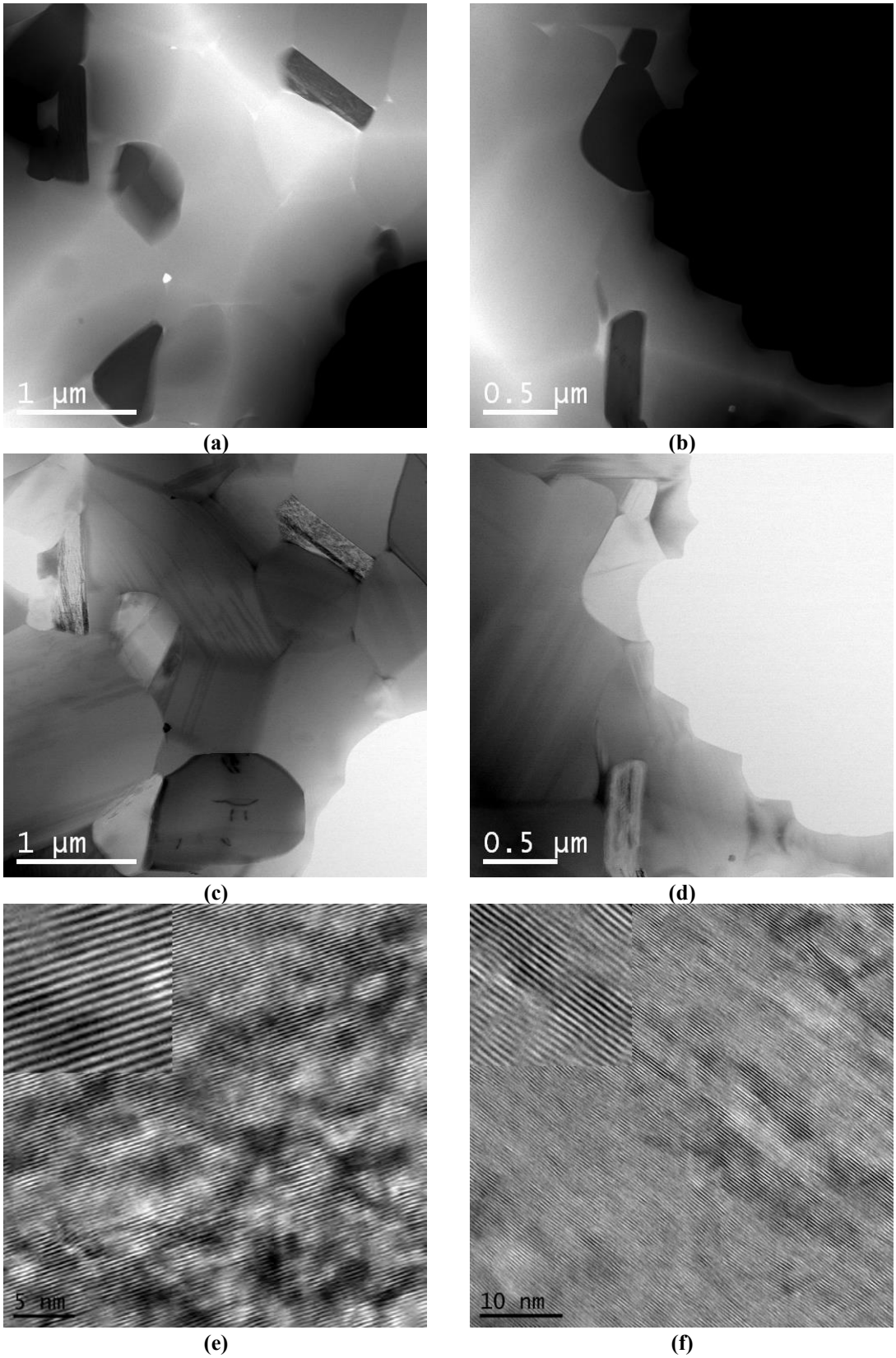

Figure 8.3. *(a, b) STEM-HAADF, (c, d) STEM-BF and (e,f) TEM images of Ar containing hBN particles*

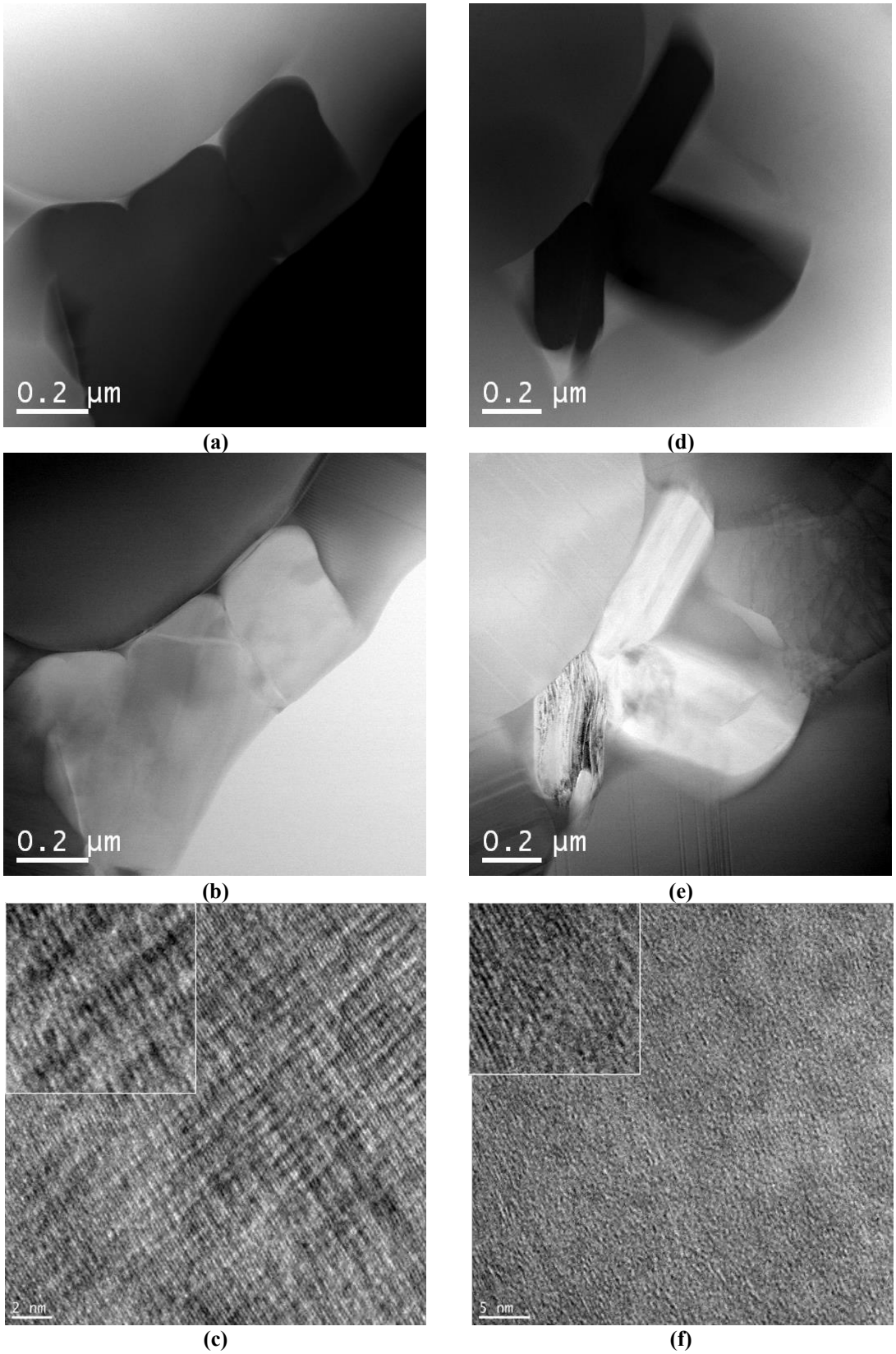

Figure 8.4. *(a, b) STEM-HAADF, (c, d) STEM-BF and (e, f) TEM images of hBN particle without Ar*

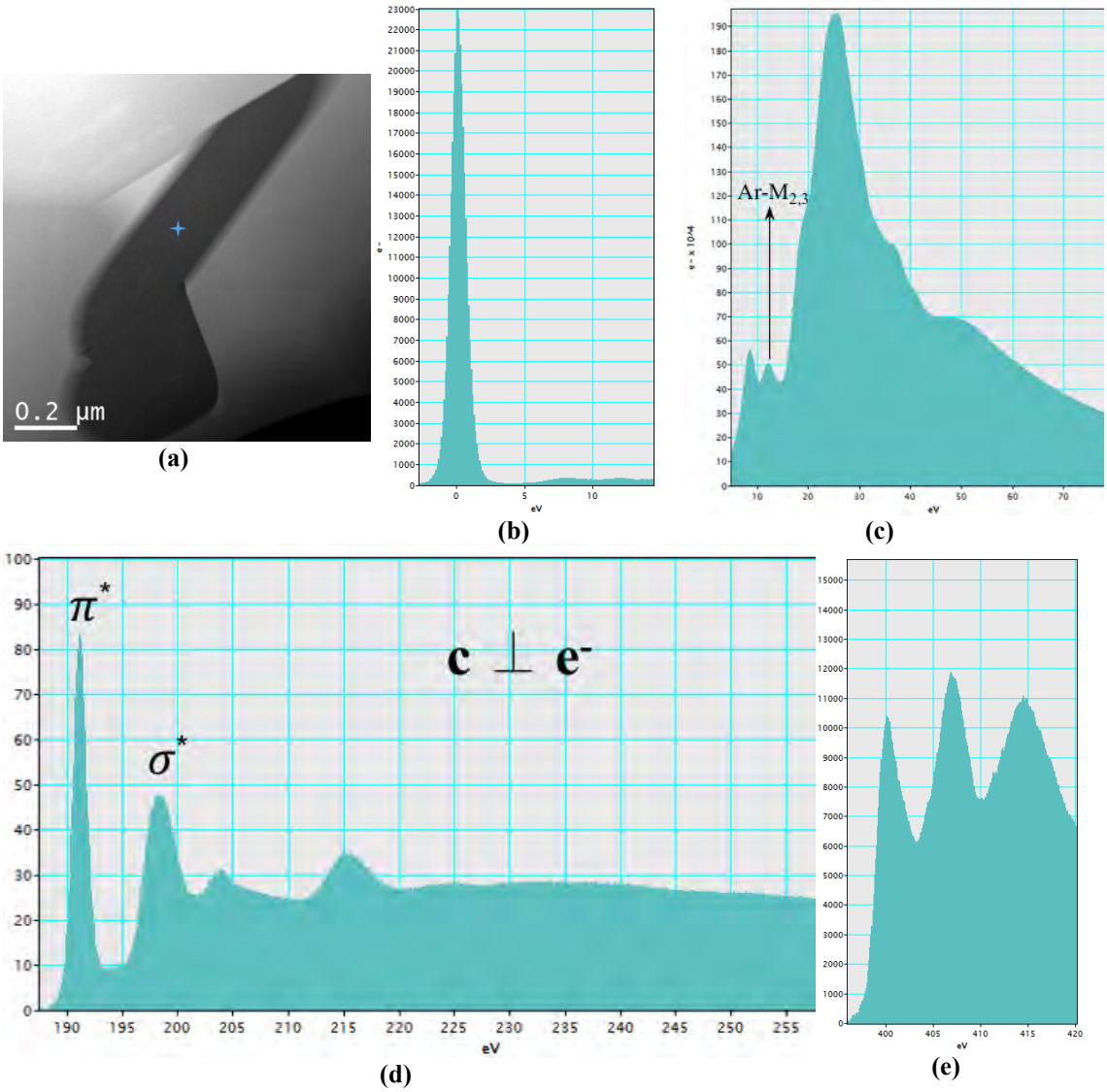

Figure 8.5. *(a) STEM-HAADF image of EELS acquisition point, (b) zero loss peak, (c) Plasmon region, (d) B-K stripped edge and (e) N-K stripped edge of a particle containing Ar*

EEL spectrum can reveal the difference in crystal structure and the orientation of crystal for the same material composition like boron nitride. For example, EELS B-K peaks for c-BN and hBN vary significantly as shown in Figure 8.7 due to the different hybridizations. Additionally, orientation of highly anisotropic materials like hBN and graphite may effect the peak intensities in EEL spectrum [58]. In this study, since both spectra were acquired from the hBN particles, reason for the intensity change could only be the orientation difference of crystals with respect to electron beam.

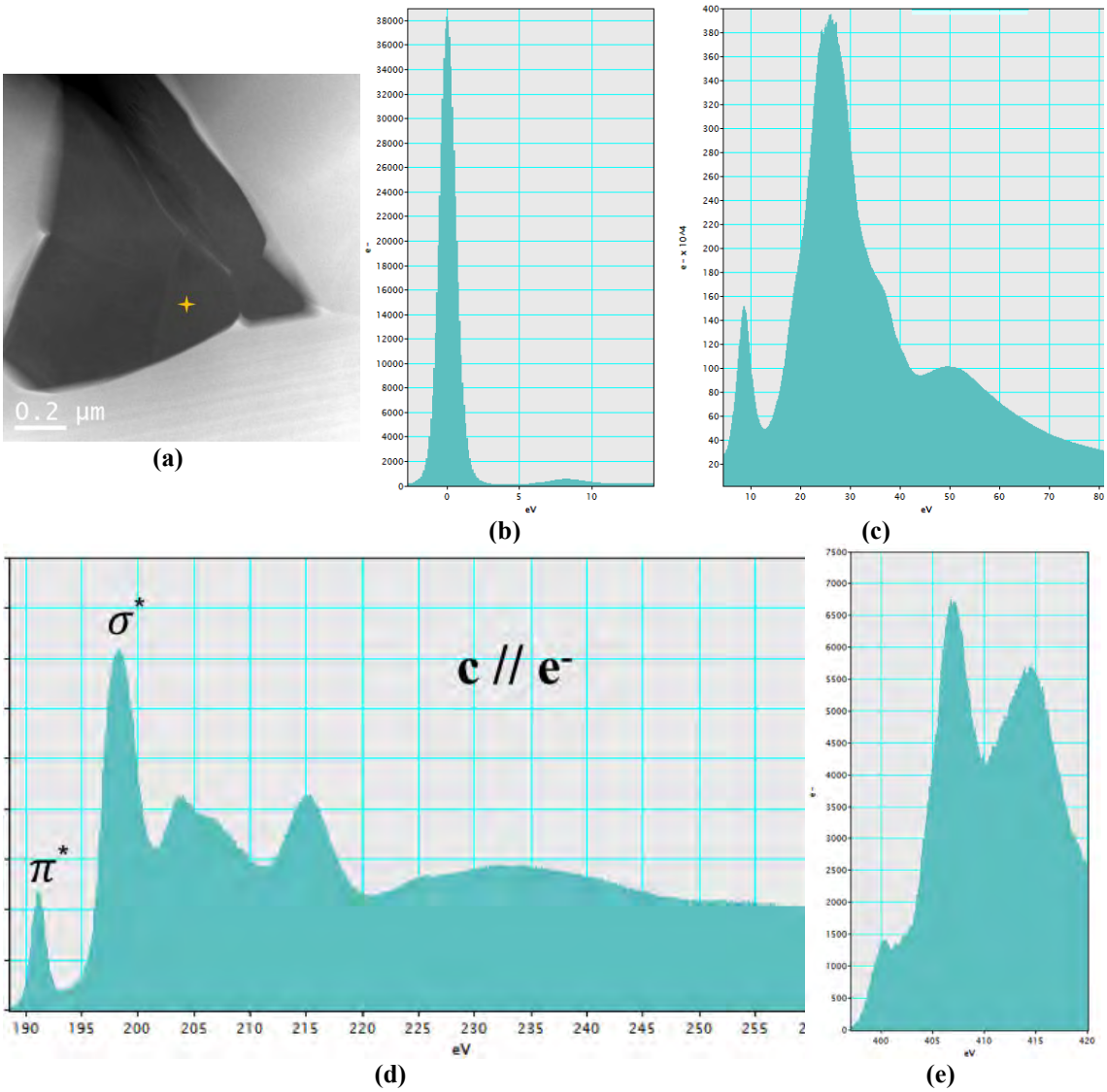

Figure 8.6. *(a) STEM-HAADF image of EELS acquisition point, (b) zero loss peak, (c) Plasmon region, (d) B-K stripped edge and (e) N-K stripped edge of particle that does not contain Ar*

For the understanding of the difference between peak intensities of EEL spectra given above, origin of these peaks needs to be understood. Intensity fluctuations just above the ionization edges are defined as Energy-loss near-edge structure (ELNES) and this structure provide information about the atomic coordination and valance numbers, atomic orbitals and type of bonding [122]. Thus, to relate ELNES peaks with the atomic bonds, structure and atomic bonds of the hBN needs to be examined. hBN composed of B and N atoms with σ and π bonds that hold together these atoms similar to the graphite. Structure of graphite is given in Figure 8.8 and in this figure; σ and π orbitals are seen along hexagonal plane and c-axis, respectively. These orbitals are the reason of two distinct peaks, σ^* and π^* as a result of transition of 1s electrons, in the ELNES of C-K

[123] as well as B-K and N-K edges [124]. Relative intensities of these peaks show variations with crystal orientation with respect to electron beam as shown in Figure 8.5 and Figure 8.6.

In the literature, relative intensity change of these peaks were investigated for several different crystal orientation of hBN with respect to the electron beam. Studies [125-128] with hBN with c // e^- orientation, intensity of the σ^* peak become higher than π^* peak intensity in the EELS results; however, other studies [129, 130] showed the opposite case regarding relative peak intensities. In the case of c $\perp$ e^- orientation, intensity of the π^* peak become dominant in EELS results [126, 131].

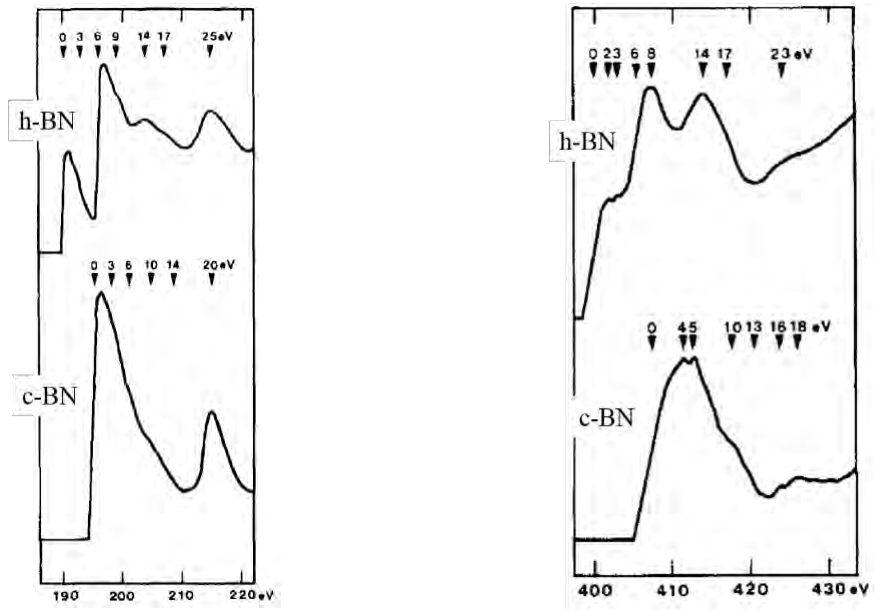

Figure 8.7. *EELS stripped edge of (a) B-K and (b) N-K for hBN and c-BN, intensity differences of peaks caused by the structural difference, modified images from [127]*

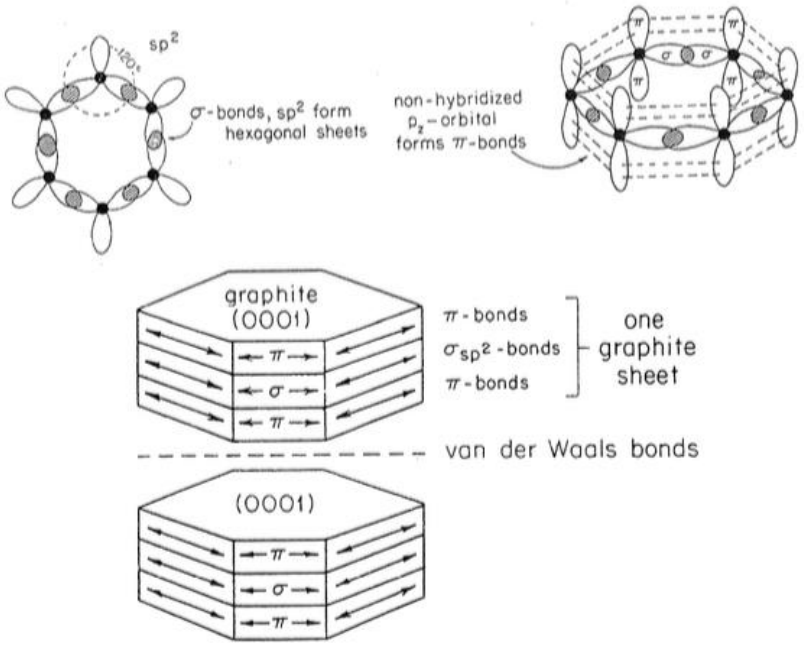

Figure 8.8. *Structure of graphite showing σ and π bonds [16]*

Even though relative intensities of σ^* and π^* peaks mostly related with the crystal orientation, it can also be changed with experimental conditions as well. In TEM it was reported that intensities of π^* and σ^* peaks can be changed by changing the camera length that affect the collection angle of the spectrometer i.e. smaller the camera length, higher the collection angle [16]. This can also be the reason for opposite results (for same orientations) obtained in the literature. Turan et. al. showed that in case of electron beam parallel to $[11\bar{2}0]$, experimental parameter did not significantly change the intensity of π^* peak and intensity of this peak is higher than σ^* peak for this orientation ($c \perp e^-$); however, in the case of electron beam parallel to [0001] direction ($c \,//\, e^-$) intensity of σ^* peak could be both relatively higher or lower than π^* peak [126]. For the comparison of different crystal orientations, same spectrum acquisition conditions should be used. Therefore, in our studies, STEM mode was used for EELS acquisitions with same camera length and entrance aperture, which was 5 mm. In the results obtained in this thesis, Ar containing hBN particles showed higher π^* peak intensity compared to σ^* and vice versa for the particles without Ar element. This means that Ar containing hBN particles are in $c \perp e^-$ orientation and others are $c \,//\, e^-$ orientation. For the $c \perp e^-$ orientation, π^* to σ^* intensity ratio is similar to literature; however, in other orientations which do not contain Ar, π^* to σ^* ratio is a bit higher than literature. In the literature, EELS results were obtained as c- axis of hBN particles were exactly parallel to the electron beam and it

resulted in very low π^* to σ^* intensity ratio and σ bond was dominant; however in our results there were also a contribution of π bonds which means that c-axis of our hBN particles were not exactly parallel to the electron beam but in a random orientation. Because of this reason, c // e^- notation might not fit to our situation, random c-axis notation might be the correct notation.

In the light of this information (TEM-BF, STEM-HAADF, STEM-BF, STEM-EDX and STEM-EELS results and results in the literature), specific orientation of the Ar containing hBN particles was also checked and confirmed by STEM-EELS analyses. Ar element was found only in hBN particles having a specific c $\perp$ e^- orientation, (0002) planes are parallel to the electron beam, which has relatively large interplanar spacing of 0.333 nm. However, in other crystal orientations Ar ions were not found. The source of an Ar and which hBN particles contain Ar were found but why only these particles contains Ar elements still needs to be explained.

Ion implantation at different accelerating voltages, e.g. from 30keV to >1 MeV with various ions like He, Li, As, Bi etc. can be used for various purposes like phase transformation, amorphization, modification of mechanical and transport properties of graphene, diamond and boron nitride. In graphite ion implantation with heavy element like Bi cause the increase of (0002) interlayer spacing about 0.6 Å and also increased dose of ions cause amorphization [132]. Ion bombardment of hBN with 150 keV with various ions (He+, B+, Li+) can also cause phase transformation of hBN into the c-BN even though it has very high phase transformation temperature of 1700°C [133]. Since ion energies are very low (<6 keV) during sample preparation, compared to the ion bombardment experiments, there is no evidence of any amorphization in hBN structure and (0002) interlayer spacing change in this study. The average interlayer spacing is 0.335 nm for hBN's with Ar implanted which is almost the same with un-implanted (0002) hBN planes that is 0.333 nm.

The amount of damage during ion implantation not only depend on the to accelerating voltage but also dose, temperature, size of ion, properties of the target (that is hBN) and crystalline state [134]. The accelerating voltage is the most probable reason of hBN interlayer spacing not to change compared with the literature in graphite [135] however it cannot explain the orientation relation of implantation, since all hBN orientations within the same sample exposed to same dose, temperature and ion type. The orientation related implantation can be explained by the channeling effect.

Channeling effect can be defined as the influence of crystal orientation on ion implantation [134] and ion beam penetrates deeper into the sample compared to the other crystallographic directions as well as amorphous state. Channeling effect occur due to the potential field applied to the ion from the surrounding atoms in the structure and with the help of this potential field ions move across the structure without any collision with surrounding atoms. When accelerated ions hit the isotropic material like amorphous phases, movement of the ions within the sample is random and not dependent to the relative orientation between ions and target material. However in crystalline materials, behavior of ions i.e. movement, depend on the relative orientation [133]. This effect was seen on low index direction (100) in c-BN [134] and N ions in Si [136]. In the literature channeling of ions are measured by the number of backscattered ions and quantified by the Rutherford backscattering yield with channeling experiments. Channeling of ions (1.2 to 2.4 MeV He ions) on different directions of highly oriented pyrolytic graphite is extensively studied and these studies revealed that channeling of ions occur if ion beam is not only perfectly parallel to c axis but also perpendicular to the c axis that is parallel to (0002) planes and backscattered ion yield for both directions is given in Figure 8.9(c) [137]. Similar channeling effect was also reported in simulations of Ar ion channeling between the walls of multi walled carbon nano tube which has 0.32 nm distance between the layers and bound by Van der Waals forces [138].

Crystal structure of the hBN is quite similar to graphite as shown in Figure 8.8 above;

- Distance between basal planes ($d_{(0002)}$) are 0.335 and 0.333 nm, for graphite and hBN, respectively.
- Basal planes hold together with Van der Waals forces in both structures
- Difference in the basal planes stacking sequence which is ..ABAB.. and ..AA'AA'.. for graphite and hBN, respectively.

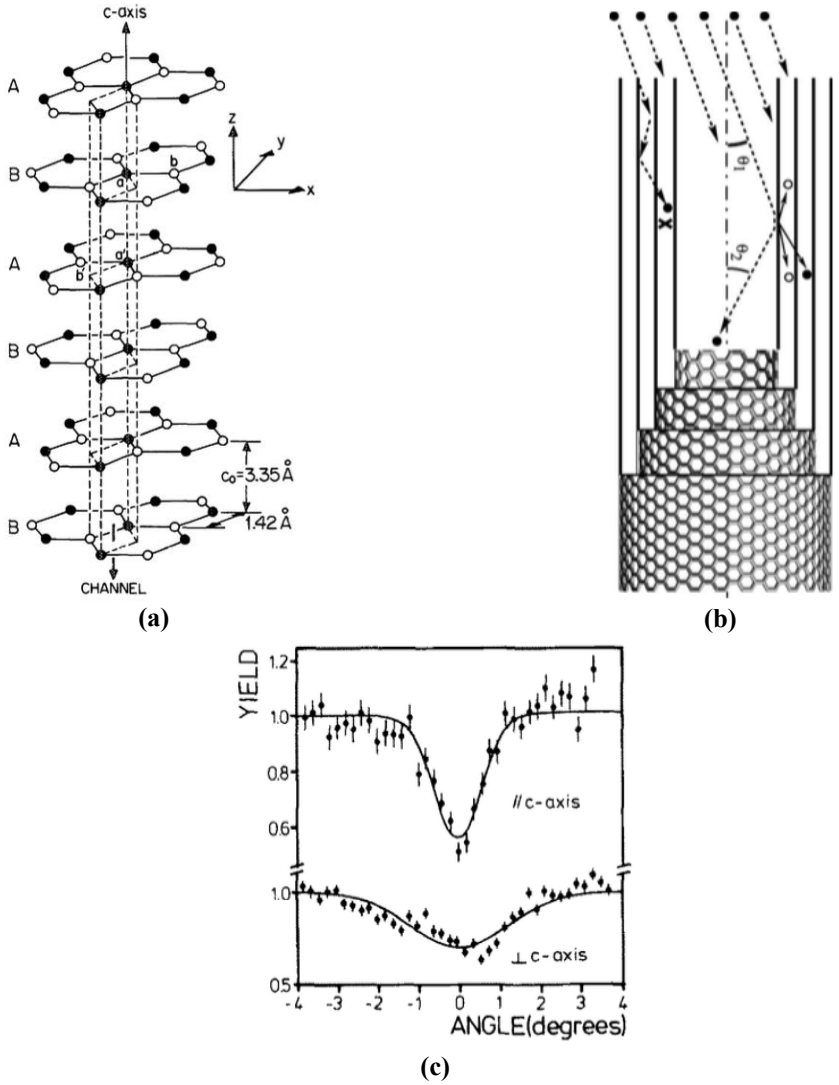

Figure 8.9. *Channeling mechanism for (a) graphite in c axis parallel to ion source [139], (b) multi walled carbon nano tube [138] and (c) Rutherford backscatter yield results of graphite with respect to crystal orientation by using Xe ion source [137]*

According to these similarities between graphite and hBN, the orientation related penetration of Ar^+ ions between hBN (0002) planes can be explained with the same manner, i.e. channeling effect, that allows low energy ions to penetrate into the basal planes and since ions are very low in energy they cannot forced to penetrate into other orientations. Hence, basal planes allow low energy ions to penetrate by channels between planes and due to the energy loss occurs during movement of ions, penetrated ions accumulated and trapped much deeper within the sample; however, the penetration depth is unknown for the energies used in ion milling procedure. The schematic representation of ion implantation between hBN basal planes is given in Figure 8.10.

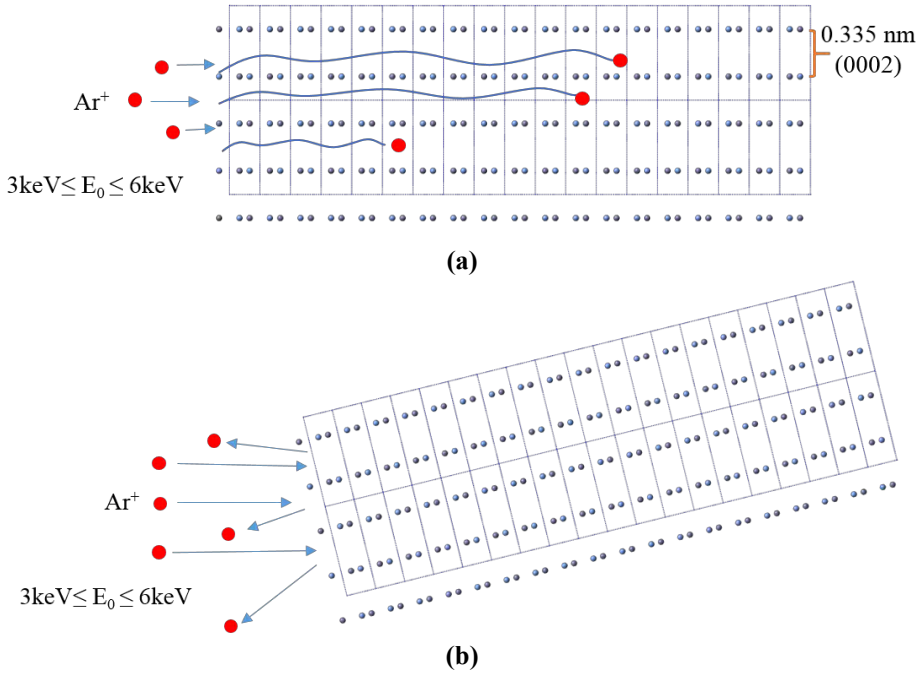

Figure 8.10. *Proposed ion channeling mechanism when c-axis perpendicular to the ion source and (b) backscattering of ions when crystal orientation is changed and c- axis is no more perpendicular to the Ar source*

In orientations, other than stated above, Ar ions may be implanted at the beginning of the ion milling where highest energy ions (6 keV) and highest incident angle (8 degrees) used however implantation depth of Ar in BN is about 15 nm according to Monte-Carlo simulations done by using Stopping and Range of Ions in Matter (SRIM) 2013 software (crystal structure, channeling and diffusions were not taken into account [132]). According to this result even though ions are implanted within 20 nm depth from the surface, this layer was removed during sample preparation stages where lowest energies (3 keV) and lowest incident angles were used (4 degrees).

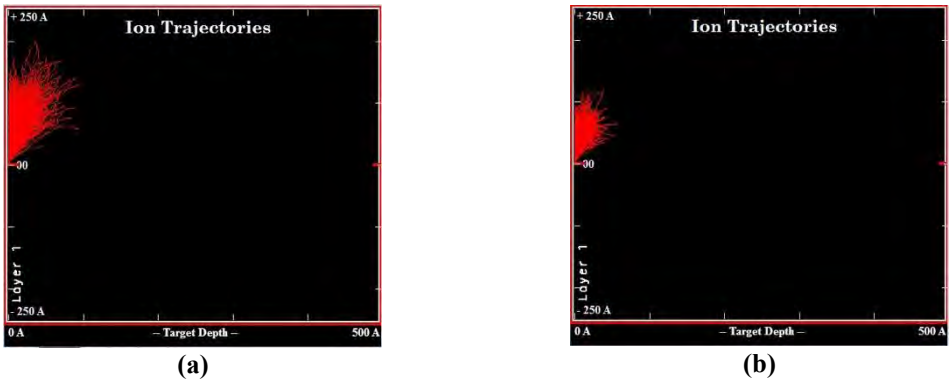

Figure 8.11. *Ion implantation simulation results for (a) 6 keV ions at 8°, and 3 keV ions at 4° of incidence angle obtained with SRIM.*

It is worth to note that these spectra and HRTEM images were obtained without doing any tilting during image and spectrum acquisitions that is specimen position was exactly in the same conditions during Ar^+ ion beam milling. Then, there could be a question about milling angles, which were not perpendicular to the specimen surface as in high energy ion bombardment and Rutherford backscattering experiments; how respective positions of sample and ions satisfy the channeling conditions?

The c-axis of Ar containing hBN particles were found perpendicular to the electron beam and it also means that c-axes are parallel to the surface of sample and (0002) planes are perpendicular to the surface of sample, as it can be seen in the Figure 8.12(a). Even though c-axis is parallel to the surface, hBN particles can be positioned according to the position of other particles in x and y axes of the sample surface. However, for the channeling conditions, c axis needs to be perpendicular to the ion beam as well as a and b axes should be parallel to the ion beam direction, which is in x direction, and in this case, some particles may satisfy this condition but others may not. This situation should end up with Ar deficient hBN particles even if they are in $c \perp e^-$ orientation; however, this was not the case in STEM and TEM results, all investigated hBN particles with $c \perp e^-$ orientation contain Ar. This situation can be explained by the ion beam milling conditions. During ion milling procedure, the sample is rotating while ion beam is positioned to the center of sample with an angle, in such case in between 4° to 8°. In Figure 8.12(a) all the hBN particles positioned with c-axis parallel to sample surface but none of a and b axes are parallel to ion beam direction (Ar ions are coming to sample within the orange dashed lines). As sample rotates during the milling procedure, particles at certain angles come into position that become fulfill the channeling criteria as shown in Figure 8.12(b) as blue particle (please note that, orientations of the colored hBN particles are given with color coded crystal structures around sample with same orientation). As it can be seen from cross-sections in Figure 8.12(c) and (d), a and b axes become parallel to ion beam direction as sample rotates and this provides required orientation condition for a and b axes, thus all $c \perp e^-$ oriented particles within the electron transparent section, satisfied this requirement at some rotation angle during milling.

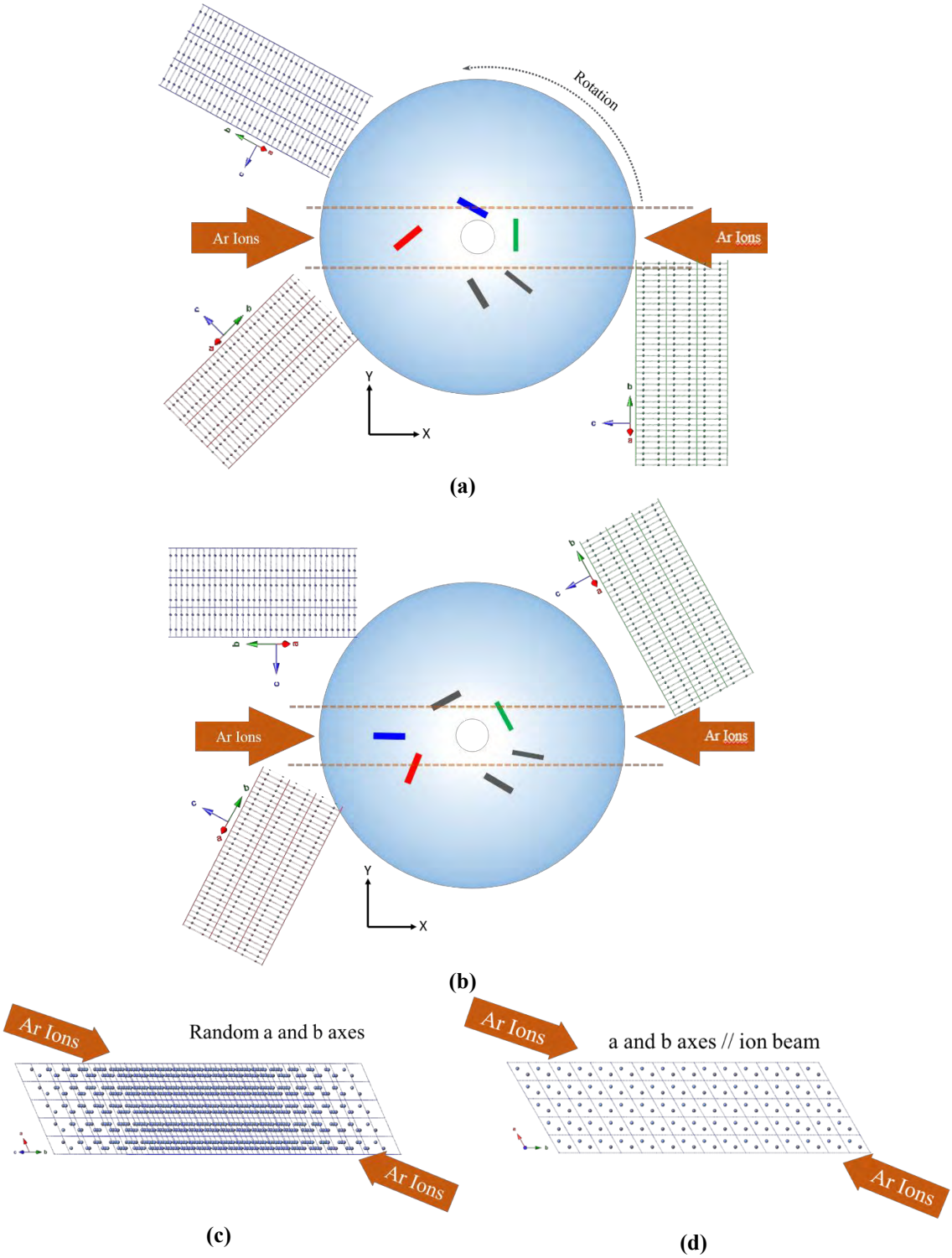

Figure 8.12. *Proposed ion implantation scheme for hBN particles that do not fulfill channeling conditions during ion beam milling (a) before rotation of the sample, none of the particles fulfill the requirements, (b) sample rotated and blue particle come into position that fulfill the requirements but others not. (c) ion beam position for blue particle in (a) condition (random a and b axes) and (d) ion beam position for blue particle in (b) condition (a and b axes are parallel to ion beam)*

8.1. Conclusions

The effect of Ar ion beam milling during sample preparation resulted in presence of Ar element in hBN particles according to the EDX spectra; however it was not present in all particles. EELS and HRTEM images were used to reflect the differences between them. According to these results, hBN particles which are oriented as $c \perp e^-$ condition contain Ar element between (0002) planes but other grains not satisfying this conditions do not contain Ar. This phenomena was explained by implantation of Ar ions in the channels between (0002) planes during Ar ion milling depending on the position of ion guns with respect to the a and b axes.

9. IN-SITU SINTERING OF ZnO NANOPARTICLES

9.1. Introduction

Sintering is the process of obtaining solid bulk materials with formation of bonding between loose ceramic powders by thermal energy, i.e. heating. Driving force for sintering process is the decrease of total surface free energy of the system via decreasing high surface area particles to bulk material having low surface area with thermal energy. Decrease of surface free energy can be obtained with two different processes. First one is the formation of solid/solid surfaces instead of high energy gas/solid surface as a result of densification. The other one is the decrease of surface area by combination of small particles to form bigger particles, which called as grain growth. Driving force during sintering is the curvature change at the contact point between particles that resulted in the pressure difference and atomic void concentration difference. The region where two particle is in contact, create the low-pressure region however, the surface of the particles form high pressure region, because of this reason material transport occurred from high pressure region to low pressure region. Atomic void formation occur with a similar fashion, voids are formed at the contact point of particles but not in the particle surface, then because of the concentration gradient, void transportation occurs opposite direction of material transport and then neck formation starts between two particles. Sintering of ceramics can be done by vitrification, liquid phase sintering and solid state sintering. In vitrification liquid phase is formed and fills the gap between particles however in liquid phase sintering liquid phase is again formed but not enough to fill the gaps. In contrast, solid state sintering do not involve formation of any liquid phase to obtain high density ceramics.

Solid state sintering process is the combination of three stages called as initial, intermediate and final stages. At the initial stage, particles, which are in contact without any bond between them, start bonding with neck formation by the application of heat. During these stages, material transportation occurs via volume diffusion, grain boundary diffusion, plastic flow and viscous flow, surface diffusion and evaporation/condensation mechanisms. Even though there is not a specific transition points between the sintering stages, it is widely accepted that initial stage ends with a neck formation and grain growth, then, the intermediate stage starts until densification up to 70-92 % of theoretical density and formation of isolated pores. At the final stage densification is achieved by reducing the pore amount.

There are two different neck formation models during sintering. In the first model, neck radius and its ratio to particle radius are used with an assumption that the distance between particle centers do not change during the neck formation. According to this mechanism, material transport occurs via surface diffusion and evaporation/condensation mechanisms. However, in the second model, neck formation occurs with decreasing the distance between particle centers and as a result shrinkage occurs. According to this model, volume diffusion, grain boundary diffusion, plastic and viscous flow occurs for material transport. Therefore, it is important for sintering kinetics to determine which model is active for a given material system [140-142].

Particle size and temperature are two important process parameters for sintering of materials and effects of particle size on sintering kinetics modelled with scaling models such as Herring's law for micron level particles. For these models, experimental data is required for appropriate temperature and particle size regimes such as diffusion coefficient and due to the lack of data for nano sized particles required data is extrapolated from micron sized particles for nano scale particles, which can result in discrepancies between theoretical and experimental data [41, 43]. Additionally, this type of scaling models can be used ideally for circular particle morphology, due to this reason particles having morphologies other than circular such as faceted cubic particles assumed as circular for these models, therefore, deviations become apparent between experimental and calculated results [143]. In addition, sintering models assume that particles are uniformly sized, which is not true for real cases.

In order to solve the discrepancies between theoretical and experimental results for sintering of nano scaled particles, direct observation of particles during sintering is required and this can be achieved by using in-situ sintering experiments via heating in TEM. During in-situ sintering in TEM, important parameters for sintering such as neck radius, dihedral angle, distance between particle centers can be measured directly with respect to time and temperature. In-situ sintering can reveal contact geometry during sintering which is important for non-circular morphologies as well as neck formation and its evolution, which provide information about the sintering dynamics with direct observation.

In the literature, there are several studies about in-situ sintering in TEM with different nano sized oxide MgO [39] and ZrO_2 [40] particles as well as metallic Pt [43] and Ag [41] nano particles. Majority of these studies investigated the sintering behavior

of two particles (with same chemistry) in contact while heating. The reason for investigation of sintering behavior of two particles is that sintering models were developed for two uniform particles. These studies have a common result (even if different material systems studied) that; during sintering the distance between particle centers did not changed during neck formation and according to these results it was concluded that active diffusion path between particles could occur via surface diffusion and/or evaporation/condensation mechanisms. Due to the low evaporation rates and presence of cooled metal surfaces in TEM, it was assumed that evaporated materials can be condensed on the cold surfaces and were not taken into account during sintering, therefore sintering between these particles took place with surface diffusion [39, 144].

Zinc oxide (ZnO) is a widely used oxide material due to its piezoelectric, pyroelectric, and semiconductor properties and used in piezoelectric ceramics, pigments, cosmetics, transparent conductive surfaces, gas sensors, photovoltaic cells etc. Its crystal structure is hexagonal with crystal lattice parameters of a=0.3296 nm and c=0.5207 nm [145]. Depending on the synthesis conditions ZnO particles can have wide range of size from nano to micron with various morphologies such as nanoparticle, nano-wire, nano-belt, nano-spiral etc. [146].

Bulk properties of materials can be modified with grain size, therefore, it is important to control sintering parameters. Because of this reason, in the literature there are quite a few studies exist about sintering and grain growth of pure ZnO particles and sintering temperatures varies between 650°C to 1400°C depending on the starting particle size and various holding times applied to obtain optimum densities and grain sizes. For example; sintering behavior and grain growth for 20 nm ZnO particles investigated at 700-900°C, however, 5-10 nm particles studied at 650-700°C in different studies [147]. It is a well-known fact that sintering temperature decreases with the decreased particle size and also grain growth rate increases due to the high surface energy of smaller particles. Due to the discrepancies in theory and practice, sintering behavior of particles with different sizes needs to be examined with ex-situ experiments to determine sintering conditions to obtain required grain size and density values, which requires quite a lot of time.

In this part of this thesis, *"in-situ TEM heating experiments are aimed to find necessary modifications of theoretical sintering models to predict the grain growth of nano sized pure ZnO particles produced with MicNo® methodology"*.

9.2. Results and Discussion

ZnO particles produced with MicNo® method resulted in micron sized hexagonal platelets with nano sized primary particles and average primary particle size is about 15±5 nm as shown in Figure 9.1.

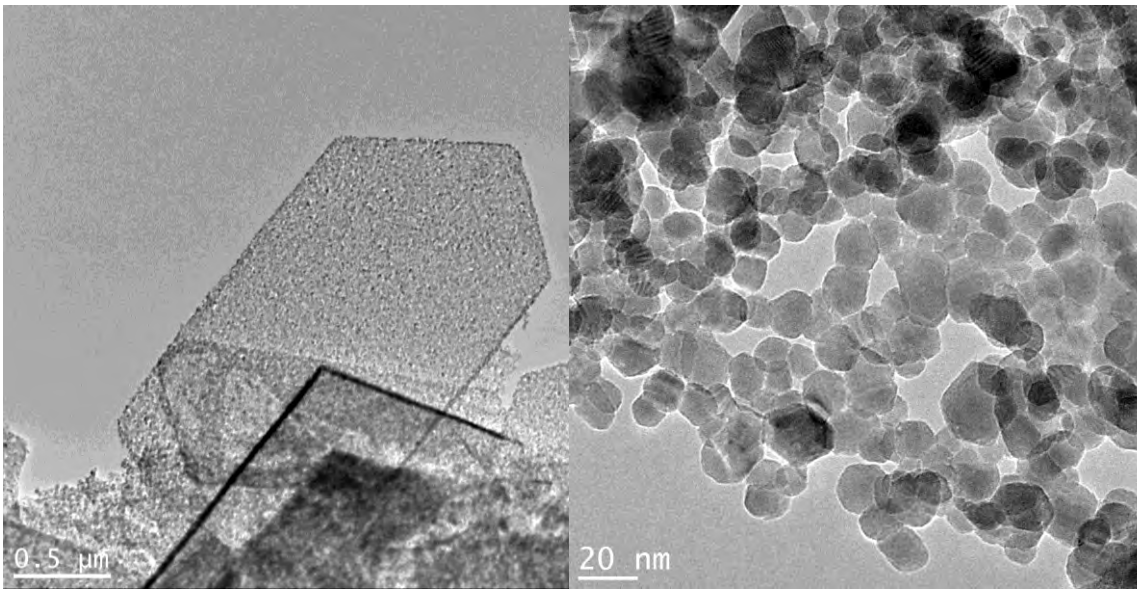

(a) **(b)**

Figure 9.1. *TEM-BF images of ZnO particles produced with MicNo® method showing (a) hexagonal platelet and (b) nano sized primary particles*

In the literature, it was reported that heat treatment in vacuum conditions resulted in a change in electrical properties of ZnO and it is related with formation of oxygen vacancies via reduction in oxygen amount [148, 149]. It clearly shows that in vacuum, evaporation of constituent elements can be observed and stoichiometry could be changed, therefore, its behavior under TEM column vacuum with application of heating is become important. Before doing any in-situ heating experiments, phase diagram of the ZnO with respect to temperature and pressure needs to be studied. In the microscope, used in this thesis, vacuum level of the column is in the range of $1x10^{-10}$ and $5x10^{-11}$ atm pressure and according to the phase diagram, given in Figure 9.2, solid ZnO become gaseous state via sublimation at 665°C and 625°C, respectively.

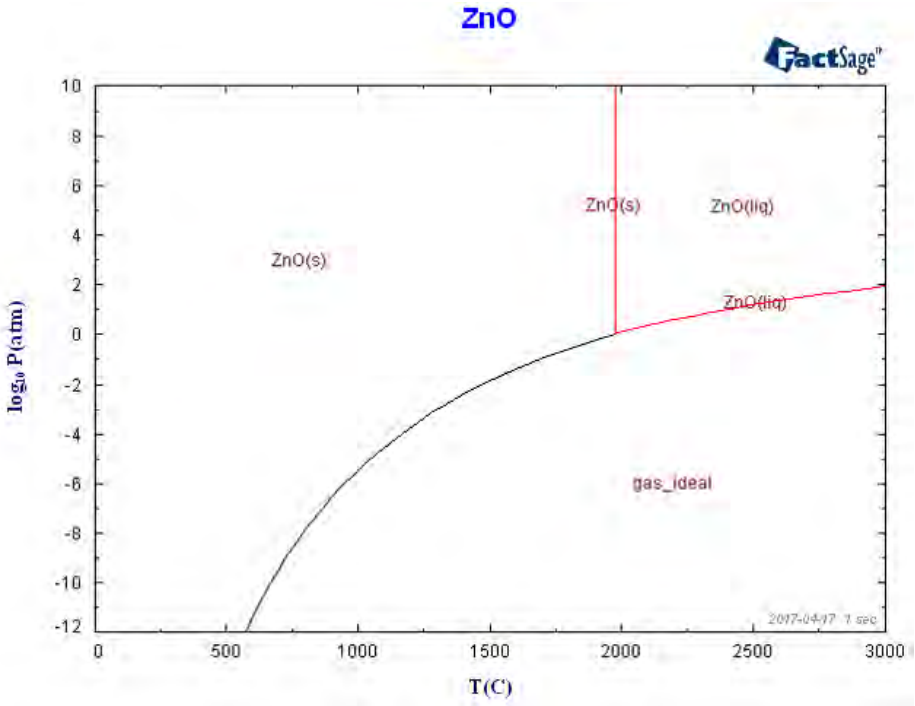

Figure 9.2. *ZnO phase diagram, calculated with FactSage software*

Preliminary in-situ heating experiment was done at 200°C for 30 minutes in order to understand the behavior of heating chip as well as ZnO particles. During temperature changes, bulging of the support film was experienced due to thermal expansion of the film in a constrained surface. Therefore, after every temperature change eucentric height of the ROI needs to be adjusted. During heating of the sample, in order to track the changes video was recorded and during this procedure sample was illuminated with e^- beam. Figure 9.3(a-d) shows the images taken from video at 5 minutes of intervals. In these images, it can be seen that spherical morphology of the primary particles lost with increasing time and pores between particles grew against all expectations towards densification. After 15 and 20 minutes, electron beam intensity gradually increased and particles were destroyed and vanished with time, which is an indication of e^- beam damage via radiolysis and sputtering [150] as shown in Figure 9.3(e-g).

In order to confirm beam damage, same beam dose were applied continuously to the same particle at room temperature and it was observed that damaging of the particles continues as given in Figure 9.4. This observation showed that during video recordings beam damaging exist in addition to the heating effect, therefore, e^- beam should be turned off during heating and the changes were tracked with still images taken with intervals in all further experiments.

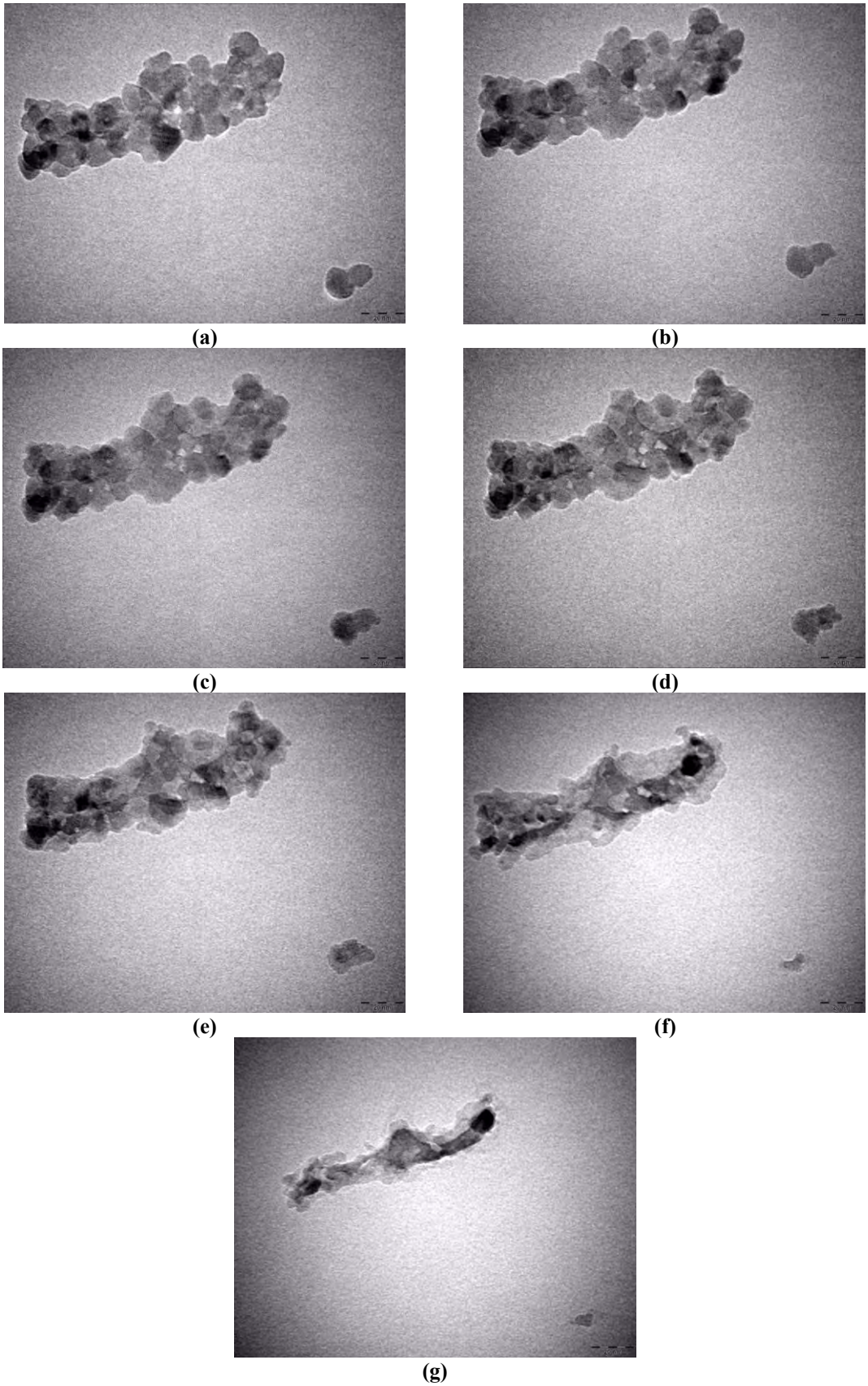

Figure 9.3. *(a-g) TEM-BF images taken from the video recordings with 5 minutes intervals during in-situ heating at 200°C. In (e) and (f) electron dose gradually increased at 15th and 20th minutes, respectively*

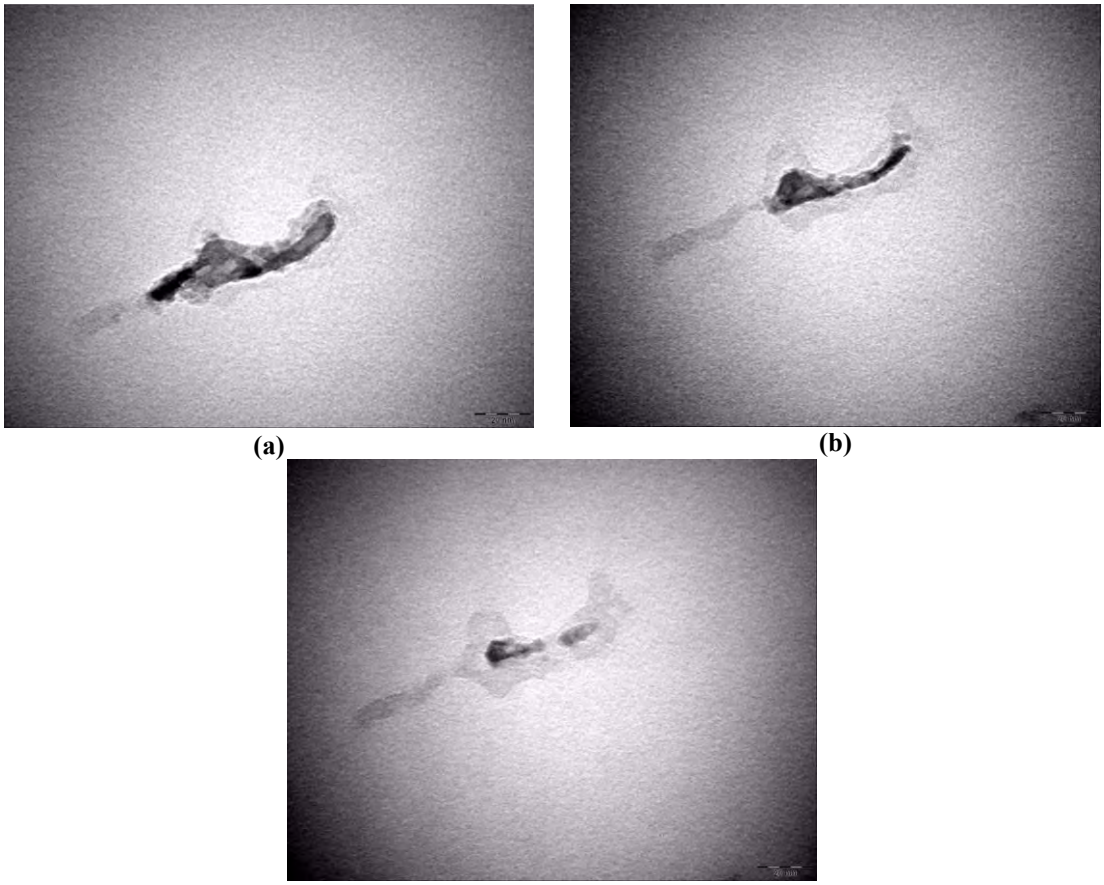

Figure 9.4. *(a-c) TEM-BF images of same region given in Figure 9.3 taken with 5 minutes intervals at room temperature but same e^- beam dose showing clear beam damage*

Sintering temperature during in-situ heating studies should be below that sublimation point, therefore, first experiment was conducted at 650°C and at that temperature, phase transformation occur via sublimation; solid particles evaporates instead of sintering and densification. TEM-BF images of the sample is given in Figure 9.5 and according to these images, it can be seen that pores between particles grow with time and after an hour, more than 50 % of total particles sublimated inside the microscope. After this result, in-situ heating temperature was decreased down to 550°C, which is lower than sublimation point according to the calculated phase diagram. In-situ heating was conducted for 3 hours and images taken during this experiment is given in Figure 9.6. According to these images, instead of sintering, sublimation occurred gradually starting from the surface of the ZnO particles. Sublimation rate was lower than experiment that conducted at 650°C and similar sublimation was observed after 3 hours at 550°C compared to experiment held at 650°C. The reason of sublimation at this temperature, which is lower than sublimation temperature, can be explained with the

effect of e^- beam. Even though electron beam was only turned on during image capturing, electron beam might activate the sublimation process via heating of the particles to above phase transformation temperature.

Based on these results, in-situ heating experiment temperature was decreased down to 500°C for 6 hours of holding time. In this experiment, any significant sublimation was not observed after 6 hours, and also any indication of sintering or densification was not observed according to the series of images taken during experiment. In these images, any neck formation or morphology change was not present, which indicates that either holding time and/or temperature was not enough for sintering. Another possible way is to increase holding time at 500°C above 6 hours, but then this experiment become unpractical.

In the literature [151], effect of oxygen pressure on the sintering of ZnO was studied at various temperatures. This study showed that decreasing sintering temperature from 800°C to 500°C resulted in a significant decrease in surface area (Δ_{SA}) for a given period. In one hour at the same oxygen pressure, 28.8 % and 90.3 % of surface area reduction were occurred for 500°C and 800°C, respectively. this study also showed that decrease in pressure at 500°C resulted in a decrease in Δ_{SA}; decreasing pressure from 0.5 atm to 0.003 atm, the required time to get the same Δ_{SA} reduction is doubled and the time is significantly increased at $1x10^{-8}$ atm which is relatively higher pressure compared to the $1x10^{-10}$ atm column pressure. Based on these results, reduction of surface area requires more than 6 hours at 500°C under the column pressure. In the same study, change of Δ_{SA} at lower pressures related with the formation of oxygen deficient metallic zinc at the surface of the particles, here it was also tried to be measured by quantification of the zinc and oxygen elements. However, due to the significant beam damage, that changes the stoichiometry, occur during STEM-EDX analyses, and quantitative measurements cannot performed successfully.

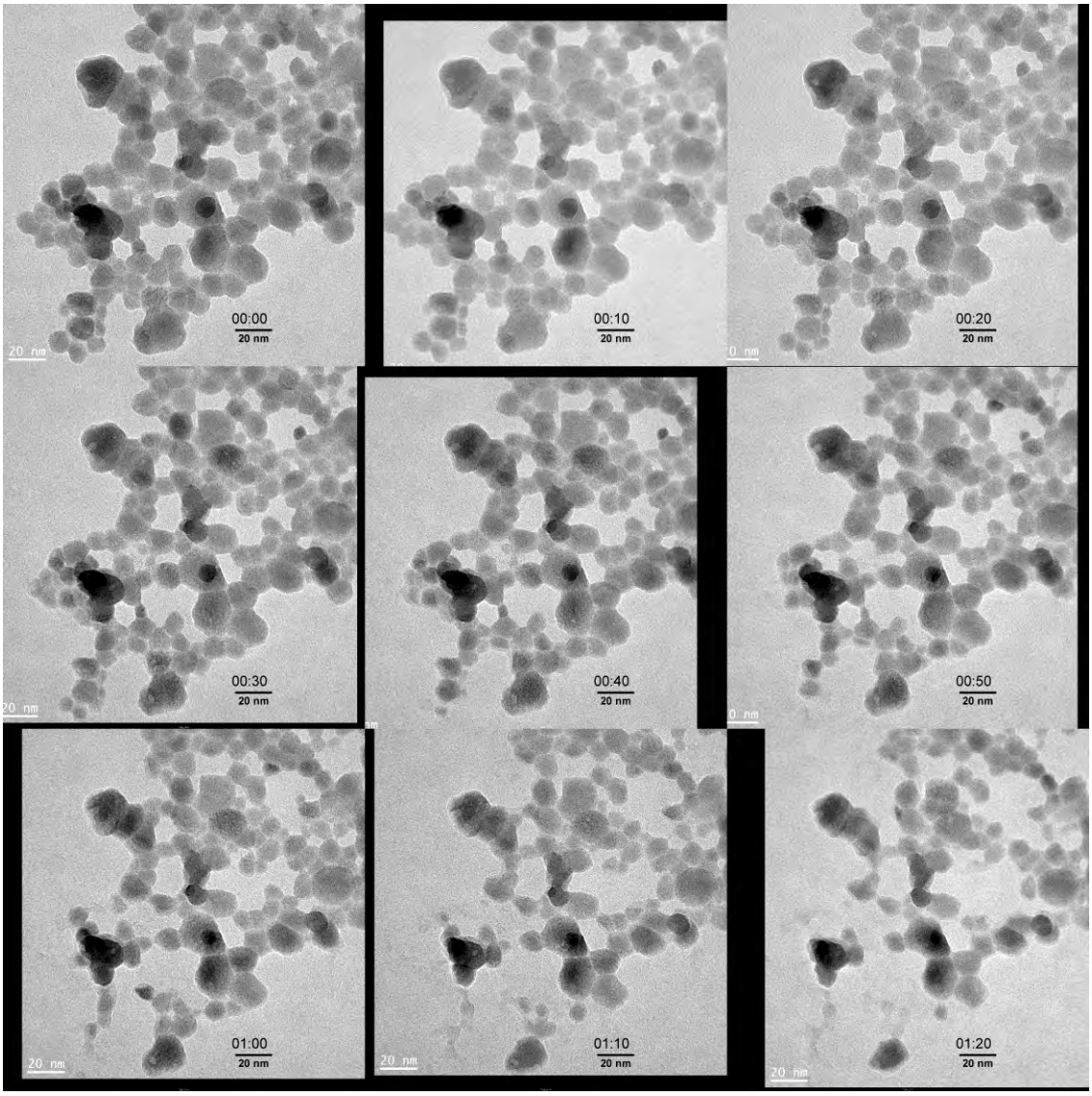

Figure 9.5. *TEM-BF images of the ZnO particles at 650°C, images were taken with 10 minutes of intervals*

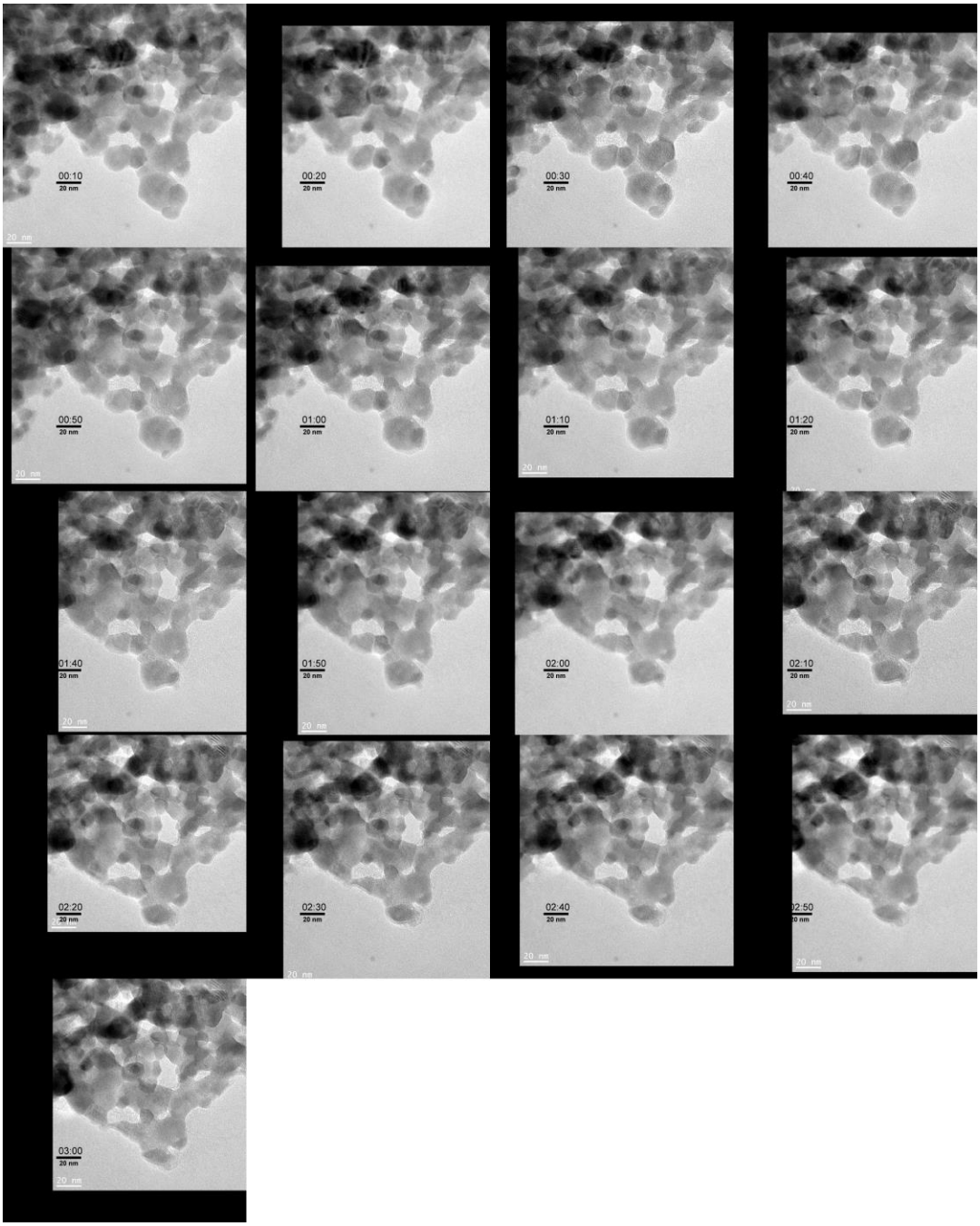

Figure 9.6. *TEM-BF images of the ZnO particles at 550°C, images were taken with 10 minutes of intervals*

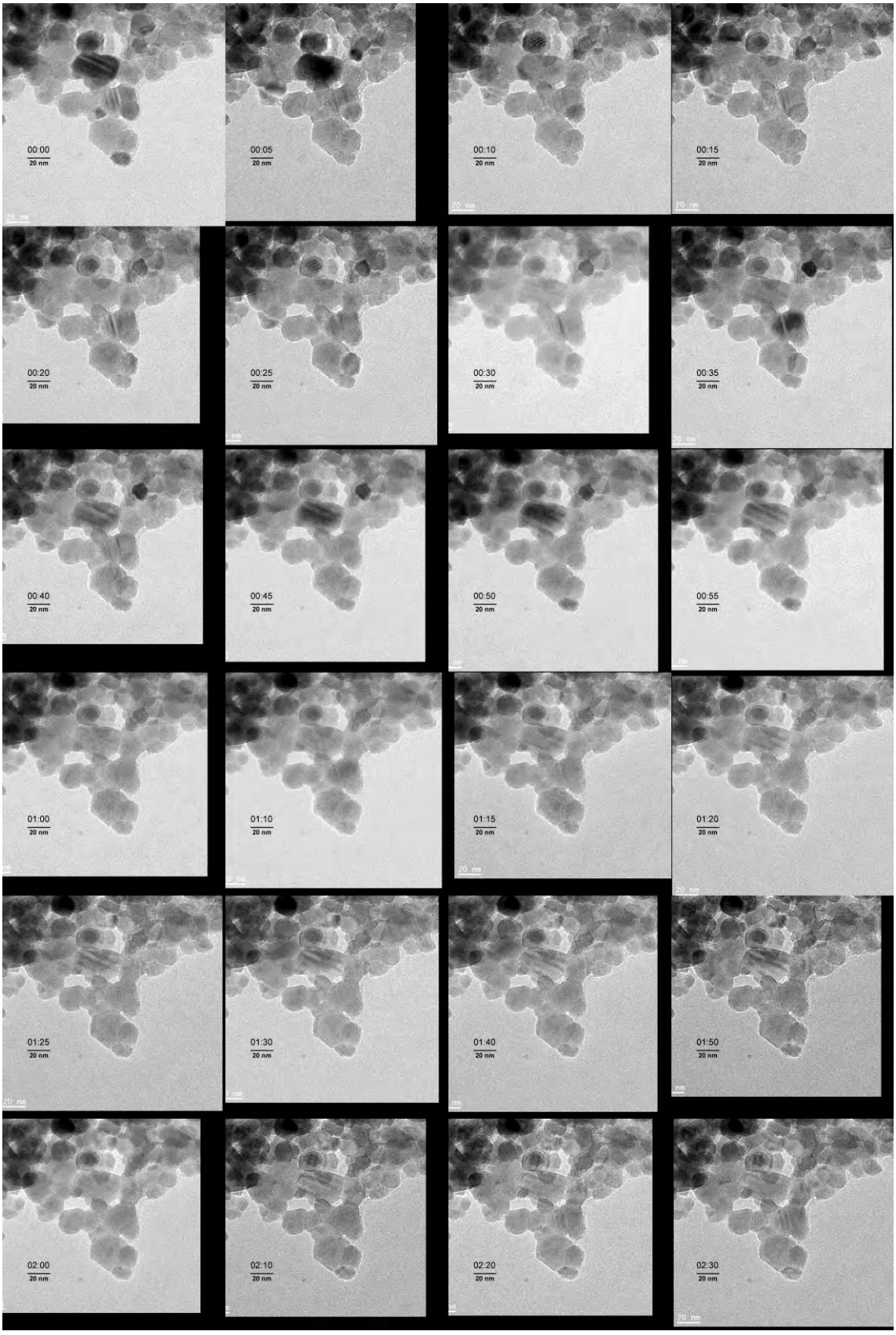

Figure 9.7. *TEM-BF images of the ZnO particles at 500°C, images were taken with 10 and 20 minutes of intervals*

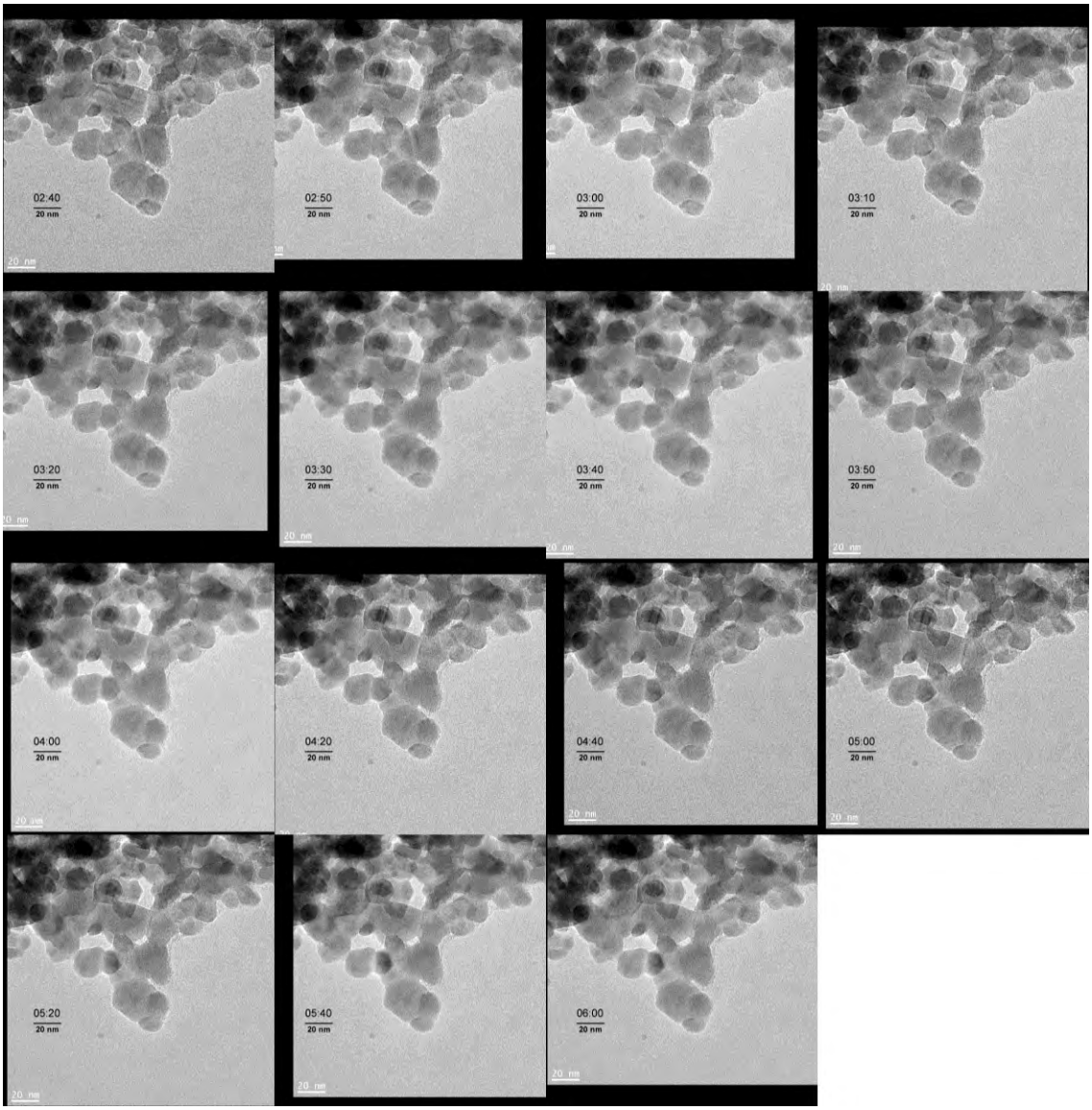

Figure 9.7. (continued) TEM-BF images of the ZnO particles at 500°C, images were taken with 10 and 20 minutes of intervals

During heating experiments, it was found that contrast in TEM-BF images for some of the primary particles changed after sintering when images compared before and after heating at 500°C for 90 minutes (Figure 9.8). When these two images are compared it can be seen that only contrast change occurred, however, morphology and particle sizes remained the same. From these results, it can be concluded that orientation change of these particles might be occurred due to the contrast mechanism of TEM-BF imaging.

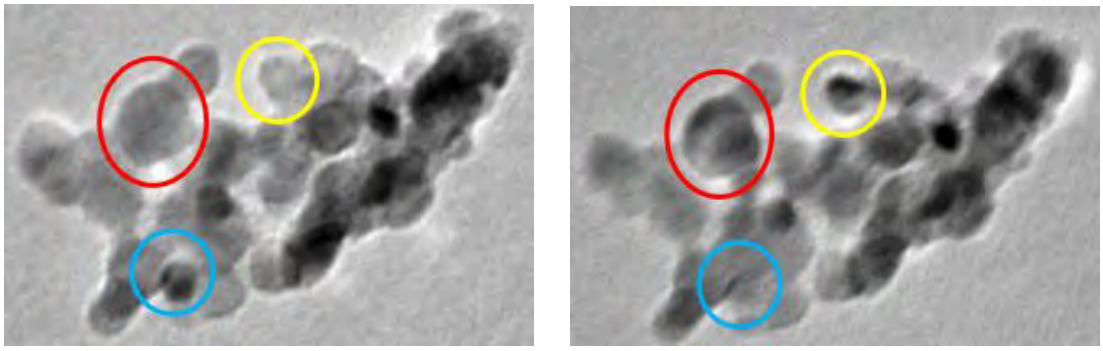

(a) **(b)**

Figure 9.8. *TEM-BF images: (a) before and (b) after 90 minutes of heating at 500°C*

Orientation change of the primary particles can be characterized with orientation mapping via TEM-PED method and for this purpose orientation maps were obtained at room temperature after every 30 minutes at 500°C. In this experiment, 0° of precession was used during scans since it gives better results compared to 0.3° and 0.7° of precession, which is not given here and during heating, beam blanker was used to prevent any possible effects caused by the e^- beam. Orientation maps after every 30 minutes showed that orientation of each particles remained the same and any orientation change was not observed in contrast with results given in Figure 9.9. Based on these results, unchanged orientation of particles can be explained as;

(i) Orientation of these particles can be thermodynamically stable due to the production method. Since it is a solution based method, during formation of platelets particles, can be arranged in the most stable conditions,

(ii) Interaction of particles with $SiN_{(x)}$ support film might prevent rotation of particles,

(iii) After few e^- beam scans over the same area during whole experiment, end up with carbon contamination build-up as shown in Figure 9.9(f) and ZnO particles trapped between carbon and $SiN_{(x)}$ layers, which might also prevent the rotation of particles.

During these experiments, one of the major limitation of TEM-PED method was experienced that is overlapped particles at the center indexed with very low reliability due to the overlapped diffraction patterns.

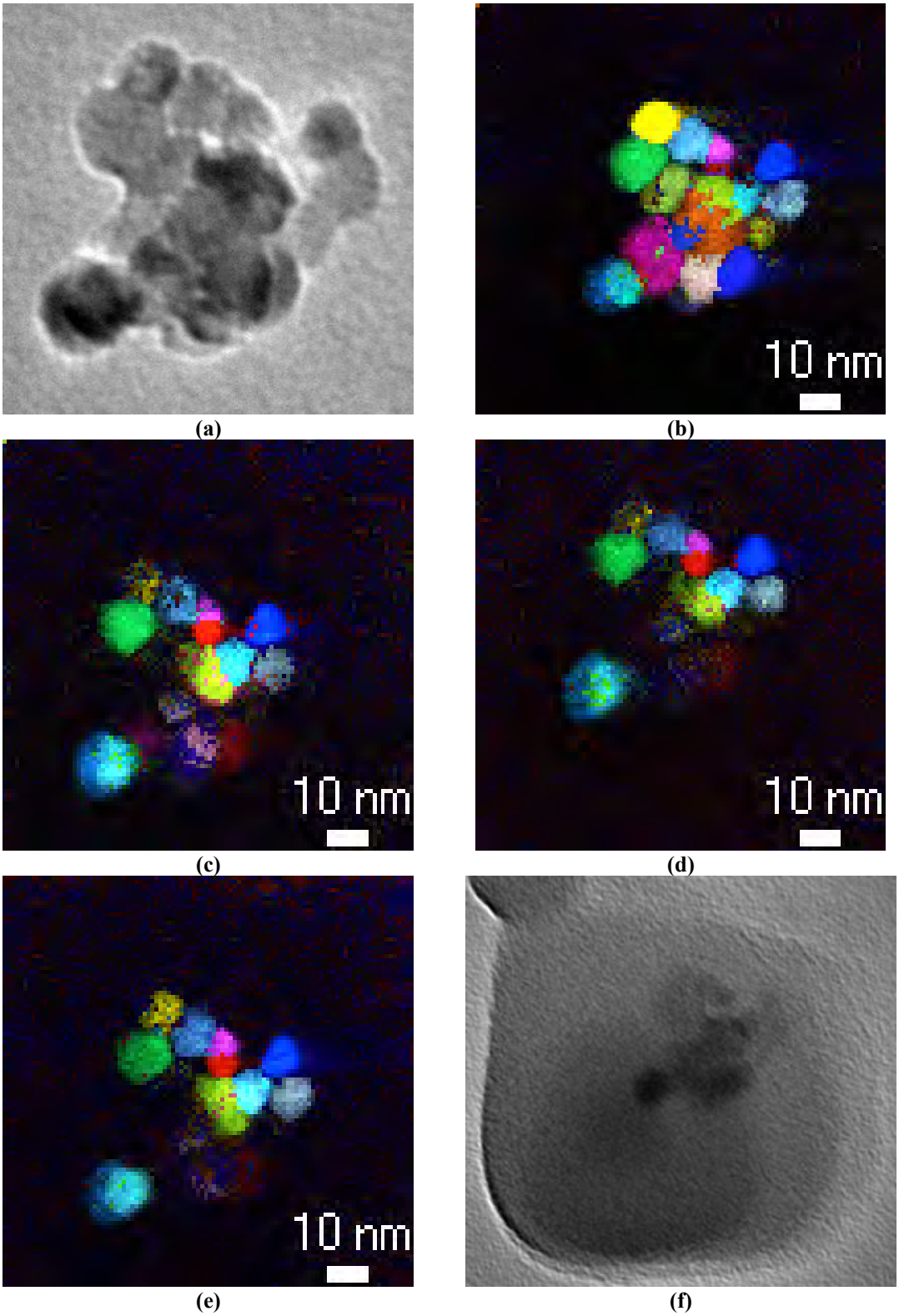

Figure 9.9. *(a) TEM-BF image and (b) orientation map before heating, orientation maps after (c) 30, (d) 60, (e) 90 minutes at 500°C and (f) TEM-BF image after the experiment*

9.3. Conclusions

In this section of this thesis, in-situ heating experiments of 15±5 nm sized ZnO particles inside TEM were conducted in order to determine sintering kinetics. During these studies, three different sintering temperatures; 500°C, 550°C and 650°C were used and higher temperatures cannot be used due to the phase transformation via sublimation at $1x10^{-10}$ and $5x10^{-11}$ atm pressures. During the in-situ heating experiments it was also found that at 550°C and 650°C, particles in solid state turn into gaseous state starting from the particle surface and phase transformation rate decreased with the decrease in temperature. At these temperatures, sublimation was occurred before sintering and densification, therefore, heating temperature was decreased down to 500°C to prevent sublimation. In the experiments done at 500°C for 6 hours, there were no change in the particles, thus, any indication of sintering and densification were not observed at this temperature due to the very low pressure and possibly low diffusion. During the experiments, effect of e^- beam on the ZnO particles was seen as sublimation and/or damage to the particles, thus during all experiments electron beam was only turned on during imaging between time intervals. In order to confirm the literature about the oxygen deficiency at the surface of ZnO particles, STEM-EDX method was used, however due to the aggressive probe damage quantitative analyses could not be performed. During the experiments at 500°C, it was found that some of the particles change its orientation according to the TEM-BF contrast and in order to track orientation changes, orientation mapping with TEM-PED method was utilized. During this experiment, however, any orientation change was not observed.

10. GENERAL CONCLUSIONS AND FUTURE STUDIES

In this thesis, precession electron diffraction and in-situ heating methods were used successfully for the characterizations of different types of materials like oxide, metal and ceramic composites. In each different material type methods stated above were used for various purposes;

(i) In ceramic composites orientation relationship between in-situ formed and matrix phase as well as phase identification were carried out by using TEM-PED method,

(ii) In petroleum steel, TEM-PED was carried for the phase identification of precipitate particle,

(iii) In-situ heating experiments were carried out for the characterization of sintering behavior of oxide nano particles.

During these experiments, several important observations were made about these methods;

(i) Overlapped particles have significant disadvantage on the TEM-PED results. Due to the template matching methodology used in this method, indexing of the overlapped particle or grains can be resulted in unreliable orientation and phase maps. During template matching, templates of both overlapped particles are searched for the best possible solution but diffraction pattern contains information from both phases and templates are matched with one of the best fitting diffraction pattern even if the matched phase is different from the present phase.

(ii) Phases that have very similar crystal lattice dimensions resulted in misindexing. Due to the limitations on sensitivity of external CCD camera during diffraction pattern recording, crystal structures with similar lattice parameters cannot be separated from each other successfully. Therefore supporting analyses should be carried out for the confirmation of the phase or orientation found according to the template matching.

(iii) Angular resolution of this method is 1° and if more precise measurements are required different methods should be used.

(iv) Phase characterization of the investigated sample can be done without doing any tilting to the zone axis with TEM-PED method.

(v) Phase and orientation maps can be obtained with and without precession during TEM-PED method. Even though, most of the cases TEM-PED results have high reliability with the application of precession, phase and orientation maps should

also be obtained without precession in order to compare the results. In addition to that in this study 0.7° of precession were used during experiments and this decision was made by trial and error by trying several different precession angles. Then precession angle which provide results with highest reliability was selected for further analyses.

(vi) In situ heating experiments inside the TEM should be designed carefully. Due to the very high vacuum levels of the conventional TEM, behavior of heated sample can be different compared to the heating at the atmospheric pressure. For example in ZnO particles phase transformation behavior and temperature change due to the very high vacuum level during in-situ heating experiments. Therefore, before starting user should be carefully design the heating experiment by considering the effect of atmosphere and vacuum of TEM.

There are several different future studies can be suggested about the material systems studied and methods used in this thesis.

(i) One possible study will be about the high resolution STEM imaging of Ar atoms inside the crystal structure of hBN particles, in order to understand position of the implanted atoms whether they are implanted in between basal planes or delamination cracks.

(ii) Effects of ion beam milling argon implantation into the graphite particles with different orientations should be carried out.

(iii) Another study should be about the (0001) twist grain boundary energy change of hBN crystal with molecular dynamic simulations in order to characterize whether twist boundaries in hBN particles thermodynamically favorable or not.

(iv) Another study should be done about the comparison of TEM-PED and SEM-TKD methods in order to understand limitations and advantages of both methods for orientation and phase mapping in various material systems.

(v) The quantitative chemical analysis of the solid solution found in B_4C-TiB_2 composites should be verified with EELS quantification methods.

(vi) To characterize the effects of sintering method on the microstructure, solid solution compositions, thermal and electrical conductivities B_4C-TiB_2 powder mixtures that were hot pressed sintered and by using SPS will be carried out.

REFERENCES

[1] Shim, S.H., Nihara, K., Auh, K.H., and Shim, K.B., *Crystallographic orientation of ZrB2-ZrC composites manufactured by the spark plasma sintering method.* Journal of Microscopy, 2002. **205**(3): p. 238-244.

[2] Zhang, D., Yang, Z., Lu, W., and Xu, D., *In Situ Synthesis of Hybrid-reinforced Titanium Matrix Composites.* Solid State Phenomena, 2007. **127**: p. 155-160.

[3] Wang, X., Song, X., Liu, X., Liu, X., Wang, H., and Zhou, C., *Orientation relationship in WC-Co composite nanoparticles synthesized by in situ reactions.* Nanotechnology, 2015. **26**(14): p. 145705.

[4] Polkowski, W., Jóźwik, P., and Bojar, Z., *Electron Backscatter Diffraction Study on Microstructure, Texture, and Strain Evolution in Armco Iron Severely Deformed by the Differential Speed Rolling Method.* Metallurgical and Materials Transactions A, 2015. **46**(5): p. 2216-2226.

[5] Engler, O. and Randle, V., *Introduction to Texture Analysis: Macrotexture, Microtexture, and Orientation Mapping*. Second edition ed. 2009: CRC Press.

[6] Suwas, S. and Kumar Ray, R., *Crystallographic Texture of Materials*. 1 ed. Engineering Materials and Processes, ed. B. Derby. 2014: Springer-Verlag London.

[7] Schwartz, A.J., Kumar, M., Adams, B.L., and Field, D.P., eds. *Electron Backscatter Diffraction in Materials Science*. 2 ed. 2009, Springer US.

[8] Jr, W.D.C. and Rethwisch, D.G., *Materials Science and Engineering: An Introduction*. 8th edition ed. 2010: John Wiley and Sons.

[9] Wang, Y.N. and Huang, J.C., *Texture analysis in hexagonal materials.* Materials Chemistry and Physics, 2003. **81**(1): p. 11-26.

[10] Moeck, P. and Rouvimov, S. (2010) Precession electron diffraction and its advantages for structural fingerprinting in the transmission electron microscope, in *Zeitschrift für Kristallographie International journal for structural, physical, and chemical aspects of crystalline materials*. 2010. p. 110.

[11] Sneddon, G.C., Trimby, P.W., and Cairney, J.M., *Transmission Kikuchi diffraction in a scanning electron microscope: A review.* Materials Science and Engineering: R: Reports, 2016. **110**: p. 1-12.

[12] Brodusch, N., Demers, H., and Gauvin, R., *Nanometres-resolution Kikuchi patterns from materials science specimens with transmission electron forward scatter diffraction in the scanning electron microscope.* J Microsc, 2013. **250**(1): p. 1-14.

[13] Zaefferer, S., *A critical review of orientation microscopy in SEM and TEM.* Crystal Research and Technology, 2011. **46**(6): p. 607-628.

[14] Schwarzer, R.A., *The Determination of Local Texture by Electron Diffraction–A Tutorial Review.* Textures and Microstructures, 1993. **20**(1-4): p. 7-27.

[15] Pennycook, S.J., David, B., and Williams, C.B., *Transmission Electron Microscopy: A Textbook for Materials Science.* Microscopy and Microanalysis, 2010. **16**(1): p. 111.

[16] Turan, S. (1995) Microstructural Characterization of Silicon Nitride-Silicon Carbide Particulate Composites, in *Churchill College*. 1995, University of Cambridge: Cambridge.

[17] Midgley, P.A. and Eggeman, A.S., *Precession electron diffraction - a topical review.* IUCrJ, 2015. **2**(Pt 1): p. 126-36.

[18] Rauch, E.F. and Véron, M., *Automated crystal orientation and phase mapping in TEM.* Materials Characterization, 2014. **98**(Supplement C): p. 1-9.

[19] Brons, J.G. and Thompson, G.B., *Orientation Mapping via Precession-Enhanced Electron Diffraction and Its Applications in Materials Science.* Jom, 2013. **66**(1): p. 165-170.

[20] Jiang, J., Jorda, J.L., Yu, J., Baumes, L.A., Mugnaioli, E., Diaz-Cabanas, M.J., Kolb, U., and Corma, A., *Synthesis and Structure Determination of the Hierarchical Meso-Microporous Zeolite ITQ-43.* Science, 2011. **333**(6046): p. 1131-1134.

[21] Morniroli, J.P., Redjaïmia, A., and Nicolopoulos, S., *Contribution of electron precession to the identification of the space group from microdiffraction patterns.* Ultramicroscopy, 2007. **107**(6): p. 514-522.

[22] Estradé, S., Portillo, J., Yedra, L., Rebled, J.M., and Peiró, F., *EELS signal enhancement by means of beam precession in the TEM.* Ultramicroscopy, 2012. **116**: p. 135-137.

[23] Liao, Y. and Marks, L.D., *Reduction of electron channeling in EDS using precession.* Ultramicroscopy, 2013. **126**: p. 19-22.

[24] Avilov, A., Kuligin, K., Nicolopoulos, S., Nickolskiy, M., Boulahya, K., Portillo, J., Lepeshov, G., Sobolev, B., Collette, J.P., Martin, N., Robins, A.C., and Fischione, P., *Precession technique and electron diffractometry as new tools for crystal structure analysis and chemical bonding determination.* Ultramicroscopy, 2007. **107**(6): p. 431-444.

[25] Izadi, E., Darbal, A., Sarkar, R., and Rajagopalan, J., *Grain rotations in ultrafine-grained aluminum films studied using in situ TEM straining with automated crystal orientation mapping.* Materials & Design, 2017. **113**: p. 186-194.

[26] Rankin, J. and Sheldon, B.W., *In situ TEM sintering of nano-sized ZrO2 particles.* Materials Science and Engineering: A, 1995. **204**(1): p. 48-53.

[27] Gatan. 2018 [cited 2018 20/10]; Available from: http://www.gatan.com/products/specimen_holders/products/628-Single-Tilt-Heating-Holder.php.

[28] DensSolutions. [cited 2018 20/10]; Available from: http://denssolutions.com/products/wildfire/.

[29] Divitini, G., Cacovich, S., Matteocci, F., Cinà, L., Di Carlo, A., and Ducati, C., *In situ observation of heat-induced degradation of perovskite solar cells.* Nature Energy, 2016. **1**: p. 15012.

[30] Gocyla, M., Kuehl, S., Shviro, M., Heyen, H., Selve, S., Dunin-Borkowski, R.E., Heggen, M., and Strasser, P., *Shape Stability of Octahedral PtNi Nanocatalysts for Electrochemical Oxygen Reduction Reaction Studied by in situ Transmission Electron Microscopy.* ACS Nano, 2018.

[31] Goris, B., Van Huis Marijn, A., Bals, S., Zandbergen Henny, W., Manna, L., and Van Tendeloo, G., *Thermally Induced Structural and Morphological Changes of CdSe/CdS Octapods.* Small, 2012. **8**(6): p. 937-942.

[32] Chankhunthod, N., Aslam, Z., Critchley, K., Evans, S.D., and Brydson, R., *Kinetically controlled fabrication of gold nanorods and investigation of their thermal stability via in-situ TEM heating.* Journal of Physics: Conference Series, 2017. **902**(1): p. 012007.

[33] Malladi, S.K., Xu, Q., van Huis, M.A., Tichelaar, F.D., Batenburg, K.J., Yücelen, E., Dubiel, B., Czyrska-Filemonowicz, A., and Zandbergen, H.W., *Real-Time*

Atomic Scale Imaging of Nanostructural Evolution in Aluminum Alloys. Nano Letters, 2014. **14**(1): p. 384-389.

[34] Hawkes, P.W. and Spence, J.C.H., eds. *Science of Microscopy*. 2007, Springer New York.

[35] Saka, H., Kamino, T., Ara, S., and Sasaki, K., *In Situ Heating Transmission Electron Microscopy.* MRS Bulletin, 2011. **33**(2): p. 93-100.

[36] Figuerola, A., Huis, M.v., Zanella, M., Genovese, A., Marras, S., Falqui, A., Zandbergen, H.W., Cingolani, R., and Manna, L., *Epitaxial CdSe-Au Nanocrystal Heterostructures by Thermal Annealing.* Nano Letters, 2010. **10**(8): p. 3028-3036.

[37] Yalcin, A.O., Goris, B., van Dijk-Moes, R.J.A., Fan, Z., Erdamar, A.K., Tichelaar, F.D., Vlugt, T.J.H., Van Tendeloo, G., Bals, S., Vanmaekelbergh, D., Zandbergen, H.W., and van Huis, M.A., *Heat-induced transformation of CdSe-CdS-ZnS core-multishell quantum dots by Zn diffusion into inner layers.* Chemical Communications, 2015. **51**(16): p. 3320-3323.

[38] Yalcin, A.O., Fan, Z., Goris, B., Li, W.-F., Koster, R.S., Fang, C.-M., van Blaaderen, A., Casavola, M., Tichelaar, F.D., Bals, S., Van Tendeloo, G., Vlugt, T.J.H., Vanmaekelbergh, D., Zandbergen, H.W., and van Huis, M.A., *Atomic Resolution Monitoring of Cation Exchange in CdSe-PbSe Heteronanocrystals during Epitaxial Solid–Solid–Vapor Growth.* Nano Letters, 2014. **14**(6): p. 3661-3667.

[39] Rankin, J. and Boatner, L.A., *Unstable Neck Formation during Initial-Stage Sintering.* Journal of the American Ceramic Society, 1994. **77**(8): p. 1987-1990.

[40] Rankin, J., *In Situ TEM Heating of Nanosized ZrO2.* Journal of the American Ceramic Society, 1999. **82**(6): p. 1560-1564.

[41] Asoro, M.A., Ferreira, P.J., and Kovar, D., *In situ transmission electron microscopy and scanning transmission electron microscopy studies of sintering of Ag and Pt nanoparticles.* Acta Materialia, 2014. **81**(0): p. 173-183.

[42] Matsuno, M., Bonifacio, C., Thron, A., Rufner, J., Holland, T., and van Benthem, K., *In situ Sintering of Ni Nanoparticles by Controlled Heating*. Vol. 17. 2011. 524-525.

[43] Asoro, M.A., Kovar, D., Shao-Horn, Y., Allard, L.F., and Ferreira, P.J., *Coalescence and sintering of Pt nanoparticles: in situ observation by aberration-corrected HAADF STEM.* Nanotechnology, 2010. **21**(2): p. 025701.

[44] Canovic, S., Jonsson, T., and Halvarsson, M., *Grain contrast imaging in FIB and SEM.* Journal of Physics: Conference Series, 2008. **126**(1): p. 012054.

[45] E. Lloyd, G., *Atomic Number and Crystallographic Contrast Images with the SEM: A Review of Backscattered Electron Techniques*. Vol. 51. 1987. 3-19.

[46] Kaburagi, Y., Yoshida, A., and Hishiyama, Y., *Microtexture of highly crystallized graphite as studied by galvanomagnetic properties and electron channeling contrast effect.* Journal of Materials Research, 2011. **11**(3): p. 769-778.

[47] Kuo, W.C.H., Briceno, M., and Ozkaya, D., *FINAL ANALYSIS: Characterisation of Catalysts Using Secondary and Backscattered Electron In-lens Detectors.* Platinum Metals Review, 2014. **58**(2): p. 106-110.

[48] Rauch, E.F. and Dupuy, L., *Rapid spot diffraction patterns identification through template matching.* Arch. Metall. Mater., 2005. **50**(1): p. 87-99.

[49] Rauch, E.F., Portillo, J., Nicolopoulos, S., Bultreys, D., Rouvimov, S., and Moeck, P., *Automated nanocrystal orientation and phase mapping in the transmission electron microscope on the basis of precession electron diffraction.* Zeitschrift für Kristallographie, 2010. **225**(2-3).

[50] Rauch, E.F. and Duft, A., *Orientation Maps Derived from TEM Diffraction Patterns Collected with an External CCD Camera.* Materials Science Forum, 2005. **495-497**: p. 197-202.

[51] Viladot, D., Veron, M., Gemmi, M., Peiro, F., Portillo, J., Estrade, S., Mendoza, J., Llorca-Isern, N., and Nicolopoulos, S., *Orientation and phase mapping in the transmission electron microscope using precession-assisted diffraction spot recognition: state-of-the-art results.* J Microsc, 2013. **252**(1): p. 23-34.

[52] Shuba, R. and Chen, I.W., *Machinable α-SiAlON/BN Composites*. 2006.

[53] Yılmaz, Z. (2017) Bor Nitrür Silisyum Karbür Kompozitlerin Sentezi ve Özelliklerinin Araştırılması, in *Malzeme Bilimi ve Mühendisliği*. 2017, Anadolu University: Eskişehir.

[54] Wang, H., Li, G., Zhao, Y., and Chen, G., *In situ fabrication and microstructure of Al2O3 particles reinforced aluminum matrix composites.* Materials Science and Engineering: A, 2010. **527**(12): p. 2881-2885.

[55] Zhao, G., Chen, J., Zheng, L., Li, Y., Zhang, H., Gai, J., and Li, M., *In-situ synthesis, microstructure and properties of Ti2AlN/TiB2 composite.* International Journal of Materials Research, 2016. **108**(2): p. 133-138.

[56] Williams, D.B. and Carter, C.B., *Transmission Electron Microscopy: A Textbook for Materials Science*. 2009: Springer.

[57] Dieter, G.E., *Mechanical Metallurgy*. Student metric ed of 3rd revised ed edition ed. 1989: McGraw Hill Education.

[58] Turan, S. and Knowles, K.M., *High resolution transmission electron microscopy of the planar defect structure of hexagonal boron nitride.* physica status solidi (a), 1995. **150**(1): p. 227-237.

[59] Hagihara, K., Mayama, T., Honnami, M., Yamasaki, M., Izuno, H., Okamoto, T., Ohashi, T., Nakano, T., and Kawamura, Y., *Orientation dependence of the deformation kink band formation behavior in Zn single crystal.* International Journal of Plasticity, 2016. **77**(Supplement C): p. 174-191.

[60] Evans, A.G. and Adler, W.F., *Kinking as a mode of structural degradation in carbon fiber composites.* Acta Metallurgica, 1978. **26**(5): p. 725-738.

[61] Huang, J.Y. and Zhu, Y.T., *Advances in the Synthesis and Characterization of Boron Nitride.* Defect and Diffusion Forum, 2000. **186-187**: p. 1-32.

[62] Louisette, P., *Grain Boundaries: From Theory to Engineering*. Springer Series in Materials Science. 2013: Springer Netherlands.

[63] Schmid, H. and Rühle, M., *Structure of special grain boundaries in SiAlON ceramics.* Journal of Materials Science, 1984. **19**(2): p. 615-628.

[64] Schapink, F.W. and Erlings, J.G., *Electron diffraction from, near-coincidence twist boundaries.* Philosophical Magazine A, 1978. **38**(1): p. 115-118.

[65] Randle, V., *The role of the coincidence site lattice in grain boundary engineering*. Institute of Materials. 1996, London: Institute of Materials.

[66] Randle, V. and Institute of, M., *The role of the coincidence site lattice in grain boundary engineering*. Book (Institute of Materials (London, England)). 1996, London: Institute of Materials. vi, 120 p.

[67] Lejček, P., *Grain Boundaries: Description, Structure and Thermodynamics*, in *Grain Boundary Segregation in Metals*, P. Lejcek, Editor. 2010, Springer Berlin Heidelberg: Berlin, Heidelberg. p. 5-24.

[68] Wang, Y., Wang, C., Yuan, L., Cai, R., Liu, X., Li, C., and Zhou, G., *Coincidence-Site-Lattice Twist Boundaries in Bicrystalline α-Fe2O3 Nanoblades.* The Journal of Physical Chemistry C, 2014. **118**(11): p. 5796-5801.

[69] Liu, X. and Wang, J., *Low-energy, Mobile Grain Boundaries in Magnesium.* Scientific Reports, 2016. **6**: p. 21393.

[70] Shimomura, J., Funahashi, T., and Koitabashi, T., *Electron microscopy of hexagonal boron nitride powder.* Journal of Materials Science, 1995. **30**(12): p. 3193-3199.

[71] Bleris, G.L., Nouet, G., Hagege, S., and Delavignette, P., *Characterization of grain boundaries in the hexagonal system based on tables of coincidence site lattices (CSL's).* Acta Crystallograpica Section A, 1982. **A38**(July 1982): p. 550-557.

[72] Bonnet, R., Cousineau, E., and Warrington, D.H., *Determination of Near-Coincident Cells for Hexagonal Crystals, Related DSC Lattices.* Acta Crystallograpica Section A, 1981. **37**: p. 184-189.

[73] Gunjishima, I., Akashi, T., and Goto, T., *Characterization of Directionally Solidified B4C-TiB2 and B4C-SiC Eutectic Composites Prepared by Floating-Zone Method.* Materials Transactions, JIM, 2002. **43**(4): p. 712-720.

[74] Sigl, L.S., *Processing and mechanical properties of boron carbide sintered with TiC.* Journal of the European Ceramic Society, 1998. **18**(11): p. 1521-1529.

[75] Sahin, F.C., Apak, B., Akin, I., Kanbur, H.E., Genckan, D.H., Turan, A., Goller, G., and Yucel, O., *Spark plasma sintering of B4C–SiC composites.* Solid State Sciences, 2012. **14**(11-12): p. 1660-1663.

[76] Ji, W., Rehman, S.S., Wang, W., Wang, H., Wang, Y., Zhang, J., Zhang, F., and Fu, Z., *Sintering boron carbide ceramics without grain growth by plastic deformation as the dominant densification mechanism.* Scientific Reports, 2015. **5**: p. 15827.

[77] Yamada, S., Hirao, K., Yamauchi, Y., and Kanzaki, S., *High strength B4C–TiB2 composites fabricated by reaction hot-pressing.* Journal of the European Ceramic Society, 2003. **23**(7): p. 1123-1130.

[78] Richerson, D.W., *Modern ceramic engineering: properties, processing, and use in design*. 2005: CRC press.

[79] Wen, G., Li, S.B., Zhang, B.S., and Guo, Z.X., *Reaction synthesis of TiB2–TiC composites with enhanced toughness.* Acta Materialia, 2001. **49**(8): p. 1463-1470.

[80] Gu, Y., Liu, J.-X., Xu, F., and Zhang, G.-J., *Pressureless sintering of titanium carbide doped with boron or boron carbide.* Journal of the European Ceramic Society, 2017. **37**(2): p. 539-547.

[81] Wang, Y.-j., Peng, H.-x., Ye, F., and Zhou, Y., *Effect of TiB2 content on microstructure and mechanical properties of in-situ fabricated TiB2/B4C composites.* Transactions of Nonferrous Metals Society of China, 2011. **21**: p. s369-s373.

[82] Cinar, A., Baskut, S., Seyhan, A.T., and Turan, S., *Tailoring the properties of spark plasma sintered SiAlON containing graphene nanoplatelets by using different exfoliation and size reduction techniques: Anisotropic mechanical and thermal properties.* Journal of the European Ceramic Society, 2018. **38**(4): p. 1299-1310.

[83] Xue, J.-X., Liu, J.-X., Xie, B.-H., and Zhang, G.-J., *Pressure-induced preferential grain growth, texture development and anisotropic properties of hot pressed hexagonal boron nitride ceramics.* Scripta Materialia, 2011. **65**(11): p. 966-969.

[84] Sasaki, G., Suga, T., Yanai, T., Suganuma, K., and Niihara, K., *Microstructure of B4C/TiB2 composite fabricated by reaction sintering of B4C and TiC.* Journal of the Ceramic Society of Japan, 1994. **102**(1184): p. 321-325.

[85] Riley, F.L., *Silicon Nitride and Related Materials.* Journal of the American Ceramic Society, 2000. **83**(2): p. 245-265.

[86] Mitomo, M. and Fukunaga, O., *The Stability of α-sialon at High Temperatures.* Journal of the Ceramic Association, Japan, 1981. **89**(1035): p. 631-633.

[87] Fan, Z.Y. and Newman, N., *Experimental determination of the rates of decomposition and cation desorption from AlN surfaces.* Materials Science and Engineering: B, 2001. **87**(3): p. 244-248.

[88] Lee, S.-H., Guo, S., Tanaka, H., Kurashima, K., Nishimura, T., and Kagawa, Y., *Thermal decomposition, densification and mechanical properties of AlN–SiC(–TiB2) systems with and without B, B4C and C additives.* Journal of the European Ceramic Society, 2008. **28**(8): p. 1715-1722.

[89] Sun, E.Y., Becher, P.F., Plucknett, K.P., Hsueh, C.-H., Alexander, K.B., Waters, S.B., Hirao, K., and Brito, M.E., *Microstructural Design of Silicon Nitride with*

Improved Fracture Toughness: II, Effects of Yttria and Alumina Additives. Journal of the American Ceramic Society, 1998. **81**(11): p. 2831-2840.

[90] Calis Acikbas, N., Yurdakul, H., Mandal, H., Kara, F., Turan, S., Kara, A., and Bitterlich, B., *Effect of sintering conditions and heat treatment on the properties, microstructure and machining performance of α-β-SiAlON ceramics.* Journal of the European Ceramic Society, 2012. **32**(7): p. 1321-1327.

[91] Failla, S., Melandri, C., Zoli, L., Zucca, G., and Sciti, D., *Hard and easy sinterable B4C-TiB2-based composites doped with WC.* Journal of the European Ceramic Society, 2018. **38**(9): p. 3089-3095.

[92] Skorokhod, V. and Krstic, V.D., *High strength-high toughness B4C-TiB2 composites.* Journal of Materials Science Letters, 2000. **19**(3): p. 237-239.

[93] Telle, R., Fendler, E., and Pettsov, G., *The quasiternary TiB2-W2B5-CrB2 system and its possibilities in evolution of ceramic hard materials.* Powder Metallurgy and Metal Ceramics, 1993. **32**(3): p. 240-248.

[94] Kuz'ma, Y.B., Svarichevskaya, S., and Telegus, V., *Systems titanium-tungsten-boron, hafnium-tantalum-boron, and tantalum-tungsten-boron.* Soviet Powder Metallurgy and Metal Ceramics, 1971. **10**(6): p. 478-481.

[95] Yasinskaya, G. and Groisberg, M., *Interaction of titanium boride with niobium and tungsten.* Soviet Powder Metallurgy and Metal Ceramics, 1963. **2**(6): p. 457-458.

[96] Sun- Yong, A. and Shinhoo, K., *Formation of Core/Rim Structures in Ti(C,N)-WC- Ni Cermets via a Dissolution and Precipitation Process.* Journal of the American Ceramic Society, 2000. **83**(6): p. 1489-1494.

[97] Wen, G., Li, S.B., Zhang, B.S., and Guo, Z.X., *Processing of in situ toughened B-W-C composites by reaction hot pressing of B_4C and WC.* Scripta Materialia, 2000. **43**(9): p. 853-857.

[98] Perrot, P., *Boron – Titanium – Tungsten*, in *Refractory metal systems: Selected Systems from B-Mo-Ni to C-Ta-Ti*, G. Effenberg and S. Ilyenko, Editors. 2010, Springer Berlin Heidelberg: Berlin, Heidelberg. p. 194-201.

[99] Tennery, V.J., Finch, C.B., Yust, C.S., and Clark, G.W., *Structure-Property Correlations for TiB_2-Based Ceramics Densified using Active Liquid Metals*, in *Science of Hard Materials*, R.K. Viswanadham, D.J. Rowcliffe, and J. Gurland, Editors. 1983, Springer US: Boston, MA. p. 891-909.

[100] He, P., Dong, S., Kan, Y., Zhang, X., and Ding, Y., *Microstructure and mechanical properties of B_4C–TiB_2 composites prepared by reaction hot pressing using Ti3SiC2 as additive.* Ceramics International, 2016. **42**(1): p. 650-656.

[101] Tuffé, S., Dubois, J., Fantozzi, G., and Barbier, G., *Densification, microstructure and mechanical properties of TiB_2-B_4C based composites.* International Journal of Refractory Metals and Hard Materials, 1996. **14**(5): p. 305-310.

[102] Hotta, M. and Goto, T., *Densification and Phase Transformation of β-SiAlON-Cubic Boron Nitride Composites Prepared by Spark Plasma Sintering.* Journal of the American Ceramic Society, 2009. **92**(8): p. 1684-1690.

[103] Garrett, J.C., Sigalas, I., Wolfrum, A.K., and Herrmann, M., *Effect of cubic boron nitride grain size in the reinforcing of α-Sialon ceramics sintered via SPS.* Journal of the European Ceramic Society, 2015. **35**(2): p. 451-462.

[104] Lenčéš, Z. and Haviar, M., *SiAlON/SiC Micro-Nano-Composites*, in *Engineering Ceramics '96: Higher Reliability through Processing*, G.N. Babini, M. Haviar, and P. Šajgalík, Editors. 1997, Springer Netherlands: Dordrecht. p. 179-187.

[105] Garrett, J.C., Sigalas, I., and Herrmann, M., *TEM investigation of the interface formation in cubic boron nitride containing α-SiAlON composites.* Ceramics International, 2014. **40**(10): p. 16169-16175.

[106] Maglica, A., Krnel, K., Pribosic, I., and Kosmac, T., *Preparation and properties of B-SiAlON/ZrN nano-composites from ZrO2-coated Si_3N_4 powder.* Processing and Application of Ceramics, 2007. **1**(1-2): p. 49-55.

[107] Ye, F., Hou, Z., Zhang, H., Liu, L., and Zhou, Y., *Spark plasma sintering of cBN/β-SiAlON composites.* Materials Science and Engineering: A, 2010. **527**(18-19): p. 4723-4726.

[108] Garrett, J.C., Sigalas, I., Herrmann, M., Olivier, E.J., and O'Connell, J.H., *cBN reinforced Y-α-SiAlON composites.* Journal of the European Ceramic Society, 2013. **33**(11): p. 2191-2198.

[109] Wolfrum, A.K., Matthey, B., Michaelis, A., and Herrmann, M., *On the Stability of c-BN-Reinforcing Particles in Ceramic Matrix Materials.* Materials (Basel), 2018. **11**(2).

[110] Yuan, S., Journet, C., Linas, S., Garnier, V., Steyer, P., Benayoun, S., Brioude, A., and Toury, B., *How to Increase the h-BN Crystallinity of Microfilms and Self-*

Standing Nanosheets: A Review of the Different Strategies Using the PDCs Route. Crystals, 2016. **6**(5).

[111] Hubáček, M. and Ueki, M., *Chemical Reactions in Hexagonal Boron Nitride System.* Journal of Solid State Chemistry, 1996. **123**(2): p. 215-222.

[112] Hoang, D.-Q., Korneychuk, S., Sankaran, K.J., Pobedinskas, P., Drijkoningen, S., Turner, S., Van Bael, M.K., Verbeeck, J., Nicley, S.S., and Haenen, K., *Direct nucleation of hexagonal boron nitride on diamond: Crystalline properties of hBN nanowalls.* Acta Materialia, 2017. **127**: p. 17-24.

[113] Hagio, T., Nonaka, K., and Sato, T., *Microstructural development with crystallization of hexagonal boron nitride.* Journal of Materials Science Letters, 1997. **16**(10): p. 795-798.

[114] Li, Z., Liu, D., Zhang, J., and Tian, W., *Precipitates in Nb and Nb-V microalloyed X80 pipeline steel.* Microsc Microanal, 2013. **19 Suppl 5**: p. 62-5.

[115] Mishra, D.K. Thermo-mechanical processing of API-X60 grade pipe line steel, in *Department of Metallurgical and MAterials Engineering*. National Institute of Technology.

[116] Suikkanen, P. (2009) Development and processing of low carbon bainitic steels, in *Department of Mechanical Engineering*. 2009, University of Oulu.

[117] Sha, Q. and Li, D., *Microstructure and Properties of Low Manganese API X70 Pipeline Steel for Sour Service Application*, in *Proceedings of the 8th Pacific Rim International Congress on Advanced Materials and Processing*, F. Marquis, Editor. 2016, Springer International Publishing: Cham. p. 2183-2190.

[118] Tekin, E. (2012) API Standardı Petrol ve Doğalgaz Boruları ÇEliklerine Genel Bir Bakış. 2012, Atılım University.

[119] Hejazi, D., Haq, A.J., Yazdipour, N., Dunne, D.P., Calka, A., Barbaro, F., and Pereloma, E.V., *Effect of manganese content and microstructure on the susceptibility of X70 pipeline steel to hydrogen cracking.* Materials Science and Engineering: A, 2012. **551**(Supplement C): p. 40-49.

[120] Qiao, G.-y., Chen, X.-w., Zhang, Z.-e., Han, X.-l., Wang, X., Liao, B., and Xiao, F.-r., *Mechanical Properties of High-Nb X80 Steel Weld Pipes for the Second West-to-East Gas Transmission Pipeline Project.* Advances in Materials Science and Engineering, 2017. **2017**: p. 13.

[121] Engün, S. (2016) Termomekanik olarak haddelenmiş X70 kalite petrol boru çeliklerinin EBSD ve TEM Teknikleri ile karakterizasyonu, in *Department of Materials Science and Engineering*. 2016, Anadolu University: Eskisehir.

[122] Keast, V.J., Scott, A.J., Brydson, R., Williams, D.B., and Bruley, J., *Electron energy-loss near-edge structure – a tool for the investigation of electronic structure on the nanometre scale.* Journal of Microscopy, 2001. **203**(2): p. 135-175.

[123] Disko, M.M., Krivanek, O.L., and Rez, P., *Orientation-dependent extended fine structure in electron-energy-loss spectra.* Physical Review B, 1982. **25**(6): p. 4252-4255.

[124] Jaouen, M., Hug, G., Gonnet, V., Demazeau, G., and Tourillon, G., *An EELS and XAS Study of Cubic Boron Nitride Synthesized under High Pressure - High Temperature Conditions.* Microscopy Microanalysis Microstructures, 1995. **6**(1): p. 127-139.

[125] Stephens, A.P. and Brown, L.M. *EXELFS in graphitic boron nitride*. in *Quantitative microanalysis with High Spatial Resolution*. 1981. London.

[126] Turan, S., Davis, C.A., and Knowles, K.M. (1995) Orientation dependence of EELS spectra from hexagonal boron nitride, in *Electron Microscopy and Analysis Group Conf EMAG95*. 1995, IOP Publishing Ltd: Birmingham. p. 63.

[127] Hosoi, J., Oikawa, T., Inoue, M., Matsui, Y., and Endo, T., *Study of boron nitride by electron energy-loss spectroscopy.* Journal of Electron Spectroscopy and Related Phenomena, 1982. **27**(3): p. 243-254.

[128] Garvie Laurence, A.J., Craven Alan, J., and Brydson, R. (1995) Parallel electron energy-losss pectroscopy(PEELS) study of B in minerals: The electron energy-loss near-edge structure (ELNES) of the B K edge, in *American Mineralogist*. 1995. p. 1132.

[129] Leapman, R.D., Fejes, P.L., and Silcox, J., *Orientation dependence of core edges from anisotropic materials determined by inelastic scattering of fast electrons.* Physical Review B, 1983. **28**(5): p. 2361-2373.

[130] Martin, J.M., Belin, M., Mansot, J.L., Hssein, K., Zanehi, G., and Sevely, J. *EELS graphitic boron nitride fine structure studies*. in *Electron Microscopy European Congress*. 1988.

[131] Arenal, R., Kociak, M., and Zaluzec, N.J., *High-angular-resolution electron energy loss spectroscopy of hexagonal boron nitride.* Applied Physics Letters, 2007. **90**(20): p. 204105.

[132] Dresselhaus, M.S., Kalish, R., and Wieser, E., *Ion Implantation in Diamond, Graphite and Related Materials. Springer-Verlag Berlin, Heidelberg, 1992, 202 Seiten, 108 Abbildungen, 5 Tabellen, Preis: DM 79.00, ISBN 3-540-54956-0 — ISBN 0-387-54956-0.* Crystal Research and Technology, 1993. **28**(3): p. 316-316.

[133] Aradi, E. (2014) INVESTIGATIONS ON THE CHARACTERIZATION OF ION IMPLANTED HEXAGONAL BORON NITRIDE, in *Faculty of Science*. 2014, University of the Witwatersrand: Johannesburg.

[134] Machaka, R. (2006) Ion Beam Modifications of Boron Nitride By Ion Implantation, in *Materials Science Physics*. 2006, University of Witwatersrand: Johannesburg.

[135] Wen, Y., He, K., Zhu, Y., Han, F., Xu, Y., Matsuda, I., Ishii, Y., Cumings, J., and Wang, C., *Expanded graphite as superior anode for sodium-ion batteries.* Nat Commun, 2014. **5**: p. 4033.

[136] Carnera, A., Gasparotto, A., Berti, M., and Fabbri, R., *Influence of channeling effects on ion distribution and damage profiles during high energy ion implantation in Si.* Microchimica Acta, 1994. **114**(1): p. 205-211.

[137] Schroyen, D., Bruggeman, M., Dezsi, I., and Langouche, G., *Ion implantation in highly oriented pyrolytic graphite.* Nuclear Instruments and Methods in Physics Research Section B: Beam Interactions with Materials and Atoms, 1986. **15**(1-6): p. 341-343.

[138] Krasheninnikov, A.V. and Nordlund, K., *Channeling of heavy ions through multi-walled carbon nanotubes.* Nuclear Instruments and Methods in Physics Research Section B: Beam Interactions with Materials and Atoms, 2005. **228**(1-4): p. 21-25.

[139] Elman, B.S., Braunstein, G., Dresselhaus, M.S., Dresselhaus, G., Venkatesan, T., and Wilkens, B., *Channeling studies in graphite.* Journal of Applied Physics, 1984. **56**(7): p. 2114-2119.

[140] Shaw, N.J., *Densification and coarsening during solid state sintering of ceramics: A review of the models Pt 1.* Powder Metallurgy International, 1989. **21**(6): p. 16-21.

[141] German, R.M., *Fundamentals of sintering.* ASM International, Engineered Materials Handbook., 1991. **4**: p. 260-269.

[142] Coble, R.L., *Sintering Crystalline Solids. I. Intermediate and Final State Diffusion Models.* Journal of Applied Physics, 1961. **32**(5): p. 787-792.

[143] Rankin, J. and Sheldon, B.W., *In situ TEM sintering of nano-sized ZrO2 particles.* Materials Science and Engineering: A, 1995. **204**(1–2): p. 48-53.

[144] Kusunoki, M., Yonemitsu, K., Sasaki, Y., and Kubo, Y., *In Situ Observation of Zirconia Particles at 1200°C by High-Resolution Electron Microscopy.* Journal of the American Ceramic Society, 1993. **76**(3): p. 763-765.

[145] Wang, Z.L., *Zinc oxide nanostructures: growth, properties and applications.* Journal of Physics: Condensed Matter, 2004. **16**(25): p. R829-R858.

[146] Wang, Z.L., *Nanostructures of zinc oxide.* Materials Today, 2004. **7**(6): p. 26-33.

[147] Roy, T.K., Bhowmick, D., Sanyal, D., and Chakrabarti, A., *Sintering studies of nano-crystalline zinc oxide.* Ceramics International, 2008. **34**(1): p. 81-87.

[148] Wang, D. and Reynolds, N., *Photoluminescence of Zinc Oxide Nanowires: The Effect of Surface Band Bending.* ISRN Condensed Matter Physics, 2012. **2012**: p. 1-6.

[149] Wang, D., Seo, H.W., Tin, C.C., Bozack, M.J., Williams, J.R., Park, M., Sathitsuksanoh, N., Cheng, A.-j., and Tzeng, Y.H., *Effects of postgrowth annealing treatment on the photoluminescence of zinc oxide nanorods.* Journal of Applied Physics, 2006. **99**(11): p. 113509.

[150] Egerton, R.F., Li, P., and Malac, M., *Radiation damage in the TEM and SEM.* Micron, 2004. **35**(6): p. 399-409.

[151] J., G.T., *Sintering of Zinc Oxide.* Journal of the American Ceramic Society, 1954. **37**(11): p. 534-538.

RESUME

Name-Surname:	Umut SAVACI
Birth Place and Date:	Ankara/1986
Foreign Language:	English
E-mail:	usavaci@gmail.com

Education

2014 - 2014 ***Erasmus Internship (3 Months)***
Denmark Technical University
Center of Electron Nanoscopy,
Supervisor; Prof. Dr. Jakob B. Wagner

2012 – 2018 ***Ph.D.***
Anadolu University, Turkey
Department of Materials Science and Engineering
Supervisor; Prof. Dr. Servet TURAN
High honor Degree (GPA: 3.96/4.00)

2009 - 2012 ***Masters***
Izmir Institute of Technology
Department of Materials Science and Engineering
Supervisor; Prof. Dr. Mustafa GÜDEN
High honor Degree (GPA: 3.79/4.00)

2005 – 2009 ***Graduate***
Anadolu University, Turkey
Department of Materials Science and Engineering
Supervisor; Prof. Dr. Ender SUVACI
1st place and High honor Degree (GPA: 3.57/4.00)

Publications

2018 G. Tuğrul, T. Gökhan, U. Savaci, A. Genç, S. Turan, E. Sarı, M.M. Demir, *"Polarized Emission from CsPbBr3 Nanowires Embedded-Electrospun PU Fibers"*, Nanotechnology, 2018, 29-13:

2018 D.Yilmaz, U. Savaci, N. Koç, S.Turan, *"Carbothermic reduction synthesis of calcium hexaboride using PVA-calcium hexaborate mixed gels",* Ceramics International,2018, 44-3:2976-2981.

2016 U. Savaci, A. Çınar, A.T. Seyhan, S. Turan*, "Scanning Transmission Electron Microscopy of SiAlON/Graphene Nano Plateletes Composites Obtained with a Novel Homogenization Approach",* Proceedings of Microscopy and Microanalysis 2016, 22-S3:1900-1901.

2012 U. Savaci, S.Yilmaz, M. Güden, *"Open cell lead foams: processing, microstructure and mechanical properties"*, Journal of Materials Science, 2012, 47:5646-5654.

… U. Toçoğlu, M. Alaf, U. Savaci, S. Turan, H. Akbulut, *"Yolk-Shell Structured Silicon/Graphene Composites as Free-Standing High Performance Li-ion Battery Electrodes"*, Under Review

… P.S. Erden, E. Özel, E. Suvacı, U. Savacı, S. Turan, *"Chemical Stability of Zinc Stannate (Zn_2SnO_4) in Aqueous Environments"*, In progress

… K.B. Dermenci, U. Savacı, S. Turan, E. Suvacı*," The Effect of Porosities on the Electrochemical Properties of ZnO Anode Materials with MicNo® Morphology",* Submitted

… A. M. Genc, O. Acar, U. Savacı, S. Turan, Y. E. Kalay, "*Investigation of Phase Selection Hierarchy in MnAl-based alloys",* Metallurgical and Materials Transactions A, In Progress

National and International Proceedings

2017 International Congress on Chemistry and Materials Science, Ankara, Turkey

U. Savacı, Z. Yılmaz, N. Ay, S. Turan, "*Characterization of In-Situ Synthesized Hexagonal Boron Nitride and Silicon Carbide Composites with Conventional and Advanced Transmission Electron Microscopy Methods",* Oral Presentation

2017 13th Nanoscience and Nanotechnology Conference, Antalya, Turkey

A. Özden, U. Savacı, H. Şar, C. Sevik, N. K. Perkgöz, S. Turan, F. Ay, "*Evolution of 2D MoS_2 Structures as a Function of the Hydrogen Flow Rate",* Oral Presentation

2017 2nd International Symposium on Materials for Energy Storage and Conversion, Kapadokya, Turkey,

S. Turan, U. Savacı, K.B. Dermenci, "*State of the Art on Electron Microscopy Techniques for the Lithium Detection in Lithium Containing Energy Materials",* Oral Presentation

2017 ElektroseramikTR 2017 Workshop, Gebze, Turkey

S. Turan, U. Savacı, S. Başkut, *"Elektron Mikroskopi Temelli Elektroseramik Karakterizasyon Tekniklerindeki Son Gelişmeler",* Oral Presentation

2017 Uluslararası katılımlı 23th Elektron Mikroskopi Kongresi, Antalya, Turkey

U. Savacı, S. Turan, *"Anadolu'da in-situ TEM Isıtma Maceraları: Hayaller ve Gerçekler",* Oral Presentation

2017 International Materials Technologies Conference, Istanbul, Turkey

U. Savacı, Z. Yılmaz, N. Ay, S. Turan, *"Characterization of Defects in Hexagonal Boron Nitride by Means of Conventional HRTEM Imaging and Advanced Electron Diffraction Methods in TEM",* Poster Presentation

2017 Uluslararası katılımlı 23th Elektron Mikroskopi Kongresi, Antalya, Turkey

U. Savacı, Z. Yılmaz, N. Ay, S. Turan, *"Application of Precession Electron Diffraction Technique on Silicon Carbide/Boron Nitride Composite in TEM",* Poster Presentation

2017 2nd International Conference on Materials Science and Technology, Cappadoccia,Turkey

S. Turan, Z. Yılmaz, U. Savacı, N. Ay, *"Production of In-situ Formed HBN-SiC Composites and Their Characterisation by Using Transmission Electron Microscopy Techniques",* Poster Presentation

2017 Uluslararası katılımlı 23. Elektron Mikroskopi Kongresi, Antalya, Turkey

U. Savacı, A. Uğur, N. Ay, S. Turan, *"Atomik Katman Biriktirme Yöntemi ile Alümina Kaplanmış Hekzagonal Bor Nitrürün Karakterizasyonu",* Poster Presentation

2017 15th Conference and Exhibition of the European Ceramic Society, Budapest, Hungary
U. Savacı, Z. Yılmaz, N. Ay, S. Turan, *"Microstructure Characterization Of Silicon Carbide/Boron Nitride Composite By Precession Electron Diffraction Technique In Transmission Electron Microscope",* Poster Presentation

2016 18th International Metallurgy & Materials Congress, Istanbul, Turkey
A. Sert, U. Savacı, O.N. Çelik, S. Turan, "*Characterization of Tribological Properties of Lubricating Oil With Silicon Nitride Nanoparticle Additives"*, Oral Presentation

2016 18th International Metallurgy & Materials Congress, Istanbul, Turkey
S.Turan, U. Savaci, S. Başkut, "*Recent Developments on the Microstructural Characterization Techniques and Strategies for Better use of Existing Microscopes"*, Oral Presentation

2016 18th International Metallurgy & Materials Congress, Istanbul, Turkey
U. Savacı, S. Turan, *"Tribological and Microstructural Characterization of Natural Diatomite Filled Epoxy Composites",* Poster Presentation

2015 22nd Electron Microscopy Congress, Istanbul, Turkey
U. Savacı, S. Turan, *"Geçirimli Elektron Mikroskopisi İn-Situ Isıtma ve Devinimli elektron Difraksiyonu Teknikleri",* Oral Presentation

2015 22nd Electron Microscopy Congress, Istanbul, Turkey
U. Savacı, S. Turan, E.K. Atan, A. Doğan, M. Sezen, D. Bondiaoli, *"Characterization of Functional Nano Coatings on Ceramic Tiles",* Poster Presentation

2014 International Microscopy Conference (IMC) 2014, Prague, Czech Republic
Katılımcı

2013 Materials Research Society (MRS) Fall Meeting 2013, Boston, A.B.D

2011 International Syntactic and Composite Foams III, Cetraro, Italy
"Development of a New Method for Production of Lead (Pb) Foams for Lead- Acid Batteries", Sözlü ve Poster Presentation

2009 5th National Nanoscience and Nanotechnology Conference, Eskişehir, Turkey

2009 Eskişehir sanayi odası proje fuarı 2009, Eskişehir, Turkey
"*Novel Application of Textured Ceramics"*, Poster Presentation

2008 Malzeme ve Teknoloji Çalıştayı, Eskişehir, Turkey

2007 SERES IVth Uluslar arası seramik, cam, emaye, sır ve boya konferansı, Eskişehir, Turkey

Projects

2017-2019 Researcher, *Düşük Histerisisli Yüksek Gerinme ve Yüksek Sıcaklık Kararlılı Sergileyen Yönlenmiş yapıda Kurşunsuz $K_{0.5}Bi_{0.5}TiO_3$-$BaTiO_3$-$Na_{0.5}Bi_{0.5}TiO_3$ Piezoelektrik Seramiklerin Geliştirilmesi*, TÜBİTAK 1001, 116M214, Project Budget: 240.192,00 TL

2015-2018 Researcher, *Geçirimli Elektron Mikroskopu ile İn-situ ve Devinimli Elektron Difraksiyonu Teknikleri Kullanılarak Malzeme*

Karakterizasyonu, Anadolu University, 1504F168 Project Budget: 39.874,40 TL

2015-2016 Researcher, *İn-situ Mikroskop Karakterizasyon Teknikleri ile Araştırma Olanaklarının İyileştirilmesi*, Anadolu University, Project Budget: 1.091.567,00 TL

2015-2016 Researcher, *Grafen İçeren SiAlON Seramiklerinin EBSD, FIB ve TEM Teknikleri ile Karakterizasyonu,* Anadolu Üniversitesi, 1505F289 Project Budget: 30.000,00 TL

2014-2017 Researcher, *Enerji Depolama ve Etkin Taşınabilir Enerji Kaynağı için Katı Hal Lityum İyon Pillerin Üretimi,* Anadolu Üniversitesi, 1502F070 Project Budget: 666.112,28 TL

2013-2016 Researcher, *Malzeme Bilimi ve Mühendisliği Eğitim Programının İyileştirilmesi,* Anadolu Üniversitesi, 1305F085, Project Budget: 1.268.270,00TL

Awards and Bursaries

2017 Poster award, Materials Science 1st position, 23. Ulusal Elektron Mikroskopi Kongresi

2015 High Resolution Electron Microscopy Summer School, Arizona State University, Bursary

2013 Highest 3th GPA between 1993-2013 years, Undergraduate Success Award, Anadolu University, Department of Materials Science and Engineering, Eskişehir,

2013-2018 TÜBİTAK 2211 Ph.D. Bursary

2012 Department of Materials Science and Engineering, Masters High Honor Degree (GPA: 3.79/4.00)

2009 Department of Materials Science and Engineering, Undergraduate Highest ranked Student Award and High Honor Degree (GPA: 3.57/4.00)